Development of Multimodal Magnetic-Plasmonic Nanocomposite Materials

Trinity College Dublin
Coláiste na Tríonóide, Baile Átha Cliath
The University of Dublin

A thesis submitted to the School of Chemistry,

Trinity College Dublin,

for the degree of Doctor of Philosophy

By

Shelley Stafford

Under the supervision of Prof. Yurii K. Gun'ko

2021

Summary

The main aim of this work was to prepare a wide range of magnetic-plasmonic nano- and micro-materials and to explore their properties and potential applications. The combination of both magnetic and plasmonic properties in one nanocomposite is the basis for development of new multifunctional nanomaterials with unique multimodal properties. These nanocomposites have great potential to find a wide range of applications in nano- and biotechnologies.

Chapter 1 of this thesis presents a review of the literature that is of relevance to this research, as well as a discussion on the underlying theory of the work carried out. This includes a discussion on magnetic and plasmonic nanomaterials alongside a broader discussion on magnetism and plasmon resonance, as well as a more general discussion and literature review of current magnetic-plasmonic nanomaterials. A broad introduction was also given to DNA and calcium carbonate based materials, which are relevent to later chapters in this work.

Chapter 2 describes all the details pertaining to the experimental work performed in this thesis, including all the starting materials used and experimental procedures carried out for each chapter. All the instrumental techniques used to characterise the materials prepared in this work were also discussed in detail in this chapter.

Chapter 3 focuses on the development of polyelectrolyte-stabilised nanocomposites formed via the electrostatic interactions between PSS-stabilised magnetite of varying concentrations, and PAH-stabilised gold nanoparticles. It details the synthesis and characterisation of three concentrations of PSS-stabilised magnetite nanoparticles as well as their comprehensive characterisation, as well as the synthesis and characterisation of PAH-stabilised gold nanoparticles. The oppositely charged magnetic and plasmonic nanocomposites were combined to form a hybrid magnetic-plasmonic nanocomposite that retained the gold nanoparticles through multiple magnetic separation cycles. As a proof-of-concept, the study was repeated using unstabilised gold nanoparticles and gold nanoparticles stabilised using acetic acid, and it was found these nanocomposite materials did not retain the gold nanoparticles through magnetic separation. The resulting polyelectrolyte nanocomposites were then tested for their ability to colourimetrically detect mercury ions in aqueous solution.

Chapter 4 details the synthesis of anisotropic gold nanoparticles, as well as the preparation of PAH-stabilised magnetite and PAH-stabilised gold nanoparticles for the development of magnetic and hybrid plasmonic nanostructures using AuAg nanowires. Owing to their monodispersity and reproduciblity, only the two PAH-stabilised nanoparticle species were used in the formation of the AuAg nanowire composite structures. Monitoring of the morphology of these nanocomposite structures over time was carried out using SEM.

Chapter 5 presents the development of a one-pot synthetic approach to several concentrations of DNA-stabilised magnetite and DNA-stabilised gold nanoparticles. These nanoparticles were characterised extensively using a variety of instrumentation techniques. These nanoparticles were then combined to form new DNA-stabilised nanocomposites which were analysed using UV-Vis and Raman spectroscopy.

Chapter 6 describes the development of magnetic-plasmonic calcium carbonate based micromaterials. The synthesis of these materials was achieved through first preparing magnetite nanoparticles stabilised using a variety of different chemical species, as well as preparation of citric acid- and PAH-stabilised gold nanoparticles. The calcium carbonate microstructures were then prepared and the magnetic and/or plasmonic nanoparticles are added to the microstructures by virtue of electrostatics or layer-by-layer deposition techniques. These nanoparticles were fully characterised by various instrumental techniques.

Finally, chapter 7 provides the conclusions of the entire work, and also outlines the main achievements of this body of research. An outline and plan for future work is also presented in this chapter.

Declaration

I declare that this report details entirely my own work. Due reference and acknowledgement of the work of others is given where appropriate.

Signed .....

Shelley Stafford B.A. (Mod.)

Acknowledgements

First and foremost, I would first like to express my most sincere gratitude to my supervisor and mentor, Prof. Yurii Gun'ko. His unwavering support, encouragement and enthusiasm over the last few years not only made carrying out this work possible, but a thoroughly enjoyable experience. Even more so after four years, I feel like I won the lottery in terms of Ph.D. supervisors. I also must acknowledge the fact that I never, not once, accidentally called him 'Dad' to his face. This is currently, and will remain one of my greatest achievements.

To my actual parents, Dave and Liz, your love, blind support (and slight confusion over what it was exactly I was studying) over the last four years has been invaluable. Every homemade school lunch, freshly ironed uniform and cup of tea at the crack of dawn has led up to this moment, and I can never thank you enough. And to Luke and Bella, the best siblings a gal could ever ask for, thank you for always being there to make me laugh and remind me that there is, in fact, more to life than just magnetic-plasmonic nanoparticles.

To my esteemed colleague and favourite person, Dr. Fearghal C. Donnelly, thank you for always being there to hold my hand and run my XRD (although thankfully never at the same time). Your love, support and many dinners made writing this thesis a hell of a lot easier, and that's not even considering the endless hours of proof-reading. This thesis, and indeed the world, is all the better because of your influence.

To Nuala and Fearghal (and the Donnellys *et al.*), thank you so much for taking me in and letting me ruin the look of your dining room to write this thesis in the midst of a global pandemic. I'm truly grateful for the endless cups of tea and baking supplies - it was a joy to spend lockdown with you all. I only hope I can repay your kindness in apple pies.

Sincere thanks must go to Dr. Manuel Ruether, Clive Dowling, Eoin McCarthy and Dermot Daly, whose help and extreme patience in teaching me various instrumentation techniques was very much appreciated. To John O'Donoghue and the Chem Ed. committee for their friendship and lemon cake, it was an honour and a lot of fun to work with you all. And to the Chemistry department more generally, of whom there are far too many to name, thank you all for being so pleasant to work with and a blast to go to the pub with.

To the Gun'ko group past and present, colleagues first but friends for life, I can never express the immense gratitude and luck I feel for having the opportunity to work with you all. Monday mornings were all the brighter for being able to sit and have coffee with you all.

Contents

List of Figures

List of Tables

Abbreviations

AFM - Atomic Force Microscopy

CTAB - Cetyl Trimethylammonium bromide

DLS - Dynamic Light Scattering

EDX - Energy Dispersive X-Ray

FTIR - Fourier Transform Infrared

MRI - Magnetic Resonance Imaging

NIR - Near Infrared

NSAID - Non-Steroidal Anti-Inflammatory Drug

PAH - Poly(allylamine Hydrochloride)

PSS - Poly(sodium styrene sulfonate)

PVP - Polyvinylpyrrolidone

SDS - Sodium Dodecyl Sulfate

SEM - Scanning Electron Microscopy

SERS - Surface Enhanced Raman Spectroscopy

SPR - Surface Plasmon Resonance

TEM - Transmission Electron Microscopy

TGA - Thermogravimetric Analysis

TIR - Total Internal Reflection

VSM - Vibrating Sample Magnetometry

XRD - X-Ray Diffraction

Chapter 1

Introduction

1.1 Nanomaterials

Nanomaterials represent one of the most diverse and colourful areas of research today, spanning various disciplines and offering a huge array of potential applications. Currently, nanomaterials have found use across many sectors, including electronics, bio-imaging, medicine, and even cosmetics[1,2]. A nanomaterial can be defined as any material that has at least one dimension between 1 - 100 nm[3]. To put this into perspective, an average strand of hair is between 80,000 - 100,000 nm wide[4]. A visual schematic representation of the nanoscale is shown in Figure 1.1.

While research and interest in the area of nanomaterials has surged over the past twenty years, nanoparticles have actually been utilised in day-to-day life for centuries. In fact, it could be said that, unbeknowst to them, medieval stained glass artisans were the first nanoscientists. In preparing stained glass, they trapped gold and silver nanoparticles in silicon dioxide, creating the deep red and yellow colours we see in ancient glass today[5].

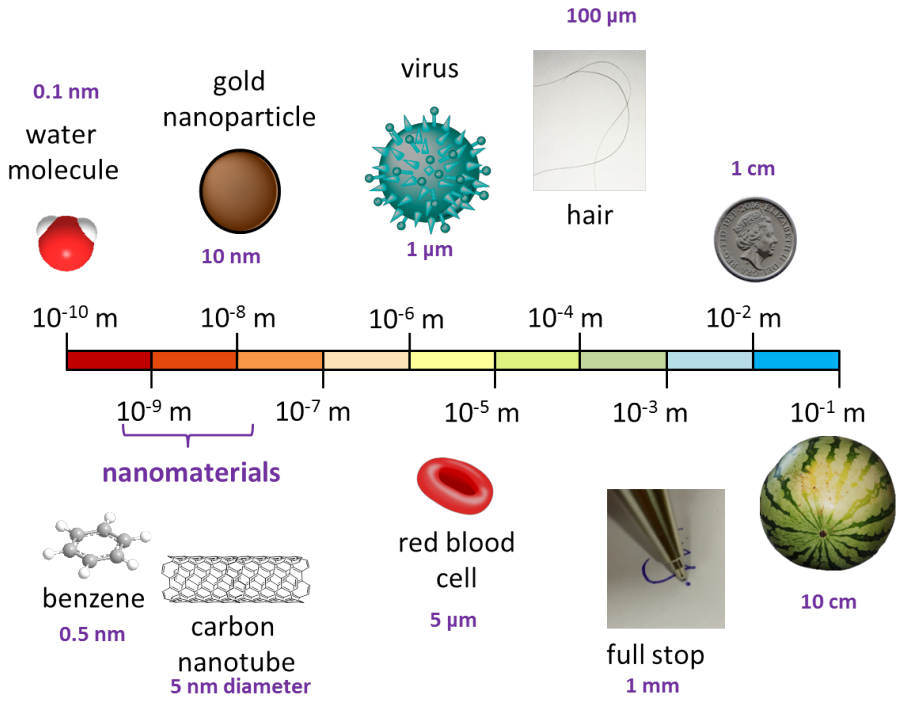

Figure 1.1: Visual representation of the nanoscale. Adapted from ref[4]

The size of a nanomaterial has a considerable effect on the physiochemical properties of the material. A well studied example is the size-colour dependence of spherical gold nanoparticles[6,7]. As the diameter of a spherical gold nanoparticle is increased, the light absorbance of the nanoparticle becomes progressively more red-shifted. A slight alteration in the region of ten nanometers can bring about a signficant colour change. An illustration of colloidal gold nanoparticles is shown in Figure 1.2. The colour of a gold nanoparticle solution will also change depending on the extent of aggregation in the solution. These properties can be exploited for a variety of sensing applications.

Arguably one of the main features of interest are the properties of nanoparticles that arise due to their large surface-to-volume ratios. In a bulk material, the number of atoms at the surface available for reaction is very small in comparison to the number of atoms contained within the material. As the size of a material is decreased, its surface area increases. This effect is at its most significant when the

Figure 1.2: Solutions of gold nanoparticles increasing in size from left to right[8].

particle is on the nanoscale. Nanoscale materials can often display radically different properties than their bulk counterparts, and can sometimes demonstrate completely new effects, such as plasmon resonance and quantum confinement, and have other properties, such as luminescence, greatly altered[9].

As a result of these exceptional properties, and due to great advances in instrumental techniques such as electron microscopy and spectroscopy, the field of nanomaterials research has experienced great prominence in recent years, and is the subject of swathes of cutting edge multi-disciplinary research. The vast number of potential and proposed applications in biomedical imaging, sensing, theranostics, catalysis, optoelectronics and many others ensures that this research will be of great interest for years to come.

1.2 Magnetic Nanoparticles

In the past few years, the development of new magnetic nanomaterials has attracted great attention. This is due to their unique size-dependent magnetic properties, which offer a huge range of current and potential applications. In biomedicine, for example, the use of an external magnetic field could be used to guide mag-

netic nanoparticles to an area of interest, thus enabling site-specific drug-delivery *in-vivo*[10]. Magnetic nanoparticles will cause local heating when subjected to an external magnetic alternating current (AC), which allows for the possibilities of hyperthermia treatment[11].

One of the attractive properties of magnetic nanoparticles is that they can be easily functionalised with a number of different functional groups and chemical species, and, in addition to this, magnetic separation can be used as a fast and easy cleaning approach to purify the nanoparticles. The magnetic nanoparticles may be functionalised with drug molecules, fluorescent compounds, and various hydrophobic and hydrophilic coatings. Moreover, magnetic nanoparticles can be coated with a layer of some other functional material, such as a metal, semi-conductor, or dielectric material etc. Size and monodispersity are of the utmost importance when synthesising magnetic nanoparticles, as these factors will have a huge impact on the magnetism of the resulting nanoparticles.

1.2.1 Structure of Magnetic Ferrite Nanoparticles

Many magnetic materials, including magnetite, are classified as ferrites. Ferrites are ionic compounds, that consist of positively charged iron and other metal ions, and negatively charged oxygen ions. They have a cubic close packed structure (ABCABC...), where the octahedral and tetrahedral sites alternate throughout the structure. Spinels can be either 'normal' or 'inverse'. In a normal spinel structure, the divalent atoms occupy the tetrahedral sites, whereas in an inverse spinel, the divalent atoms occupy the octahedral sites.

Magnetite (Fe_3O_4) is used throughout this work, and is an example of an inverse spinel. In magnetite, the divalent Fe^{2+} occupy half the octahedral sites, and the

trivalent Fe^{3+} ions occupy the rest of the octahedral sites and all the tetrahedral sites. A diagram showing the inverse spinel structure of magnetite is shown in Figure 1.3. This inverse spinel structure is adopted for Fe_3O_4 due to the larger Fe^{2+} ions prefering to occupy the more spacious octahedral positions.

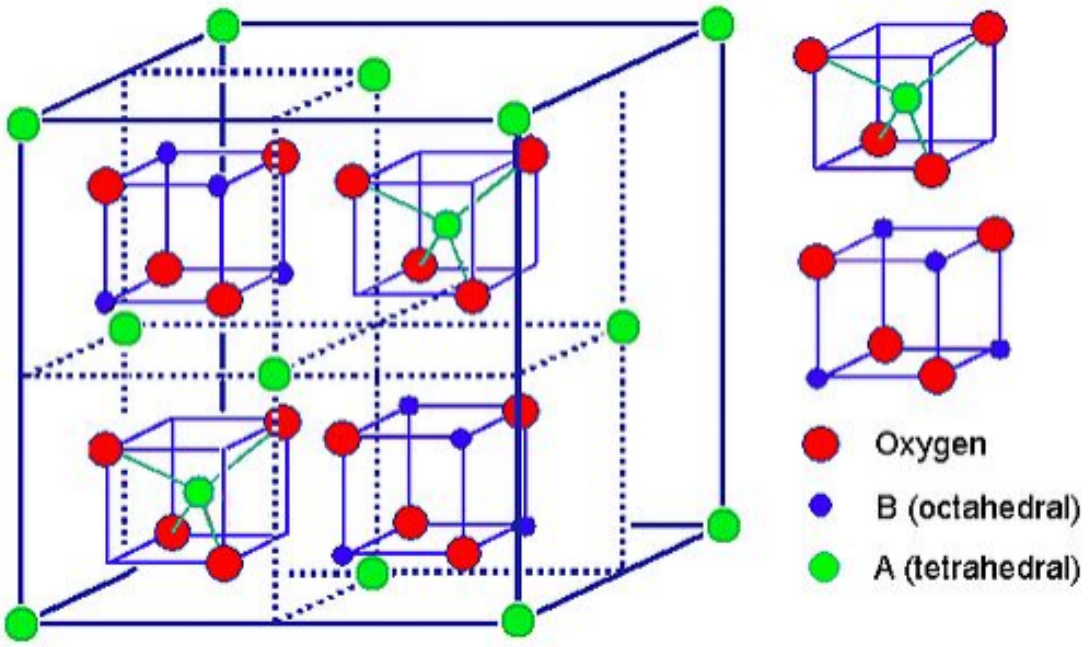

Figure 1.3: Diagram showing an inverse spinel structure. In the case of magnetite, half of the B sites are occupied by Fe^{2+}, and Fe^{3+} ions occupy the rest of the B sites and all of the A sites. Taken from ref[12].

Above a certain temperature, known as the Verwey transition temperature (T_v), the Fe^{2+} and the Fe^{3+} are randomly distributed over the octahedral sites, permitting the relatively easy exchange of valence as follows:

$$Fe^{2+} - e^{-} \longleftrightarrow Fe^{3+} \tag{1.1}$$

i.e. thermally activated fast-electron hopping occurs over T_v. When magnetite is cooled below the Verwey transition temperature, charge ordering occurs together with the reduction of crystal symmetry from cubic to monoclinic. This is a metal-

insulator transition and occurs at 122 K[13].

1.2.2 Magnetism of Magnetic Ferrite Nanoparticles

Magnetite is the main subject of the magnetic studies carried out in this work, and was in fact the first encounter man had with magnetism as a concept. Magnetite, also known as 'lodestone' was first discovered roughly 4,000 years ago by a Greek shepherd named Magnes. He found that the nails in his boot were attracted to the rock that he was standing on[14]. In the following years and up to the present day, magnetite has been utilised in a vast array of day-to-day applications.

Magnetism occurs due to the intrinsic property of electron spin. Every electron has its own orbital and spin moment. At a sufficiently high temperature, all materials are paramagnetic, but below a certain critical temperature, the electron spins can adopt a number of different ordered arrangements, namely they can be diamagnetic, ferromagnetic, anti-ferromagnetic, ferrimagnetic and paramagnetic. Diamagnetic materials have no unpaired electrons, and therefore they have no magnetic moment. When a magnetic field is applied, these materials will be repelled and a small magnetic moment will be induced, which will disappear as soon as the external magnetic force is removed. Paramagnetic materials have unpaired electrons that are randomly oriented throughout the sample. If an external magnetic moment is applied to these materials, their electron spins will align with the applied magnetic field.

Below a certain critical temperature, iron oxide will undergo a transition to a magnetically ordered state, they will be ferromagnetic, antiferromagnetic or ferrimagnetic[15]. This transition occurs at the Curie temperature for ferro- and ferri-magnetic materials, and the Néel temperature for anti-ferromagnetic materials. An illustration showing the different spin states is shown in Figure 1.4.

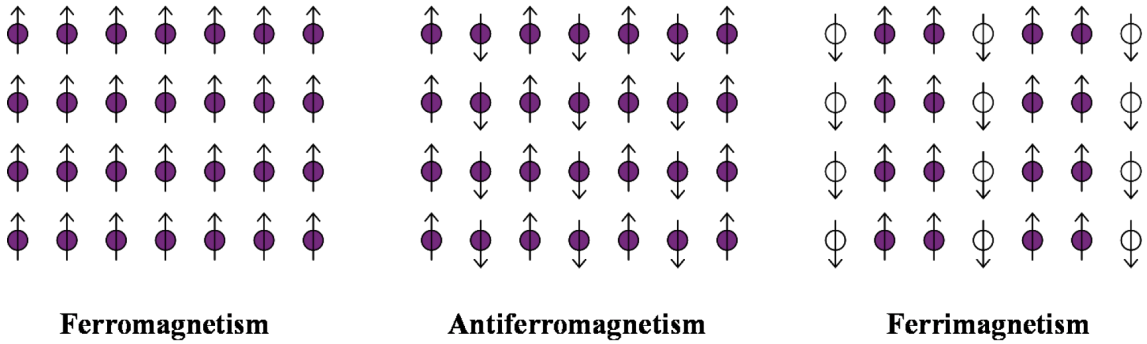

Figure 1.4: Illustration showing the different magnetic orders in ferrites. Taken from ref[15].

Both ferri- and ferro-magnetic materials will be strongly attracted to an applied magnetic field. Ferromagnetic materials have a magnetic moment due to the parallel alignment of their magnetic spins, whereas antiferromagnetic materials have an overall magnetic moment of zero, because their spins are antiparallel to eachother. Similarly, ferrimagnetic materials have spins that are antiparallel, but they do have a magnetic moment as the different spins have unequal magnetic moments.

All of these different magnetic materials will have a domain structure. A domain refers to a region in which all of the spins are aligned in the same manner (either parallel or antiparallel). The saturation magnetisation (M_s) refers to the point at which all of the magnetic domains in a particle are aligned in the same direction. Superparamagnetism, a special case of paramagnetism, occurs in nanoparticles when their size is equal to a single magnetic domain. Nanoparticles that have uniaxial anisotropy will randomly flip in the direction of their magnetisation due to thermal energy. The average time to perform such a flip is called the Néel relaxation time, which is described in the equation below.

$$\tau = \tau_0 exp(\frac{\Delta E}{K_B T}) \tag{1.2}$$

Where τ_0 is the length of time characteristic of the probed material (normally this

has magnitude of between 10^{-9} to 10^{-12} seconds), ΔE is the energy barrier that has to be overcome thermally, K_B is the Boltzman constant and T is the temperature. Without an external magnetic field, the net magnetic moment of superparamagnetic nanoparticles will be zero. As soon as a magnetic field is applied the nanomaterials react similarly to a paramagnet, with the exception that their magnetic susceptibility is much larger (hence the term - 'super' paramagnetism).

Superparamagnetic, paramagnetic, ferromagnetic and diamagnetic nanoparticles all behave differently under the influence of an external magnetic field. An example of the behaviour of each type of magnetic material is shown in Figure 1.5. Paramagnetic and diamagnetic materials behave oppositely in an applied magnetic field. Diamagnetic materials will be repelled by the magnetic field, whereas as the strength of the external magnet is increased, the magnetisation of the paramagnetic material will increase. For ferromagnetic materials, a hysteresis loop is obtained, for multi-domain particles this loop will be quite broad, and will get narrower as the number of domains decreases. Superparamagnetic materials will respond to the magnetic field but retain no magnetic memory, this can be seen in their sigmoidal shape with no hysteresis loop. The difference between ferromagnetic behaviour and superparamagnetic behaviour is primarly determined by the size of the particle. As the particle gets small enough (i.e. one particle is a single magnetic domain) it will become superparamagnetic.

1.2.3 Main Methods of Synthesis of Magnetic Nanoparticles

Coprecipitation Method

Chemical coprecipitation is a common method of synthesis for magnetic nanoparticles, and involves mixing chosen metal precursors in a specific ratio, then using a base, such as NH_4OH, to precipitate out the nanoparticles[17,18]. Ordinarily, coprecip-

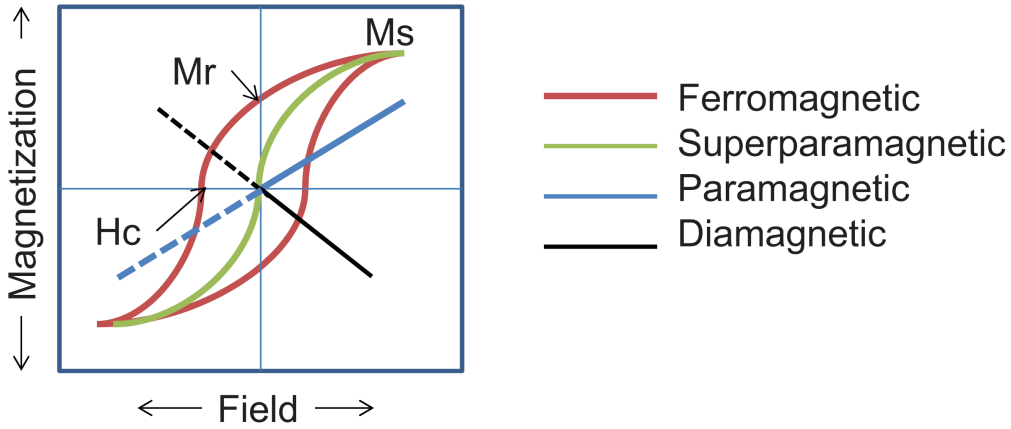

Figure 1.5: Sample magnetisation curves showing the different responses of ferromagnetic, superparamagnetic, paramagnetic and diamagnetic materials[16].

itation is carried out in aqueous media, which lends itself to biomedical applications — phase transfer reactions are not usually necessary, and the stabilising agent and coating material can be easily chosen to fit a specific purpose. A common approach involves precipitating magnetic nanoparticles and stabilising them *in-situ*, before further functionalisation with another outer layer on the nanoparticles that can facilitate either the attachment or targeting of another species. This method can be applied to a wide range of ferrites; magnetite is the most common and a sample equation is shown below.

$$Fe^{2+} + 2\,Fe^{3+} + 8\,OH^- \longrightarrow Fe_3O_4\downarrow + 4\,H_2O \tag{1.3}$$

The resulting magnetite nanoparticles are normally spherical and approximately 10 nm in diameter. Coprecipitation is a simple, highly reproducible method of producing magnetic ferrite nanoparticles.

Thermal Decomposition

Thermal decomposition, initially used to synthesise high quality semiconductor nanocrystals, is now also commonly employed to synthesise monodisperse magnetic nano-crystals[19–21].

Thermal decomposition involves the heating (often to temperatures in the region of 300 °C) of organometallic precursors in organic solvents that contain a stabilising surfactant. Examples of such organometallic precursors include, but are not limited to, metal acetylacetonates (e.g., $Fe(acac)_3$) and metal carbonyls (e.g., $Fe(CO)_5$)[22].

Solvothermal Methods

Solvothermal methods are now routinely used to prepare magnetic iron oxide nanoparticles[23]. In the first studies on this synthetic approach, Cupferron transition metal ion complexes were used as precursors to numerous metal oxide nanoparticles[24]. Presently, the solvothermal method can also be used to synthesise and stabilise magnetite in a single step. This is achieved by dissolving $FeCl_3$ salts in ethylene glycol with gelatin and sodium acetate, and reacting at 200 °C for 6 hours[25].

1.2.4 Applications of Magnetic Nanoparticles

Sensing

One of the most promising applications for magnetic nanoparticles is magnetic sensing. Magnetic nanoparticles are highly favoured for this application due to their high saturation magnetisation, superparamagnetism, stable magnetic and surface properties as well as their sensing specific properties[26]. However, magnetism can also be a double-edged sword in terms of sensing. Generally speaking, the stronger the magnetism of the nanoparticles, the better for the collection of analytes for separation and sensing. This can be an issue however when the nanoparticle solution is not sufficiently superparamagnetic, which can be harmful for the result of the sensing assay, or even fatal if the sensing is being carried out *in-vivo* as it can cause the formation of an embolism[27,28].

A highly important factor in the use of magnetic nanoparticles for sensing is that

they respond quickly and strongly to an external magnetic field. When the superparamagnetic nanoparticles become magnetised by the external magnet, they undergo magnetophoresis. The term 'magnetophoresis' is used to describe the movement of a magnetic nanoparticle through a viscous medium under the influence of an external magnetic field[29]. Two factors improve magnetophoresis: a high saturation magnetisation and a high magnetic susceptibility. This allows the fast, strong response of the nanoparticles even with the use of a low applied magnetic field. Just as important is that the nanoparticles must rapidly demagnetise as soon as the external magnet is removed.

In order to carry out sensing with the nanoparticles, they must be first functionalised with a species that will cause the binding of the analyte. When these nanoparticles are then dispersed throughout the solution, they will bind to the analyte of interest before collection using a magnetic field. The analtye-bound magnetic nanoparticle can then either be removed from the rest of the sample when brought to a surface for detection (preconcentration) or redispersed in a purified solution (separation). An illustration showing the preconcentration and separation techniques is shown in Figure 1.6.

One of the first examples of magnetic nanoparticles being utilised for sensing was by Wang *et al.* in 2001[30]. In this work, DNA was detected at low concentrations through preconcentration and then measured in a separate solution. DNA-stabilised nanoparticles were added to a solution in which they then bound with their complementary biotinylated target oligonucleotides. These nanoparticles were magnetically separated from this solution and added to a second solution of streptavidin-coated gold nanoparticles. The gold nanoparticles were bound with the captured biotinylated DNA, and then the gold tag was dissolved so that the amount of DNA present could be quantified through measurements of the gold by anodic stripping analysis.

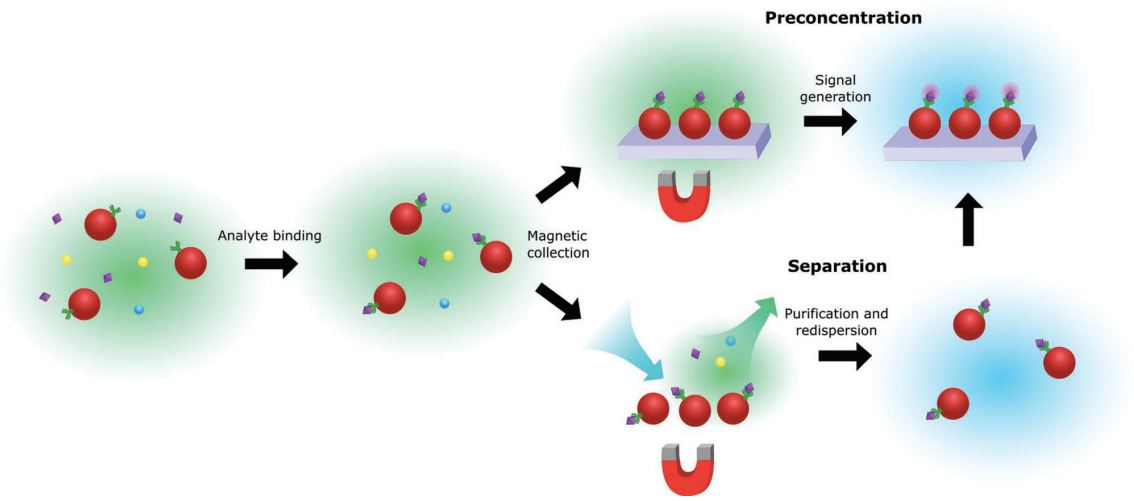

Figure 1.6: Illustration showing both the preconcentration and separation approaches to sensing using magnetic nanoparticles. Taken from ref[26].

Other examples of magnetic nanoparticles being used for sensing include work by Mirkin *et al.* which utilised magnetic separation as an ultra-sensitive method for detecting protein analytes using DNA-encoded magnetic nanoparticles[31]. The technique used in this work was 1 - 6 orders of magnitude more sensitive than a conventional ELISA-based assay. Magnetic nanoparticles can also be used for the detection and quantification of circulating tumour cells (CTCs). CTCs are cells that have been shed from a primary tumour into the vascular system of a patient where they then circulate in the blood system[32]. The preconcentration and detection of CTCs remains one of the ultimate analytical challenges, with concentrations of as little as 10 cells mL^{-1} being of major diagnostic and prognostic significance[26]. Magnetic nanoparticles modified with antibodies have been shown to detect very low concentrations of specific targets over a large number of nontargeted species. This is demonstrated by CELLSEARCH, which is an FDA-approved system of detecting and enumerating CTCs[33]. The use of magnetic nanoparticle sensing has also been used to obtain information on the heterogeneity of CTCs in a number of papers by Kelley *et al.*[34,35]. This then allowed the separation of subpopulations of CTCs that express different quantities of surface proteins.

Magnetic nanoparticles are still the subject of significant research for the development of sensing and diagnostics, and extremely significant progress has been made. While there are already a small number of commercially available magnetic nanoparticle sensing products, there are still challenges that exist, for example designing more and more precise and sensitive magnetite nanoparticles with ideal magnetic behaviour.

MRI Contrast Agents

Magnetic resonance imaging (MRI) is a non-invasive imaging technique used to provide three-dimensional detailed images of the anatomy and physiological tissues of living subjects. It is based on the use of strong magnetic fields to excite and detect a change in direction of the rotational axis of protons found in the water that makes up living tissues[36]. The technique works through the exploitation of nuclear magnetic resonance (NMR) and electromagnetic radiation. NMR is based on the principle that nuclei that have unpaired electrons will have a small magnetic moment. In the case of MRI, hydrogen atoms are the target, as they are present throughout the body in both water and fat molecules. When a large external magnet is applied to the body, all these unpaired electrons in the hydrogen nuclei will align with the external magnetic field. When a pulse of radio-frequency (RF) radiation is then applied, the direction of the magnetisation of the atomic nuclei will be shifted.

^{1}H nuclei have two possible spin arrangements, they will either be aligned 'with' or 'against' the magnetic field. At equilibrium, slightly more of the nuclei will be aligned with the external magnetic field, producing a small net longitudinal magnetisation. When the RF pulse is applied, this longitudinal magnetisation will shift planes, and this will emit a detectable signal. As soon as the RF pulse is turned off, the direction of the magnetisation will then slowly realign itself with its original

axis in a process known as relaxation. Relaxation occurs via two mechanisms - longitudinal relaxation (T_1) and transverse relaxation (T_2). T_1 is the time it takes for the net magnetisation to return to its equilibrium state, and T_2 is the loss of phase coherence and the decrease in the transverse magnetisation. In T_1 the energy is lost through interaction of the nuclei with its surroundings (spin-lattice relaxation) and T_2 relaxation happens when the spinning nuclei lose energy through collisions with other spinning nuclei (spin-spin relaxation). Generally, T_2 relaxation occurs more quickly than T_1.

Although there is a large number of protons in the hydrogen atoms across the human body, it still results in a relatively low signal. Thus, the use of a contrast agent is required in order to enhance the image quality through shortening of the relaxation times. The most common commercially used contrast agent is a chelated gadolinium ion (Gd^{3+}) complex, which can greatly enhance the signal in T_1-weighted images[37]. Gadolinium ions, however, are toxic and can accumulate in the liver and body tissue, and so there is a drive towards the development of biocompatible and non-toxic alternatives[38].

Iron oxide based contrast agents present themselves as a viable alternative to gadolinium ions as they are non-toxic[39]. In addition to their biocompatibility, the fact that they can be readily functionalised presents opportunities for enhanced stability in biological media as well as being used for targeting and diagnostic purposes[38]. In addition to this, iron oxides are of interest because they can provide strong contrast in T_2-weighted images[40].

A number of SPIONs (SuperParamagnetic Iron Oxide Nanoparticles) have been developed for use as contrast agents and approved by the FDA, for example Lumiren for bowel imaging, Feridex IV for liver and spleen imaging, and Combidex

for lymph node metastases imaging[41–43]. Magnetite nanoparticles have been used to obtain MRI images of tumours *in-vivo* (Figure 1.7). In this work by Veiseh *et al.*, a nanoprobe consisting of a near IR fluorophore conjugated to a polyethylene glycol-grafted chitosan-coated iron oxide nanoparticle was used to image tumours in mice.

Magnetic nanoparticles are currently, and have already been used as MRI contrast agents and for imaging *in-vivo*. Although there are a variety of these magnetic complexes available, it will still be a number of years before they are widely utilised, owing still to studies on their long term stability and physiological effects.

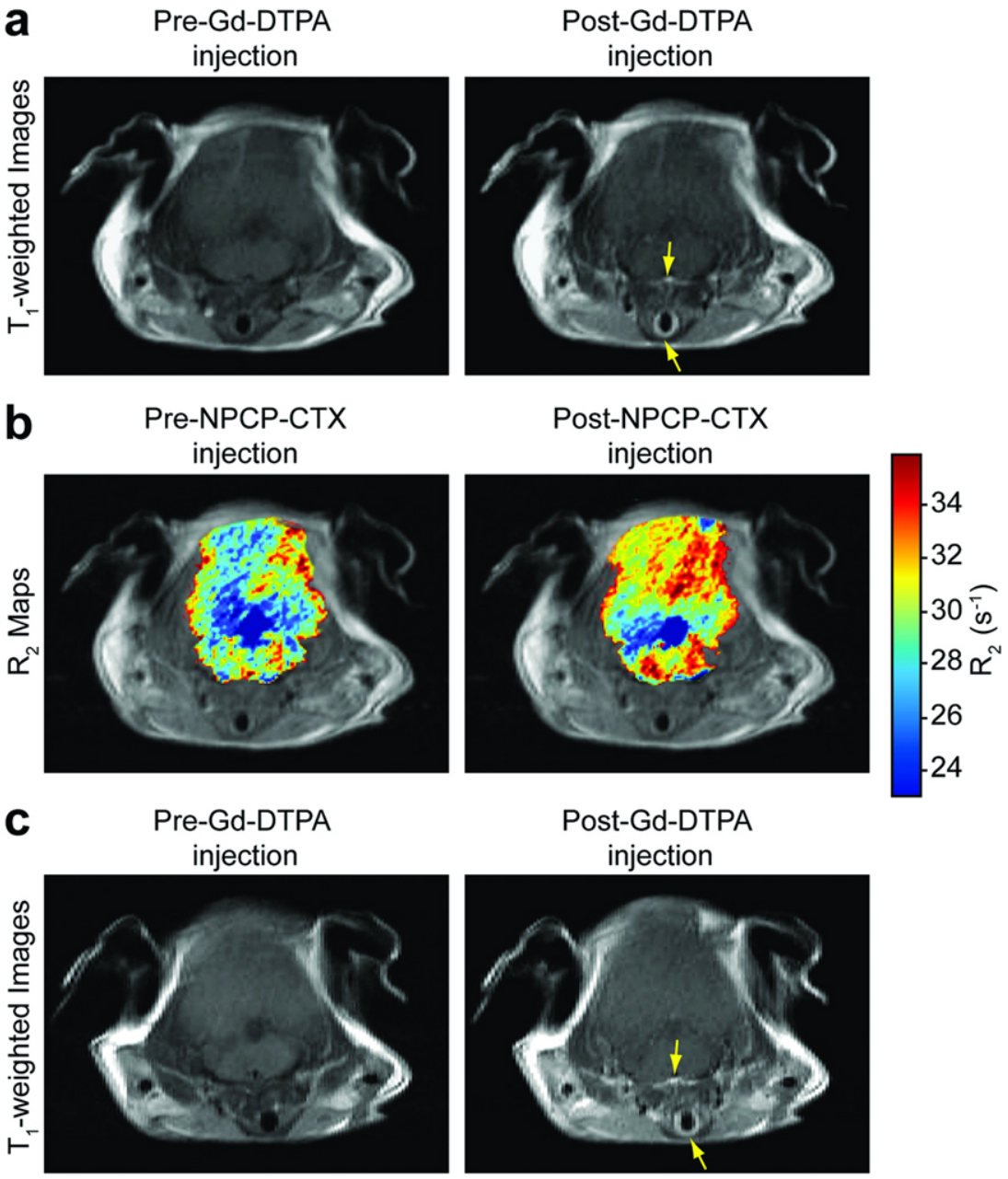

Figure 1.7: Tumours imaged in mouse brains using magnetic nanoparticles. Adapted from ref[44].

1.3 Plasmonic Nanomaterials

Plasmonic nanoparticles, such as gold, silver and nickel, have been the subject of extensive research in recent years. Even though plasmonic nanoparticles have been studied comprehensively over the last number of decades, the area is still rapidly expanding due to progression in new analytical and microscopic techniques, as well as recent advances in synthesis, assembly and characterisation[45]. Gold nanoparticles are by far the most studied of the plasmonic nanoparticles, and are used throughout this work. Gold nanoparticles, as well as being plasmonic, are highly remarkable for their other intrinsic properties, such as their optical, electronic and physio-chemical characteristics[46]. Moreover, these properties can be readily altered through altering their synthetic approaches, resulting in nanoparticles with a variety of shapes, sizes and aspect ratios. In some instances even a change in environment can have a profound impact on the spectroscopic behaviour of the nanoparticles[47].

Similarly to magnetic nanoparticles, gold nanoparticles (in addition to the variety of shapes and properties that can be attained through synthesis alone) can also be further functionalised with a number of functional groups and chemical species to allow for a vast array of potential applications. As a result of these features, gold nanoparticles have found applications across a broad region of fields, including biomedicine, electronics and imaging.

1.3.1 Structure and Properties of Plasmonic Nanomaterials

Platonic and Non-Platonic Structures

The most common gold nanoparticles are spherical in shape. Spherical nanoparticles have been prepared and studied over the past 100 years, and synthetic approaches to gold nanoparticles are the subject of hundreds of review articles every year[48]. Spherical gold nanoparticles are an example of a convex nanoparticle. Convex nanoparticles have platonic geometries and present as shapes such as cubes, tetrahedrons, hexahedrons, octahedrons, dodecahdedrons and icosahedrons, representing five regular tessellations of a sphere. All these nanoparticles are considered platonic nanoparticles, which are convex polyhedra with faces composed of identical regular convex polygons[49]. As these nanoparticles are composed of highly regular facets, and they can assemble into highly ordered structures.

Concave nanoparticles are less studied, and significantly less understood. These nanoparticles have non-platonic geometries, and are spiky, oddly-shaped and anisotropic. Although a large number of these concave nanoparticles exist, there is still great debate over their exact mechanism of formation[50]. Concave nanoparticles, as a result of their anisotropy, can have a number of interesting features, including a much larger surface area, strong near-infrared (NIR) absorbance, and plasmonic hot spots[50]. An example of concave nanoparticles, namely gold nanostars, is shown in Figure 1.8.

While concave nanoparticles are useful for their enhanced photochemical properties in comparison with convex nanoparticles, they are inherently thermodynamically unstable and can potentially transform into spherical particles over time[52]. This is due to increased strain put on the nanoparticle due to their incredibly high surface-to-volume ratio. This strain often results in polycrystallinity and lattice defects,

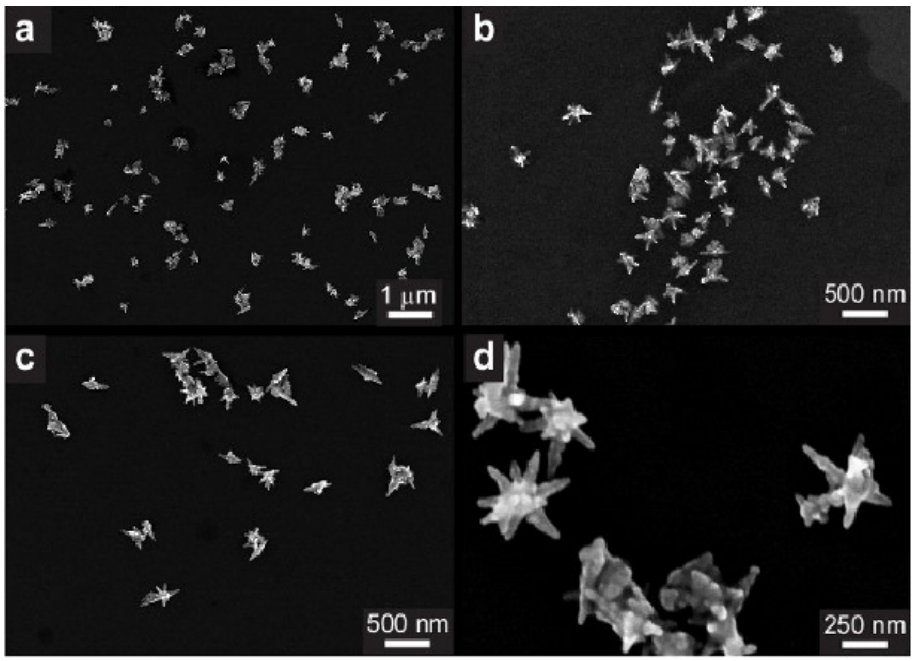

Figure 1.8: SEM images of gold nanostars. Taken from ref[51].

which in turn allow the nanoparticle to reach a more thermodynamically stable state. This is achieved through decreasing the surface area in order to minimise the surface energy.

The synthetic protocols for concave nanoparticles are often found serendipitously, which is not helpful in the efforts to understand the formation mechanisms of these materials. Usually they are ascribed to different stabilising agents preferentially stabilising one crystal face over another, thus contributing to anisotropic growth, and the focus of the research is on the properties of the resulting anisotropic material. The role of surface defects on the seed nanoparticles has also been discussed as a reason for the formation of spikes under rapid growth conditions. However, this theory is dubious at best because, for example, the spikes on a nanostar grow without any apparent symmetrical relation between them. Another field of thought is that an atom-by-atom growth approach occurs for these spiky nanoparticles, that starts with seeds of a critical size and grown in line with the kinetics of ion/atom attachment to different crystal faces[53]. This model is not very accurate in determining the

growth of the nanoparticles, or their resulting shapes[54,55]. Kotov *et al.* suggest a self-limiting self-assembly approach to the growth of spiky anisotropic structures[50]. In this work, they demonstrated the successful growth of spiky self-assembled supra-particles from gold and magnetite nanoparticles. It was found in this case that the gold seeds self-assemble through attractive Van der Waals forces into nanostars.

The larger variety of convex plasmonic nanoparticles are thought to arise due to the low twinning energy of noble metals - these twin planes can then create twinned particles like icosahedra and dodecahedra[56]. Gold and silver are among a variety of noble metals that have face centered cubic (fcc) crystal packing. Crystal planes with close packed atoms will minimise the surface energy and thus result in a more stable nanoparticle. Examples of concave nanoparticles that contain low index crystal planes such as {100}, {110}, and {111} are shown in Figure 1.9. Crystal planes of a higher index are unstable and will reconstruct. This then creates unstable facets, resulting in the formation of anisotropic structures such as nanorods, nanowires and branched nanoparticles[56].

Surface Plasmon Resonance

A plasmon is a 'quantum of plasma oscillation' and describes the collective longitudinal excitation of the electrons in a metal[57]. Surface plasmon resonance is the interaction between the free electrons in a metal and electromagnetic fields. The free electrons in the metal can be excited by the electrical component of electromagnetic raditation to produce collective oscillations. There are two modes formed by this interaction - surface plasmon polaritons (SPPs) and localised surface plasmon resonance (LSPR). The SPP can propagate along the surface of the metal or dielectric material; and LSPR is confined to a small volume or around a single nanoparticle. In both cases, the incident electromagnetic field can be localised at a deep sub-

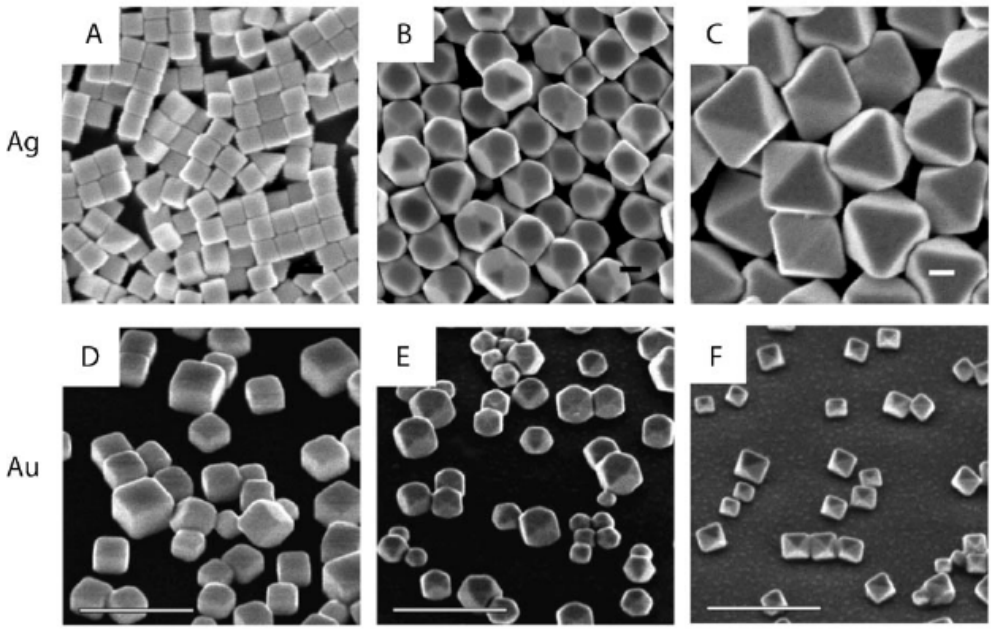

Figure 1.9: Convex nanoparticles bound by low index planes. Gold (A-C) and silver (D-F) nanocrystals are bound by fcc {100} and {110} planes. Taken from ref[56].

wavelength scale with a remarkable enhancement of the local field[45]. Because these plasmonic oscillatons occur at well-defined frequencies, they are classified as bosonic quasi-particles[58]. A quasi-particle is a term used to define a non-physical concept, and because plasmons are not made of matter, they are called quasi-particles, and a boson is used to describe a particle or quasi-particle that has integral spin[59]. Plasmons can be described as a cloud of negatively charged electron density that is coherently displaced from its equilibrium position. In an analogy to real plasma, this coherent displacement of the negative electron cloud occurs around a lattice composed of positively charged ions[60].

Plasmon resonance does not occur in bulk metallic materials. However, the presence of a surface in real materials allows for the existence of certain specific plasmon modes. These plasmon modes can be excited by the external electric field of incident electromagnetic radiation. This will cause displacements of the electron gas with respect to their initial equilibrium position[59,61]. For metal nanoparticles, like

gold and silver, the size of the nanoparticle itself is comparable with the metal skin depth. Here, the electric field of the incident light can penetrate the metal and polarise the conduction electrons. These are called localised surface plasmons because the plasmonic oscillation is distributed over the whole particle volume[59]. As the displacement of the negatively charged electrons from the positively charged lattice is coherent, it then generates a restoring force that will pull the polarised electrons back towards the lattice, i.e. the nanoparticles act like nanoantennae[62]. The plasmon resonance in a nanoparticle can therefore be thought of in terms of a simple mass-spring harmonic oscillator. The electron cloud oscillates like a dipole in a parallel direction to the electric field of the incident electromagnetic radiation. The mass is the electron density, and the spring constant will be determined by the Coulomb restoring force. Only light that has frequencies that are in resonance with the oscillation will be able to excite the localised surface plasmon.

In the case of a gold nanoparticle, the size is much smaller than the wavelength of light. This distortion of the electron cloud in response to the electric field can be expressed by the metal polarisability, shown below.

$$\alpha = 4\epsilon_0 \pi R^3 (\frac{\epsilon - 1}{\epsilon + 2}) \tag{1.4}$$

where ϵ is the relative permittivity, and R^3 is the radius of the sphere. The metal polarisability will determine how strongly a particle can scatter and absorb light, and also the degree to which the incident field will be enhanced in the area surrounding the particle. The scattering and absorption spectra can be calculated using the metal polarisability using the following equations[63].

$$\alpha_{\text{sca}} = \frac{k_0^4 |\alpha|^2}{6\pi\epsilon_0^2} \tag{1.5}$$

$$\alpha_{\text{ext}} = \frac{k_0}{\epsilon_0\sqrt{\epsilon_1}}\xi(\alpha) \tag{1.6}$$

where α_{sca} and α_{ext} are the scattering and extinction cross-sections, k_0 is the free-space wavevector, ϵ_0 is the permittivity of free space, ϵ_1 is the relative permittivity of the medium in which the particle is embedded and $\xi(\alpha)$ is the imaginary part of the polarisability.

The derivation of formula for the scattering cross section will be discussed below. Firstly, the absorption cross section will be given by the following.

$$\alpha_{\text{abs}} = \alpha_{\text{ext}} - \alpha_{\text{sca}} \tag{1.7}$$

The formula for the metal polarisability is shown in equation (1.4). From this, it can be seen that if the denominator is one, resonance will occur, i.e. if $\epsilon = 2$. This is often called the Frölich mode[64]. The polarisability is a means used to measure how easily the charge within an object can be displaced by an applied electric field. As the conduction ions have an incredibly low mass in comparison to the ion cores, they can be considered to be free to move about the fixed positively charged ion lattice. These electrons will move in response to an external applied electric field, creating a net positive charge on one side and a net negative charge on the other. This movement of the net positive and negative charges means that a dipole moment is created, and the strength of this dipole moment will be dependent on the metal polarisability.

Resonance occurs due to the Coulombic restoring force between the displaced charges. The frequency of the resonance will be determined by the strength of the restoring force, and the width of the resonance will be determined by the damping. The restoring force is related to the strength of the electric field inside the particle due to the displaced charge[64]. The Frölich condition defines the localised surface plasmon resonance condition, and states that the frequency of the SPR is tunable by changing the permittivity of the surrounding medium, but is also strongly influenced by the nanoparticles size, shape and composition[58].

Multiple articles have been published showing extensive derivations of the scattering cross section for SPR[58,64,65], and discussing each of the factors affecting each parameter at each step of the derivation, but a full discussion and derivation of these terms is beyond the scope of this work.

As has been discussed previously, the metal polarisability is dependent on a number of different factors, including the size and shape of a nanoparticle. Each of these factors can be tuned to change the wavelength of the resonance, however, some factors have a more profound effect than others. For example, for spherical gold nanoparticles, the wavelength of the surface plasmon resonance will depend on the nanoparticle radius and the refractive index of the medium. If either of these factors is increased, it will cause a red-shift in the resulting plasmon resonance. Gans theory states that the polarisability, and therefore the plasmon resonance wavelength, is highly dependent on both the shape and size of the nanoparticle[66]. If the symmetry of a nanoparticle is broken, it will gain additional modes of plasmon resonance. For example, in the case of gold nanorods, there will be two surface plasmon resonance wavelengths corresponding to the two axes of symmetry. An illustration of this is shown in Figure 1.10.

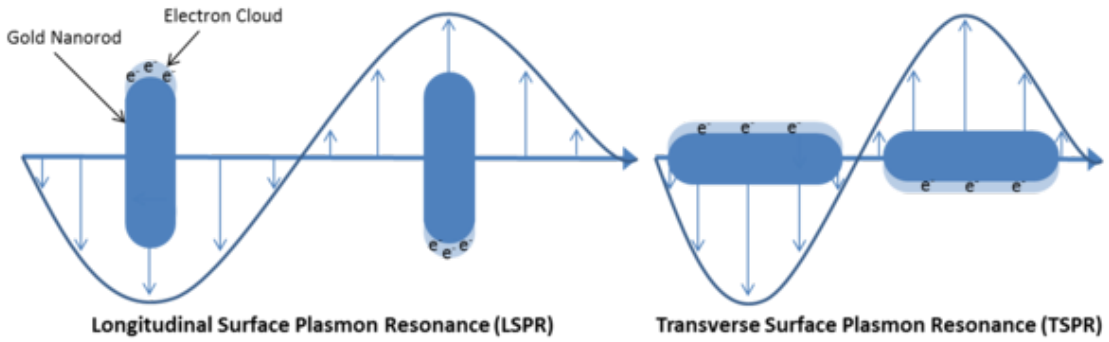

Figure 1.10: Scheme showing the two SPRs for gold nanorods. Taken from ref[67]

Gold nanorods will have two SPR wavelengths, transverse and longitudinal. The longitudinal polarisation of the nanorod occurs more readily than the transverse polarisation, and so the longitudinal SPR will occur at a lower energy and higher wavelength. It is more sensitive to changes in aspect ratio and is more polarisable. The longitudinal SPR can be tuned from 550 nm to over 2000 nm by adjusting the aspect ratio, while the transverse SPR remains between 510 - 520 nm.

As gold nanoparticles with increasingly complex shapes are synthesised, their plasmon resonances too, increase in complexity. Generally speaking, 'star-shaped' or 'branched' nanoparticles are not as monodisperse as gold nano-spheres or nanorods, but in some cases well defined plasmon peaks have been observed in the ensemble UV-Vis spectra for these particles[68]. When nanoparticles have tips that are geometrically different, and are asymmetric in shape, it could be thought that that any LSPRs would be lost in any measurements of the nanoparticle solution. It may also be thought that these asymmetric nano-star like structures would have incredibly complicated LSPR behaviour, and so to determine whether or not this is the case, Nehl *et al.* investigated the scattering spectra of a single gold nanostar structure using single particle spectroscopy[69]. A TEM image of a single nanostar beside its absorption spectrum and a reference spectrum of a spherical gold nanoparticle is shown in Figure 1.11.

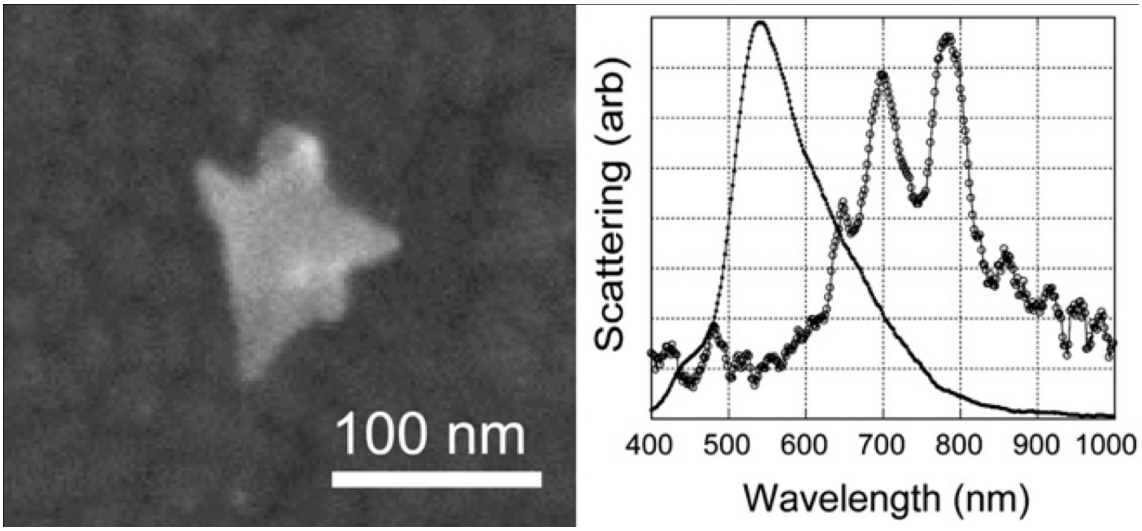

Figure 1.11: TEM image of a single gold nanostar. The smooth spectrum corresponds to a 100 nm spherical gold nanoparticle, and the second more complicated spectrum corresponds to a single nanostar from the same solution as the one shown to the left. Adapted from ref[69]

.

Typical single spectra for the nanostars consisted of multiple sharp peaks in the visible and near-infrared. Through tracking of the amplitudes of the peaks as a function of the angle of the analyser, it was found that each spectral peak from a single nanostar was polarised in a different direction, and each of these directions matched that of a tip of the nanostar.

In complicated plasmonic structures, like gold nanostars, the LSPR can be understood in terms of the plasmon hybridisation (PH) model[70]. The PH model calculates the LSPR of complicated structures by approximating them to be the result of the interactions of the LSPRs of simpler structures. Although it has been shown to be successful for many complicated structures, it experiences limitations with asymmetric branched structures, such as that shown in Figure 1.11.

The surface plasmon resonance of metallic nanoparticles is a hugely interesting and useful property of these nanoparticles, dependent on the polarisibility of that nanoparticle. The metal polarisability of a nanoparticle is dependent on a great number of factors, including size, shape and the coating of the nanoparticle. The shape of a nanoparticle in particular has a significant effect on the resulting LSPR, and this could potentially be exploited for a number of potential applications.

1.3.2 Synthesis of Plasmonic Nanomaterials

Turkevich Method

The Turkevich method involves the synthesis of colloidal gold nanoparticles by reducing chloroauric acid using sodium citrate[71]. This is one of the oldest and simplest methods of preparing a mostly monodisperse solution of spherical gold nanoparticles in the region of 10 - 20 nm in diameter. In this case, the sodium citrate acts as both a reducing and capping agent. Colour change is a crucial component in the Turkevich method, as the reaction proceeds the solution changes from yellow, to dark blue and finally turning ruby red, indicating the formation of the spherical gold nanoparticles. Recently, it was discovered that the dark colour arises due to the formation of a nanowire intermediate[72].

Reduction using Sodium Borohydride

Sodium borohydride is a powerful reducing agent used widely throughout organic and inorganic chemistry. In the synthesis of gold nanoparticles using chloroauric acid and sodium borohydride ($NaBH_4$), the $NaBH_4$ reduces the chloroauric acid, and similarly to the Turkevich method it acts as both a stabilising and capping agent. Gold nanoparticles synthesised in this manner are smaller than those prepared using the previous method and are generally monodisperse spherical nanoparticles in the region of 3-6 nm[73].

Sodium borohydride is also utilised in the formation of silver seeds. In this synthesis, sodium citrate monobasic ($Na_3C_6H_5O_7$) along with silver nitrate ($AgNO_3$) and sodium borohydride ($NaBH_4$) are used to prevent aggregation of the silver seeds at 0 °C. This is important as it slows down the reduction kinetics of $AgNO_3$ resulting in smaller, more monodisperse nanoparticles. The formation of a yellow solution confirms the presence of silver seeds that are approximately 10 nm in diameter[74].

Seed-Mediated Gold Nanostar Synthesis

Small silver seeds serve as the nucleation sites of the gold nanostars. Gold nanostar formation is a highly sensitive synthesis, and even minute changes in factors such as concentration, temperature, light, stirring speed and the exact time at which the reactants are added can have a major impact on the final product[51]. In this approach, chloroauric acid ($HAuCl_4$) is added to a solution containing silver nitrate ($AgNO_3$ - a source of silver ions) and CTAB (Cetyl Trimethylammonium bromide). The CTAB acts as a mild reducing agent causing the reduction of Ag^{3+} to Ag^{+}. Ascorbic acid ($C_6H_8O_6$) was then added to reduce the Ag^{+} ions to the silver nanoparticles. Silver seeds are then added to serve as a nucleation site for the growth of the gold nanostars. During the formation of the nanostars, the suspension changes in appearance from a clear solution to a blue solution and after 1 hour, the solution turns red brown.

1.3.3 Applications of Plasmonic Nanomaterials

In metallic nanoparticles, the incident electromagnetic field can be localised at a deep subwavelength scale that causes a remarkable enhancement of the local field. This gives rise to a huge array of applications in the fields of biology, chemistry and information technology[45]. There are a number of reasons why plasmonics have had such a major influence on the field of nanomaterials, the first being that plas-

mons can resonate with light at a particular frequency to a great degree of freedom, eg. 0D nanoparticles, 1D nanowires and 2D metasurfaces. These surfaces can be used to highly control the LSPR to achieve the selective absorption or reflection of light. Plasmons can also produce an enormous enhancement of light intensity, as well as trap electromagnetic energy in sub-wavelength volumes, areas and lengths.

Surface Plasmon Resonance for Sensing

Surface plasmon resonance (SPR) sensor research was kickstarted nearly a hundred years ago by Wood[75], and carried forward by Liedberg *et al.* who introduced means for gas and biosensing using SPR[76]. SPR sensors are highly desirable due to their sensitivity, real-time detection, and label-free assay[77].

When the wavelength of light on a metallic nanostructure is considerably larger than that of a plasmonic nanostructure, local oscillations will be produced around the nanostructure[78]. The resonant wavelength of the LSPR is dependent on the refractive index of the environment, as well as the geometric shape and structure. LSPR results in a high-intensity and strongly localised electromagnetic field that can be extremely sensitive to even small changes in the surrounding dielectric medium[79].

The Kretschmann configuration is the most common set-up used for SPR applications (Figure 1.12). In this set-up, a metal film (usually gold or silver) is placed at the interface of two dielectric media. Medium 1 has a higher refractive index (n_1) and is normally a prism, and medium 2 has a lower refractive index (n_2), and can be air, or perhaps a solution of interest. When the light travels from the higher refractive index (medium 1) to the lower refractive index (medium 2), total internal reflection (TIR) can occur in medium 1 as long as the incident angle θ is greater than the critical angle θ_c, where $sin(\theta_c) = n_2 / n_1$. Evanescent waves are formed in

the medium with the lower refractive index (medium 2) under the condition of TIR.

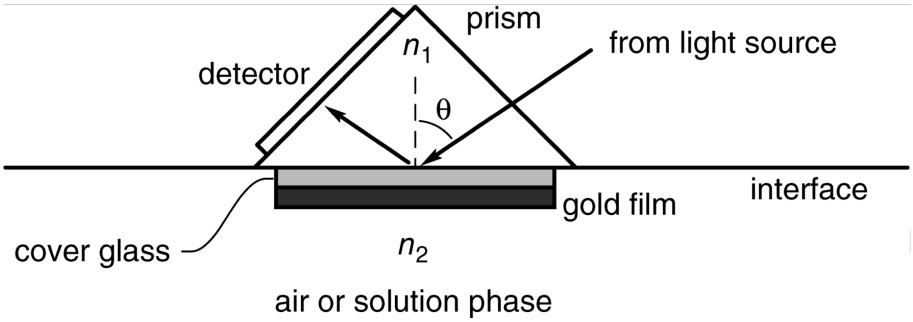

Figure 1.12: Scheme showing the typical set-up for surface plasmon resonance[80].

The amplitude of this type of standing wave exponentially decays with the distance to the interface of mediums 1 and 2. The magnitude of the parallel wave vector of the evanescent wave $k_{evan,\ II}$ is shown below in equation (1.8).

$$k_{\text{evan, II}} = \frac{2\pi}{\lambda} n_1 sin(\theta) \tag{1.8}$$

where λ is the wavelength of the incident light, n_1 is the refractive index of the higher refractive index medium 1, and θ is the incident angle.

In the case of the sensor set-up, the surface plasmon is a surface electromagnetic wave whose propagation is confined to the metal-dielectric surface. The magnitude of the wave vector of the surface plasmon (k_{sp}) is dependent on both the dielectric constant of the gold film and medium 2 (lower refractive index). For a non-absorbing media, the dielectric constant is the square of the refractive index, $\epsilon = n^2$, where ϵ is the dielectric constant and n is the refractive index. Therefore, k_{sp} is determined by n_2 and n_g according to the following equation.

$$k_{\mathrm{sp}} = \frac{2\pi}{\lambda}\sqrt{\frac{n_2^2 n_{\mathrm{g}}^2}{n_2^2 + n_{\mathrm{g}}^2}} \tag{1.9}$$

where n_2 is the refractive index of medium 2 and n_g is the refractive index of the gold film[80].

Thus, when the evanescent wave excites the surface plasmon on the gold film, SPR occurs. When this occurs, the intensity of the reflected light will decrease sharply. As the excited surface plasmon decays, energy conversion to photons or phonons will occur. As a requirement of SPR is that k_{sp} and $k_{evan,\ II}$ are equal, we can combine equations (1.8) and (1.9) to obtain the following expression for θ_{SPR}, the angle required for the resonance to occur.

$$\theta_{\mathrm{SPR}} = sin^{-1}\left(\frac{1}{n_1}\sqrt{\frac{n_2^2 n_{\mathrm{g}}^2}{n_2^2 + n_{\mathrm{g}}^2}}\right) \tag{1.10}$$

Thus it can be seen from this equation that the angle required for resonance is related to n_2 when n_1 and n_g are fixed.

When an analyte of interest adsorbs or desorbs on the gold film, it will change the refractive index of medium 2 near the metal-dielectric surface and the resonance angle will change accordingly. This means that the adsorption/desorption or association/dissociation can be monitored through the changing of θ_{SPR}[80].

In the development of new SPR sensors, the light source is the most critical com-

ponent, and sensor configuration is also of vital importance. The new underlying principles of SPR sensors tends towards minimisation, portability and disposability[77]. Proof-of-concept studies showing light-emitting diodes (LEDs), organic light-emitting diodes (OLEDs) and smartphone displays as future low-cost SPR sensor platforms have been carried out[77].

Surface Enhanced Raman Spectroscopy (SERs)

Surface enhanced Raman scattering (SERs) is an analytical technique that offers an enhancement of up to $10^{14\text{-}15}$ in Raman intensity, in comparison with traditional Raman spectroscopy. This overcomes the main drawback of traditional Raman, which is its inherent weakness. The level of enhancement offered is sufficient to even allow single molecule detection[81]. Surface enhancement takes place on a metal surface that has roughness at a nanoscale level. Molecules are then adsorbed onto this rough surface. Plasmonic metals, such as gold and silver, are most commonly used, and can be added to the surface via electrochemical roughening, metallic coating of a nano-structured substrate or deposition of a dispersion of colloidal metallic nanoparticles onto the surface. When these surfaces are excited using a laser, a highly localised plasmonic field is generated. When a molecule is adsorbed on or near to the enhanced field at the surface, a larger enhancement in the Raman signal is absorbed. This Raman signal can then be enhanced even further when the incident laser wavelength is matched to the absorption maxima of the molecule[82].

A substantial body of work has been carried out showcasing SERs effects for different molecules, using a variety of nanoparticles of different shapes and concentrations, to the extent that is not easy to determine exactly what parameters are needed for effective and reproducible SERs[83]. In fact, even the classic explanation for SERs that attributes the excitation of plasmon resonances with the incident laser source has been called into question. This is due in part to the low enhancement levels re-

ported for spherical gold nanoparticles, which varies widely from particle-to-particle and also fluctuates with its environment[84]. Recently, an alternative explanation for the origin of SERs on metal nanoparticles has been proposed. In this theory, the enhancement is not based on the intrinsic nanoparticle surface, but rather local field 'hotspots' due to surface roughness between aggregated nanoparticles, or between nanoparticles and a metal surface. The SERs contribution of these hotspots can then dominate the response[85–90].

Increasing the curvature of the nanomaterials can also be an effective means of increasing the plasmon response for SERs. The vertices of silver nanotriangles, for example, showed a 10 - 100 times higher field strength than the surface of a nanosphere[91]. Similarly, nanostars, with their many spikes, have also been shown to be highly sensitive to changes in the local dielectric environment, as well as show larger enhancements in the electric field around the nanoparticles[92]. Other work with spiky, anisotropic gold structures has shown similar results, and so there is a massive drive towards the synthesis of monodisperse, spiky anisotropic plasmonic nanoparticles[69,83,84].

SERs holds significant advantages over more conventional analytical techniques such as fluorescence and high performance liquid chromatography (HPLC) as it provides fingerprint signatures of different analytes[93]. Thus, the synthesis and optimisation of plasmonic nanoparticles for use as the surface for the SERs is an avid area of current research. In particular, anisotropic, spiky nanoparticles have been found to be excellent SERs agents, and so there is increasing demand to develop synthetic techniques that produce stable, monodisperse solutions of these nanostructures.

1.4 Magnetic-Plasmonic Nanomaterials

The combination of both magnetic and plasmonic properties in one nanocomposite is the basis for new multi-functional nanomaterials with unique multimodal properties. These nanocomposites have great potential in a wide range of applications in nano- and biotechnologies.

Many magnetic-plasmonic nanocomposites consist of an inner magnetic core and an outer plasmonic shell. These nanocomposites retain all the functionalities of both their magnetic and plasmonic moieties - however, they can be difficult to synthesise due to the large mismatches in the crystal lattice of the ferrite core and the noble metal shell. A wide variety of approaches are utilised to try and overcome this difficulty, for example, modifying the core through a coating which would facilitate easier attachment of the magnetic or plasmonic moiety. Silica is a common choice for coating the magnetic nanoparticles as it is biocompatible and can be functionalised with a variety of surface functional groups[94]. This allows for the seeding of the gold nanoparticles onto the surface of the core, allowing the further reduction of the gold.

A range of polymers have also been used as intermediate layers, for example polypyrrole (PPY), which is a conductive polymer that has been demonstrated to induce photothermal effects, and is already widely used in many biomedical applications[95,96]. Polyvinylpyrrolidone (PVP) was used to form a negatively charged shell on a magnetite core, which then allowed for the electrostatic adsorption of Au^{3+} onto the PVP, and consequently the reduction which forms the gold shell. PVP is amphiphilic, non-toxic and non-ionic and already has a broad spectrum of biomedical applications[97]. Polyethyleneimine (PEI) was utilised in a similar manner to produce Fe_3O_4@Au nanoparticles. Multimodal magnetic plasmonic structures can also be synthesised by coprecipitation followed by direct attachment of the plasmonic moiety to the magnetic particles. Hydroxylamine has frequently been utilised as a

seeding and reducing agent in a number of cases for coating of magnetic nanoparticles with a plasmonic shell[98–100].

The synthesis of magnetic-plasmonic nanostructures with non-platonic geometries is a growing area of interest within this field, as these novel structures have a large surface area, strong NIR absorbance, and plasmonic hot spots[56,101,102]. In these cases, the magnetite can act as a seed, which acts as a nucleation site for the formation of a non-platonic gold surface layer. This approach was utilised by Zhou *et al.* and is illustrated in Figure 1.13[50]. Variation in the redox potential of the gold reducing agent is used to alter the morphology of the gold layer. Specifically,the smooth layer of gold on the surface of the Fe_3O_4 nanoparticle is grown through introducing the pre-formed citrate-stabilised Fe_3O_4 nanoparticles into the boiling chloroauric acid solution (as previously mentioned, citrate acts as both the stabilising and the reducing agent). Hydroquinone is then used as the reducing agent in the formation of the gold spikes, as it has a more negative redox potential than citrate.

Other approaches to magnetic-plasmonic nanocomposites include suspending the magnetic and plasmonic nanoparticles together in a matrix. Such work was carried out by Ivashchenko *et al.*, who prepared self-organising silver and ultra-small iron oxide nanoparticles were recently made using a green synthetic approach[103]. Ginger rhizome extract was used as a stabilising agent, as well as serving as an antioxidant to prevent oxidation of the Fe^{2+} ions. Silver nitrate was added dropwise to the iron salts and ginger root extract, followed by NaOH, and the resultant mixture was heated under reflux. The entire process takes place exclusively in aqueous solution, with magnetic separation utilised to clean and purify the Ag-Fe_3O_4 nanocomposite product.

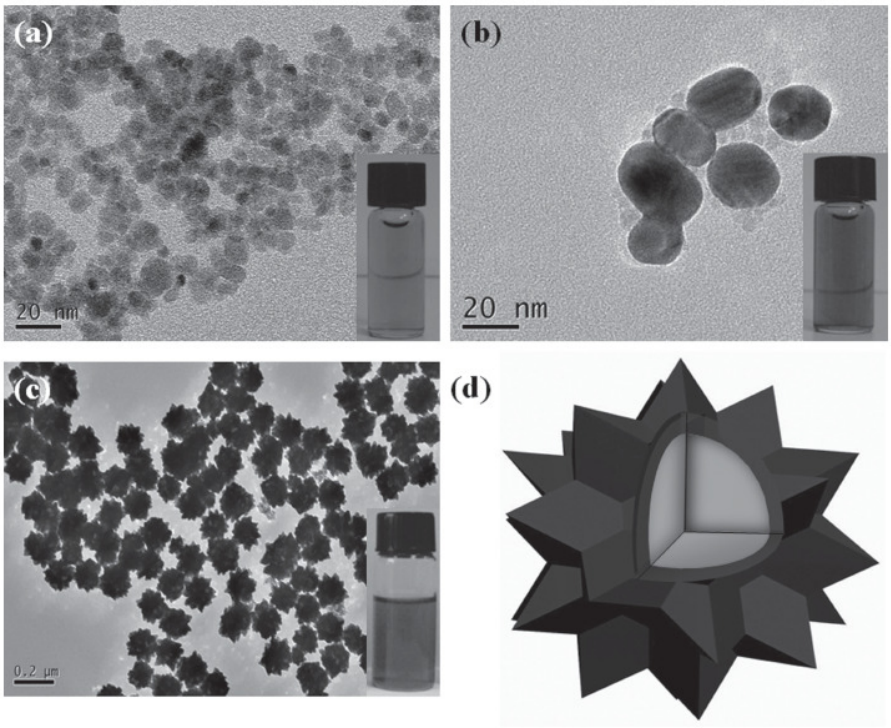

Figure 1.13: (a) Fe_3O_4 convex nanoparticles,(b) Au-coated Fe_3O_4 convex nanoparticles, (c) concave spiky Au-coated Fe_3O_4 core-shell nanostars, (d) schematic drawing of a spiky particle[50].

1.4.1 Applications of Magnetic-Plasmonic Nanocomposites

The dual modalities of a magnetic-plasmonic nano-system opens up a range of potential biomedical applications. The multimodal nature of these nanoparticles paves the way for their use as theranostic agents—i.e., materials that can be used to both diagnose, or quantify a disease, and also simultaneously provide treatment. In an ideal world, a single nanoparticle with these theranostic properties should be easy to functionalise with tunable size and properties.

Photothermal Therapy

Photothermal therapy is an attractive approach to cancer therapy as it is can be a highly selective theranostic approach if nanoparticles (most commonly gold) are

delivered to tumour sites. An external NIR laser can be applied, causing the oscillation of the plasmons and resulting in the nanoparticles generating heat, which has been shown to be highly effective in the thermal ablation of cancer cells[104,105].

Nanoparticles based on gold are the most popular choice for photothermal agents as it is biocompatible, thus enabling a thiol functionalisation which allows the easy attachment of antibodies and other targeting agents. Gold nanoparticles also have an effective light to heat conversion, and small sizes which can be tuned to efficiently absorb NIR light, which penetrates tissue better than other wavelengths of light. Utilising multimodal magnetic-plasmonic nanoparticles means that additional functionalities are now possible. Not only can the gold component be used to facilitate photothermal therapy, but the magnetic component can be used to direct the nanoparticles to the tumour site using an external magnet, the gold nanoparticles can be used for dark field imaging and the magnetite could potentially act as an MRI agent during the process. Also, targeting moieties could be conjugated to the surface of the gold to endow extra cell specificity. The litany of possible applications for these multimodal nanosystems ensures that they remain the subject of intensive research efforts. Some magnetic-plasmonic nanoparticle systems proposed for use in photothermal therapy are discussed below.

Gelatin was used as a mediator in the synthesis of Fe_3O_4@Au nanoparticles proposed for use as photothermal agents. This is of particular importance as gelatin can be readily degraded by a subclass of metalloproteinases in the body, which further ensures that the system is suitable for use *in-vivo*[25]. The biocompatibility and bioelimination of this system was closely examined, and it was found that in the acidic tumour microenvironment the Fe_3O_4@Au nanoparticle assemblies were successfully broken in conjunction with the metalloproteinases. An 808 nm NIR laser was found to cause significant temperature increases, and high doses of the nanoparticle composites were found to be non-toxic, thus illustrating its potential for use *in-vivo* as

a photothermal agent. This material also showed potential for uses in MRI, CT and PAT (photoacoustic therapy). A similar chitosan Fe_3O_4@Au nanomaterial showed a temperature increase at various concentrations under illumination of a NIR laser[99]. Chitosan is a polysaccharide often used due to its interesting biopharmaceutical properties; for example, its high mucoadhesion and suitability for facilitating drug delivery, and is the subject of many reviews[106–109]. The authors also highlighted the multiple uses of the synthesised nanoparticles—not only as photothermal agents but for use in simultaneous MRI and dark field imaging. While these proposed photothermal agents have under-gone heating tests using NIR lasers *ex-vivo*, more comprehensive biocompatibility and *in-vivo* testing on these multimodal magnetic photothermal agents is urgently required. These magnetic-plasmonic nanocomposites may also be used for magnetic hyperthermia therapy in addition to photothermal therapy, enabling the delivery of multiple potential therapies using one nanocomposite material.

Drug Delivery and Targeting

Multimodal magnetic nanoparticles have long been the subject of investigation for use as drug delivery vehicles, and many strategies for their synthesis, drug loading and release have been examined[110]. However, comparatively, few comprehensive studies on magnetic-plasmonic based drug delivery systems have been carried out, despite the many potential theranostic applications which these systems would have. This could be due in part to a number of difficulties as well as the complexity of making these materials, and how biocompatible the resulting systems may be. For example, a balance must be drawn between the complexity of the nanomaterial in tandem with the time and cost of its synthesis, with the increase in efficacy of the cancer treatment it can provide. Not only this, but the size and morphology of the magnetic plasmonic nanoparticles needs to be precisely controlled in order to optimise uptake *in-vivo* —too small (less than 50 nm) and the nanoparticles are washed

out of the body, too large (greater than 300 nm) and they accumulate in the liver and spleen[111].

In spite of these challenges, such multimodal nanoparticles comprising of anisotropically shaped Fe_3O_4@Au were prepared with a biocompatible mesoporous silica shell, which also allowed anticancer drug delivery[112]. The doxorubicin containing pores were capped with double stranded DNA, which decomposed under NIR light, causing the heating of the gold component of the nanoparticle. The magnetite, in this case, provided magnetic guidance, which was shown to increase uptake of the nanoparticles into HeLa cells (Figure 1.14).

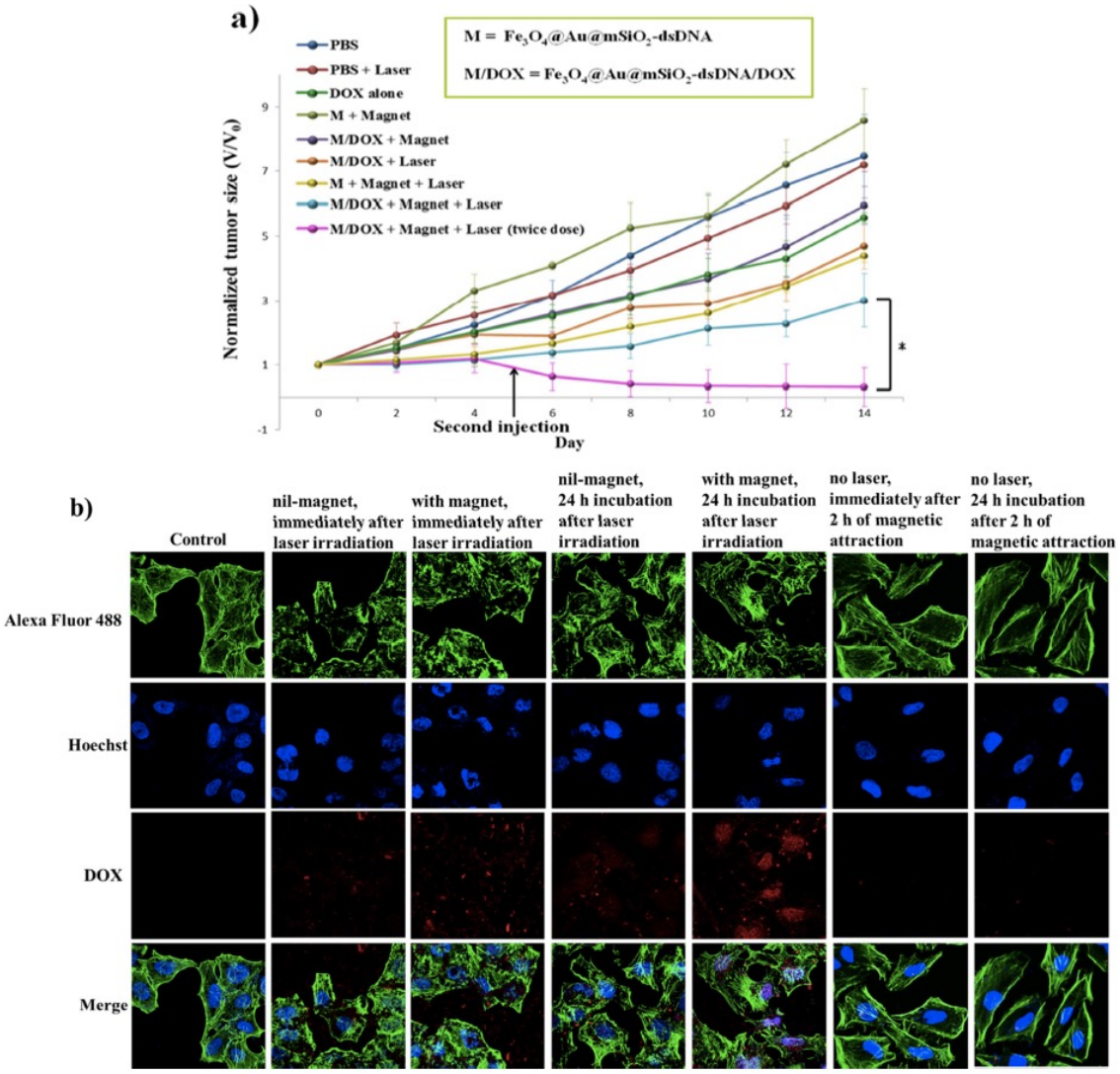

Figure 1.14: (a) A plot illustrating the changes in tumour size in mice following a number of different treatments. The tumours were seen to shrink following treatment with the drug-carrying magnetic plasmonic nanoparticles; (b) Also shown are confocal microscopy images of cells treated with different compounds after a range of incubation times and conditions. Taken from ref[112]

1.5 DNA-Stabilised Nanoparticles

Deoxyribonucleic acid (DNA) is the hereditary material in humans and almost every other organism on earth. It was first isolated in 1869 by Friedrich Miescher, and its structure was first published by James Watson and Francis Crick in 1953, who were awarded a Nobel prize for this work[113]. Watson and Crick relied heavily on findings by Rosalind Franklin, who was investigating the structure of DNA using X-ray crystallography[114].

DNA is comprised of two strands wrapped around each other resulting in a double helical shape. Each of these strands is composed of a chain of nucleotides. A nucleotide itself is comprised of 3 components - a sugar group, a phosphate group, and a DNA base. Firstly, the sugar group in DNA is called deoxyribose, and is a five membered ring. The carbons in deoxyribose molecules are numbered specifically, with the carbon to the right of the oxygen being labelled 1'. Each carbon in turn is then represented with a dash (e.g. 3', which is pronounced 3-prime). The second component in DNA is the phosphate group, and is bound to the deoxyribose molecule at the 5' carbon atom. The last component of the structure of DNA is the DNA base. These attach to the deoxyribose ring at the 1' carbon atom. These three constituents comprise a single nucleotide. A diagram showing a nucleotide and a deoxyribose molecule are shown in Figure 1.15.

There are four bases in DNA, cytosine (C), thymine (T), adenine (A) and guanine (G). Adenine and guanine are called purines, and thymine and cytosine are called pyrimidines. The four DNA bases are shown in Figure 1.16. The bases bind to the deoxyribose through a nitrogen group in a condensation reaction. The individual nucleotides bind together through the 3' carbon bonding to the phosphate group on the next nucleotide, another condensation reaction. The ordering of these bases in a strand of DNA forms a genetic code, which determines the creation of all life.

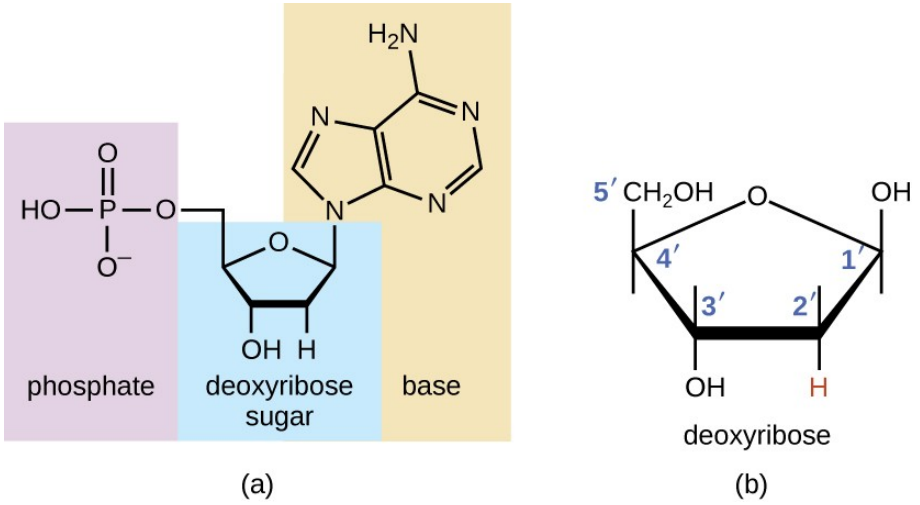

Figure 1.15: Diagram showing (a) a nucelotide and its constituent parts and (b) a deoxyribose molecule. Taken from ref[115].

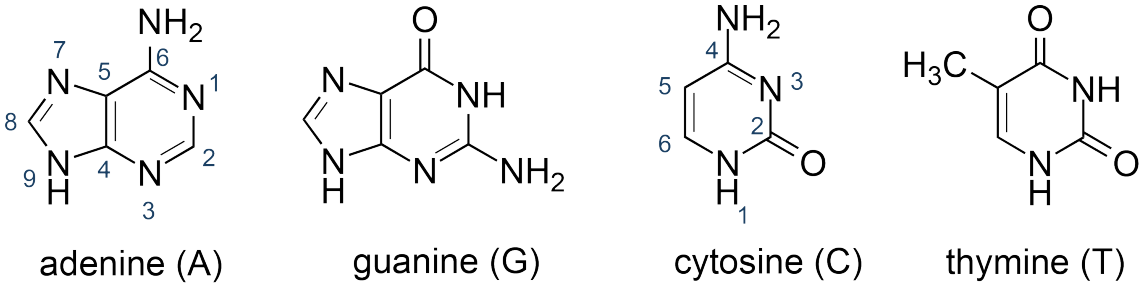

Figure 1.16: Structure of the four heterocyclic DNA bases. Taken from ref[116].

The DNA bases will only bond in a specific way. Adenine will only bond with thymine, and cytosine will only bond with guanine. The two strands of DNA are therefore bound through hydrogen bonds between adenine and thymine, and cytosine and guanine. These base pairs hydrogen bond very strongly, and these bonds hold the two strands together, as well as keep the distance between the two strands fixed. It is also worth noting that the two strands of DNA will run in opposite directions. A scheme showing the structure of the nucleotides in the two strands of DNA is shown in Figure 1.17.

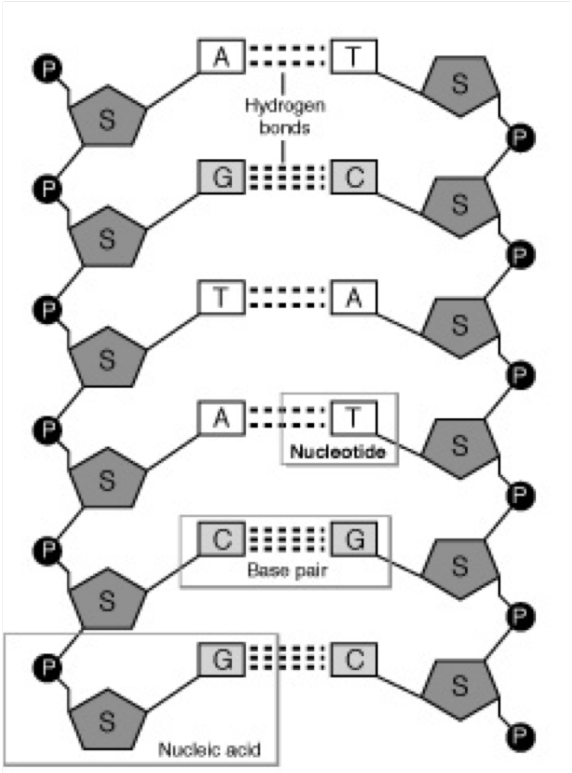

Figure 1.17: Diagram showing the hydrogen bonding between base pairs on the double strands of DNA. Adapted from ref[117].

The use of DNA-based technology has already made significant contributions in the genomic and diagnostic advances in the last few decades[118–121]. In these cases, the DNA was utilised primarily for its sequence recognition and complementarity as primers to access information in terms of genomic sequencing for applications in polymerase chain reactions (PCR), and as probes for hybridisation assays[122–124]. One of the ongoing goals of nanotechnology is the combination of favourable features from a number of different species to make multi-modal materials[125]. For example, theranostics, as mentioned, is a field of research that pursues the development of multimodal nanomaterials that would enable *in-situ* drug delivery, monitoring and diagnostics using one nanocomposite material. In this case, the nanomaterial would be functionalised with a biological molecule, for example a peptide, aptamer or antibody, to provide the recognition, biocompatibility, active sensing and drug activity, while the nanomaterial would host the biological species on its surface and also pro-

vide contrast and the possibility of activation by radio or near-infrared radiation. Other applications could include multimodal nanomaterials for bioremediation, sensors, biocomputers etc.

1.5.1 DNA-Functionalised Gold Nanoparticles

Gold nanoparticles that have been functionalised with DNA are perhaps the best investigated and most developed of all the different types of DNA-functionalised nanomaterials. Over the last few years they have been studied for a variety of applications, for example sensing, imaging, catalysis, diagnostics and drug delivery, to name but a few[126–128]. One of the primary reasons that gold is of such avid interest in terms of DNA-functionalisation is its surface plasmon resonance. Ordinary molecules, or fluorophores that are conjugated to the surface of the nanoparticles (or even in close proximity with the nanoparticles) will generate stronger Raman signals as well as quenching, or conversely, enhancing the fluorescence when interacting with the unique fields and plasmons[129–131]. The interactions between gold nanoparticles and fluorophores are complex, and no single model has yet been found to describe the behaviour[125].

While vast swathes of researchers have contributed to the advancements of the DNA-functionalisation of gold nanoparticles, the works of the Mirkin and Alivisatos groups have been to the forefront over the last number of years[132,133]. One of the key features in the binding of DNA to gold nanoparticles is the unusually strong binding affinity that alkyl thiols have for gold surfaces. DNA strands that are modified with thiol groups are now routinely prepared for loading DNA onto gold nanoparticles[134,135]. Another approach towards the preparation of DNA-functionalised gold nanoparticles is known as the 'salt-aging' approach. The electrostatic repulsion that originated from the negatively charged citrate groups in gold nanoparticles, and the negative

phosphate backbone in DNA meant that loading DNA onto the nanoparticles was highly challenging. These difficulties were overcome through slowly increasing the salt concentration of the media to counterbalance the charge[136]. This meant that higher concentrations of DNA can be loaded onto the surface of the gold nanoparticles, and that the nanoparticles are stable at high salt concentrations which is essential in the promotion of hybridisation reactions.

Gold nanoparticle - nucleic acid conjugates can be used in the detection of a wide range of analytes, and often the result can be determined colourimetrically by eye. For example, work carried out by Storhoff *et al.* showed how 3' and 5'-(alkanethiol)oligonucleotide capped gold nanoparticles could be used to complex a 24-base polynucleotide target. The hybridisation of the gold nanoparticle-nucleic acid conjugate with the polynucleotide target caused a red shift in the colour of the solution due to the formation of extended nanoparticle/polynucleotide aggregates[137]. However in this instance the detection limits were quite high. Work by Bai *et al.* showed how smaller nanoparticles could be used, which would produce micro-aggregates, and the signal could then be amplified by subsequent electrodeposition of gold onto them as shown in Figure 1.18. The particles grow and come into contact with each other thus causing a stronger plasmonic coupling resulting in an optically detectable blue shift[138].

Double-stranded and single-stranded DNA will adsorb differently onto gold nanoparticle surfaces; this too can be exploited for sensing purposes. The most commonly synthesised gold nanoparticles are citrate-stabilised gold nanoparticles, which have a slight negative surface charge. In double-stranded DNA, there are two negatively charged phosphate backbones to contend with, whereas in single-stranded DNA there is only one. Moreover, single-stranded DNA is flexible enough to uncoil its bases and avoid repulsion. Subsequently, as there is less repulsion when ssDNA is used, the result is that more DNA can be coated onto the surface of the nanopar-

ticle, therefore affording it better stability against aggregation at high salt concentrations[125]. This idea of selective adsorption was utilised in a hybridisation assay for the detection of untagged oligonucleotides[139]. The assay was found to be fast, inexpensive, sensitive to a limit as low as 4.3 nm and down to a single base mismatch.

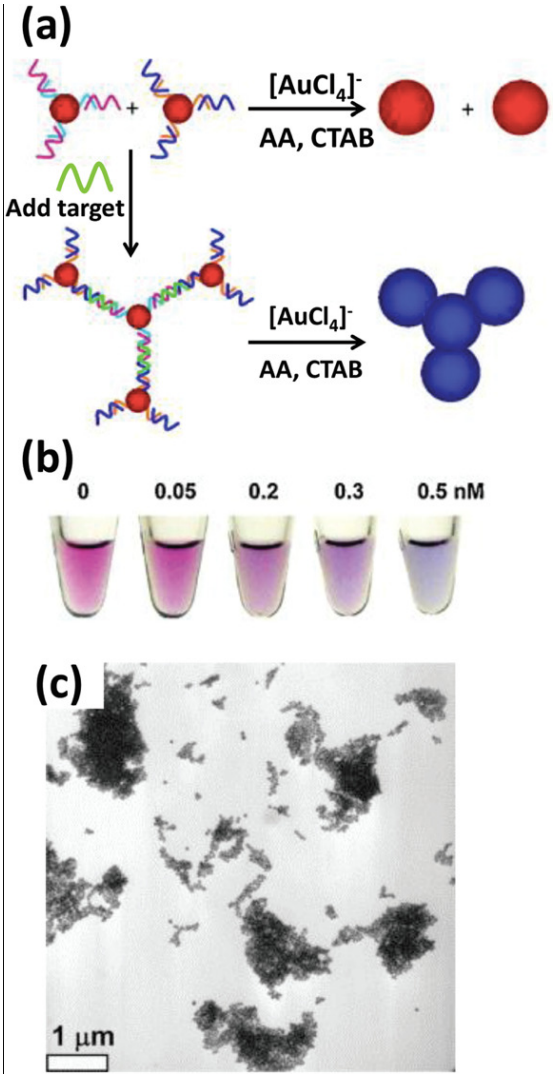

Figure 1.18: (a) Illustration of a DNA assay based on colour change from purple to blue due to target DNA driven aggregation of gold nanoparticles followed by their seeded growth, (b) a photo of the assays after the reduction reaction showing a stronger blue shift with increasing target DNA concentration and (c) a TEM image showing the aggregated nanoparticles after their chemical enlargement. Taken from ref[138].

In addition to colourimetric detection, DNA-functionalised gold nanoparticles are also attractive candidates for drug and gene delivery, and could also be promising candidates for catalysis. DNA could also be used to direct assembly of gold nanoparticles into well-defined suprastructures[140–142]. In short, DNA-functionalised gold nanoparticles are an exciting area of research due to their numerous current and potential applications.

1.5.2 DNA-Functionalised Magnetic Nanoparticles

Magnetic nanoparticles present themselves as viable hosts for DNA functionalisation due to their numerous favourable properties. Similar to most other nanoparticles, their high area-to-volume ratio means that they are prone to agglomeration, and so require an appropriate coating agent. Various coating and stabilising agents have been used to stabilise magnetic nanoparticles, including polymers such as dextran, or PSS, a PEG surfactant or silica. These coating agents also provide an opportunity to attach biomolecules, such as DNA, through chemical conjugation[143]. However, the level of coating of a non-magnetic material must be carefully controlled, as too thick of a coating can drastically decrease the observed magnetic moment. A large variety of different biomolecules have been conjugated to magnetic nanoparticles for a variety of applications, including dopamine, DNA and larger proteins[143].

DNA has been coated onto magnetic nanoparticles via chemical conjugation, whereby the DNA forms a covalent bond with the reactive surface functional groups on the nanoparticle. Simple electrostatic adsorption has also been used to prepare DNA-coated magnetite, where a positively charged overcoating material, such as polyethyleneimine (PEI), is used to stabilise the magnetite nanoparticles first, and then the DNA adsorbs to this. This approach was shown by Scherer *et al.* where they demonstrated that magnetic nanoparticles that had been encapsulated in PEI

were excellent gene delivery agents to cells and tissues through simple adsorption of the DNA onto the PEI-stabilised nanoparticle[144].

Covalent conjugation techniques have also been utilised in the functionalisation of magnetic nanoparticles with DNA. This has been achieved using standard chemistry involving 1-ethyl-3-(3-dimethylaminopropyl)carbodiimide (EDC) coupling, succinimidyl 4-(N-maleimidomethyl)cyclohexane-1-carboxylate) (SMCC) coupling, or even click chemistry[143]. For example, work by Cutler *et al.* used click chemistry to produce magnetite nanoparticles functionalised with a dense layer of DNA added through the copper (I) catalysed azide-alkyne cycloaddition reaction[145].

The use of magnetic nanoparticles as MRI contrast agents, and their ability to reduce the spin-spin relaxation time of surrounding water protons has previously been discussed. The ability of magnetic nanoparticles to reduce the T_2 relaxation time as been used as a novel means of detecting DNA, alongside real-time monitoring of DNA methylation and cleavage by Perez *et al.*[146]. In this work, they made 300 - 400 nm aggregates of two different sets of magnetic nanoparticles that were functionalised with complementary strands of DNA that showed a much slower T_2 relaxation time compared to individual free magnetic nanoparticles in a buffer solution. When an appropriate DNA restriction enzyme was used, the particles were released from the aggregates which increased the T_2 relaxation time. They also showed that methylation followed by DNA cleavage could be monitored via MRI.

Magnetic nanoparticles can also be used for magnetic hyperthermia. In this case, an external alternating magnetic field can be used to generate local heating, as with every pulse, the magnetic dipoles will attempt to realign themselves[147]. This hyperthermia can be sufficiently hot to denature any dsDNA present on the surface of the magnetic nanoparticle and hence release drugs or any other molecules that had

been intercalated into the DNA.

As can be seen, DNA-functionalised magnetic nanoparticles have been shown to have an array of interesting potential applications. The development of DNA-functionalised nanoparticles that are both plasmonic and magnetic are, therefore, of a huge research interest, as it would combine the features of both the nanoparticle species discussed.

1.6 Calcium Carbonate Microparticles

Calcium carbonate is a truly ubiquitous material, comprising over 4% of the Earth's crust and found all over the globe in various forms including limestone, chalk and marble[148,149]. Calcium carbonate also plays a pivotal role in marine life, where not only does it form the shells and bones of many aquatic creatures and but is also involved in biomineralisation. One of the most important functions of calcium carbonate is its ability to absorb atmospheric CO_2. In an age plagued with climate change induced natural disasters, research into CO_2 sinks is ever more important[150].

Calcium carbonate is of huge commercial interest, and its impact on our day-to-day lives, whether we realise it or not, is colossal. As a precursor of cement, and the prime constituent in marble; as a buffer in soil and water; as a white pigment in paint and high gloss paper, down to a binding agent in medicinal tablets and antacids; life as we know it would not exist without calcium carbonate[151–153]. While calcium carbonate has a huge array of applications on a macroscopic level, and has been studied for centuries, only in recent years have scientists begun investigating it on the microscopic and nano-scales.

Calcium carbonate occurs naturally in six different forms; three anhydrous crystalline polymorphs, two hydrated phases and one amorphous phase. The three crystalline polymorphs are calcite, vaterite and aragonite. The two hydrated phases are monohydrocalcite and ikaite, and the amorphous phase is amorphous calcium carbonate[149]. The monohydrocalcite structure has 8-fold coordinated calcium ions, with water situated between the screw axes bound to the carbonate ions via hydrogen bridges[154]. It has been found to be metastable under all conditions, but it does form in some predominantly freshwater environments[155,156]. Ikaite, the second hydrate form, is characterised by hydrated calcium carbonate chains linked together by hydrogen bonds. Ikaite is found to be stable at high pressures and low temperatures such as in the bottom waters in fjords and deep sea floors[157].

The three crystalline polymorphs and ACC are the most common forms of calcium carbonate. Of these four, calcite is the most thermodynamically stable at room temperature and pressure with a trigonal rhombohedral structue, and typically has a rhombohedral morphology. Aragonite is the most stable in high-pressure conditions, however, it can form at atmospheric pressure under certain conditions, such as in hot springs[158]. It has an orthorhombic crystal structure and and typically displays an acicular or needle-like morphology[159,160]. Vaterite is metastable, and will either change to form another polymorph or can be stabilised by water or other additives on its surfaces[161]. Vaterite has a hexagonal crystal system and polycrystalline spherulite morphology[162]. ACC is the least stable. The ACC phase is short-lived and acts mainly as a seed for the crystal growth of other polymorphs[152]. The most common crystal polymorphs are shown in Figure 1.19.

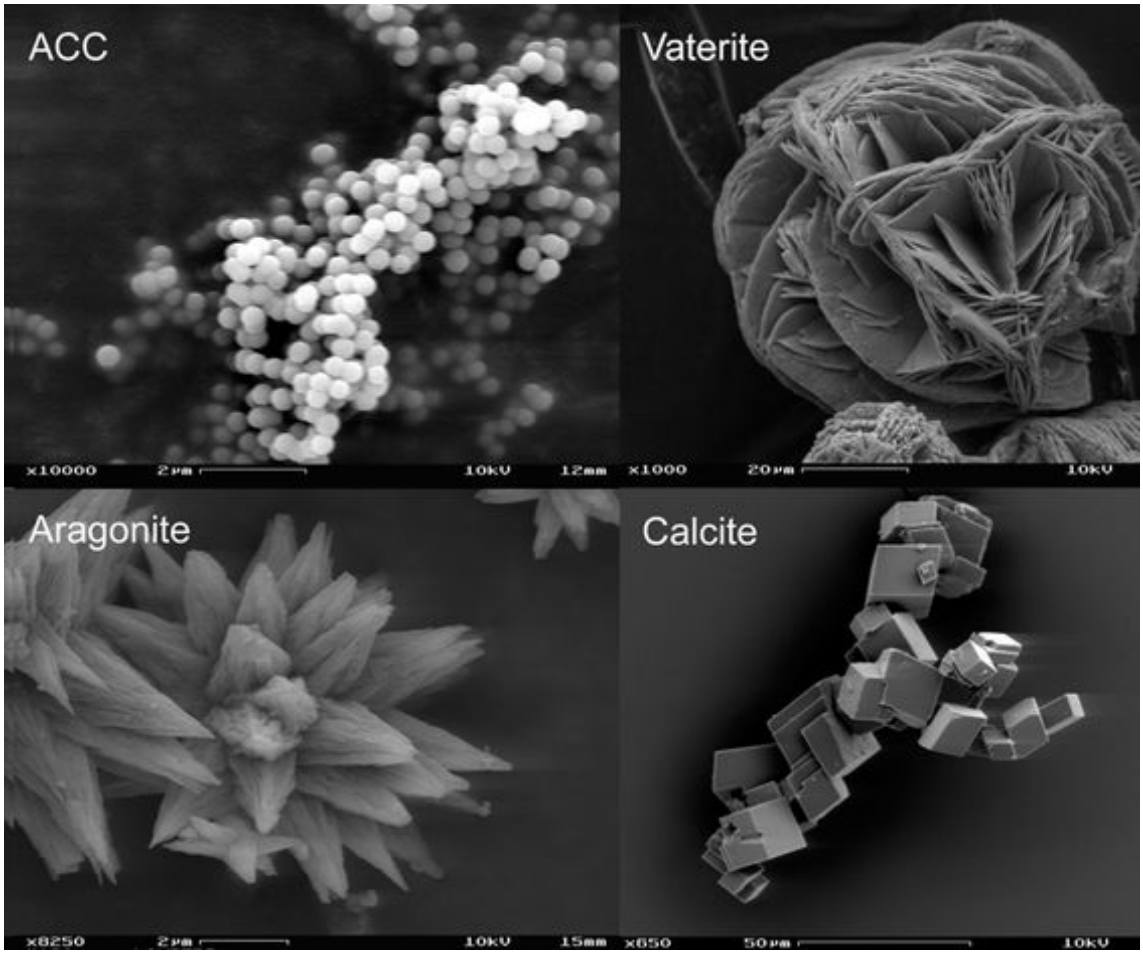

Figure 1.19: The four most common polymorphs of calcium carbonate. Adapted from ref[163].

The formation of calcium carbonate into any one of the aforementioned polymorphs is guided by the equilibrium between H_2O and CO_2. The equilibrium between gaseous CO_2 and the dissolved CO_2 in solution may be described in the following manner[164].

$$CO_{2(g)} \rightleftharpoons CO_{2(aq)} \tag{1.11}$$

Where $K_H = 29$ atm/(mol/L) at 25 °C. Carbonic acid will then be formed as the dissolved CO_2 reacts with water. This reaction is governed by the hydration equi-

librium constant[165] K_h = 1.7 x 10^{-3} at 25 °C.

$$CO_{2(aq)} + H_2O \rightleftharpoons H_2CO_{3(aq)} \tag{1.12}$$

Initially the carbonic acid will dissociate in water to form the bicarbonate ion, but as it is a diprotic acid it is then capable of undergoing a second ionisation in order to form the carbonate ion. These reactions are described in the equations below.

$$H_2CO_{3(aq)} \rightleftharpoons HCO_3^- + H^+ \tag{1.13}$$

Where the equilibrium constant is described by the following expression:

$$K_{a1} = \frac{[H^+][HCO_3^-]}{[H_2CO_3]} \tag{1.14}$$

Where K_{a1} = 4.9 x 10^{-7} at 25 °C.

The second ionisation to form the carbonate ion then proceeds as follows:

$$HCO_{3(aq)}^- \rightleftharpoons CO_{3(aq)}^{2-} + H^+ \tag{1.15}$$

Where the equilibrium constant is described by K_{a2} which is

$$K_{a2} = \frac{[H^+][CO_3^{2-}]}{[HCO_3^-]} \tag{1.16}$$

where K_{a2}= 5.6 x 10^{-11} at 25 °C.

The carbonate ion is then free to react with calcium ions to form calcium carbonate.

$$Ca^{2+}{}_{(aq)} + CO_{3(aq)}{}^{2-} \rightleftharpoons CaCO_{3(s)} \tag{1.17}$$

The equilibrium between H_2CO_3, HCO_3^- and CO_3^{2-} is highly pH dependent. Generally, at pH values near 7, HCO_3^- is dominant, with H_2CO_3 being predominant at lower pH values, and CO_3^{2-} being favoured at high pH values[166]. As is evident, the formation of calcium carbonate is a complex multi-step process.

The first stage in the formation of crystalline calcium carbonate will be nucleation. Classical studies assume that single ion attachment results in the formation of a critical nucleus, however, modern studies have proposed the formation of pre-nucleation clusters in the first steps of $CaCO_3$ formation[167–169]. In any case, the first stage in calcium carbonate formation is the formation of ACC[170–174]. This amorphous phase will then either tend towards proto-calcite or proto-vaterite depending on the pH. This occurs due to the polymorphism of ACC and its ability to exist in a number of different morphologies[175]. The instability of the amorphous calcium carbonate phase means that the ACC will rapidly transform into vaterite, which will then normally transform into calcite at ambient temperatures and pressures. At temperatures above 50 °C, the vaterite will transform into aragonite, which will gradually turn into calcite over a period of months[160,176].

Solvent choice plays a crucial role in the stability of the metastable calcium carbonate phases. The choice of solvent will have a significant influence on the solvent-crystal interface energy and can have a stabilising effect on the otherwise unstable preliminary phases of calcium carbonate crystallisation. The addition of alcohols in the synthesis of calcium carbonate can be used to stabilise the otherwise unstable vaterite phase, and prevent its transition to calcite[177–179].

While there are various industrial and experimental approaches to preparing calcium carbonate, the two most common are CO_2 gas bubbling and precipitation reactions between two salt solutions. In this work, precipitation reactions are utilised in order to obtain a number of microsphere structures. Precipitation reactions describe the reaction between soluble calcium and carbonate containing salts which result in the formation of an insoluble calcium carbonate precipitate, and an aqueous byproduct. An equation illustrating an example of this reaction is shown below.

$$\mathrm{CaCl_{2(aq)} + Na_2CO_{3(aq)} \longrightarrow CaCO_{3(s)} + 2\,NaCl_{(aq)}} \tag{1.18}$$

The precipitation approach is an easy and highly reproducible method of obtaining calcium carbonate. A modified version of the precipitation reaction are microemulsion based syntheses. In this method, a combination of water and oil soluble materials are used in order to control the parameters of the synthesis. The most common type of microemulsion is a water in oil (W/O) microemulsion. (W/O) microemulsions involve using an aliphatic/aromatic hydrocarbon, an ionic surfactant and water. The surfactant and co-surfactant form a mixed film at the interface of the oil and water which spontaneously generates reverse micelles. The use of this approach means that materials that are otherwise water insoluble, such as many pharmaceutical compounds, can be incorporated into calcium carbonate structures.

CO_2 bubbling is another common approach to the preparation of calcium carbonate, and this is the industrially preferred approach due to its easy scalability. CO_2 is bubbled through calcium hydroxide to produce a solid $CaCO_3$ precipitate. However, precise morphological control is not generally possible with this approach due to the diffusion limited nature of the reaction.

The great potential applications of magnetic and plasmonic materials, as well as DNA-functionalised materials have all previously been discussed. It would be remiss, however, to say the same of calcium carbonate, which already has swathes of applications across a huge variety of fields. It is more accurate to say that calcium carbonate still, amongst all its current applications, has much more to offer.

Biomedicine is one of the most promising and exciting areas of current $CaCO_3$ research, particularly the use of $CaCO_3$ microparticles[180]. These are attractive drug delivery vesicles, as they readily degrade *in-vivo* through phagocytosis by macrophages or through bodily dissolution by lysomal enzymes[181]. $CaCO_3$ is also highly pH sensitive, and this has enabled its use as an anti-cancer drug delivery agent. Tumour cells are acidic, and so if a drug is encapsulated in a $CaCO_3$ microparticle, it will only be released at the tumour site as the $CaCO_3$ is dissolved by the acidic tumour environment[182]. In these drug delivery systems, the Ca^{2+} ions that are produced are then used in metabolism and bone generation without any accompanying tissue calcification, before being excreted by the kidneys and liver. CO_3^{2-} is released into the extracellular matrix prior to excretion[181].

A variety of approaches for preparing $CaCO_3$ drug delivery vehicles have been developed. As has been previously discussed, a modification of the precipitation approach, the microemulsion approach, can be used to encapsulate pharmaceutical compounds in the $CaCO_3$ matrix. This approach is highly efficient as the drug loading can be

carried out *in-situ* as the microstructures are being made. A solvent evaporation approach can also be used for loading a drug into a microparticle after its initial synthesis. Here, the pre-made $CaCO_3$ microparticles are soaked in a solvent containing the drug of choice, and then the solvent is evaporated at a reduced pressure[183]. While this technique allows the loading of compounds that are poorly soluble in many solvents, there will be a disparity between the amount of the drug loaded into the microspheres and the amount of the drug coating the microspheres. This will result in two different drug release profiles for the drugs from the microspheres.

Calcium carbonate has been utilised by humans for centuries for a wide variety of applications, and yet still, as technology and instrumentation techniques improve, it has been shown to have even more interesting and useful applications at the nano- and micro-scale. Its biocompatibility, abundance, acid-sensitivity and easy synthesis means that is a prime candidate for use in many multi-modal, sensing and biomedicinal applications.

1.7 Aims of the Project

The main goal of this project is to prepare and develop a range of new multimodal magnetic and plasmonic nano- and micro-structures. We plan to use a range of synthetic techniques, including coprecipitation, the Turkevich approach, and layer-by-layer syntheses. These methods should allow us to prepare a variety of multi-modal, multifunctional nano- and micro-materials. The intended application of these nanomaterials is in the fields of separation, biosensing and biomedicine.

The prepared materials are to be characterised by various techniques including, but not limited to, TEM, SEM, EDX, XRD, DLS, UV-Vis, FT-IR and Raman spectroscopy.

In the first instance, the main focus is to prepare a simple and robust magnetic-plasmonic nanocomposite material which is easily accessible and highly reproducible. This approach will utilise the complementary charges of two polyelectrolytes in order to achieve binding through electrostatic interactions. This method is then to be extended to other systems, and more complex plasmonic nanostructures are to be investigated. The self-assembly of magnetic-plasmonic nano-and micro-structures over time will be investigated and analysed. The use of another biocompatible polyelectrolyte, such as DNA, will be investigated for its use in the synthesis and stabilisation of magnetic and plasmonic nanoparticles. Furthermore, the difference between the single-stranded and double-stranded DNA with the nanoparticles will also be analysed. Finally, a variety of $CaCO_3$-based micro-structures will be prepared and further functionalised with magnetic and plasmonic nanoparticles.

Thus, the scientific and technical objectives of this project are as follows:

1. To prepare a range of polyelectrolyte (PE) -stabilised magnetite nanoparticles.

2. To optimise the synthesis of PE-stabilised magnetite nanoparticles such that both the colloidal stability and magnetic properties are maintained.

3. To prepare a range of PE-stabilised gold nanoparticles and optimise their syntheses.

4. To prepare a variety of anisotropic gold nanoparticles.

5. To synthesise and characterise a range of magnetic-plasmonic nanocomposite materials and investigate their properties.

6. To develop a range of single-stranded and double-stranded DNA stabilised magnetic and plasmonic nanoparticles.

7. To prepare and optimise a range of calcium carbonate microstructrues functionalised with magnetic and gold nanoparticles using a layer-by-layer technique.

8. To test these materials for the detection of aqueous heavy metal ions and other toxins, as well as the testing for the detection of viruses.

It is expected that this work will contribute to the further development of multimodal magnetic-plasmonic materials as well as their other sensing and biomedical applications.

Bibliography

(1) Z. Aguilar, *Nanomaterials for Medical Applications*, Elsevier Inc., 2013.

(2) S. Raj, S. Jose, U. S. Sumod and M. Sabitha, *Nanotechnology in cosmetics: Opportunities and challenges*, 2012.

(3) I. Khan, K. Saeed and I. Khan, *Arabian Journal of Chemistry*, 2017, DOI: 10.1016/J.ARABJC.2017.05.011.

(4) ChemBam.com, *Size of the Nanoscale — Nano, [Online, accessed May 2020].*

(5) P. Colomban, *Journal of Nano Research*, 2009, **8**, 109–132.

(6) X. Huang and M. A. El-Sayed, *Gold nanoparticles: Optical properties and implementations in cancer diagnosis and photothermal therapy*, 2010.

(7) Y. C. Yeh, B. Creran and V. M. Rotello, *Gold nanoparticles: Preparation, properties, and applications in bionanotechnology*, 2012.

(8) Nanocomposix, *Nanocomposix.eu · Aqueous Gold Spheres [Online, accessed April 2020].*

(9) P. K. Jain, X. Huang, I. H. El-Sayed and M. A. El-Sayed, *Accounts of Chemical Research*, 2008, **41**, 1578–1586.

(10) V. V. Mody, A. Cox, S. Shah, A. Singh, W. Bevins and H. Parihar, *Magnetic nanoparticle drug delivery systems for targeting tumor*, 2014.

(11) S. Stafford, R. Serrano Garcia and Y. Gun'ko, *Applied Sciences*, 2018, **8**, 97.

(12) *8.7: Spinel, Perovskite, and Rutile Structures - Chemistry LibreTexts [Online - accessed May 2020].*

(13) A. Mitra, J. Mohapatra, S. S. Meena, C. V. Tomy and M. Aslam, *The Journal of Physical Chemistry C*, 2014, **118**, 19356–19362.

(14) *Who Discovered the Very First Magnet? — Dowling Magnets [Online, accessed May 2020].*

(15) R. M. Cornell and U. Schwertmann, *The Iron Oxides*, Wiley, 2003.

(16) A. Kolhatkar, A. Jamison, D. Litvinov, R. Willson and T. Lee, *International Journal of Molecular Sciences*, 2013, **14**, 15977–16009.

(17) T. Sato, T. Iijima, M. Seki and N. Inagaki, *Journal of Magnetism and Magnetic Materials*, 1987, **65**, 252–256.

(18) Y. Qu, H. Yang, N. Yang, Y. Fan, H. Zhu and G. Zou, *Materials Letters*, 2006, **60**, 3548–3552.

(19) S. O'Brien, L. Brus and C. B. Murray, *Journal of the American Chemical Society*, 2001, **123**, 12085–12086.

(20) X. Peng, J Wickham and A. P. Alivisatos, *Journal of the American Chemical Society*, 1998, **120**, 5343–5344.

(21) J. Park, K. An, Y. Hwang, J.-G. Park, H.-J. Noh, J.-Y. Kim, J.-H. Park, N.-M. Hwang and T. Hyeon, *Nat Mater*, 2004, **3**, 891–895.

(22) A.-H. Lu, E. Salabas and F. Schüth, *Angewandte Chemie International Edition*, 2007, **46**, 1222–1244.

(23) J. Rockenberger, E. C. Scher and A. P. Alivisatos, *Journal of the American Chemical Society*, 1999, **121**, 11595–11596.

(24) S. Thimmaiah, M. Rajamathi, N. Singh, P. Bera, F. Meldrum, N Chandrasekhar and R. Seshadri, *Journal of Materials Chemistry*, 2001, **11**, 3215–3221.

(25) L. Li, S. Fu, C. Chen, X. Wang, C. Fu, S. Wang, W. Guo, X. Yu, X. Zhang, Z. Liu, J. Qiu and H. Liu, *ACS Nano*, 2016, **10**, 7094–7105.

(26) L. Gloag, M. Mehdipour, D. Chen, R. D. Tilley and J. J. Gooding, *Advances in the Application of Magnetic Nanoparticles for Sensing*, 2019.

(27) Z. Zhao, Z. Zhou, J. Bao, Z. Wang, J. Hu, X. Chi, K. Ni, R. Wang, X. Chen, Z. Chen and J. Gao, *Nature Communications*, 2013, **4**, 1–7.

(28) J. E. Kim, J. Y. Shin and M. H. Cho, *Magnetic nanoparticles: An update of application for drug delivery and possible toxic eVects*, 2012.

(29) J. G. Webster, M. Zborowski and J. J. Chalmers, in *Wiley Encyclopedia of Electrical and Electronics Engineering*, John Wiley & Sons, Inc., 2015, pp. 1–23.

(30) J. Wang, D. Xu, A. N. Kawde and R. Polsky, *Analytical Chemistry*, 2001, **73**, 5576–5581.

(31) J. M. Nam, C. S. Thaxton and C. A. Mirkin, *Science*, 2003, **301**, 1884–1886.

(32) P. Potdar and N. Lotey, *Journal of Cancer Metastasis and Treatment*, 2015, **1**, 44.

(33) *CELLSEARCH® — Product and Systems Overview — CTC Kit [Online, accessed May 2020].*

(34) M. Poudineh, P. M. Aldridge, S. Ahmed, B. J. Green, L. Kermanshah, V. Nguyen, C. Tu, R. M. Mohamadi, R. K. Nam, A. Hansen, S. S. Sridhar, A. Finelli, N. E. Fleshner, A. M. Joshua, E. H. Sargent and S. O. Kelley, *Nature Nanotechnology*, 2017, **12**, 274–281.

(35) M. Labib, R. M. Mohamadi, M. Poudineh, S. U. Ahmed, I. Ivanov, C. L. Huang, M. Moosavi, E. H. Sargent and S. O. Kelley, *Nature Chemistry*, 2018, **10**, 489–495.

(36) *Magnetic Resonance Imaging (MRI) [Online, accessed May 2020].*

(37) P. Caravan, J. J. Ellison, T. J. McMurry and R. B. Lauffer, *Chemical Reviews*, 1999, **99**, 2293–2352.

(38) M. Rogosnitzky and S. Branch, *Gadolinium-based contrast agent toxicity: a review of known and proposed mechanisms*, 2016.

(39) C. Sun, K. Du, C. Fang, N. Bhattarai, O. Veiseh, F. Kievit, Z. Stephen, D. Lee, R. G. Ellenbogen, B. Ratner and M. Zhang, *ACS Nano*, 2010, **4**, 2402–2410.

(40) R. C. Semelka and T. K. Helmberger, *Radiology*, 2001, **218**, 27–38.

(41) Y. X. Wang, S. M. Hussain and G. P. Krestin, *European Radiology*, 2001, **11**, 2319–2331.

(42) B. Bonnemain, *Superparamagnetic agents in magnetic resonance imaging: Physicochemical characteristics and clinical applications. A review*, 1998.

(43) M. G. Harisinghani, J. Barentsz, P. F. Hahn, W. M. Deserno, S. Tabatabaei, C. H. Van de Kaa, J. De la Rosette and R. Weissleder, *New England Journal of Medicine*, 2003, **348**, 2491–2499.

(44) O. Veiseh, C. Sun, C. Fang, N. Bhattarai, J. Gunn, F. Kievit, K. Du, B. Pullar, D. Lee, R. G. Ellenbogen, J. Olson and M. Zhang, *Cancer Research*, 2009, **69**, 6200–6207.

(45) J. Liu, H. He, D. Xiao, S. Yin, W. Ji, S. Jiang, D. Luo, B. Wang and Y. Liu, *Recent advances of plasmonic nanoparticles and their applications*, 2018.

(46) N. Elahi, M. Kamali and M. H. Baghersad, *Recent biomedical applications of gold nanoparticles: A review*, 2018.

(47) N. U. Islam, K. Jalil, M. Shahid, A. Rauf, N. Muhammad, A. Khan, M. R. Shah and M. A. Khan, *Arabian Journal of Chemistry*, 2019, **12**, 2914–2925.

(48) T. Mori and T. Hegmann, *Determining the composition of gold nanoparticles: a compilation of shapes, sizes, and calculations using geometric considerations*, 2016.

(49) W. Shi, Z. Zhang and S. Li, *Journal of Physical Chemistry Letters*, 2018, **9**, 373–382.

(50) H. Zhou, J.-P. Kim, J. H. Bahng, N. A. Kotov and J. Lee, *Advanced Functional Materials*, 2014, **24**, 1439–1448.

(51) Z. Kereselidze, V. H. Romero, X. G. Peralta and F. Santamaria, *Journal of visualized experiments : JoVE*, 2012, DOI: 10.3791/3570.

(52) N. A. Kotov, *Inorganic nanoparticles as protein mimics*, 2010.

(53) A. Guerrero-Martínez, S. Barbosa, I. Pastoriza-Santos and L. M. Liz-Marzán, *Nanostars shine bright for you. Colloidal synthesis, properties and applications of branched metallic nanoparticles*, 2011.

(54) Z. Tang, Z. Zhang, Y. Wang, S. C. Glotzer and N. A. Kotov, *Science*, 2006, **314**, 274–278.

(55) A. Querejeta-Fernàndez, J. C. Hernàndez-Garrido, H. Yang, Y. Zhou, A. Varela, M. Parras, J. J. Calvino-Gàmez, J. M. Gonzàlez-Calbet, P. F. Green and N. A. Kotov, *ACS Nano*, 2012, **6**, 3800–3812.

(56) A. R. Tao, S. Habas and P. Yang, *Small*, 2008, **4**, 310–325.

(57) E. Margapoti, D. Gentili, M. Amelia, A. Credi, V. Morandi and M. Cavallini, *Nanoscale*, 2014, **6**, 741–744.

(58) V. Amendola, *Physical Chemistry Chemical Physics*, 2016, **18**, 2230–2241.

(59) U. Kreibig and M. Vollmer, *Optical properties of metal clusters*, Springer, 1995, p. 532.

(60) C. Kittel, *Introduction to Solid State Physics*, 2004, 453–486.

(61) S. A. Maier and S. A. Maier, in *Plasmonics: Fundamentals and Applications*, Springer US, 2007, pp. 5–19.

(62) P. Biagioni, J.-S. Huang and B. Hecht, *Reports on Progress in Physics*, 2012, **75**, 024402.

(63) W. L. Barnes, *American Journal of Physics*, 2016, **84**, 593–601.

(64) C. F. Bohren and D. R. Huffman, *Absorption and scattering of light by small particles*, Wiley, 1983, p. 530.

(65) R. C. Jones, *Physical Review*, 1945, **68**, 93–96.

(66) R. Gans, *Annalen der Physik*, 1912, **342**, 881–900.

(67) *NanoHybrids - Plasmonics Nanoparticles [Online, accessed May 2020].*

(68) C. L. Nehl and J. H. Hafner, *Shape-dependent plasmon resonances of gold nanoparticles*, 2008.

(69) C. L. Nehl, H. Liao and J. H. Hafner, *Nano Letters*, 2006, **6**, 683–688.

(70) E. Prodan, C. Radloff, N. J. Halas and P. Nordlander, *Science*, 2003, **302**, 419–422.

(71) J. Turkevich, P. C. Stevenson and J. Hillier, *The Journal of Physical Chemistry*, 1953, **57**, 670–673.

(72) Boon-Kin Pong, Hendry I. Elim, Jian-Xiong Chong, Wei Ji, Bernhardt L. Trout, †, and Jim-Yang Lee*, †, 2007, DOI: 10.1021/JP0686660.

(73) A. R. Prado, J. P. Oliveira, W. J. Keijok, B. Milaneze, B. V. Nogueira, M. C. Guimarães, M. J. Pontes and M. R. Ribeiro, *BMC Proceedings*, 2014, **8**, P252.

(74) W. Brullot, R. Strobbe, M. Bynens, M. Bloemen, P.-J. Demeyer, W. Vanderlinden, S. De Feyter, V. K. Valev and T. Verbiest, *Materials Letters*, 2014, **118**, 99–102.

(75) R. Wood, *The London, Edinburgh, and Dublin Philosophical Magazine and Journal of Science*, 1902, **4**, 396–402.

(76) B. Liedberg, C. Nylander and I. Lunström, *Sensors and Actuators*, 1983, **4**, 299–304.

(77) B. A. Prabowo, A. Purwidyantri and K. C. Liu, *Surface plasmon resonance optical sensor: A review on light source technology*, 2018.

(78) C. Y. Chang, H. T. Lin, M. S. Lai, T. Y. Shieh, C. C. Peng, M. H. Shih and Y. C. Tung, *Scientific Reports*, 2018, **8**, 1–8.

(79) E. M. Larsson, J. Alegret, M. Kăll and D. S. Sutherland, *Nano Letters*, 2007, **7**, 1256–1263.

(80) Y. Tang, X. Zeng and J. Liang, *Journal of Chemical Education*, 2010, **87**, 742–746.

(81) *Raman FAQs - What is surface enhanced Raman scattering, or SERS? - HORIBA [Online, accessed May 2020].*

(82) N. P. Ivleva, M. Wagner, H. Horn, R. Niessner and C. Haisch, *Journal of Biophotonics*, 2010, **3**, 548–556.

(83) B. Ren, G. Picardi and B. Pettinger, *Review of Scientific Instruments*, 2004, **75**, 837–841.

(84) F. Tian, F. Bonnier, A. Casey, A. E. Shanahan and H. J. Byrne, *Analytical Methods*, 2014, **6**, 9116–9123.

(85) M. Moskovits, *Physical Chemistry Chemical Physics*, 2013, **15**, 5301–5311.

(86) P. K. Aravind and H. Metiu, *Surface Science*, 1983, **124**, 506–528.

(87) K. Kneipp, H. Kneipp, I. Itzkan, R. R. Dasari and M. S. Feld, *Surface-enhanced Raman scattering and biophysics*, tech. rep., 2002, pp. 597–624.

(88) P. K. Aravind and H. Metiu, *Chemical Physics Letters*, 1980, **74**, 301–305.

(89) P. K. Aravind, A. Nitzan and H. Metiu, *Surface Science*, 1981, **110**, 189–204.

(90) Y. Fang, N. H. Seong and D. D. Dlott, *Science*, 2008, **321**, 388–392.

(91) V. S. Tiwari, T. Oleg, G. K. Darbha, W. Hardy, J. P. Singh and P. C. Ray, *Chemical Physics Letters*, 2007, **446**, 77–82.

(92) F. Hao, C. L. Nehl, J. H. Hafner and P. Nordlander, *Nano Letters*, 2007, **7**, 729–732.

(93) Y. Zhang, C. Li, Z. Fakhraai, B. Moosa, P. Yang and N. M. Khashab, *ACS Omega*, 2018, **3**, 14399–14405.

(94) X. Jin, H. Li, S. Wang, N. Kong, H. Xu, Q. Fu, H. Gu and J. Ye, *Nanoscale*, 2014, **6**, 14360–14370.

(95) C. He, W. Nie and W. Feng, *Journal of Materials Chemistry B*, 2014, **2**, 7828–7848.

(96) A. Vaitkuviene, V. Kaseta, J. Voronovic, G. Ramanauskaite, G. Biziuleviciene, A. Ramanaviciene and A. Ramanavicius, *Journal of Hazardous Materials*, 2013, **250**, 167–174.

(97) D Le Garrec, S Gori, L Luo, D Lessard, D. C. Smith, M. A. Yessine, M Ranger and J. C. Leroux, *Journal of Controlled Release*, 2004, **99**, 83–101.

(98) L. Xie, W. Qian, S. Yang, J. Sun and T. Gong, *MATEC Web Conf.*, 2017, **88**.

(99) X. Wang, H. Liu, D. Chen, X. Meng, T. Liu, C. Fu, N. Hao, Y. Zhang, X. Wu, J. Ren and F. Tang, *ACS Applied Materials & Interfaces*, 2013, **5**, 4966–4971.

(100) E. Fantechi, P. M. Castillo, E. Conca, F. Cugia, C. Sangregorio and M. F. Casula, *Interface Focus*, 2016, **6**.

(101) Y. Ma, Q. Kuang, Z. Jiang, Z. Xie, R. Huang and L. Zheng, *Angewandte Chemie International Edition*, 2008, **47**, 8901–8904.

(102) P.-Y. Lee, H.-S. Teng and C.-S. Yeh, *Nanoscale*, 2013, **5**, 7558–7563.

(103) O. Ivashchenko, J. Gapiński, B. Peplińska, Przysiecka, T. Zalewski, G. Nowaczyk, M. Jarek, A. Marcinkowska-Gapińska and S. Jurga, *Materials & Design*, 2017, **133**, 307–324.

(104) R. S. Riley and E. S. Day, *Wiley Interdisciplinary Reviews: Nanomedicine and Nanobiotechnology*, 2017, **9**, e1449–n/a.

(105) L. Zou, H. Wang, B. He, L. Zeng, T. Tan, H. Cao, X. He, Z. Zhang, S. Guo and Y. Li, *Theranostics*, 2016, **6**, 762–772.

(106) L. Hu, Y. Sun and Y. Wu, *Nanoscale*, 2013, **5**, 3103–3111.

(107) S. Rodrigues, M. Dionísio, C. Remuñán López and A. Grenha, *Journal of Functional Biomaterials*, 2012, **3**, 615–641.

(108) A. D. Sezer and E. Cevher, *Expert Opinion on Drug Delivery*, 2012, **9**, 1129–1146.

(109) A. Fernanda, A. Filipa, N. Ana Vanessa, S. Sara Baptista da, N. Jose das, F. Domingos and S. Bruno, *Current Drug Discovery Technologies*, 2011, **8**, 157–172.

(110) R. Tietze, J. Zaloga, H. Unterweger, S. Lyer, R. P. Friedrich, C. Janko, M. Pöttler, S. Dürr and C. Alexiou, *Biochemical and Biophysical Research Communications*, 2015, **468**, 463–470.

(111) G. De Crozals, R. Bonnet, C. Farre and C. Chaix, *Nano Today*, 2016, **11**, 435–463.

(112) W.-P. Li, P.-Y. Liao, C.-H. Su and C.-S. Yeh, *Journal of the American Chemical Society*, 2014, **136**, 10062–10075.

(113) J. D. Watson and F. H. Crick, *Nature*, 1953, **171**, 737–738.

(114) *The Chemical Structure of DNA – Compound Interest [Online, accessed May 2020].*

(115) *Structure and Function of DNA — Microbiology [Online, accessed May 2020].*

(116) *Nucleic acid structure, https://www.atdbio.com/, [Online, accessed May 2020].*

(117) *MLA CE Course Manual: Molecular Biology Information Resources (Genetics Review: Nucleotide) [Online, accessed May 2020].*

(118) S. D. Patil, D. G. Rhodes and D. J. Burgess, *DNA-based therapeutics and DNA delivery systems: A comprehensive review*, 2005.

(119) O. Kallioniemi, A. Kallioniemi, J. Piper, J. Isola, F. M. Waldman, J. W. Gray and D. Pinkel, *Optimizing comparative genomic hybridization for analysis of DNA sequence copy number changes in solid tumors*, 1994.

(120) D. R. Call, M. K. Borucki and F. J. Loge, *Detection of bacterial pathogens in environmental samples using DNA microarrays*, 2003.

(121) R. T. Ranasinghe and T. Brown, *Fluorescence based strategies for genetic analysis*, 2005.

(122) C. Debouck and P. N. Goodfellow, *Nature Genetics*, 1999, **21**, 50.

(123) Y. Krishnan and F. C. Simmel, *Nucleic acid based molecular devices*, 2011.

(124) L. Berti, J. Xie, I. L. Medintz, A. N. Glazer and R. A. Mathies, *Analytical Biochemistry*, 2001, **292**, 188–197.

(125) A. Samanta and I. L. Medintz, *Nanoparticles and DNA-a powerful and growing functional combination in bionanotechnology*, 2016.

(126) M. De, P. S. Ghosh and V. M. Rotello, *Advanced Materials*, 2008, **20**, 4225–4241.

(127) E. C. Dreaden, A. M. Alkilany, X. Huang, C. J. Murphy and M. A. El-Sayed, *The golden age: Gold nanoparticles for biomedicine*, 2012.

(128) X. Huang, P. K. Jain, I. H. El-Sayed and M. A. El-Sayed, *Gold nanoparticles: Interesting optical properties and recent applications in cancer diagnostics and therapy*, 2007.

(129) M. D. Porter, R. J. Lipert, L. M. Siperko, G. Wang and R. Narayanan, *Chemical Society Reviews*, 2008, **37**, 1001–1011.

(130) E. Dulkeith, A. C. Morteani, T. Niedereichholz, T. A. Klar, J. Feldmann, S. A. Levi, F. C. van Veggel, D. N. Reinhoudt, M. Möller and D. I. Gittins, *Physical Review Letters*, 2002, **89**, 203002.

(131) E. Dulkeith, M. Ringler, T. A. Klar, J. Feldmann, A. M. Javier and W. J. Parak, *Nano Letters*, 2005, **5**, 585–589.

(132) A. P. Alivisatos, K. P. Johnsson, X. Peng, T. E. Wilson, C. J. Loweth, M. P. Bruchez and P. G. Schultz, *Nature*, 1996, **382**, 609–611.

(133) C. A. Mirkin, R. L. Letsinger, R. C. Mucic and J. J. Storhoff, *Nature*, 1996, **382**, 607–609.

(134) C. D. Bain, J. Evall and G. M. Whitesides, *Journal of the American Chemical Society*, 1989, **111**, 7155–7164.

(135) H. Grönbeck, A. Curioni and W. Andreoni, *Journal of the American Chemical Society*, 2000, **122**, 3839–3842.

(136) S. J. Hurst, A. K. Lytton-Jean and C. A. Mirkin, *Analytical Chemistry*, 2006, **78**, 8313–8318.

(137) J. J. Storhoff, R. Elghanian, R. C. Mucic, C. A. Mirkin and R. L. Letsinger, *Journal of the American Chemical Society*, 1998, **120**, 1959–1964.

(138) X. Bai, J. Wu, X. Han and Z. Deng, *Anal. Chem*, 2011, **83**, 18.

(139) H. Li and L. Rothberg, *Proceedings of the National Academy of Sciences of the United States of America*, 2004, **101**, 14036–14039.

(140) M. Thomas and A. M. Klibanov, *Proceedings of the National Academy of Sciences of the United States of America*, 2003, **100**, 9138–9143.

(141) M. Comotti, C. Della Pina, R. Matarrese and M. Rossi, *Angewandte Chemie - International Edition*, 2004, **43**, 5812–5815.

(142) A. Samanta, S. Banerjee and Y. Liu, *DNA nanotechnology for nanophotonic applications*, 2015.

(143) K. E. Sapsford, W. R. Algar, L. Berti, K. B. Gemmill, B. J. Casey, E. Oh, M. H. Stewart and I. L. Medintz, *Functionalizing nanoparticles with biological molecules: Developing chemistries that facilitate nanotechnology*, 2013.

(144) F. Scherer, M. Anton, U. Schillinger, J. Henke, C. Bergemann, A. Krüger, B. Gänsbacher and C. Plank, *Gene Therapy*, 2002, **9**, 102–109.

(145) J. I. Cutler, D. Zheng, X. Xu, D. A. Giljohann and C. A. Mirkin, *Nano Letters*, 2010, **10**, 1477–1480.

(146) J. M. Perez, F. J. Simeone, Y. Saeki, L. Josephson and R. Weissleder, *Journal of the American Chemical Society*, 2003, **125**, 10192–10193.

(147) J. P. Fortin, F. Gazeau and C. Wilhelm, *European Biophysics Journal*, 2008, **37**, 223–228.

(148) *What is Calcium Carbonate? - Industrial Minerals Association - North America.*

(149) W. Sekkal and A. Zaoui, *Scientific Reports*, 2013, **3**, 1–10.

(150) S. C. Doney, M. Ruckelshaus, J. Emmett Duffy, J. P. Barry, F. Chan, C. A. English, H. M. Galindo, J. M. Grebmeier, A. B. Hollowed, N. Knowlton, J. Polovina, N. N. Rabalais, W. J. Sydeman and L. D. Talley, *Annual Review of Marine Science*, 2012, **4**, 11–37.

(151) F. Karakaş, B. Vaziri Hassas and M. S. Çelik, *Progress in Organic Coatings*, 2015, **83**, 64–70.

(152) Y. Boyjoo, V. K. Pareek and J. Liu, *Synthesis of micro and nano-sized calcium carbonate particles and their applications*, 2014.

(153) S. Wang, P. Ihalainen, J. Järnström and J. Peltonen, *Journal of Dispersion Science and Technology*, 2009, **30**, 961–968.

(154) I. P. Swainson, *American Mineralogist*, 2008, **93**, 1014–1018.

(155) H. Hull and A. G. Turnbull, *Geochimica et Cosmochimica Acta*, 1973, **37**, 685–694.

(156) K. Dahl and B. Buchardt, *Journal of Sedimentary Research*, 2006, **76**, 460–471.

(157) J. H. F. Jansen, C. F. Woensdregt, M. J. Kooistra, S. J. van der Gaast, J. H. F. Jansen, C. F. Woensdregt, M. J. Kooistra and S. J. van der Gaast, *Geo*, 1987, **15**, 245.

(158) R Frye, *editor. Aragonite Group in Encyclopedia of Mineralogy*, 1981.

(159) T. Ogino, T. Suzuki and K. Sawada, *Geochimica et Cosmochimica Acta*, 1987, **51**, 2757–2767.

(160) J. Jiang, S. F. Chen, L. Liu, H. B. Yao, Y. H. Qiu, M. R. Gao and S. H. Yu, *Chemical Communications*, 2009, 5853–5855.

(161) N. H. De Leeuw and S. C. Parker, *Journal of Physical Chemistry B*, 1998, **102**, 2914–2922.

(162) U. Wehrmeister, A. L. Soldati, D. E. Jacob, T. Häger and W. Hofmeister, *Journal of Raman Spectroscopy*, 2010, **41**, 193–201.

(163) N. K. Dhami, M. S. Reddy and M. S. Mukherjee, *Biomineralization of calcium carbonates and their engineered applications: A review*, 2013.

(164) S. L. Goss, K. A. Lemons, J. E. Kerstetter and R. H. Bogner, *Journal of Pharmacy and Pharmacology*, 2007, **59**, 1485–1492.

(165) R. Sander, *Atmospheric Chemistry and Physics*, 2015, **15**, 4399–4981.

(166) *Buffers for duffers . . . – microscopesandmonsters.com [Online, accessed May 2020].*

(167) R. Becker and W. Döring, *Annalen der Physik*, 1935, **416**, 719–752.

(168) S. Karthika, T. K. Radhakrishnan and P. Kalaichelvi, *Crystal Growth and Design*, 2016, **16**, 6663–6681.

(169) D. Gebauer, M. Kellermeier, J. D. Gale, L. Bergström and H. Cölfen, *Pre-nucleation clusters as solute precursors in crystallisation*, 2014.

(170) C. W. Turner and D. W. Smith, *Industrial and Engineering Chemistry Research*, 1998, **37**, 439–448.

(171) S. Y. Yang, H. H. Chang, C. J. Lin, S. J. Huang and J. C. Chan, *Chemical Communications*, 2016, **52**, 11527–11530.

(172) S. Sun, D. Gebauer and H. Cölfen, *Chemical Communications*, 2016, **52**, 7036–7038.

(173) J. Ihli, A. N. Kulak and F. C. Meldrum, *Chemical Communications*, 2013, **49**, 3134–3136.

(174) S. F. Chen, H. Cölfen, M. Antonietti and S. H. Yu, *Chemical Communications*, 2013, **49**, 9564–9566.

(175) J. H. Cartwright, A. G. Checa, J. D. Gale, D. Gebauer and C. I. Sainz-Díaz, *Calcium carbonate polyamorphism and its role in biomineralization: How many amorphous calcium carbonates are there?*, 2012.

(176) W. Sun, S. Jayaraman, W. Chen, K. A. Persson and G. Ceder, *Proceedings of the National Academy of Sciences of the United States of America*, 2015, **112**, 3199–3204.

(177) Q. Li, Y. Ding, F. Li, B. Xie and Y. Qian, *Journal of Crystal Growth*, 2002, **236**, 357–362.

(178) F. Manoli and E. Dalas, *Journal of Crystal Growth*, 2000, **218**, 359–364.

(179) L. Zhang, L. H. Yue, F. Wang and Q. Wang, *Journal of Physical Chemistry B*, 2008, **112**, 10668–10674.

(180) V. L. Kudryavtseva, L. Zhao, S. I. Tverdokhlebov and G. B. Sukhorukov, *Colloids and Surfaces B: Biointerfaces*, 2017, **157**, 481–489.

(181) M.-G. Ma and R.-C. Su, in *Advances in Biomimetics*, InTech, 2011.

(182) E. Persi, M. Duran-Frigola, M. Damaghi, W. R. Roush, P. Aloy, J. L. Cleveland, R. J. Gillies and E. Ruppin, *Nature Communications*, 2018, **9**, DOI: 10.1038/s41467-018-05261-x.

(183) M. Farzan, R. Roth, G. Québatte, J. Schoelkopf, J. Huwyler and M. Puchkov, *Pharmaceutics*, 2019, **11**, DOI: 10.3390/pharmaceutics11010032.

Chapter 2

Experimental

2.1 Materials and General Procedures

2.1.1 Starting Materials

All starting materials have been supplied by Sigma Aldrich unless otherwise stated. All syntheses described in this work were carried out in water from a Millipore filtration system operating at 18 MΩ. Henceforth this will be referred to in the text as Millipore (MP) water. All solvents were obtained from the Trinity College Dublin Hazardous Waste facility. All starting materials were used without further purification unless otherwise stated. PVP-stabilised AuAg nanowires were previously prepared in the group and provided by Dr. Daniel Kehoe.

Depending on the volume of product produced, two centrifuges were used throughout this work - a Hettich Zentrifugal Universal 32 for larger volumes, and a Hermle Z233 M-2 for smaller volumes of non-magnetic materials.

A Wise Clean WUC-A03H ultrasonic bath operated at 40 Hz was used for ultrasonic agitation throughout this work .

2.2 Experimental Procedures for Chapter 3

2.2.1 Synthesis of PSS-Stabilised Magnetite Nanoparticles

PSS solutions of varying concentrations were prepared in Millipore water. An iron precursor solution (0.06 M) was prepared using iron (III) chloride hexahydrate (1.1 g, 4 mmol) and iron (II) chloride tetrahydrate (0.4 g, 2 mmol) in degassed water (100 mL). The PSS solution (30 mL) was then added to a three-necked RBF. Three final PSS concentrations were prepared, and these are shown in Table 2.1.

Solution	Concentration
A	1.90 x 10^{-5} M
B	1.43 x 10^{-5} M
C	7.14 x 10^{-6} M

Table 2.1: PSS Concentrations

The reaction mixture was then stirred under argon at 90 °C for 15 minutes. After this time, the pH was adjusted to 9 using NH_4OH. The precipitated nanoparticles were stirred at 90 °C for 60 or 100 minutes. The solution was cooled and cleaned using Millipore water (5 x 20 mL). The resulting nanoparticles were stored in the minimum amount of ethanol.

2.2.2 Synthesis of PAH-Stabilised Gold Nanoparticles

A chloroauric acid (0.1 M) solution and a sodium borohydride (0.02 M) solution were both prepared using degassed Millipore water. PAH (0.025 g) was added to millipore water (10 mL) in a 15 mL two-necked RBF and degassed using Argon. The chloroauric acid solution (200 μL) was added to the two-necked RBF and stirred

for 5 mins. The sodium borohydride solution (400 μL) was then added drop-wise to the gold solution. The resulting mixture was left to stir for 45 mins. A dark red solution indicates the formation of gold nanoparticles. The nanoparticles were cleaned through centrifugation and washing with methanol (5 x 20 mL).

2.2.3 Synthesis of Unstabilised Gold Nanoparticles

A chloroauric acid (0.1 M) solution and a sodium borohydride (0.02 M) solution were both prepared using degassed Millipore water. Millipore water (10 mL) was added to a 15 mL two-necked RBF and degassed using Argon. The chloroauric acid solution (200 μL) was added to the two-necked round bottomed flask and stirred for five minutes. The sodium borohydride solution (400 μL) was then added drop-wise to the gold solution. The resulting mixture was left to stir for 45 mins. A dark red solution indicates the formation of gold nanoparticles. The nanoparticles were cleaned through centrifugation and washing with methanol (5 x 20 mL).

2.2.4 Synthesis of Magnetic-Plasmonic Nanocomposites

Synthesis of PSS-stabilised magnetite nanoparticles and PAH-stabilised gold nanoparticle composites were carried out through titrations and monitoring by UV-Visible spectroscopy. The gold nanoparticles (both unstabilised and PAH-stabilised gold nanoparticles) were added to a 10 mg/mL solution of each concentration of the PSS-stabilised magnetite until a clear plasmon peak was visible in the UV-Visible spectrum. Each nanocomposite solution was cleaned through magnetic separation 5 times and washed using Millipore water.

2.2.5 Synthesis of Gold and Magnetite Nanocomposites Using Acetic Acid

PSS magnetite nanoparticles (30 mg) were dispersed in Millipore water (50 mL) and sonicated for 15 minutes. (X) μL of gold chloride solution (0.1 M) in (Y) mL of acetic acid are then added (Table 2.2). The resulting nanocomposites were cleaned through magnetic separation 5 times and washed with Millipore water.

Sample	X (μL)	Y (mL)
E	300	1.5
F	600	3
G	2400	12

Table 2.2: Concentrations of gold chloride (X) and acetic acid (Y).

2.2.6 Colourimetric Testing with Mercury Ions

A serial dilution approach was taken using a 1 mM mercury chloride solution in order to obtain several concentrations of Hg^{2+} ion solutions. This serial dilution approach is summarised below in Table 2.3. Briefly, 11.11 mL of the 1mM stock solution of mercury chloride was added to sample tube 1. 1.11 mL of sample tube 1 was then taken and added to sample tube 2 to which 10 mL of MP water was then added. This was then repeated until dilution 5, whereby 10 mL MP water was added and 1.11 mL of the final solution was discarded.

Dilution	Mercury (II) Chloride Solution (mL)	Water (mL)	Final Mercury Concentration (Moles/L)
1	11.11	0	1 x 10^{-3}
2	1.11	10	1 x 10^{-4}
3	1.11	10	1 x 10^{-5}
4	1.11	10	1 x 10^{-6}
5	1.11	10	1 x 10^{-7}

Table 2.3: Serial dilution table for the preparation of five concentrations of Hg^{2+} ions.

0.5 mL of each mercury solution was then added to 0.5 mL of a given PAH-stabilised gold or nanocomposite solution in an Eppedorf and shaken for 30 seconds. These solutions were then examined by eye and samples were taken for analysis by UV-Vis in each case.

2.3 Experimental Procedures for Chapter 4

2.3.1 PSS/PAH-Stabilised Magnetite

PSS (0.08 g, 5.71 x 10^{-7} M) and sodium carbonate (5.29 g) were added to 200 mL of degassed Millipore water, and the solution was heated to 90 ^{o}C under Argon. $FeCl_3.6H_2O$ (0.675 g) and $FeCl_2.4H_2O$ (0.248 g) were added to 50 mL Millipore water and dissolved completely. The 50 mL iron salt solution was added to a dropping funnel and added dropwise to the PSS/Na_2CO_3 solution at 90 ^{0}C and stirred under Argon for 1 hour. The resulting solution was cleaned using magnetic separation (3 x MP water, 3 x EtOH) and stored in 10 mL of EtOH. To further stabilise the nanoparticles in PAH, the excess EtOH was removed from the magnetite solution

using magnetic separation, and the nanoparticles were dispersed in 100 mL of a 5 x 10^{-5} M PAH solution and sonicated for 1 hour. The resulting nanoparticles were cleaned using magnetic separation (3 x MP water, 3 x EtOH) and dried in air at 80 ^{o}C for 1 hour.

2.3.2 Synthesis of PAH-Stabilised Gold Nanoparticles

Chloroauric acid (0.1 M) and a sodium borohydride (0.02 M) solutions were both prepared using deoxygenated Millipore water. PAH (0.025 g) was added to Millipore water (10 mL) in a 15 mL two necked round bottomed flask and degassed using Argon. 3. The chloroauric acid (200 μL) was added to the two-necked round bottomed flask and stirred for 5 minutes. The sodium borohydride solution (400 μL) was then added dropwise to the gold solution. The resulting mixture was left to stir for 45 minutes. The nanoparticles were cleaned through centrifugation and washed with methanol (5 x 20 mL).

2.3.3 CTAB-Stabilised Gold Nanorods

Gold seeds production

All glassware must first be cleaned thoroughly with aqua regia. $HAuCl_4.3H_2O$ (0.5 mL, 0.01 M) and sodium citrate (0.5 mL, 0.01 M) were added to 18 mL degassed Millipore water with stirring. Freshly prepared $NaBH_4$ (0.5 mL, 0.1 M) was added. The colour of the solution changed from colourless to orange. The stirring is then stopped and the particles are allowed to age at room temperature (21 ^{o}C) for 2 hours. The resulting nanoparticles are gold seeds.

Gold Nanorods Growth Solution

The process is shown in the form of a schematic in Figure 2.1. The resulting nanorods from flask C were cleaned using centrifugation at 5000 RPM (5 x methanol).

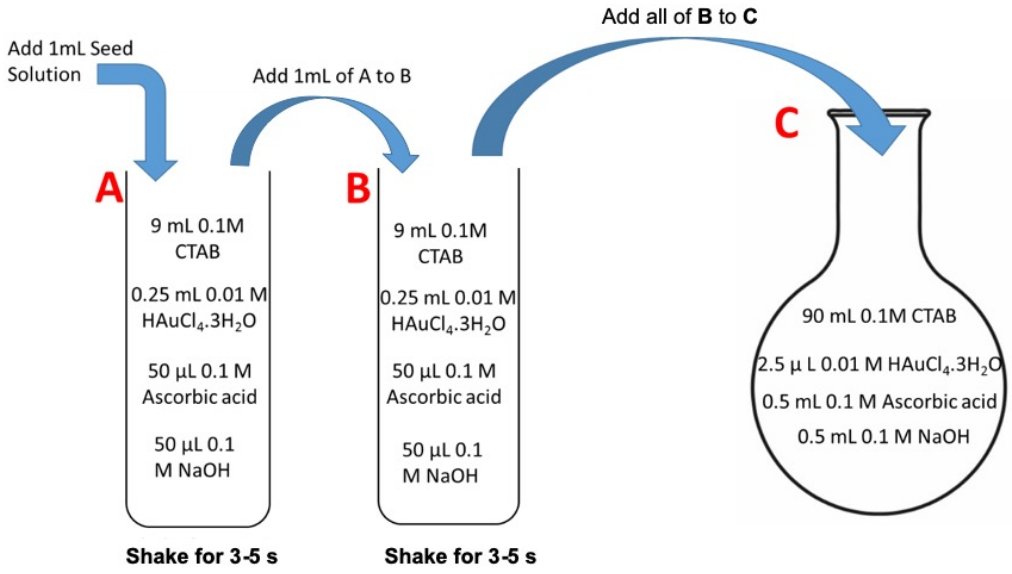

Figure 2.1: Reaction scheme illustrating the synthetic procedure for the growth of gold nanorods.

2.3.4 Preparation of Gold Nanostars

Silver Seeds Synthesis

Silver nitrate (0.0171 g, 0.1 mmol) was added to Millipore water (100 mL) and stored in the dark. A 5 mM solution of sodium citrate monobasic (0.150 g, 0.05 mmol) was prepared in Millipore water (10 mL) in a vial. The vial was shaken until the sodium citrate monobasic had dissolved. A 40 mmol solution of sodium borohydride (0.0150 g, 0.4 mmol) was prepared in Millipore water (10 mL) in a vial. The vial was closed immediately after addition of the $NaBH_4$ and shaken until the crystals had dissolved. The sodium borohydride solution was then placed into a beaker con-

taining ice and refrigerated for 15 mins. A timer was started (t=0). Silver nitrate solution (2.5 mL) was added to a vial fitted with a stirring rod. Millipore water (7.5 mL) was then added to this vial. Sodium citrate monobasic solution (0.25 mL) was then added. At t=15 mins, the sodium borohydride solution was removed from the fridge. Immediately, sodium borohydride solution (0.4 mL) was added to the silver nitrate solution via a syringe. The solution changed from colourless and transparent to pale yellow. This solution was stirred for 5 minutes. At t=20 mins the vial was removed, and the vial was left open and in darkness for a minimum of 2 hrs. A scheme illustrating this reaction is shown in Figure 2.2.

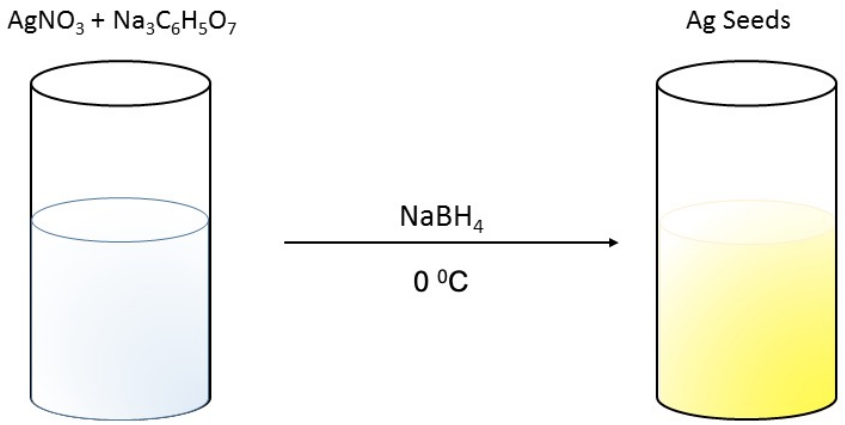

Figure 2.2: Reaction scheme showing the synthesis of silver seeds.

Gold Growth Solution

Ascorbic acid (0.140 g, 0.08 mmol) was added to Millipore water (10 mL) in one vial. In a second vial, CTAB (0.364 g, 1 mmol) was added to Millipore water (20 mL), heated to 30 °C, and stirred until all CTAB had dissolved. Once all CTAB was dissolved, the heat was turned off, however stirring was continued until the end of the reaction. Stock silver nitrate (1.03 mL, 1 mM) was added to the CTAB solution. A timer was started, (t=0). At t=1 mins, stock chloroauric acid solution (0.21 mL, 25 mM) was added, and the reaction mixture turned orange. At t=2 mins, the

ascorbic acid solution (0.1 mL) was added and a transparent solution was formed. At t=2 mins and 20 s, the silver seed solution (0.05 mL) was added. This resulted in a change in colour from colourless to blue. At t=17 mins, the stirring rod was removed, and the solution was kept in the dark at room temperature for 24 hrs. Over this time, the solution changed from blue to brown-red in colour.

The resultant gold nanostars had to be isolated from CTAB in order to facilitate characterisation and further modification. The gold nanostar CTAB suspensions were sonicated for two minutes at 30 °C. Subsequently, they were centrifuged for 10 minutes at 15,000 RPM. The supernatant was removed and the centrifugation was repeated two more times. The gold nanostars were stored in ethanol (10 mL). A scheme illustrating this reaction procedure is shown in Figure 2.3.

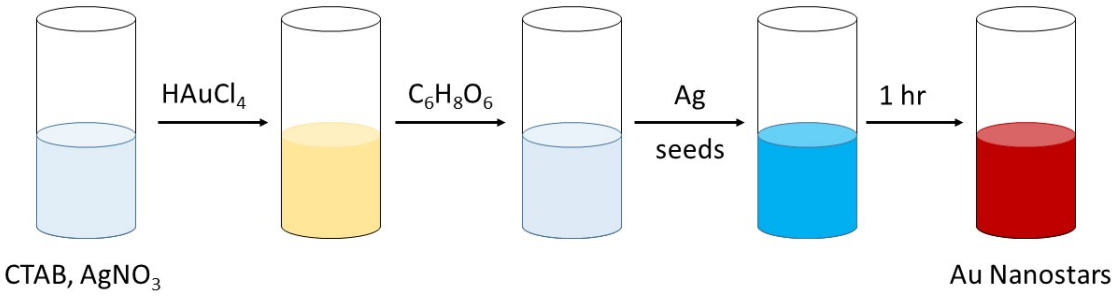

Figure 2.3: A reaction scheme illustrating the synthesis of gold nanostars.

2.3.5 Preparation of PAH-stabilised Magnetite Nanoparticles and PVP-stabilised AuAg Nanowire Composites

Serial dilution was used to obtain three solutions of different concentrations of the PSS/PAH-stabilised magnetite nanoparticles for use in the formation of a nanocomposite with the PVP-stabilised AuAg nanowires prepared by Dr. Daniel Kehoe. Dried PSS/PAH-stabilised magnetite (10 mg) was added to EtOH (10 mL). A further 3 solutions of EtOH (9 mL) were prepared. 1 mL of the initial magnetite solution was added to the first EtOH solution, and 1 mL of this solution was taken and

added to the second solution of EtOH. 1 mL of this second solution was then added to the third and final EtOH solution. 1 mL was then taken from the third EtOH-magnetite solution and discarded. These three concentrations were then tested in the formation of the nanowire composite structures.

Two methods were used for the addition of these magnetite solutions to the nanowires; both with and without stirring.

For the stirring approach, 1 mL of the nanowire solution was added to EtOH (10 mL). 3 mL of each concentration of magnetite was added to 3 sample tubes that had been fitted with stirring bars. The stirring was set to 960 RPM and 1 mL of the nanowire solution was added to each sample tube. Each was left to stir for 10 mins at RT, and then placed in the fridge at 4 ^{o}C for 8 days.

The same approach was utilised for the non-stirring method, however, in this instance the sample tubes were not fitted with stirring bars and were allowed to sit at RT for 10 minutes before being placed in the fridge at 4 ^{o}C for 8 days.

2.3.6 Preparation of PAH-stabilised Gold Nanoparticles and PVP-stabilised AuAg Nanowire Composites

The cleaned gold nanoparticles were suspended in 10 mL of EtOH. A serial dilution approach was utilised in order to obtain three concentrations of PAH-stabilised gold nanoparticles. 3 solutions of EtOH (9 mL) were prepared. 1 mL of the initial gold nanoparticle solution was added to the first EtOH solution, and 1 mL of this solution was taken and added to the second solution of EtOH. 1 mL of this second solution was then added to the third and final EtOH solution. 1 mL was then taken from the

third EtOH-gold nanoparticle solution and discarded. These three concentrations were then tested in the formation of the nanowire composite structures.

Two methods were used for the addition of these magnetite solutions to the nanowires; both with and without stirring.

For the stirring approach, 1 mL of the nanowire solution was added to EtOH (10 mL). 3 mL of each concentration of gold nanoparticles was added to 3 sample tubes that had been fitted with stirring bars. The stirring was set to 960 RPM and 1 mL of the nanowire solution was added to each sample tube. Each was left to stir for 10 mins at RT, and then placed in the fridge at 4 ^{o}C for 8 days.

The same approach was utilised for the non-stirring method, however, in this instance the sample tubes were not fitted with stirring bars and were allowed to stay at RT for 10 minutes before being placed in the fridge at 4 ^{o}C for 8 days.

2.4 Experimental Procedures for Chapter 5

2.4.1 Preparation of Double-Stranded DNA Solutions

Several initial concentrations of the herring sperm DNA (4.4 % H_2O, crude oligonucleotides) were prepared. After preliminary investigations this was narrowed to 5, 10 and 15 mg of DNA. The given amount of herring sperm DNA was added to 10 mL of Millipore water and hydrated in a sonic bath for 60 minutes. This solution was then added to a 25 mL volumetric flask and made up to the mark with Millipore water.

2.4.2 Preparation of Single-Stranded DNA Solutions

Either 5, 10 or 15 mg of herring sperm DNA were added to 20 mL of Millipore water and heated under reflux to 80 ^{o}C for 60 minutes to denature the double strand of DNA. The DNA solutions were then cooled immediately in ice. These solutions were then added to a 25 mL volumetric flask and made up to the mark with Millipore water.

2.4.3 Preparation of *In-Situ* DNA-Stabilised Magnetite

$FeCl_3.6H_2O$ (1.1 g, 0.08 M) and $FeCl_2.4H_2O$ (0.4 g, 0.04 M) were added to 100 mL of Millipore water and dissolved. The iron solution was then added to 100 mL of a 5 M NaCl solution. 10 mL of each concentration of either the double-stranded or single-stranded DNA was was added to 10 mL of the iron salt solution with stirring. Concentrated NH_4OH was then added dropwise to precipitate the nanoparticles until a pH of 9 was reached. The resulting nanocomposites were washed using Millipore water until the solution was pH neutral.

2.4.4 *In-Situ* Synthesis of DNA-Stabilised Gold Nanoparticles

200 μL of a chloroauric acid solution (0.1 M) was added to 10 mL of a given DNA solution and allowed to stir for 10 minutes. 800 μL of ascorbic acid solution (0.02 M) was added dropwise to the solution and allowed to stir for 5 minutes. 100 μL of a $NaBH_4$ solution (0.02M) was then added to the solution and allowed to stir for 15 minutes. The resulting solution was cleaned through centrifugation and washed with methanol.

2.4.5 Preparation of DNA-Stabilised Magnetic-Plasmonic Nanocomposites

20 mg of a given DNA-stabilised magnetite solution was added to 20 mL of MP water and sonicated for 10 minutes. 500 μL of the DNA magnetite solution was added to a sample tube. 500 μL of a given DNA-stabilised gold nanoparticle solution was then added to the sample tube and shaken to form the nanocomposite. The resulting nanocomposites were cleaned through magnetic separation (3 x MP water).

2.5 Experimental Procedures for Chapter 6

2.5.1 Synthesis of Bare Magnetite Nanoparticles

$FeCl_3.6H_2O$ (6.75 g) and $FeCl_2.4H_2O$ (2.48 g) were added to 50 mL Millipore water and dissolved completely. Sodium carbonate (5.29 g) was added to 200 mL Millipore water and heated to 90 ^oC under Argon. The 50 mL iron solution was added to a dropping funnel and added dropwise to the sodium carbonate solution under constant stirring. The solution was refluxed with stirring at 90 ^oC for 100 minutes. The resulting nanoparticles were cleaned using magnetic separation (3 x MP water, 3 x EtOH).

2.5.2 Synthesis of PSS-Stabilised Magnetite Nanoparticles

$FeCl_3.6H_2O$ (6.75 g) and $FeCl_2.4H_2O$ (2.48 g) were added to 50 mL Millipore water and dissolved completely. Sodium carbonate (5.29 g) and PSS (0.248 g) were added to 200 mL Millipore water and heated to 90 ^oC under Argon. The 50 mL iron solution was added to a dropping funnel and added dropwise to the sodium carbonate solution under constant stirring. The solution was refluxed with stirring at 90 ^oC for

100 minutes. The resulting nanoparticles were cleaned using magnetic separation (3 x MP water, 3 x EtOH).

2.5.3 Synthesis of *L*-Cysteine Stabilised Magnetite Nanoparticles

Previously synthesised bare magnetite nanoparticles (1 g) were sonicated in 100 mL Millipore water for 30 minutes. *L*-Cysteine (1.29 g) was dissolved in 50 mL Millipore water. 10 mL of the *L*-Cysteine solution was added dropwise to the magnetite nanoparticle solution and was sonicated for 20 minutes. The resulting particles were cleaned through magnetic separation (3 x MP water, 3 x EtOH) and dried in air at 70 ^{o}C for 24 hours.

2.5.4 Synthesis of Gold Nanoparticles via the Turkevich Method

1.8 mL of NaOH solution (0.015 M) and 2 mL of chloroauric acid solution (0.025 M) were added to 16 mL Millipore water with stirring. The resulting solution was heated to 100 ^{o}C. 0.6 mL of sodium citrate monobasic (0.2 M) was added quickly under high agitation. The resulting solution is refluxed with stirring at 100 ^{o}C for 30 minutes. The resulting nanoparticles were cleaned using centrifugation with methanol.

2.5.5 Synthesis of Hollow $CaCO_3$ Microspheres

Sodium dodecyl sulfate (SDS)(0.5 g), polyvinyl pyrrolidone (PVP)(0.5 g) and *L*-Cysteine (0.6 g, 5 x 10^{-3} M) were added to 50 mL of a Na_2CO_3 solution (0.53 g, 5 x 10^{-3} M) and stirred for 60 minutes. SDS (0.721 g) and $CaCl_2$ were added to 50 mL of Millipore water and stirred for 15 minutes. The SDS/$CaCl_2$ solution was then added to the SDS/PVP solution and stirred for a further 60 minutes. The resulting microspheres were cleaned through centrigugation (3 x MP water, 3 x EtOH) and dried in air at 70 ^{o}C for either 24 or 72 hours.

2.5.6 Preparation of Magnetic Hollow $CaCO_3$ Microspheres

$CaCO_3$ microspheres (0.149 g) were added to Millipore water (5 mL) and sonicated for 1 minute. Bare, PSS- or *L*-Cysteine-stabilised nanoparticles (0.07 g) were added to Millipore water (5 mL) and NaOH was added dropwise until the solution was pH neutral. The magnetite solution was sonicated for 15 minutes and then added to the $CaCO_3$ solution and sonicated for a further 3 minutes. The Fe_3O_4@$CaCO_3$ was shaken for 30 minutes. The particles were then cleaned using centrifugation (3 x MP water) and dried in air at 70 ^{o}C for 24 hours.

2.5.7 Layer-by-Layer (LbL) Deposition of PSS and PAH onto Microspheres

Fe_3O_4@$CaCO_3$ microspheres prepared according to *2.5.6* were suspended in 1 mL of Millipore water. 1 mL of PAH solution (16 mg/mL in 0.01 M NaOH) was added to the microspheres solution, and the pH was adjusted to 8 using 1 M NaOH solution. This solution was sonicated for 5 minutes and then shaken for a further 20 minutes. The microspheres were then cleaned using centrifugation (3 x MP water).

This procedure was repeated with a 1 mL of a PSS solution (16 mg/mL in 0.01 M) NaOH). This process was then repeated in order to obtain two PAH/PSS bilayers.

2.5.8 Synthesis of Plasmonic LbL Magnetic Hollow $CaCO_3$ Microspheres

The citrate-stabilised gold nanoparticles (0.5 mL) prepared according to *2.5.4* were dispersed in 3 mL of a PSS solution (16 mg/mL in 0.01 M NaOH) and sonicated for 10 minutes. The LbL coated microspheres prepared in *2.5.7* were suspended in 2 mL Millipore water and sonicated for 10 minutes. The two solutions were then combined and shaken for 2 hours. The resulting particles were centrifuged (3 x MP water) and dried in air at 70 ^{o}C for 24 hours.

2.5.9 Synthesis of Magnetic Calcium Carbonate Microraspberries

2.5 mg of *L*-Cysteine-stabilised magnetite nanoparticles were added to 2.5 mL of Millipore water and heated to 25 ^{o}C. An additional 7.5 mL of Millipore water was then added and this solution was stirred for 5 minutes. Two separate solutions - 625 μL of 1 M Na_2CO_3 and 625 μL of 1 M $CaCl_2$ were added to the magnetite solution at the same time and stirred for 30 seconds. The stirring was then ceased and the solution was left to sit at 25 ^{o}C for 3 minutes. The resulting particles were the washed using centrifugation (3 x MP water) and dried in air at 70 ^{o}C for 2 hours.

The microparticles were then added to 1 mL of a PAH solution (2 mg/mL in 1 M NaCl) and shaken for 15 minutes. The PAH-stabilised microstructures were then added to 1 mL of a PSS solution (2 mg/mL in 1 M NaCl) and shaken for 15 min-

utes. These microparticles were then cleaned using centrifugation (3 x MP water) and dried in air. This procedure was repeated twice resulting in three bilayers of PAH/PSS. The PE-coated microparticles were dried in air at 70 ^{o}C for 16 hours.

2.5.10 Template-Directed Synthesis of Gold-Encapsulated $CaCO_3$ Microspheres

PVP (0.5 g), SDS (0.5 g), and citrate-stabilised gold nanoparticles (0.1 mL) were added to a 50 mL Na_2CO_3 solution (0.1 M) and stirred for 30 minutes. SDS (0.721 g) was dissolved in 50 mL of a $CaCl_2$ solution in water. The $CaCl_2$ solution was then added to the Na_2CO_3 solution and stirred for 60 minutes. The resulting microspheres were cleaned using centrifugation (2 x MP water, 2 x EtOH) and dried in air at 70 ^{o}C for 24 hours.

2.5.11 Preparation of Fe_3O_4@$CaCO_3$ Microspheres

The microparticles prepared in *2.5.10* were added to 15 mL EtOH alongside 5 mg of *L*-Cysteine-stabilised magnetite nanoparticles. This solution was sonicated for 20 minutes and then shaken for a further 2 hours. The resulting microparticles were cleaned using centrifugation (3 x EtOH) and dried in air at 70 ^{o}C for 2 hours.

2.5.12 Preparation of Au@$CaCO_3$ Microspheres

The microparticles prepared in *2.5.10* were added to 15 mL EtOH alongside 0.1 mL of citrate-stabilised gold nanoparticles. This solution was sonicated for 20 minutes and then shaken for a further 2 hours. The resulting microparticles were cleaned using centrifugation (3 x EtOH) and dried in air at 70 ^{o}C for 2 hours.

2.6 Instrumentation

2.6.1 UV-Visible Absorbance Spectroscopy

In this technique, light in the UV-Visible spectrum (typically between 300 - 900 nm) is passed through a sample, and the absorbance of that sample is then measured. The light source is commonly an incandescent white light source which is then passed through a monochromator, for example a prism, which splits the light source into its various wavelengths.

The absorbance of a given sample is described by the Beer-Lambert law:

$$A = \epsilon C l \tag{2.1}$$

where A is absorbance, ϵ is the molar extinction coefficient, C is the concentration of the sample and l is the path length that the light passes through. The molar extinction coefficient is a metric for how strongly a chemical species or substance absorbs light at a particular wavelength[1]. It is an intrinsic property of a chemical species that is dependent on its composition and structure. Hence the absorbance of a sample is directly proportional to its concentration.

All UV-Visible spectroscopy studies were carried out using a Cary 50 spectrophotometer. All measurements were carried out using a quartz cuvette with a 10 mm path length.

2.6.2 Dynamic Light Scattering (DLS) Spectroscopy

Dynamic light scattering (DLS) is used to determine the diameters of spherical particles in the nanometer range. It is based on the principle of Brownian motion. Particles dispersed in a liquid will move randomly in all directions, and these particles will therefore be in constant collisions with solvent molecules. As these collisions cause the transfer of energy and therefore particle movement, smaller particles will move faster as they have smaller masses. If the other parameters that affect particle movement are known, then speed can be utilised in order to determine the particle size. The relationship between particle size and speed is determined by the Stokes-Einstein equation, shown below[2].

$$D = \frac{k_{\mathrm{B}}T}{6\pi\eta R_{\mathrm{H}}} \tag{2.2}$$

D refers to the translational diffusion coefficient, or 'speed' of the particles (m^2/s), k_B is the Boltzmann constant (m^2Kg/s^2), η is the viscosity of the solvent (Pa s) and R_H is the hydrodynamic radius (m). A basic requirement for these measurements is that the particles are suspended in the solution and no sedimentation occurs.

The basic set-up of a DLS spectrophotometer is that a laser light of a single frequency is shined on a sample in a cuvette. The particles in the sample will then scatter light in all directions. The scattered light is then detected at a certain angle over time, and this signal is then used to determine the diffusion coefficient and the particle size using the Stokes-Einstein equation.

Zeta-Potential Measurements using the DLS Spectrophotometer

Zeta-potential measurements are used to determine the surface charge of nanoparticles in a solution, and is a useful tool in determining their stability. Nanoparticles have a surface charge that will then attract a thin layer of counter-ions, this is called the Stern layer. It is an immobile layer at the surface of the nanoparticle that moves with it throughout the solution. The electric potential at the interface of this double layer is known as the Zeta-potential. Zeta-potential is a useful means of determining how stable a colloidal solution will be; if a solution has a zeta-potential between -25 mV to +25 mV it will eventually agglomerate due to interparticle interactions[3].

The experimental set-up of Zeta-potential measurements is also carried out in a DLS spectrophotometer and is illustrated in Figure 2.4. An electric field is applied to the solution in a zeta-potential cell, and the cell is also illuminated with laser light. The particles move due to the applied electric field, and this motion is measured through the amount of light that they scatter. The frequency of the scattered light is a function of the particle velocity due to the Doppler effect. A reference beam is mixed with the scattered beam in order to effectively extract the frequency of the scattered light. The measured magnitude of the frequency shift is then used to determine the particle velocity.

The particle mobility can then be determined from the known applied electric field and the measured particle velocity. The zeta-potential can then be calculated from the particle mobility using a model, most commonly used is the Smoluchowski model. The only parameters required for determining the zeta-potential are the liquid dielectric constant, refractive index and viscosity.

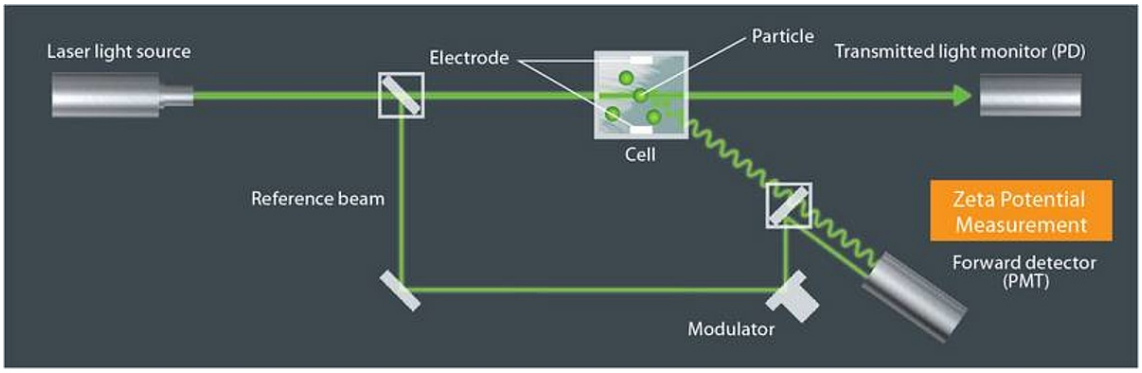

Figure 2.4: Scheme showing experimental set-up for zeta-potential measurements. Adapted from ref[4].

In this work, DLS and zeta-potential measurements were carried out using a Malvern Zeta-Sizer Nano series using a quartz cuvette for the DLS measurements and a folded capillary zeta cell for the zeta-potential measurements.

2.6.3 Fourier Transform-Infrared Spectroscopy

FT-IR is a non-destructive analytical technique that is used to identify organic (and in certain cases, inorganic) materials. This technique measures the absorption of infrared radiation by the material as a function of the wavelength of the light absorbed. These absorption bands can then be used to identify the functional groups and therefore the chemical composition of the compound.

Infrared spectroscopy works on the principle that certain frequencies of light are absorbed by different functional groups in a molecule, which then causes a change in the dipole moment of the molecule. If the IR-light doesn't cause a change in the dipole moment of the molecule, then it is said to be IR-inactive. Linear molecules have 3N-5 degrees of freedom and non-linear molecules have 3N-6 degrees of freedom, in terms of vibrational modes. Any IR radiation that is absorbed by the molecule will normally excite the molecules into a higher vibrational state; the wavelength of the

light that is absorbed by a particular molecule is a function of the energy difference between the at-rest and the excited vibrational states. The absorbed wavelengths are characteristic of the molecular structure.

An FT-IR spectrometer uses an interferometer (instead of a monochromator) to modulate the wavelength of a broad-band infrared light source. An interferometer splits the light source into two light beams - one passes through a stationary mirror and the second passes to movable mirror. This will introduce a time delay which then enables the measurement of the temporal coherence of the two signals. A detector then measures the intensity of the transmitted or reflected light as a function of its wavelength.

In this work, FT-IR spectrometry was carried out using a Bruker: Tensor II FT-IR spectrometer with a diamond UATR.

2.6.4 Vibrating Sample Magnetometry (VSM)

Vibrating Sample Magnetometry (VSM) is a method of determining the magnetic properties of bulk and nanomaterials. It gives information on the magnetic moment of the material and whether it is ferromagnetic, ferrimagnetic, or superparamagnetic based on the hysteresis loop obtained. When a sample is exposed to an external magnetic field, it induces a magnetic moment in that sample. Mechanical vibration will then cause a magnetic flux. This magnetic flux then results in a voltage in the sensing coils. The magnetic moment in the sample is then proportional to this voltage. The hysteresis loop for the material is then plotted, and shows the behaviour of the material in terms of its saturation magnetisation (M_s), magnetic remanence (M_r), and coercitivity (H_c)[5]. A superparamagnetic material has a coercitivity of 0 Am^2/Kg. A scheme showing the layout of a VSM is shown in Figure 2.5.

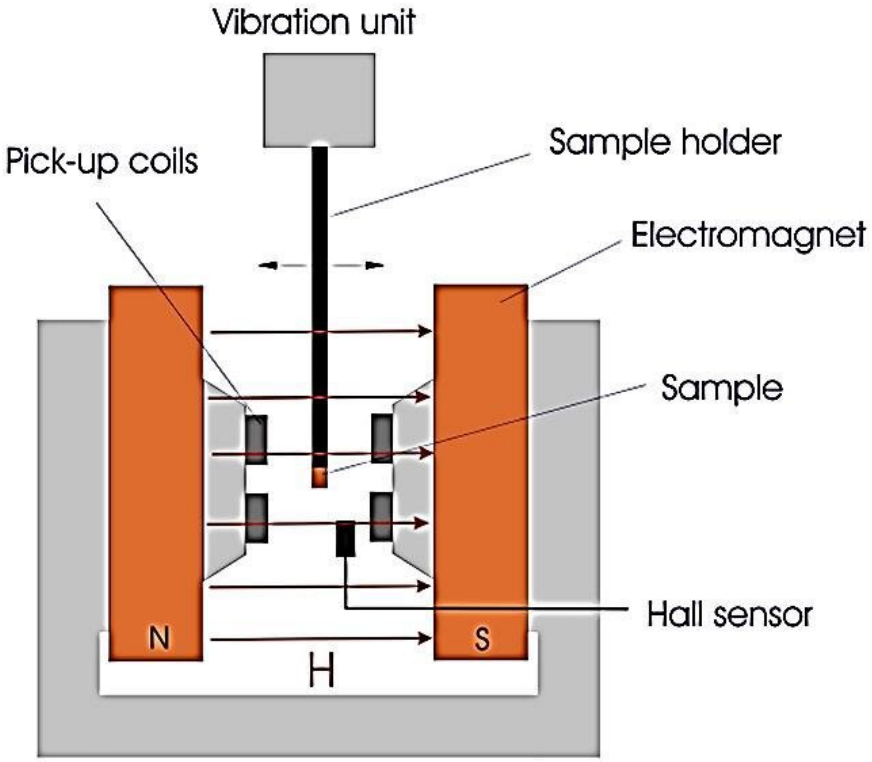

Figure 2.5: Scheme showing the internal layout of a VSM. Adapted from ref[6].

VSM measurements were carried out on 'The Magic Roundabout' VSM apparatus, courtesy of Prof. Michael J. Coey. The measurements were carried out at room temperature with an applied field of up to 1 T. The VSM was calibrated using a nickel sample of known mass with a magnetic moment of 55.4 Am^2/Kg at 1 T at room temperature. The sample was dried, weighed precisely and placed in paper in a PVC holder in order to carry out measurements.

2.6.5 Scanning Electron Microscopy (SEM)

A scanning electron microscope (SEM) uses a focused beam of electrons to scan the surface of a material and thus determine information about its topography and atomic structure. The electron beam will interact with the material and produce back-scattered and secondary electrons which can be used to form an image of the

surface. A simple scheme showing the internal structure of an SEM is shown in Figure 2.6.

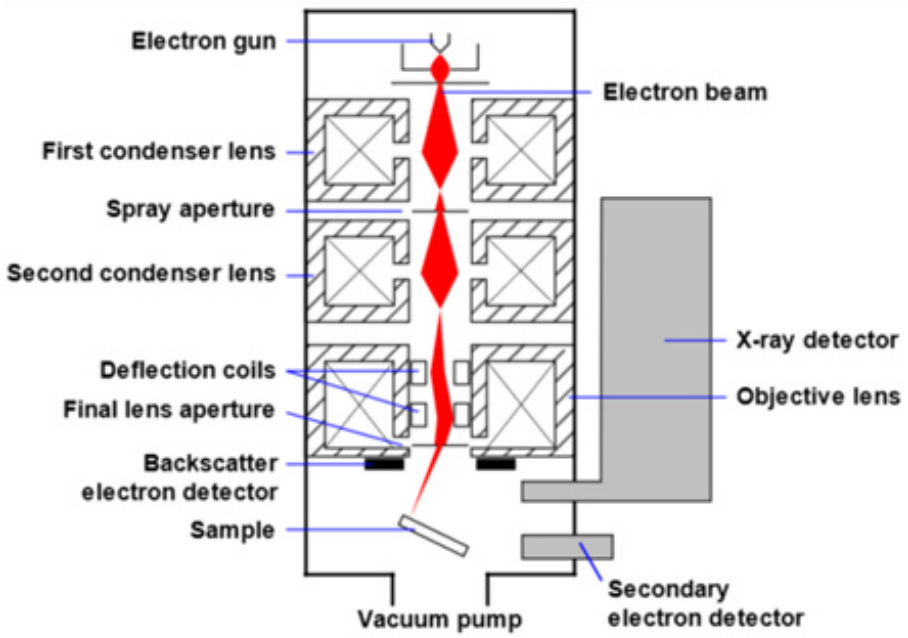

Figure 2.6: Scheme of an SEM. Adapted from ref[7]

Electrons are generated at the top of the column by an electron gun or an electron source. The three most common types used are tungsten electron filament, lanthanum hexaboride/cerium hexaboride or field emission guns. These are emitted from the electron source/cathode when the thermal energy of the electrons surpasses the work function of the gun. These electrons are then accelerated by an anode, and a series of electromagnetic lenses are used to control the path and size of the beam. These electromagnetic lenses consist of coils of wire inside metal pole pieces, as a current is passed through the coil of wire, a magnetic field is generated and this can then be used to control the path of the electron beam. There are two types of electromagnetic lens in an SEM; the condenser lenses, which are used to converge the beam, and the objective lens, which is used to converge the beam immediately before it interacts with the sample. Deflection coils then raster the beam onto the sample, and the aperture is used to control the beam size.

The interaction of the electrons with the sample will produce a variety of types of electrons, as well as other irradiations. Two types of electrons are generally used for the generation of an SEM image - backscattered electrons and secondary electrons. Backscattered electrons are an example of elastic scattering. They originate from the electron beam itself and penetrate deeper into the sample than secondary electrons. Backscattered electrons can provide atomic and phase information as they are highly sensitive to atomic number; the higher the atomic number the brighter the resulting image will appear. Secondary electrons are an example of inelastic interactions between the electron beam and the sample, and give more topographical information. X-rays are also produced in the interaction between the beam and sample, and these too provide useful information. This will be discussed in section *2.6.7*. Multiple detectors are required in order to detect the elastic and inelastic scattered electrons. Backscattered electrons are collected by solid state detectors that are positioned above the sample, and secondary electrons are detected by (most commonly) Everhart-Thornley detectors positioned at an angle to the sample.

All scanning electron microscopy images were obtained using a Zeiss Ultra Plus Scanning Electron Microscope.

2.6.6 Transmission electron microscopy (TEM)

Transmission electron microscopy (TEM) is similar to SEM in that they both utilise an electron beam to image materials that are beyond the resolution of a traditional light microscope. The primary differences between the two techniques are that in TEM a much higher accelerating voltage is used (typically 60 - 300 kV compared to 1 - 5 kV for an SEM), and the electrons are transmitted through the sample, rather than used to scan the surface of the material. Owing to the significantly higher accelerating voltage of the TEM, much higher resolution images can be obtained.

SEM can have resolutions of up to 10 nm, whereas TEM can be used to obtain crystallographic information.

A scheme showing the internal structure of a TEM can be seen in Figure 2.7. The instrument can be broken down into three main components. The first is the electron source. For TEM, this can either be a thermionic electron source (such as tungsten or lanthanum hexaboride), or a field emission gun (Schottky-type or cold field emission). The electrons from the source are accelerated towards a cylindrical anode, which the beam then passes through and towards the sample. The second component of a TEM is the condenser system. In the same way as discussed in Section *2.6.5*, the condenser system is used to converge and focus the beam onto the sample. The final component of a TEM is the imaging system. Here, the electron beam is focused onto the sample and transmitted through it into another series of condenser lenses that focus the electrons onto a fluorescent or phosphorescent screen in order to create the image.

The features of SEM and TEM can be combined in the TEM in order to scan the sample at much higher accelerating voltages, this is called Scanning Transmission Electron Microscopy, or STEM.

Transmission electron microscopy images were either obtained on an FEI Titan – Transmission Electron Microscope operating at 300 kV, or on a JEOL 2100 operating at 200 kV. Samples were prepared on 300 mesh lacey carbon copper grids and allowed to dry in air overnight.

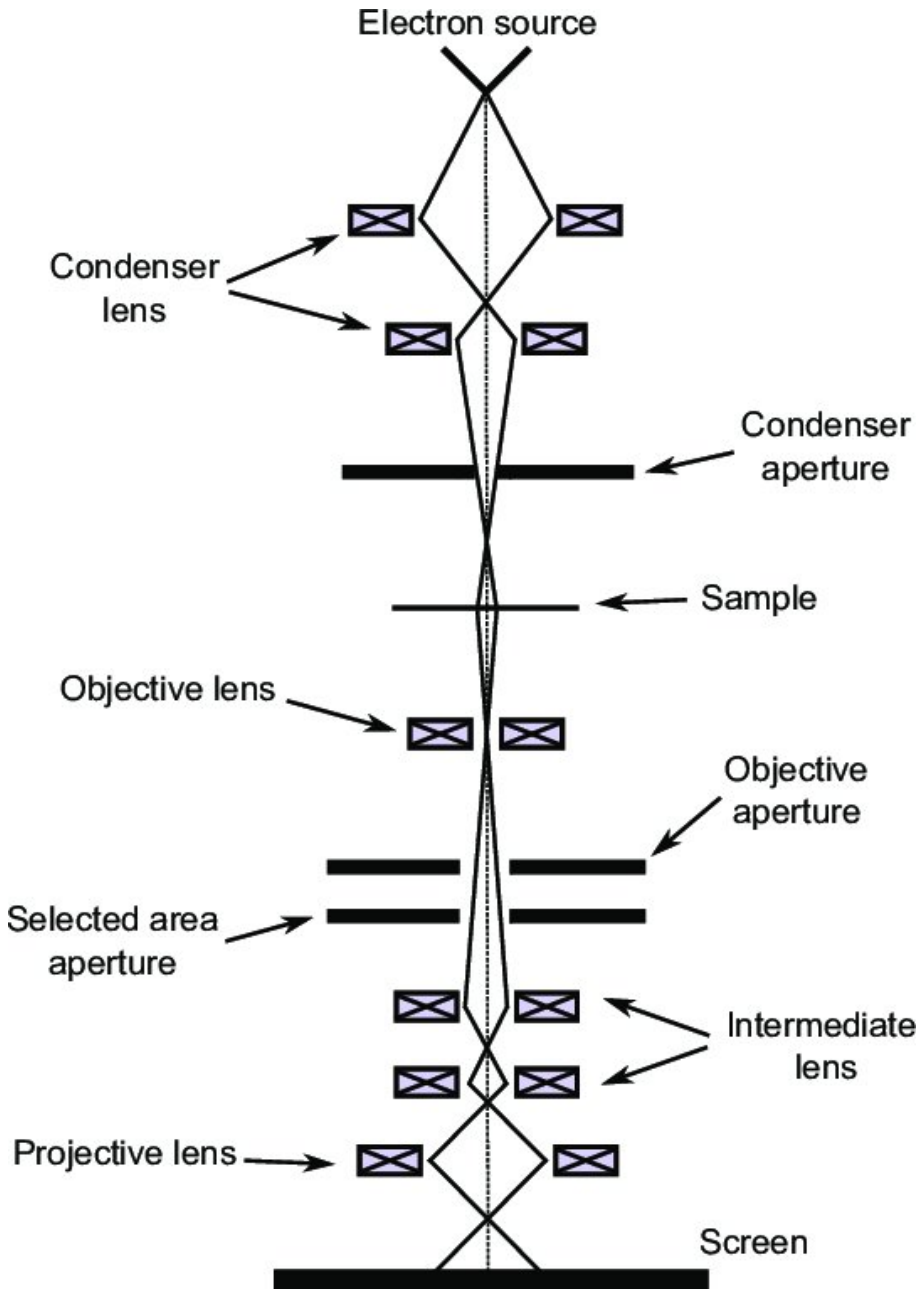

Figure 2.7: Scheme illustrating a TEM. Adapted from ref[8].

2.6.7 Energy Dispersive X-Ray Spectroscopy

Energy Dispersive X-Ray spectroscopy (EDX) is used to identify and quantify elements present throughout a sample.The principle behind EDX spectroscopy is Moseley's law, which states that there is an increase in the characteristic x-ray energies with increasing atomic number. When a high energy electron beam is incident on the sample, electrons will be ejected from the atoms on the surface of the sample. The vacancies caused by these electrons being ejected from the sample will then be filled with electrons from a higher electron shell. As this electron relaxes to the lower energy shell, an x-ray is released that balances the energy difference between the two states. This x-ray energy is characteristic of the element from which it is emitted.

The characteristic x-rays are labelled depending on which shell that the ionisation and relaxation happens from. A scheme of this process is shown in Figure 2.8. The shells are called K, L, M and N, where K is the inner-most shell. If ionisation occurs from the K-shell, (i.e. the incident electron beam causes the an electron to be ejected from this shell) and it is replaced with an electron from the L-shell, then the emitted x-ray is dubbed K_α, as L is one shell away from K. If relaxation occurs from the M to the K-shell, then this is called K_β, and so on and so forth.

The EDX detector measures the relative abundance of emitted x-rays versus their energy. When an x-ray hits the detector, a charge pulse is created which is proportional to the energy of the x-ray. These pulses are sorted by voltage and their energy is determined. The x-ray energy versus counts are then plotted which enables the determination of the elemental composition of the sample.

In this work EDX spectroscopy was carried out using 20 mm^2 Oxford Inca EDX detector fitted to a Zeiss ULTRA Plus SEM.

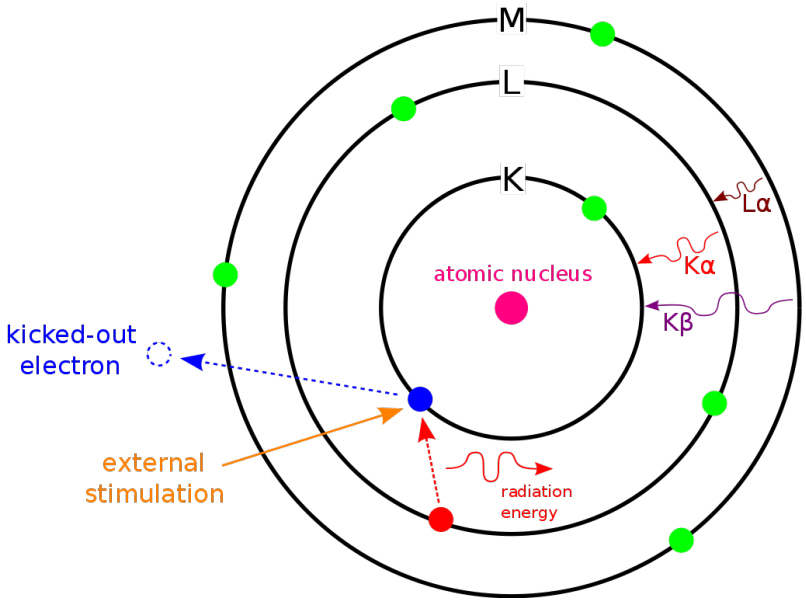

Figure 2.8: Scheme showing the basic principle of EDX. Image produced from ref[9]

2.6.8 X-Ray Diffraction (XRD)

X-Ray Diffraction (XRD) is a fast, non-destructive analytical technique that can be used to identify phases of a crystalline material and to provide information on unit cell dimensions. The principle of XRD is that x-rays are scattered by electrons, and the extent and pattern of the scattering is dependent on the number of surrounding electrons. Due to this, a periodic array of atoms will diffract light in such a way as to construct a pattern that can be measured.

When Bragg's law is satisfied, the incident rays will interact with the sample to produce constructive interference and a diffracted ray. Miller indices are used in the analysis of XRD patterns, and they describe planes of atoms using (hkl) coordinates. The d_{hkl} vector which that extends from the origin to the hkl plane is used in tandem with Bragg's law to estimate the diffraction peaks. Bragg's law is shown below.

$$n\lambda = 2d_{(\mathrm{hkl})}sin\theta \tag{2.3}$$

Where n is a positive integer, λ is the wavelength, which is fixed, d_{hkl} is the vector

previously mentioned, and θ is the angle at which constructive interference from the x-rays will produce diffraction peaks.

In this work, powder XRD is used, and this is a specific case that utilises Bragg-Bretano geometry to calculate the diffraction pattern. In this approach, the sample is rotated in order to increase the number of crystallites observed and therefore obtain a reliable pattern. An illustration showing Bragg-Bretano geometry is shown in Figure 2.9.

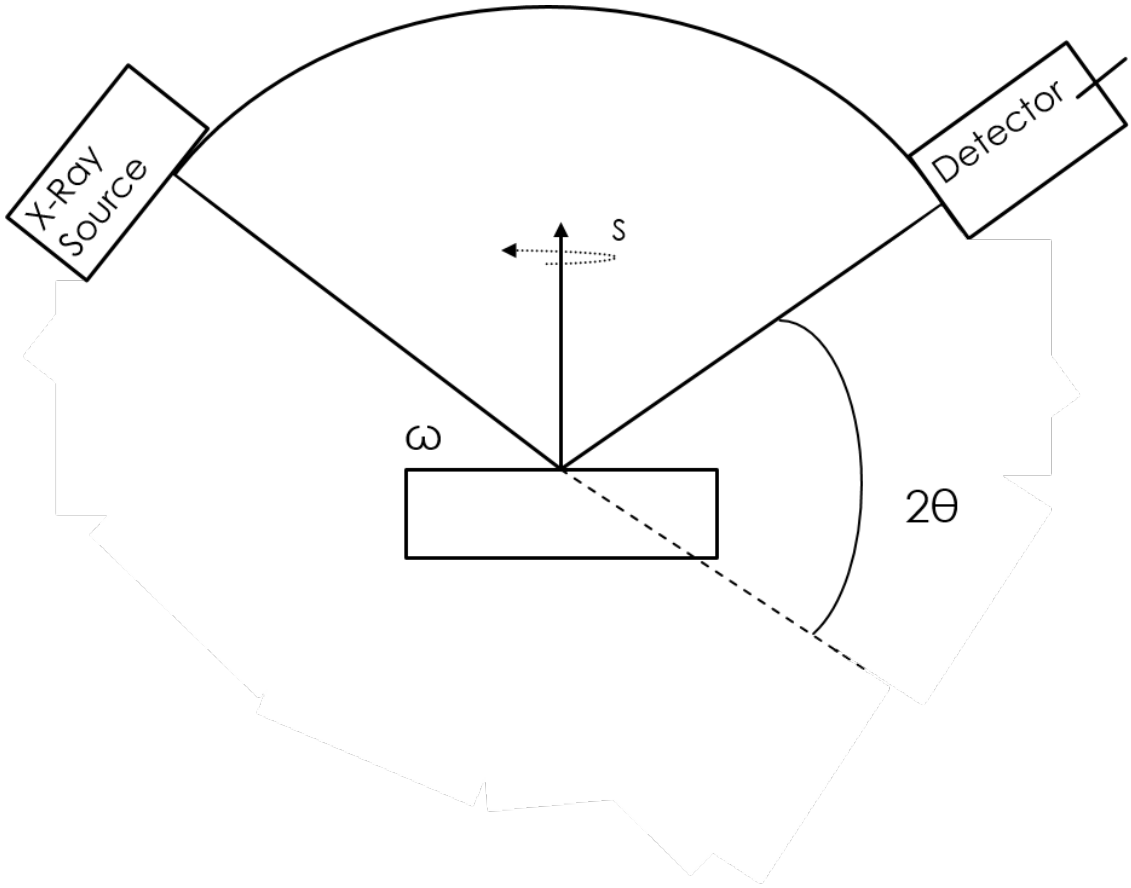

Figure 2.9: Illustration of Bragg-Bretano geometry for powder XRD, where ω is the incident angle, 2θ is the diffraction angle and S is the plane rotation angle.

The Scherrer equation is used to calculate the average crystallite size through the relationship to the width of a specific peak, typically the Full Width at Half Maxi-

mum (FWHM) or integral breadth (which measures the total area under a curve). The Scherrer equation is shown below.

$$\tau = \frac{K\lambda}{\beta Cos\theta} \tag{2.4}$$

Where τ is the mean crystallite size, K is the shape factor (typically taken to be 0.9, but depends on the crystallite shape), β is the peak width and θ is the Bragg angle.

X-ray powder diffraction was carried out on a zero background Si sample holder using a Bruker: D2 Phaser 2nd Gen. benchtop diffractometer using Cu K_α radiation ($\lambda = 1.5418$ Angstrom) across a 2θ range of 12 to 55 ^{0} with a step-size of 0.01 ^{0} at 1s/step. These measurements were carried out by Dr Fearghal C. Donnelly.

2.6.9 Raman Spectroscopy

Raman spectroscopy is a technique whereby scattered light is used to measure the vibrational energy modes of a sample. Raman is used to measure the inelastic scattering of light by a molecule. Elastic scattering, or Rayleigh scattering, occurs when the energy of the incident and emitted light is equal. In Raman scattering, the light is scattered inelastically. This means that the energy of the incident photon and the energy of the emitted photon will be different. Raman scattering where the emitted photon is of a higher energy is termed an anti-Stokes shift, and when the emitted photon is of a lower energy than the incident photon is a Stokes shift.

In Raman spectroscopy, a notch filter is used to block out any Raleigh scattered light so that only Stokes and anti-Stokes shifts may be observed. A transition is considered Raman active if there is a change in the polarisability of the molecule. This differs from IR-spectroscopy, where a molecule is considered IR-active if there is a change in the dipole moment of the molecule upon irradiation with IR-light. The

polarisability of a molecule refers to the ease at which electrons can be distorted from their original position. The polarisability decreases with increasing electron density, increasing bond length and decreasing bond strength.

As in both measurements IR-radiation is utilised, Raman and IR-spectroscopy can be utilised as complementary techniques. Raman and infrared-spectroscopy are mutually exclusive; that is if a transition is strongly Raman-active it will be weakly IR-active and vice-versa.

Raman measurements were carried out on an ANT Raman Flipper 683.

2.6.10 Thermogravimetric Analysis (TGA)

Thermogravimetric analysis is a technique in which a sample is heated at a constant rate whilst the weight of the sample is measured constantly. It is used in order to determine the thermal stability of a sample as well as its fraction of volatile materials. It can be used to show adsorption or desorption of different species, phase transitions, loss of solvent, and a number of other chemical events.

The instrument consists of a sample pan composed of a highly heat resistant material, commonly ceramic. The sample pan is supported by a precision balance, which monitors the weight of the sample throughout the heating process. The pan is placed into a furnace which is heated at a constant rate, and a plot of the change in sample mass as a function of temperature is then measured.

Thermogravimetric analysis was carried out in this work using a ceramic sample pan on a Pyris 1 TGA Thermogravimetric Analyzer.

Bibliography

(1) *What is a molar extinction coefficient? — AAT Bioquest [Online, accessed May 2020].*

(2) *ISO - ISO 22412:2017 - Particle size analysis — Dynamic light scattering (DLS) [Online, accessed May 2020].*

(3) A. Kumar and C. K. Dixit, in *Advances in Nanomedicine for the Delivery of Therapeutic Nucleic Acids*, Elsevier Inc., 2017, pp. 44–58.

(4) *Zeta Potential: Layout, Calculating, Analysis [Online, accessed May 2020].*

(5) B. C. Dodrill, *Magnetic Media Measurements with a VSM*, tech. rep.

(6) *(PDF) Study of the Magnetoelectric Properties of Multiferroic Thin Films and Composites for Device Applications [Online, accessed May 2020].*

(7) *Scanning Electron Microscopy - Nanoscience Instruments [Online, accessed May 2020].*

(8) *scanR — Vison and visual servoing for nanomanipulation and nanocharacterization using scanning electron microscope [Online, accessed May 2020].*

(9) *Energy Dispersive X-Ray Spectroscopy — EDS Failure Analysis — EDS Material Analysis — EDX Failure Analysis — EDX Material Analysis [Online, accessed May 2020].*

Chapter 3

Polyelectrolyte-Stabilised Magnetic-Plasmonic Nanocomposites

3.1 Introduction

The combination of both magnetic and plasmonic moeities into one nanocomposite material has been an avid area of research in recent years[1]. This is due to their vast number of potential applications, including magnetic hyperthermia, photothermal therapy, sensing, imaging and theranostics. The most common permutation of magnetic-plasmonic nanoparticles in the literature are core-shell type structures, wherein the inner "core" part of the nanoparticle is magnetic, and the outer "shell" part is a plasmonic metal. However, while this approach has been utilised widely, it still has a number of inherent difficulties. The addition of any non-magnetic material to the surface of a magnetic nanoparticle will have a significant impact on the magnetic moment and this, in turn, will then limit the potential applications. Reproducibility is another key issue among these core-shell type nanostructures. Highly precise procedures and harsh reaction conditions must be adhered to in or-

der to prevent separate seeding and the subsequent growth of independent plasmonic nanoparticles. The direct coating of a plasmonic metal onto a magnetic core, or vice versa, is remarkably difficult due to a mismatch in their crystal lattices[2]. This often means that other intermediate layers must be used in order to allow seeding of the plasmonic nanoparticles onto the magnetic core, and this in turn will increase the complexity and number of steps in the synthesis, as well as have implications for the magnetic moment of the resulting multimodal nanoparticle.

The combination of magnetic and plasmonic moieties is the basis for many new multifunctional materials with unique multimodal properties. The main objective of this strategy is the retention of full functionality of both the magnetic and plasmonic properties for the new material. To this end, it was decided to synthesise the magnetic and plasmonic components separately to have better control over their size and morphology, before utilising oppositely charged electrolytes in order to combine the two species. This approach was used to develop a new magnetic-plasmonic nanocomposite where both components are bound through electrostatic interactions. PAH (polyallylamine hydrochloride) and PSS (polystyrene-4-sulfonate) were chosen as the positive and negatively charged polyelectrolytes respectively as they are both non-toxic, biocompatible, and have already found uses in biomedicine[3,4]. These composite materials were found to be stable through multiple successive magnetic separation cycles, and furthermore it was also demonstrated that the successful separation was dependent on the oppositely charged polyelectrolytes.

3.2 Aims of this work

The main goal of this part of our work was the development of a new magnetic-plasmonic nanocomposite material bound through electrostatic interactions. In order to achieve this, our first aim is to synthesise PSS-stabilised magnetite of varying concentrations using a modified coprecipitation approach. PAH-stabilised gold nanoparticles of a fixed concentration will then be prepared through the reduction of chloroauric acid using sodium borohydride. These two species are planned to be titrated together until the gold plasmon peak is clearly identifiable in the UV-Visible spectrum. Subsequently, the nanocomposites are to be isolated by successive magnetic separations in order to determine if the electrostatic interactions are sufficient to bind the two species. Our objective is to prove that it is in fact the interaction between the two nanocomposites that causes the retention of the gold by showing that in similar systems, where gold nanoparticles are stabilised by acetic acid, or where no stabilising agent is used, there is a very low concentration of gold present post-magnetic separation cycle.

We also aim to explore the potential for these nanocomposites as sensors for the detection of low levels of mercury through colourimetric detection. Therefore, these nanomaterials are planned to be tested for their ability to potentially separate and colorimetrically detect Hg^{2+} ions in solution. We plan to characterise these particles using VSM, UV-Vis, XRD, FT-IR and TEM.

3.3 Results and Discussion

The layer-by-layer assembly technique, based on electrostatic interactions, is widely used for the preparation of nanoscale films on a variety of different substrates[5]. In our work, we utilise polyelectrolyte mediated electrostatic interactions between magnetite and gold nanoparticles to assemble new magnetic-plasmonic nanocomposites in solution. A scheme of this process is shown below in Figure 3.1. In order to form these nanocomposites, we need to first synthesise magnetite and gold separately, and then allow them to combine electrostatically.

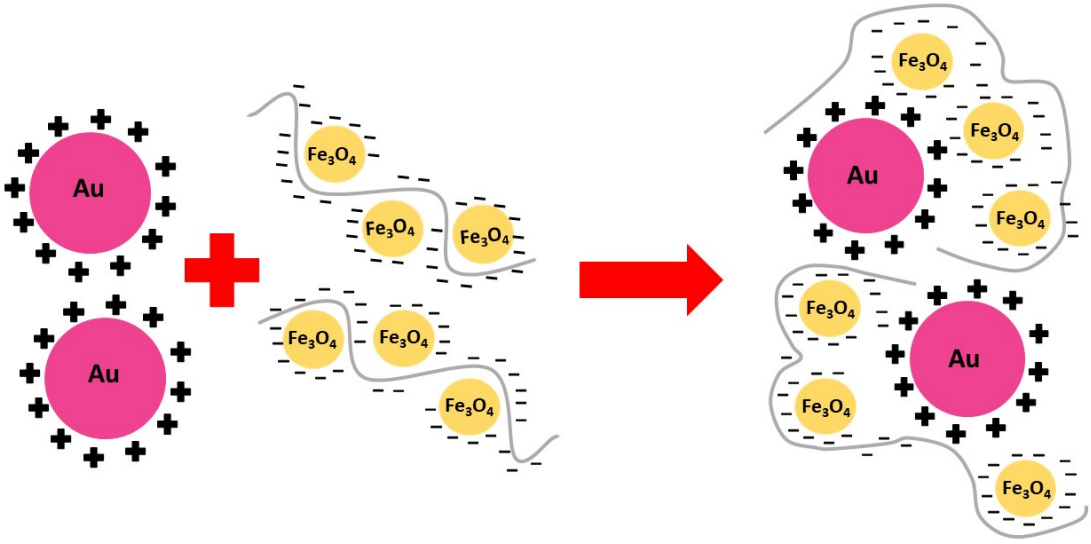

Figure 3.1: Scheme that illustrates the formation of the magnetic-plasmonic nanocomposite. The minus signs around the Fe_3O_4 nanoparticles depict the negative charge of the PSS, while the positive signs around the Au nanoparticles depict the positive charge of the PAH.

3.3.1 Synthesis of Magnetic Nanoparticles

A number of selected concentrations of PSS were tested in order to determine which produced the most stable and monodisperse solution of magnetite nanoparticles. These concentrations were chosen based on work previously carried out in the group. This PSS concentration could then be further used in the formation of the magnetic-plasmonic nanocomposite. The concentrations of the PSS solutions used are shown in the table below (Table 3.1).

Solution	Concentration
A	1.90 x 10^{-5} M
B	1.43 x 10^{-5} M
C	7.14 x 10^{-6} M

Table 3.1: PSS concentrations used for the preparation of magnetic nanoparticles.

VSM analysis of the magnetite nanoparticles was performed at room temperature (295 K). The absence of a hysteresis loop confirms that the nanoparticles are superparamagnetic (Figure 3.2). Lower concentrations of PSS result in magnetite nanoparticles that have higher saturation magnetisations: 53.2 Am^2/Kg for 1.90x10^{-5} M, 55.1 Am^2/Kg for 1.43x10^{-5} M and 68.5 Am^2/Kg for 7.14x10^{-6} M. This is expected as the polyelectrolyte itself is not magnetic, and thus, increasing the concentration of the PSS will reduce the effective magnetic moment of the final magnetite samples. Higher concentrations of PSS decrease the magnetisation due to the fact that the PSS is itself non-magnetic, but adds to the total mass of the sample. The values obtained for the magnetisation of magnetite in this experiment are comparable to that of bulk magnetite, 92 Am^2/Kg[6].

TEM analysis for the PSS-stabilised magnetite found no major differences in diame-

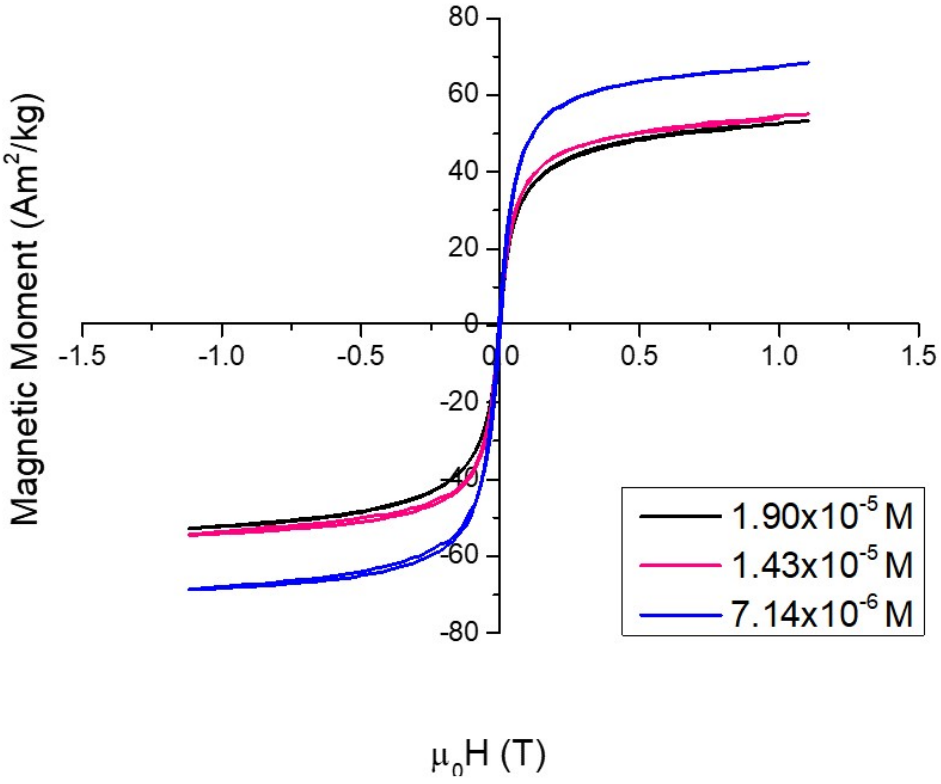

Figure 3.2: VSM of PSS-stabilised magnetite.

ter between the PSS-stabilised magnetite of different concentrations. No differences in morphology were found either. TEM images of the PSS-stabilised magnetite can be found in Figure 3.3.

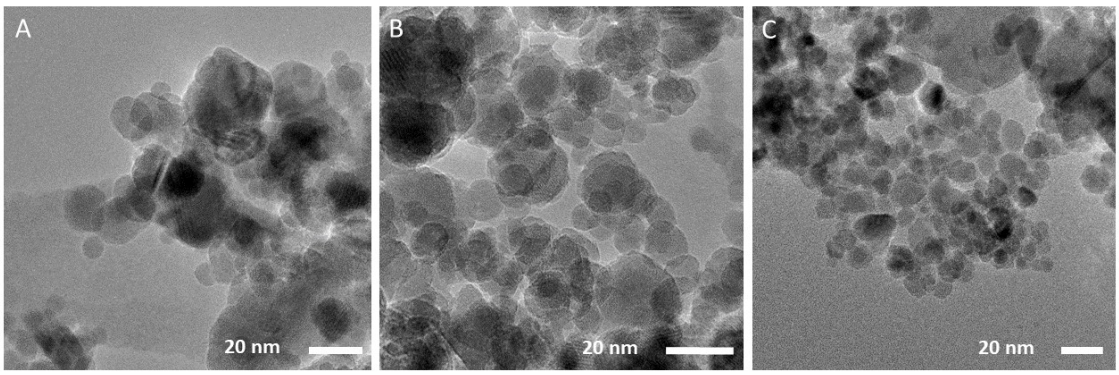

Figure 3.3: TEM images of PSS-stabilised magnetite for each concentration of PSS (A) 1.90x10^{-5} M, (B) 1.43x10^{-5} M and (C) 7.14x10^{-6} M.

Size distribution analysis was also carried out for each concentration of PSS-stabilised magnetite (Figure 3.4). It was found that the average size of the nanoparticles was 10.8 nm ± 3.3 nm for 1.90 x 10^{-5} M, 10.3 nm ± 2.6 nm for 1.43 x 10^{-5} M and 10.5 nm ± 3.2 nm for 7.14 x 10^{-6} M.

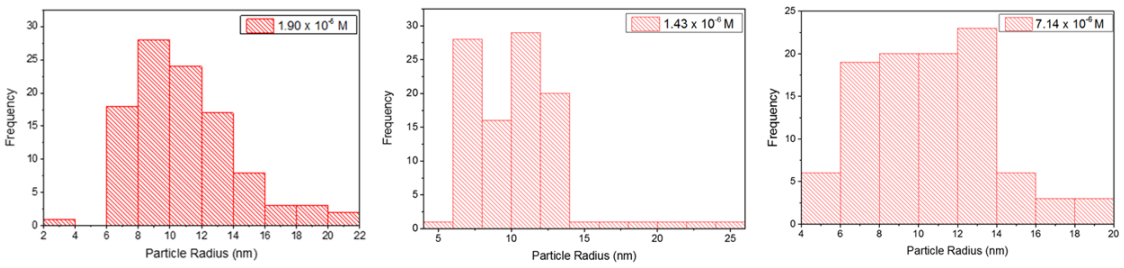

Figure 3.4: Size distributions for PSS-stabilised magnetite for each concentration of PSS (A) 1.90x10^{-5} M, (B) 1.43x10^{-5} M and (C) 7.14x10^{-6} M. (n = *100*)

In addition to TEM, DLS analysis was also carried out in order to ascertain the hydrodynamic radius of the PSS-stabilised nanoparticles (Figure 3.5). It shows the presence of large aggregates between 200 nm and 500 nm. This disparity between the sizes of the magnetite nanoparticles in the TEM images and the size shown by the DLS measurements is likely due to the large hydrodynamic radius of the nanoparticles. This occurs due to the swelling of the hydrophilic polyelectrolyte in water. It could also be due to the fact that multiple nanoparticles may be suspended across the same long strand of PSS, which would lead to the formation of larger aggregates in solution.

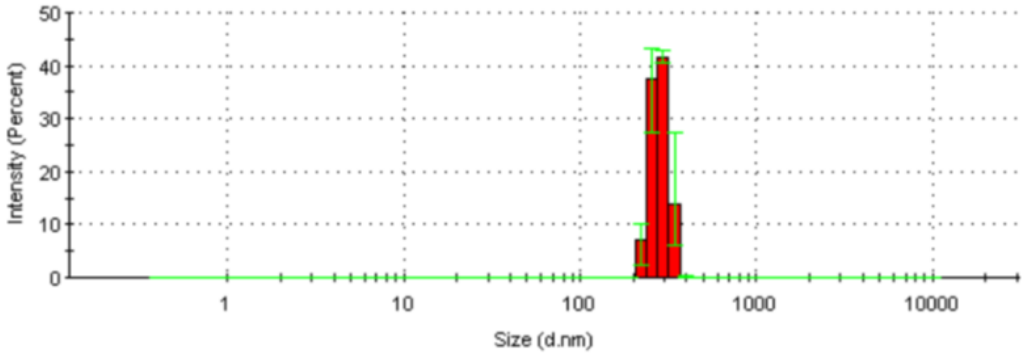

Figure 3.5: DLS analysis of a sample of the PSS-stabilised magnetite.

Zeta potential measurements were carried out on the same sample, and this showed that the PSS-stabilised magnetite nanoparticles did in fact have a negative surface charge of approximately -25 mV (Figure 3.6).

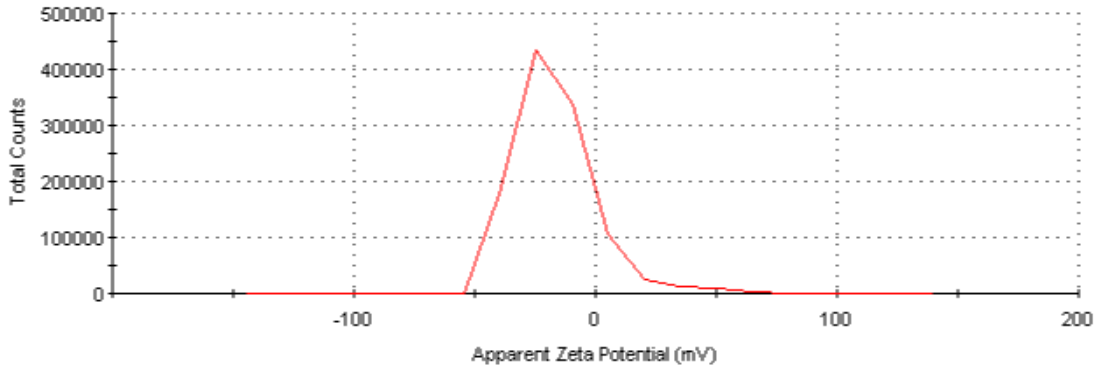

Figure 3.6: Zeta Potential measurement of PSS-stabilised magnetite showing a negative surface charge.

XRD analysis was carried out on the PSS-stabilised magnetite to ensure that it was Fe_3O_4 that was formed, and not another form of iron oxide, such as maghemite. The XRD confirmed the formation of magnetite, and this is shown in the XRD pattern below (Figure 3.7).

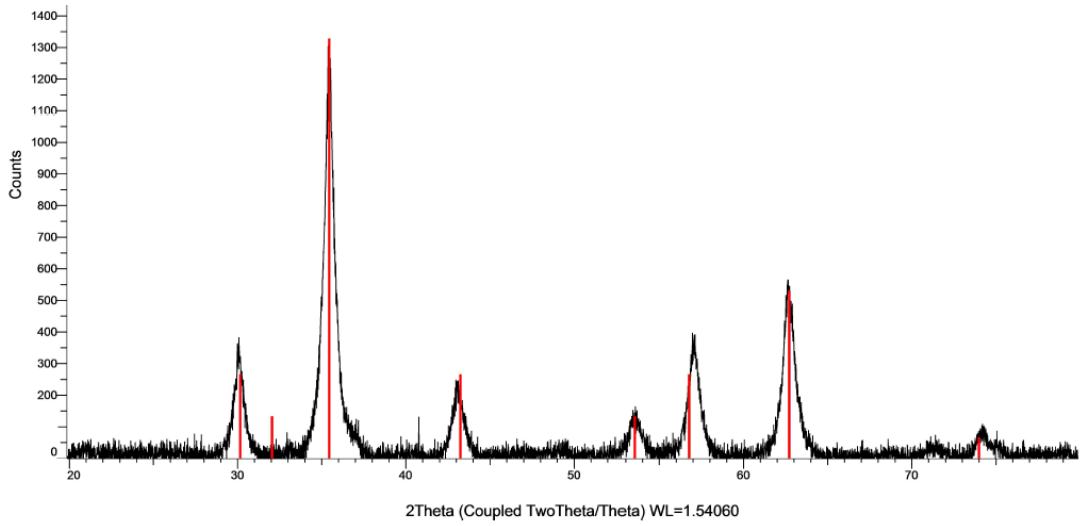

Figure 3.7: XRD pattern of PSS-stabilised magnetite.

As there were no significant differences between each concentration of PSS-stabilised magnetite, only differing slightly in magnetic moment, it was decided to test each concentration with the PAH-stabilised gold nanoparticles. It is thought that the slight variation in electrostatic strength of each concentration of PSS may lead to differences in the retention of gold in the nanocomposite material after five successive magnetic separations.

Thermogravimetric analysis (TGA) was carried out on each concentration of the PSS-stabilised magnetite to quantify the loading of PSS on the magnetite nanoparticles (Figure 3.8). The samples were heated to 600 °C at a heating rate of 10 °C/min. In each case, the first region of weight loss, between 100 - 200 °C can be attributed to the loss of water from the sample. The weight loss in the region of 275 °C can be attributed to the desorption of impurities from the sample, according to studies by Ong *et al.*[7], which found that when the sample was calcined at 275 °C, the magnetisation moment increased. The weight loss in the region below 200 °C can also partially be attributed to the loss of water adsorbed to the PSS[8]. The weight loss between 300 and 450 °C is attributed to the thermal degradation of the PSS[8]. The % weight loss from each of the three different concentrations of PSS-stabilised magnetite is as expected for the 1.9 x 10^{-5} M PSS-stabilised magnetite and the 1.43x10^{-5} M PSS-stabilised magnetite. The final % weight loss for the 7.14x10^{-6} M PSS-stabilised magnetite is considerably lower as it is an order of magnitude less concentrated than the other two samples.

FTIR analysis was also carried out for each concentration of PSS-stabilised magnetite and can be found in Appendix A1. It exhibits the peak at 570 cm^{-1} for magnetite and peaks at 1190 cm^{-1}, 1120 cm^{-1} and 1040 cm^{-1} which can be attributed to PSS. These peaks correspond well to literature values[9,10].

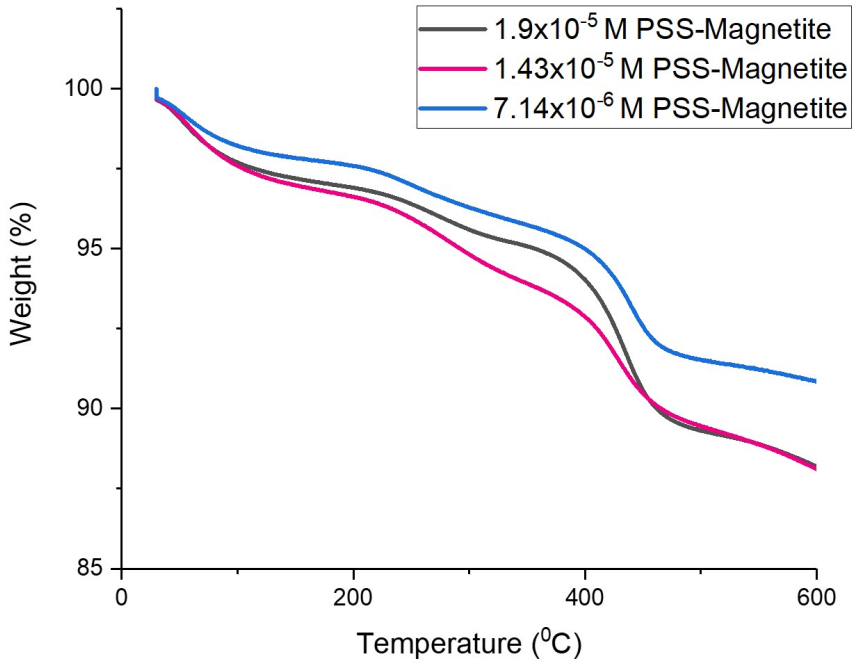

Figure 3.8: TGA analysis of each sample of PSS-stabilised magnetite.

3.3.2 Synthesis of Gold Nanoparticles

Gold nanoparticles were synthesised and stabilised with a complementary polyelectrolyte, PAH, which is positively charged. This was achieved through reduction with $NaBH_4$ in the presence of PAH, adapted from da Silva Campos *et al.*[11]. This is important because, as mentioned, the overall goal of this piece of work is to synthesise a magnetic-plasmonic nanocomposite fluid that can be extracted from solution using magnetic separation whilst retaining the gold nanoparticles.

Firstly, gold nanoparticles were synthesised using one concentration of PAH (4.5 x 10^{-7} M) as a stabilising agent. Only one concentration was used in order to determine if there were any significant differences in gold retention for the different PSS concentrations of magnetite. Gold nanoparticles were also synthesised without PAH (i.e. with no stabilising agent) and also using an alternative stabiliser, acetic acid,

to illustrate that the interaction of the two oppositely charged polyelectrolytes is imperative for the retention of the gold nanoparticles through multiple successive magnetic separation cycles.

UV-Vis analysis of the PAH-stabilised gold nanoparticles shows two plasmon peaks, at 530 nm and 640 nm respectively (Figure 3.9). While two peaks such as those shown in the UV-Vis spectrum can sometimes be indicative of nanorod structures, it was found through TEM analysis that this was in fact due to two slightly different size distributions of nanoparticles, or larger aggregates that may be present in solution.

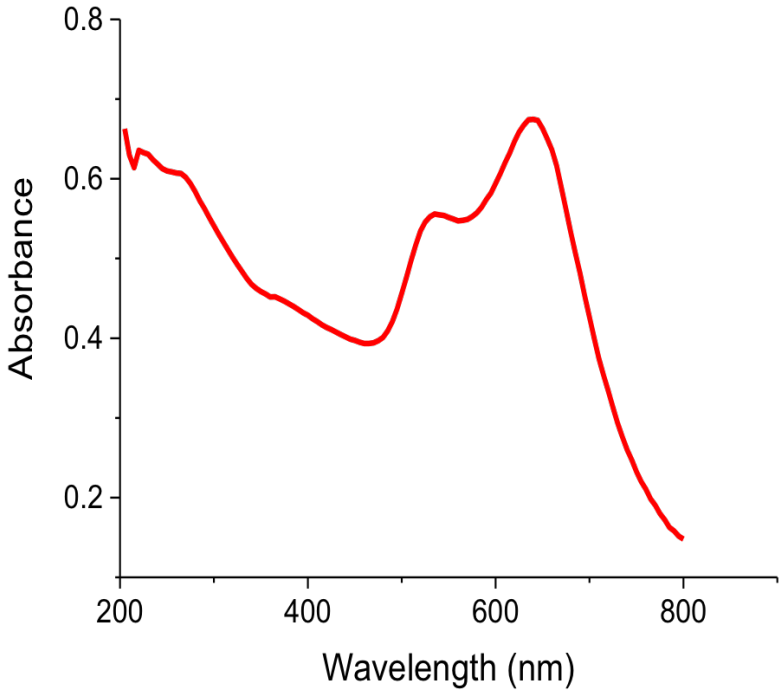

Figure 3.9: UV-Vis Spectrum of PAH-stabilised gold nanoparticles.

TEM images of the PAH-stabilised gold nanoparticles can be found in Figure 3.10. It can be seen in these images that there are larger particles present (approximately 20 nm in diameter) and slightly smaller particles (approximately 12 nm in diameter) present throughout the solution.

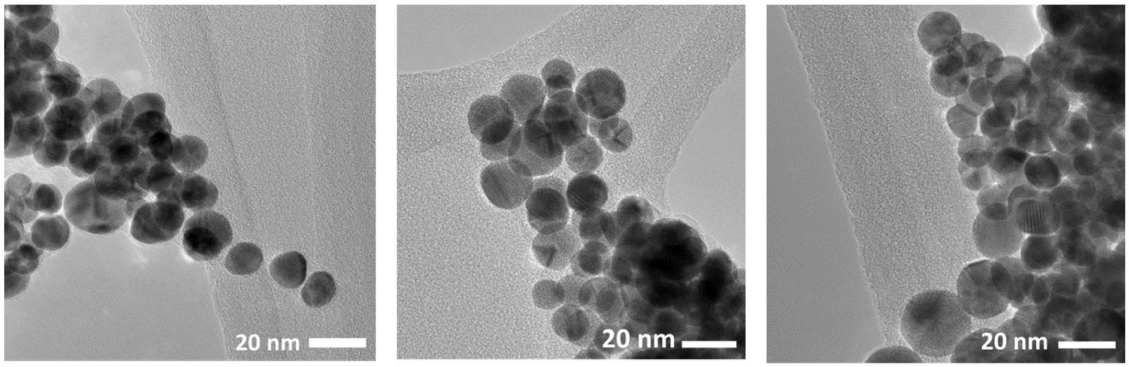

Figure 3.10: TEM images showing PAH-stabilised gold nanoparticles.

The mean size of the nanoparticles from size distribution analysis was found to be 13.7 nm ± 3.5 nm, as is shown in Figure 3.11.

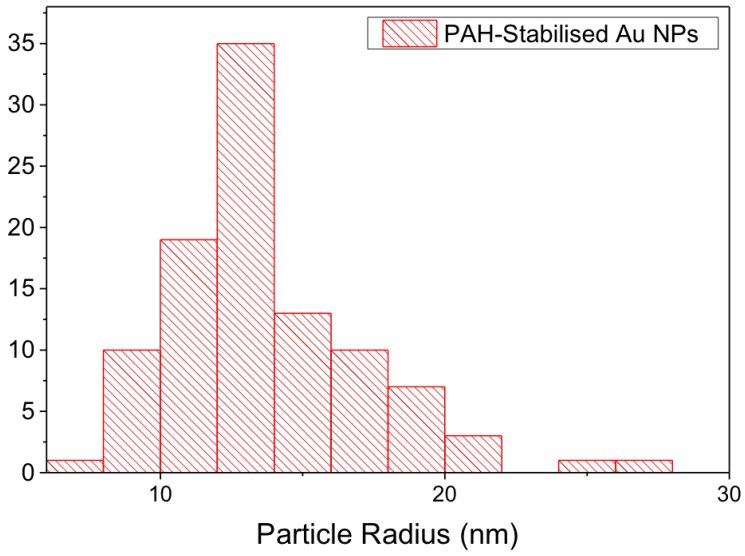

Figure 3.11: Size distribution for PAH-stabilised gold nanoparticles. (*n=104*).

It is thought that the two plasmon peaks may be present due to the polyelectrolyte stabiliser cross-linking the particles and causing the formation of larger clusters. DLS analysis was used to confirm this idea (Figure 3.12). Similar to the PSS-stabilised magnetite sample, this disparity between the TEM and UV-Vis/DLS analysis is

due to the large hydrodynamic radius of the polyelectrolyte and also perhaps the cross-linking by multiple polymer chains.

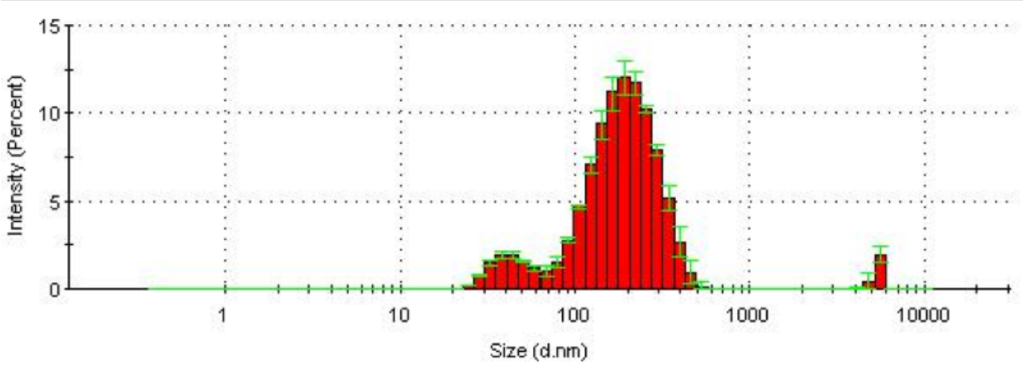

Figure 3.12: DLS spectrum of PAH-stabilised gold nanoparticles.

Zeta-potential measurements were also carried out on the PAH-stabilised gold nanoparticles, and it was confirmed that they have a positive surface charge of approximately +25 mV, similar in magnitude to that found for a sample of the PSS-stabilised magnetite (Figure 3.13).

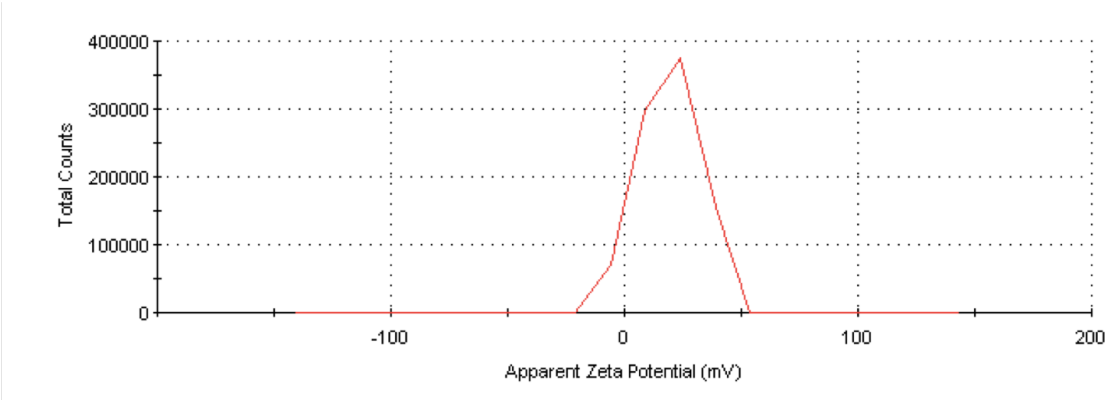

Figure 3.13: Zeta-potential measurements for PAH-stabilised gold nanoparticles.

TGA was carried out on the PAH-stabilised gold nanoparticles, however, due to the analysis being run from an aqueous sample and the low dried mass of the gold nanoparticles, the measurements are within the margin of error of the instrument. Nevertheless, the TGA results for the PAH-stabilised gold nanoparticles are shown in Figure 3.14. The TGA was run at a heating rate of 10 °C/min, and the temperature was held at 80 °C for 60 minutes to allow complete evaporation of the water from the sample before heating to 600 °C. Even though the mass of the dried gold nanoparticles is less than 0.2 mg, two distinct weight loss regions are evident, the first between 200 and 300 °C, and the second between 400 and 500 °C. These regions of weight loss are in line with those reported for the decomposition of PAH[12], which has three stages: water desorption between 80 and 300 °C, the degradation of the side polymer chains between 300 and 460 °C and the decomposition of the main polymer chain between 460 and 600 °C.

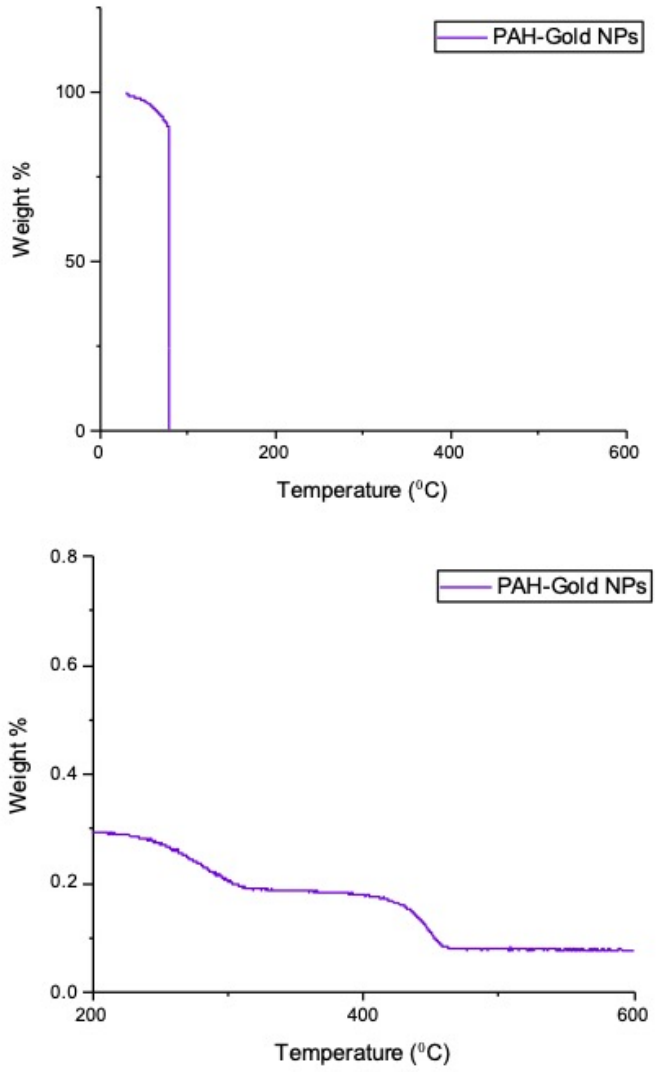

Figure 3.14: TGA analysis of the PAH-stabilised gold nanoparticles.

3.3.3 PSS-Magnetite-Gold Nanocomposites

In each case as follows, the prepared gold solutions (4.5 x 10^{-7} M in each case) were added to each concentration of PSS stabilised magnetite (Table 3.1). The gold solution was added until the plasmon peak was clearly visible. The plasmon peak is obscured slightly due to the dark solution of magnetite. The gold solution was added to each magnetite sample until approximately the same absorption was observed in each case. This is illustrated in the two UV-Vis spectra shown in Figure 3.15.

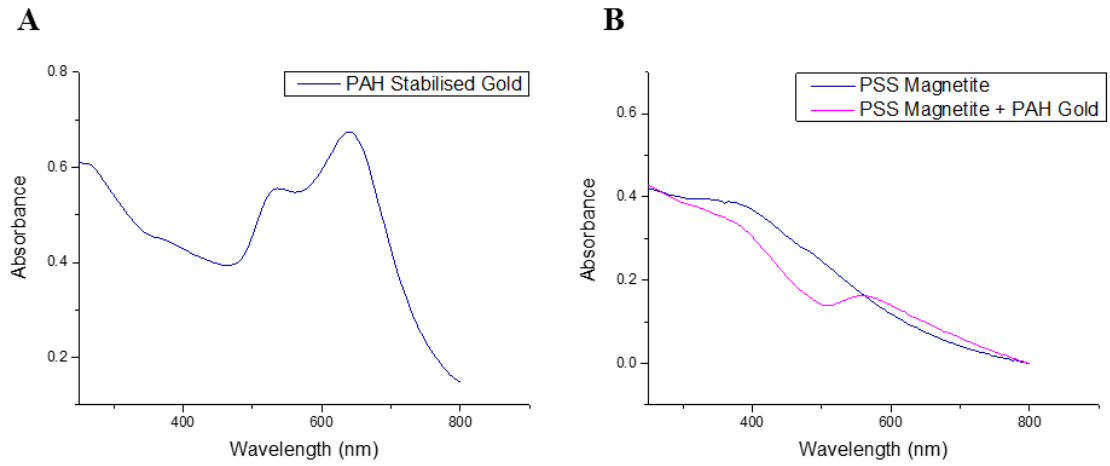

Figure 3.15: UV-Vis spectra of (A) PAH-stabilised gold nanoparticles and (B) PSS-stabilised magnetite nanoparticles and PAH-stabilised gold nanoparticles.

The UV-Vis spectroscopy and TEM analysis were then carried out on each sample after five successive magnetic separation cycles. The goal is to retain as much gold as possible in the nanocomposite after each successive cycle, as it demonstrates how this nanocomposite system could then be further functionalised with a sensing moiety and utilised for the detection of different toxins through magnetic extraction. It is necessary to retain enough gold so the plasmon peak is still visible after multiple magnetic separations as it is the shift in the position of the gold peak that facilitates detection of the heavy metal ions.

PSS-Stabilised Magnetite and Unstabilised Gold Nanoparticles

The unstabilised gold nanoparticles in this experiment were prepared in exactly the same way as those stabilised with PAH, but the PAH was omitted in the synthesis. Thus we refer to the gold nanoparticles synthesised in this procedure as "unstabilised" as they have no designated stabilising agent. These nanoparticles were found to be larger than those synthesised with PAH, in the region of 50 nm in diameter.

UV-Vis analysis (Figure 3.16) shows no observable plasmon peak for any concentration of PSS-stabilised magnetite nanocomposites after five successive magnetic separations. This indicates that either there is a very low concentration of gold, or that the gold has been washed completely out of the nanocomposite.

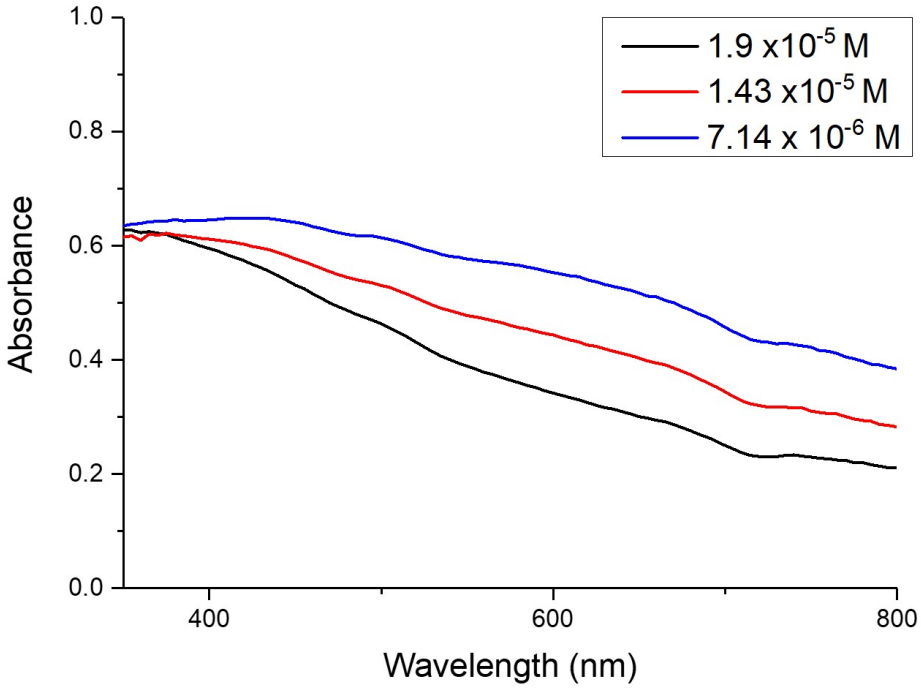

Figure 3.16: UV-Vis spectra of PSS-magnetite and unstabilised gold nanocomposites after five magnetic separations.

TEM analysis confirms that there is a very low concentration of gold present in the solution after multiple washing steps (Figure 3.17). This confirms that, in the case where there is no stabilising agent present on the gold nanoparticles, that they are not retained in the nanocomposite solution after multiple magnetic separation cycles.

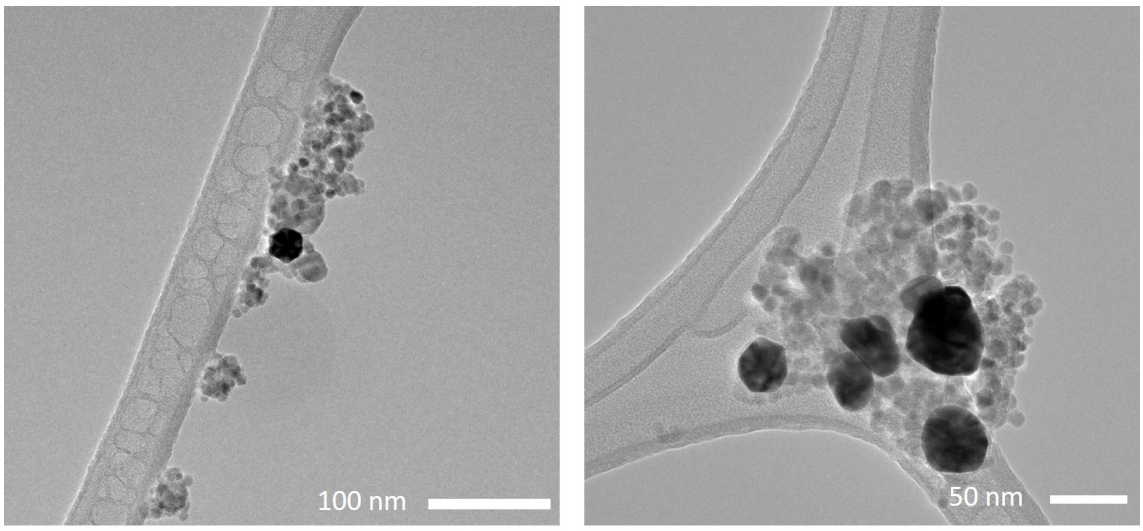

Figure 3.17: TEM images showing the nanocomposite containing PSS-Stabilised magnetite and unstabilised Au nanoparticles after five magnetic separations.

In order to conclusively determine whether or not it is in fact the charge of the stabilising agent that determines whether or not it is retained in the nanocomposite solution, gold nanoparticles stabilised by an uncharged species, in this case acetic acid, were prepared.

PSS-Stabilised Magnetite and Acetic Acid-Stabilised Gold Nanoparticles

To further investigate the role of PAH in the formation of the stable nanocomposite, acetic acid-stabilised gold nanoparticles were synthesised in the presence of 30 mg of a sample of the PSS-stabilised nanoparticles (1.90 x 10^{-5} M). The formation of the gold nanoparticles *in-situ* caused the colour of the magnetite solution to change from dark brown to a definitive reddish dark brown, which is indicative of the formation of gold nanoparticles. Immediately after the formation of the *in-situ* nanocomposite, five successive magnetic separations were carried out and the nanocomposite was then analysed using UV-Vis spectroscopy and TEM.

The reaction was carried out at three different concentrations of acetic acid, in order to test the effect of the acetic acid concentration on the interaction of the two species. Briefly, PSS-stabilised magnetic nanoparticles (30 mg) were dispersed in 50 mL of Millipore water and sonicated for 15 minutes. (x) mL of gold chloride solution (0.1 M) in (y) μL of acetic acid are then added. Details of this are shown in Table 3.2 below.

Solution	x (μL)	y (mL)
E	300	1.5
F	600	3
G	2400	12

Table 3.2: Concentrations of gold chloride and acetic acid for the formation of *in-situ* PSS-stabilised magnetite and acetic acid-stabilised nanocomposites.

UV-Vis analysis of the nanocomposites after the magnetic separations is shown in Figure 3.18. The weak plasmon peak can be attributed to a small concentration of gold nanoparticles present in the solution for concentration F, however, no significant plasmon peak is observable for either concentration E or G. This suggests that there is a very low concentration of gold nanoparticles present in the nanocomposite solution.

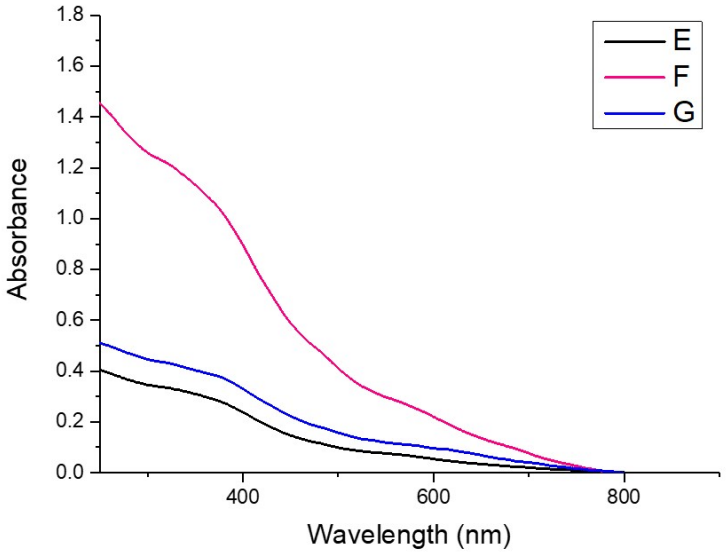

Figure 3.18: UV-Vis spectra for PSS-stabilised magnetite and acetic acid-stabilised gold nanoparticles.

This was then confirmed by TEM analysis (Figure 3.19). Similar to the unstabilised gold sample, the gold nanoparticles here are significantly larger than those synthesised separately using PAH, in the region of 30 - 50 nm.

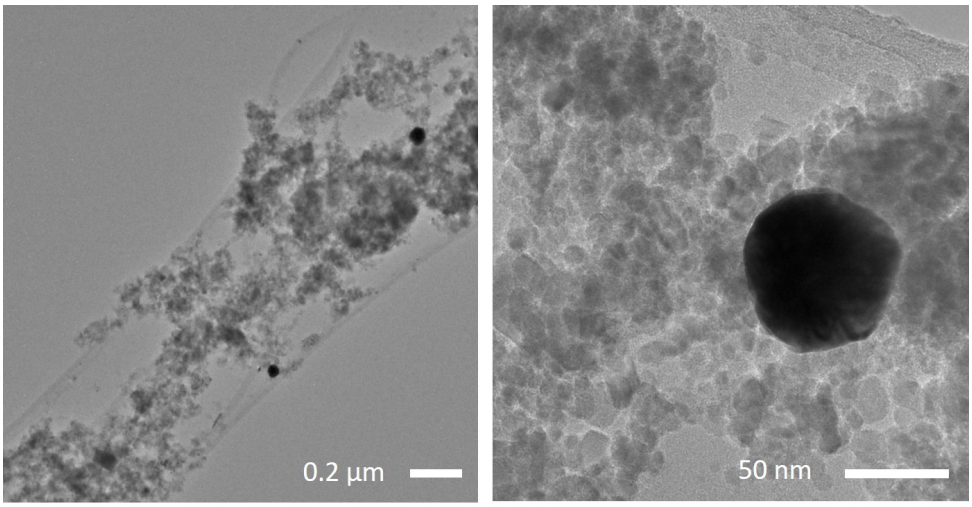

Figure 3.19: Representative TEM images of the PSS-magnetite and acetic acid-stabilised gold nanoparticles after five magnetic separations.

Gold nanoparticles are present in a very low concentration, arguably in even lower concentration than those synthesised using no stabilising agent. This could perhaps be due to a very weak negative charge of the acetic acid resulting in a weak repulsion of the two species, leading to an even more pronounced leaching of the gold nanoparticles through the magnetic separations. Thus, from these two samples (unstabilised gold and acetic acid-stabilised gold) it can be concluded that the positively charged polyelectrolyte, PAH, is intrinsic to the retention of the gold nanoparticles in the magnetic-plasmonic nanocomposite solution.

PSS-Stabilised Magnetite and PAH-Stabilised Gold Nanoparticles

PAH-stabilised gold nanoparticles were synthesised through reduction using sodium borohydride, and titrated into each of the three concentrations of PSS-stabilised magnetite such that a plasmon peak was clearly observable. This nanocomposite solution then underwent five successive magnetic separations and the resulting nanocomposite was examined using UV-Vis spectroscopy and TEM.

UV-Vis analysis (Figure 3.20) shows the presence of a plasmon peak for two of the three PSS concentrations - 1.43 x 10^{-5} M and 7.14 x 10^{-6} M, but not for 1.90 x 10^{-5} M. This could most likely indicate a lower concentration of gold nanoparticles in this solution, or a comparatively higher concentration of magnetite compared to gold in this particular nanocomposite. As it is the highest concentration of PSS in the solution, it does not stand to reason that the electrostatic interactions between the two species are not strong enough, rather it might mean that the bond between the two species is of sufficient strength so that the magnetite nanoparticles are effectively "coating" the gold in the nanocomposite matrix. This suggestion makes sense when we examine the plasmon peaks for the two lower concentrations, which are more pronounced the lower the initial concentration of PSS. This means that

for any potential applications, and testing of the nanocomposite for the detection of mercury, only the lowest concentration of PSS-stabilised magnetite PAH-stabilised gold sample (7.14 x 10^{-6} M) should be used and tested, as this has the clearest and most easily identifiable plasmon peak.

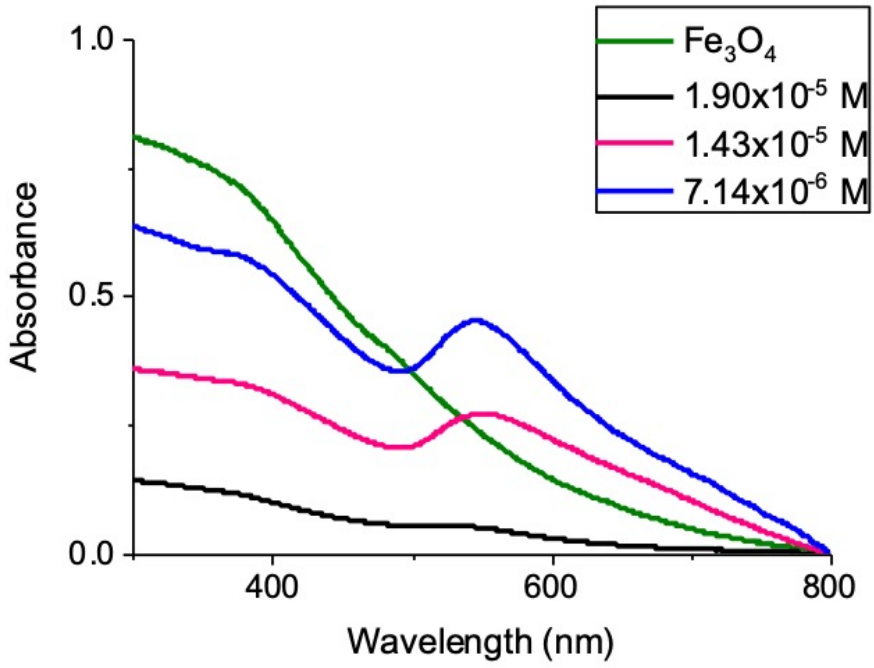

Figure 3.20: UV-Vis spectra of each PSS-stabilised magnetite concentration titrated with PAH-stabilised gold after five magnetic separation cycles.

TEM analysis (Figure 3.21) does not confirm this, however, rather simply illustrates a significant concentration of gold in each PSS-stabilised magnetite concentration. This clearly demonstrates that the electrostatic interaction between the negatively charged PSS and the positively charged PAH is sufficient to bind the two nanoparticle species. It would be difficult to corroborate the above hypothesis from conventional TEM; perhaps *in-situ* solution TEM and observing the change in the composition of the nanocomposite upon application of magnetic field would provide some clues as to the true behaviour of the two species in solution.

It is also evident from the TEM images that the gold nanoparticles are significantly larger than the magnetite nanoparticles in each case, and also that the gold nanoparticles seen in the nanocomposites are, in some cases, significantly larger than those initially synthesised (Figure 3.9) which have an average diameter of 13.7 nm. While there are some gold nanoparticles that still appear to be in that size range, there are a number of considerably larger gold nanoparticles. There are three possible explanations for this: the first is that the initial sample of the PAH-stabilised gold nanoparticles do in fact have two different size distributions, as was first suggested. It is possible that these larger particles were not observed in initial TEM due to their falling out of solution, a common phenomenon in nanoparticle synthesis, prior to dropping on TEM grids. The second possible explanation is that the stabilisation of the nanoparticles using PAH is not sufficient to prevent further nanoparticle growth. A third explanation is that the PAH does not completely coat all of the gold nanoparticles, with some remaining uncoated. As PAH exists in long polymer chains, it could be said that the smaller gold nanoparticles are stabilised along this chain, and the larger unstabilised gold nanoparticles continued to grow.

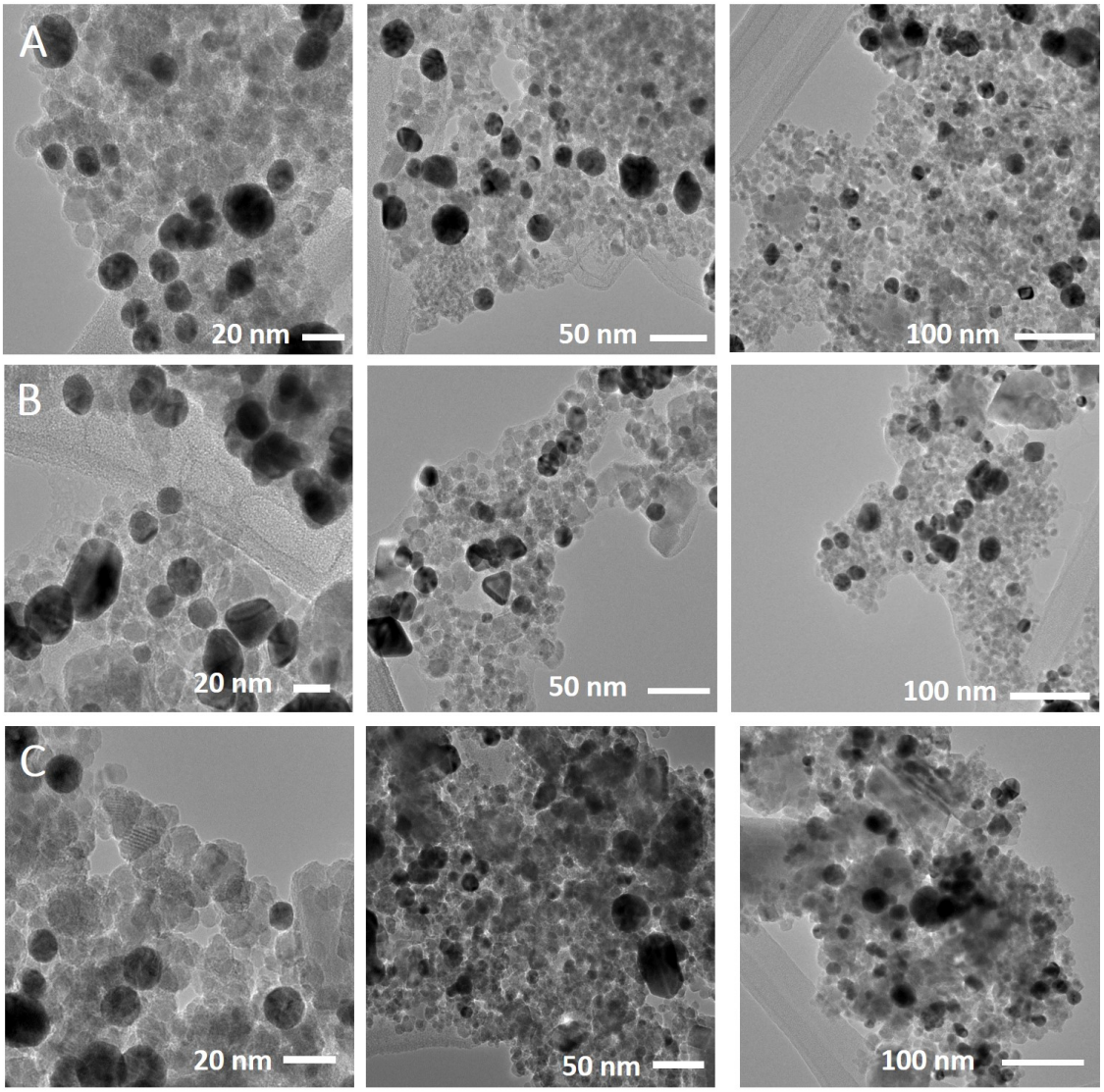

Figure 3.21: TEM images of the magnetic-plasmonic nanocomposites for each concentration of PSS-stabilised magnetite; (A) 1.90 x 10^{-5} M, (B) 1.43 x 10^{-5} M and (C) 7.14 x 10^{-6} M.

3.3.4 Colourimetric Mercury Ion Testing

A 1 mM stock solution of mercury (II) chloride was prepared, and, using this, five concentrations of mercury ion solutions were prepared using serial dilution. The concentration of each of these solutions are shown in Table 3.3 below. 1.11 mL of solution was removed from dilution number 5 such that the final volume of each mercury solution was 10 mL.

Dilution	Mercury (II) Chloride Solution (mL)	Water (mL)	Final Mercury Concentration (Moles/L)
1	11.11	0	1×10^{-3}
2	1.11	10	1×10^{-4}
3	1.11	10	1×10^{-5}
4	1.11	10	1×10^{-6}
5	1.11	10	1×10^{-7}

Table 3.3: Serial dilution table for the preparation of five concentrations of Hg^{2+} ions.

Preliminary studies were carried out with each concentration of the Mercury solution with a solution of the PAH-stabilised gold nanoparticles. UV-Vis spectra of these reactions are shown in Figure 3.22 and 3.23. A blue-shift can be seen for increasing concentrations of mercury, which is indicative that the PAH-stabilised gold nanoparticles and the mercury ions are interacting in a meaningful way. However, the slight blue-shift was unexpected, as in traditional Hg^{2+} ion testing, the interaction between the mercury ions and the nanoparticles causes aggregation leading to a red-shift[13,14]. It may be the case that as the gold nanoparticles are already bridged by the PAH polymer that the binding of the Hg^{2+} ions to the gold nanoparticle surface causes a slight unfolding or lengthening of the polymer chain, resulting in the slight blue shift. Unfortunately, as the blue-shift in the UV-Vis spectra is very small (less than 5 nm) the colourimetric change is not detectable by eye. Images

of the PAH-gold nanoparticles solutions and each mercury solution can be found in Appendix A2.

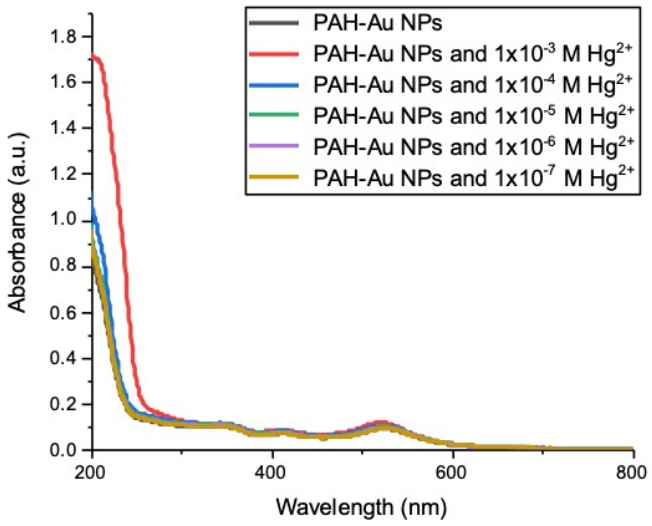

Figure 3.22: UV-Vis spectra of PAH-stabilised gold nanoparticles and each mercury solution.

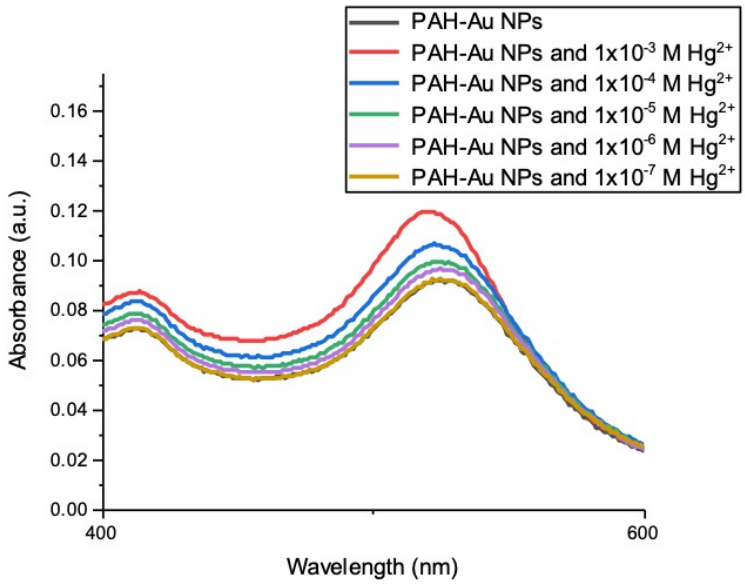

Figure 3.23: Subsection of the UV-Vis spectra of PAH-stabilised gold and each mercury solution showing the blue shift of the plasmon peak.

However, as there was a detectable difference in the position of the plamson peak after the addition of the mercury solutions, the nanocomposite solutions for each magnetite concentration ($1.9x10^{-5}$ M PSS, $1.43x10^{-5}$ M PSS and $7.14x10^{-6}$ M PSS) were tested with the mercury solutions. The results for nanocomposite A, containing $1.9x10^{-5}$ M PSS-stabilised magnetite and PAH-stabilised gold, are shown in Figure 3.24 and 3.25.

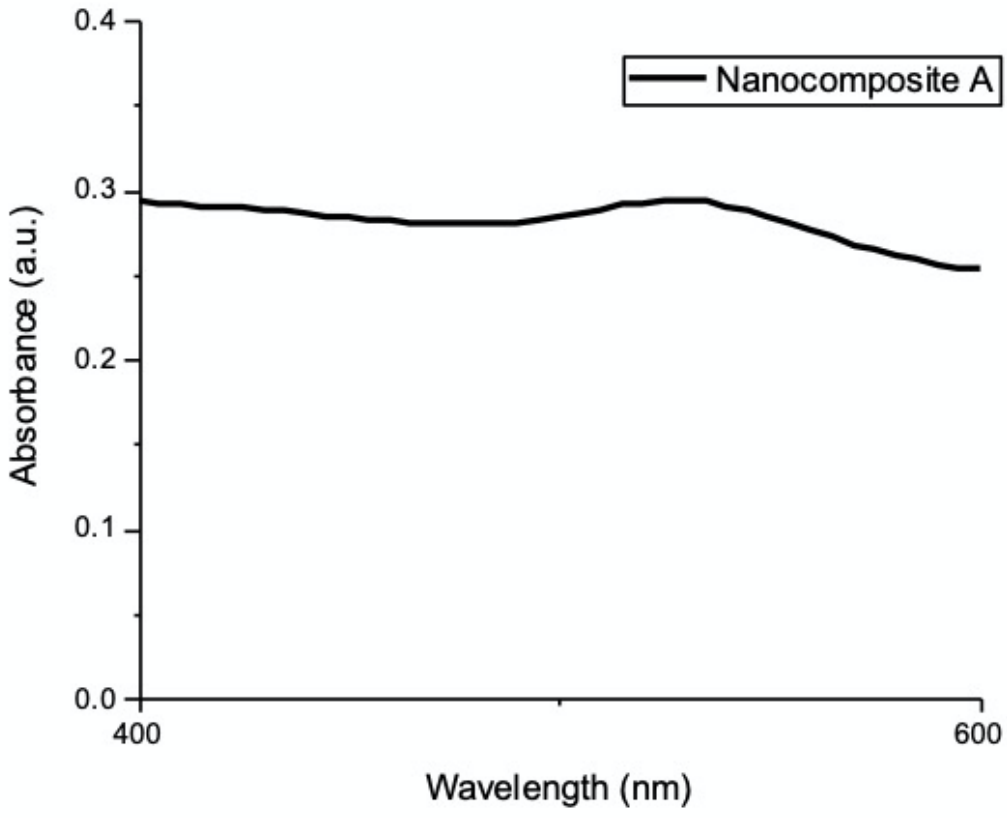

Figure 3.24: UV-Vis spectrum of nanocomposite A ($1.9x10^{-5}$ M PSS).

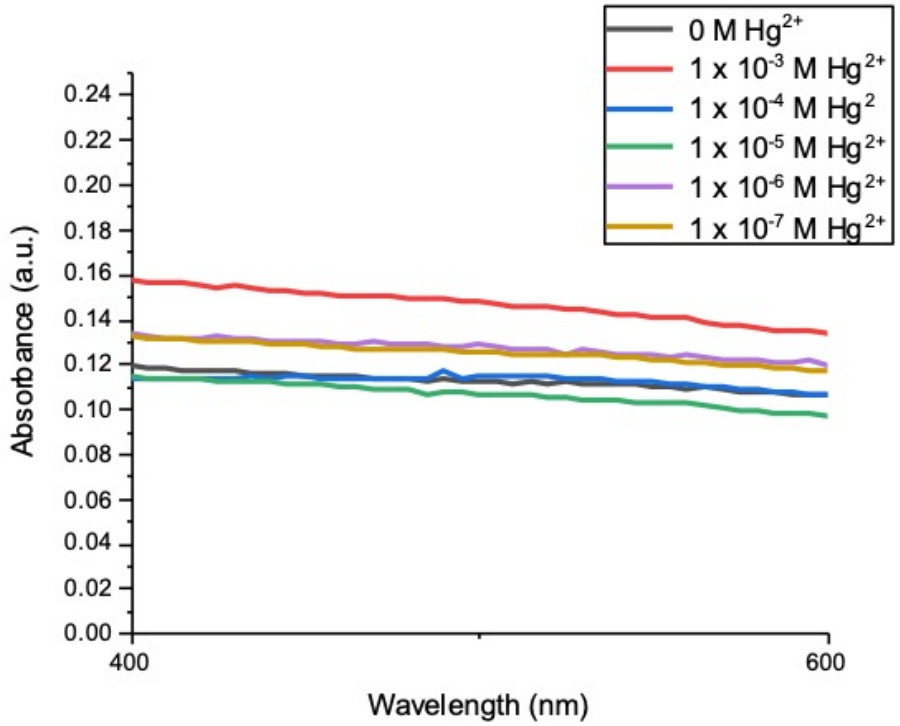

Figure 3.25: UV-Vis spectra of nanocomposite A with each of the solutions of mercury.

As can be seen in Figure 3.24 and 3.25, the broad absorption of the magnetite nanoparticles causes a reduction in the intensity of the plasmon peak, and as a result of this, no blue-shift due to mercury interaction can be detected for any concentration of mercury ions. This is also the case for the two nanocomposites B and C, which consist of 1.43×10^{-5} M PSS and PAH-stabilised gold nanoparticles and 7.14×10^{-6} M PSS and PAH-stabilised gold nanoparticles respectively. These spectra can be found in Appendix A3 and A4.

However, the initial studies with PAH-stabilised gold nanoparticles show promise and should be further investigated through varying the concentration of the PAH used to coat the nanoparticles in order to determine whether the concentration of the PAH has an effect on the extent of the blue-shift on interaction with the mercury ion solutions.

3.4 Conclusions

A new magnetic-plasmonic nanocomposite consisting of PSS-stabilised magnetite and PAH-stabilised gold nanoparticles has been prepared and characterised. To the best of our knowledge, this is the first reported magnetic-plasmonic nanocomposite where the two components are bound entirely through electrostatics. TEM analysis of the nanocomposite was used to confirm this, as well as UV-Vis spectroscopic analysis of the washings. A modified co-precipitation approach was used to prepare the PSS-stabilised magnetite, and gold nanoparticles were prepared through the reduction of chloroauric acid using sodium borohydride. The electrostatically-bound nanocomposite was found to retain gold over a range of PSS concentrations.

Initial mercury detection studies showed that the Hg^{2+} ions caused a blue shift in the plasmon peak of the PAH-stabilised gold nanoparticles, but that the presence of magnetite in the nanocomposites obscured this peak such that it was no longer clearly discernable. Future work will involve optimisation of the PAH concentration in order to develop a fast mercury ion detection platform.

Bibliography

(1) S. Stafford, R. Serrano Garcia and Y. Gun'ko, *Applied Sciences*, 2018, **8**, 97.

(2) N. R. Jana, *Design and development of quantum dots and other nanoparticles based cellular imaging probe*, 2011.

(3) P. I. Georgianos, I. Liampas, A. Kyriakou, V. Vaios, V. Raptis, N. Savvidis, A. Sioulis, V. Liakopoulos, E. V. Balaskas and P. E. Zebekakis, *International Urology and Nephrology*, 2017, **49**, 2217–2221.

(4) P. A. Janeesh, H. Sami, C. R. Dhanya, S. Sivakumar and A. Abraham, *RSC Adv.*, 2014, **4**, 24484–24497.

(5) X. Zhang, H. Chen and H. Zhang, *Layer-by-layer assembly: From conventional to unconventional methods*, 2007.

(6) B Andrzejewski, W Bednarski, M Kaźmierczak, K Pogorzelec-Glaser, B Hilczer, S Jurga, M Matczak, B Łęska, R Pankiewicz and L Kępiński, *Magnetization Enhancement in Magnetite Nanoparticles capped with Alginic Acid*, tech. rep.

(7) B. Ong, N. K. Devaraj, M. Matsumoto and M. H. Abdullah, *MRS Proceedings*, 2008, **1118**, 03–09.

(8) R. Suresh, J. V. Antony, R. Vengalil, G. E. Kochimoolayil and R. Joseph, *Industrial Crops and Products*, 2017, **95**, 66–74.

(9) M. Stoia, R. Istratie and C. Păcurariu, *Journal of Thermal Analysis and Calorimetry*, 2016, **125**, 1185–1198.

(10) Y. Wang, Y. Shen, Y. Zhang, B. Yue and C. Wu, Journal of Macromolecular Science, Part B: Physics, 2006, vol. 45 B, pp. 563–571.

(11) W. N. da Silva Campos, A. E. T. Leite, D. A. Sonego, M. A. de Andrade, F. D. Pizzinatto, V. S. Marangoni, V. Zucolotto, L. Nakazato, E. M. Colodel and R. L. de Souza, *Ciencia Rural*, 2017, **47**, DOI: 10.1590/0103-8478cr20161001.

(12) *(13) Study on synthesis and property of poly(allylamine hydrochloride) [Online, accessed August 2020].*

(13) Y. Chen, S. Han, S. Yang and Q. Pu, *Dyes and Pigments*, 2017, **142**, 126–131.

(14) J. Du, Z. Wang, J. Fan and X. Peng, *Sensors and Actuators, B: Chemical*, 2015, **212**, 481–486.

Chapter 4

Anisotropic Metal Nanostructures and their Assemblies

4.1 Introduction

The shape and anisotropy of nanoparticles has a hugely significant effect on the physical and chemical characteristics of nanomaterials[1]. Anisotropic gold nanoparticles, in particular, were first noticed by Zsigmondy in 1909, when he wrote that gold nanoparticles are "not necessarily spherical when their size is under 40 nm"[2], and in 1912, Gans extended Mie's theory to account for the optical properties of these new nanoparticles[3]. However, even with this pioneering work, it is only in the last twenty years that the field of anisotropic nanoparticles has truly taken off and undergone significant development.

The most common gold nanoparticles are spherical, or convex, in shape. As discussed previously, their colour can be tuned by changing the size of the nanoparticle, and there are a number of highly reproducible methods to obtain gold nanoparticles in a variety of sizes and in a variety of solvents. However, concave nanoparticles are an area of increasing interest, and there is still much debate over their exact

mechanisms of formation. Concave nanoparticles differ from convex nanoparticles in their shape - concave nanoparticles can be oddly-shaped, spiky and anisotropic. Anisotropic nanoparticles have asymmetric axes and this break in symmetry is a cause of the unusual properties in metallic and semi-conducting nanomaterials[4]. Anisotropic seed-mediated growth is used in this work, and involves two steps - a nucleation and a growth phase. These two stages need to be separated temporally, frequently this means spatial separation of the two phases in different reaction vessels. Incredibly careful manipulation of the growth kinetics is required in order to achieve anisotropy in nanoparticles. Other synthetic approaches to anisotropic growth include changing of the reaction parameters, for example pH or temperature. It was found by Xue and Mirkin that silver nanoprisms could be tuned through precise alteration of reaction pH[5]. Temperature also plays an important role in the preparation of anisotropic nanoparticles. Li and Peng reported the temperature effects of the controlled synthesis of colloidal CdSe quantum disks[6] .

Nanowires are an example of a one (1D) dimensional material, the synthesis of which involves two steps - nucleation and growth. Nanowires can be prepared via a number of approaches, mostly involving vapour-phase and colloidal techniques. In this work, a colloidal approach was used to prepare the nanowires, which is the most common and frequently used approach[7]. In the colloidal syntheses of metal nanowire structures, two general approaches are used - a "top-down" and a "bottom-up" approach. The "top-down" approach is widely utilised in industry for the fabrication of microelectronic components. It utilises lithographic techniques in order to carve out a desired structure from a given material. The "bottom-up" approach is more common in synthetic chemistry, and it utilises chemical reactions and self-assembly of atoms or molecules to form increasingly larger structures[8]. This synthetic approach again relies on the balance between the nucleation and growth phases. In the nucleation step, seeds are formed which act as the building blocks for the nanowire, and, as the concentration of the seeds increases, they combine to form a larger structure.

These nanostructures can be prepared in solution, as particles in a vapour or on a solid support. "Bottom-up" self-assembly processes include metal catalyst-assisted laser ablation syntheses, solution phase syntheses and template-based methods[9]. In this work, the AuAg nanowires were prepared via a modified "bottom-up" approach previously reported by Jiu *et al.*[10]. Nanowires can be prepared using a variety of different metals but gold-based nanowires are the most extensively studied due to their biocompatibility, plasmon resonance and catalytic possibilities.

4.2 Aims

The main goal of this work is to develop new anisotropic metal nanostructures and their assemblies, and to investigate the properties of these new nanocomposites. In this work, we aim to synthesise both convex and concave nanoparticles: namely magnetite nanoparticles, spherical gold nanoparticles, gold nanostars and gold nanorods. We plan to firstly make and characterise a variety of anisotropic structures, gold nanostars and gold nanorods, as well as PAH-stabilised magnetite and PAH-stabilised gold. We then aim to investigate self-assemblies of these structures around AuAg nanowires over various periods of time and at different concentrations. The goal of this chapter is to prepare multi-modal anisotropic nanowire structures. The prepared nanoparticles that are deemed to have appropriate monodispersity and capping agents will then be used in the formation of composite nanostructures. This is to be achieved through the use of complementary charges of the capping agents on the two species to be self-assembled. We plan to characterise these structures fully using UV-Vis, TEM, SEM and EDX techniques. These materials are expected to have a range of potential applications in sensing and detection of various biological species.

4.3 Results and Discussion

4.3.1 PSS/PAH-Stabilised Magnetite Nanoparticles

PSS-stabilised magnetite nanoparticles were synthesised by a modified co-precipitation approach used in Chapter 3. In this instance, only a PSS-concentration of 5.71 x 10^{-7} M was used. In this experiment, however, the reaction time was varied. Two reflux times were tested, 60 and 100 minutes.

In both cases, the resulting nanoparticles were brown/black in colour. It was immediately noted that the product that had been heated under reflux for 100 minutes was easier and faster to separate magnetically from solution. This observation was later confirmed by VSM analysis. 15 mg of both the samples was used for VSM measurements. As can be seen in Figure 4.1, both samples are superparamagnetic as they show no hysteresis loop. Sample **A** (reflux time = 100 minutes) has a slightly higher magnetic moment of 73 Am^2/Kg when compared to sample **B** (reflux time = 60 minutes) which has a magnetic moment of 68 Am^2/Kg.

However, in order to determine whether or not it is statistically significant this would need to be repeated over multiple different syntheses, as their may have been other external factors which could have led to this difference. The values noted here are still smaller than those reported for bulk magnetite (92 Am^2/Kg)[11], however this is due to the fact that PSS is a non-magnetic material will increase the mass of the nanoparticles and hence decrease the magnetisation value per unit mass[11].

Zeta-potential measurements were also carried out on the two magnetite samples (Figure 4.2).

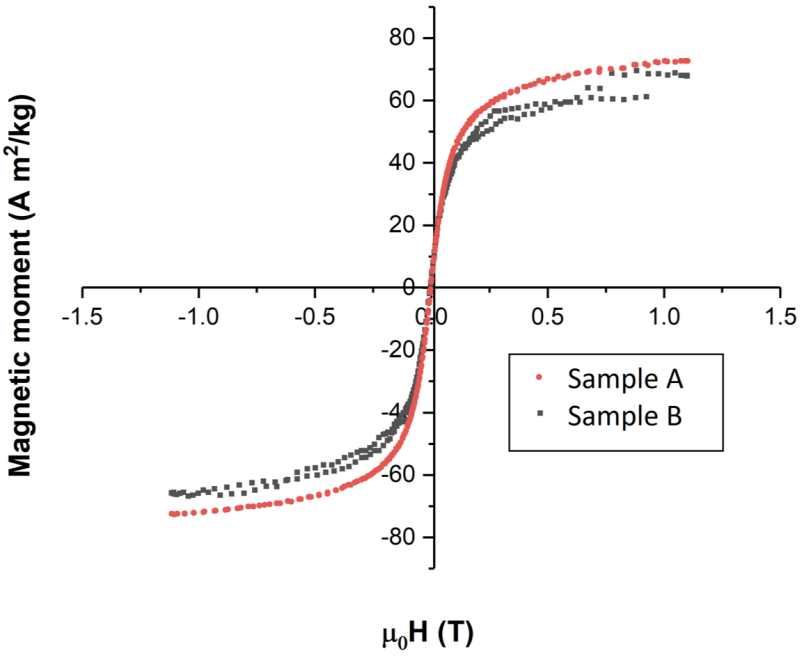

Figure 4.1: VSM plot of Sample **A** (reflux time = 100 minutes) and Sample **B** (Reflux time = 60 minutes).

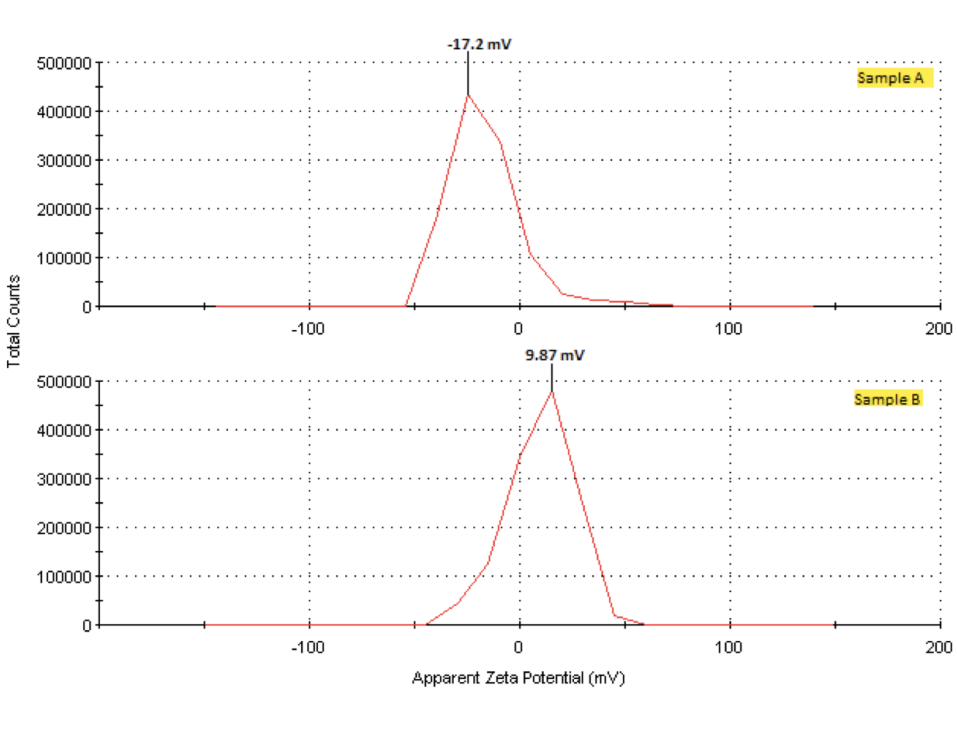

Figure 4.2: Zeta-Potential measurements for sample **A** (reflux time = 100 minutes) and sample **B** (reflux time = 60 minutes).

An unusual trend was noted for all samples synthesised with the lower reflux time. These samples all had a positive zeta-potential, which is unexpected as it is known that PSS is negatively charged. However, the measurement for the zeta-potential of sample **B** was 9.87 mV, which is considered unstable. For nanoparticles in solution or suspension, a zeta-potential value of ± 0 - 10 mV is considered unstable, and a zeta-potential value of ± 10 - 20 mV is considered relatively stable[12]. This means that the sample heated under reflux for the shorter amount of time is unstable in solution. Sample **A**, which was refluxed for 100 minutes, has a zeta-potential of -17.2 mV, which is in line with what we would expect for these particles. These unexpected values could mean that in the shorter reflux the PSS polymer did not properly bind to the magnetite nanoparticles and was then washed out during the magnetic separation step. This would then lead to the formation of unstable aggregates, which would explain sample **B**'s low zeta-potential value.

TEM analysis was also carried out with these samples in order to determine whether or not there was any significant morphological or size differences between the two samples. The TEM images are shown below in Figure 4.3.

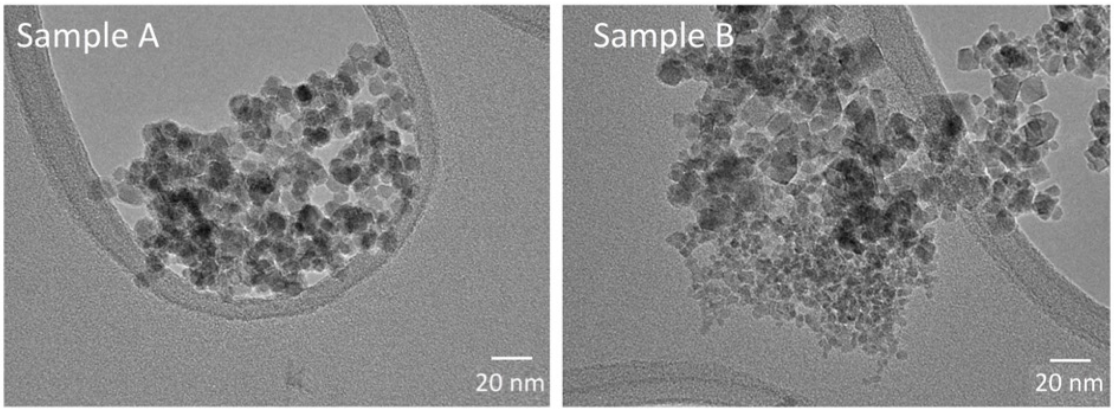

Figure 4.3: TEM images of sample **A** (100 minute reflux) and sample **B** (60 minute reflux).

It is clear from the TEM images that sample **A**, with the longer reflux time, has a much better monodispersity than sample **B**. The nanoparticles in sample **A** seem

to be uniform in size and morphology, whereas sample **B** has two very distinct size distributions as well as larger aggregates. This confirms the result from the zeta-potential of insufficient PSS coating resulting in the formation of larger, unstable and non-uniform aggregates.

Particle size distributions were calculated using Image J (Figure 4.4). Sample **A** was found to have an average diameter of 11.1 ± 2.9 nm, and sample **B** was found to have an average diameter of 10.6 ± 4 nm.

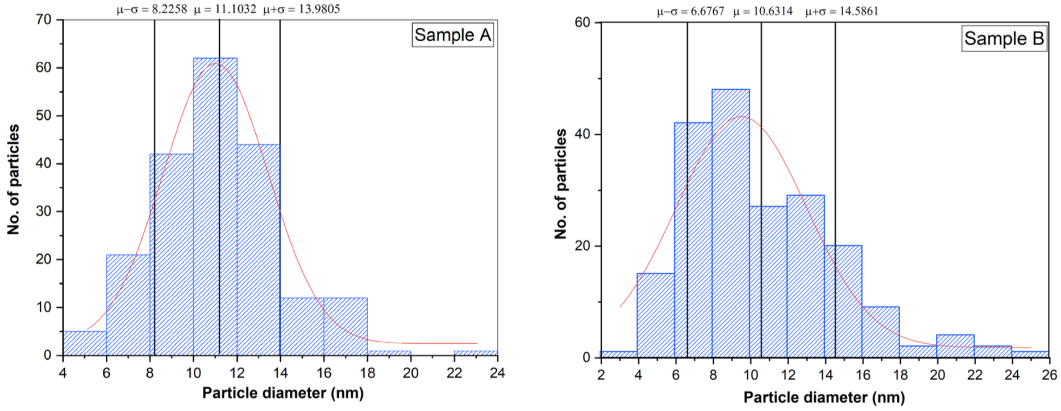

Figure 4.4: Size distribution analysis of Sample **A** (reflux = 100 minutes)(n = *100*) and Sample **B** (reflux = 60 minutes)(n = *100*).

VSM, zeta-potential and TEM analysis all confirm that the magnetite nanoparticles that were heated under reflux for 100 minutes rather than 60 minutes have better magnetic properties, as well as stability and monodispersity. However, these nanoparticles have a negative surface charge due to the PSS-stabilisation. As we want the nanoparticles to interact electrostatically with the negatively charged PVP-coated nanowires, we will need to further modify the magnetite nanoparticles by adding a layer of PAH.

Initially, a PAH concentration of 5.71 x 10^{-5} M was used. The coating was achieved through sonication of the PSS-stabilised magnetite in the PAH solution over a time period of 60 minutes. Zeta-potential measurements found that these nanoparticles were highly stable and positively charged with a zeta-potential of + 70.3 mV (Figure 4.5 (A)). However, it was found that these nanoparticles were unresponsive to a magnet and could not be separated magnetically. It was also found that these nanoparticles would not precipitate out of aqueous solution even after centrifugation at 9000 RPM for 30 minutes. There are two possible explanations for this, both accounted for by the fact that the initial PAH concentration used was too high. The first is that the magnetisation per unit mass of the nanoparticles is sufficiently low that magnetic separation is no longer feasible, due to multiple layers of PAH surrounding each nanoparticle. However, this does not explain the nanoparticles staying in suspension through multiple centrifugation steps. What is more likely is that the PAH concentration was sufficiently high to make the solution acidic, which would cause the magnetite to dissolve. To investigate this, the pH of the 5.71 x 10^{-5} M PAH solution was measured, and was found to be 5.5. As a result of this, the concentration of the PAH solution was dropped to 5.71 x 10^{-6} M, and the PSS-stabilised magnetite were sonicated for 30 minutes instead of an hour. The resulting nanoparticle solution was easily magnetically separable and was found to be a stable suspension with a zeta-potential value of +19.1 mV (Figure 4.5 (B)). These PAH-stabilised magnetite nanoparticles were then used in the synthesis of the multimodal nanowire composites.

A VSM plot for the PAH-stabilised magnetite nanoparticles is shown in Figure 4.6. The sample shows no hysteresis loop, which indicates that it has retained its superparamagnetism through the additional coating of PAH, and has a magnetic moment of 53 Am^2/Kg. This is considerably lower than the magnetic moment before the addition of PAH, however, this is expected as the polymer would contribute to the mass of the sample but not its overall magnetic moment.

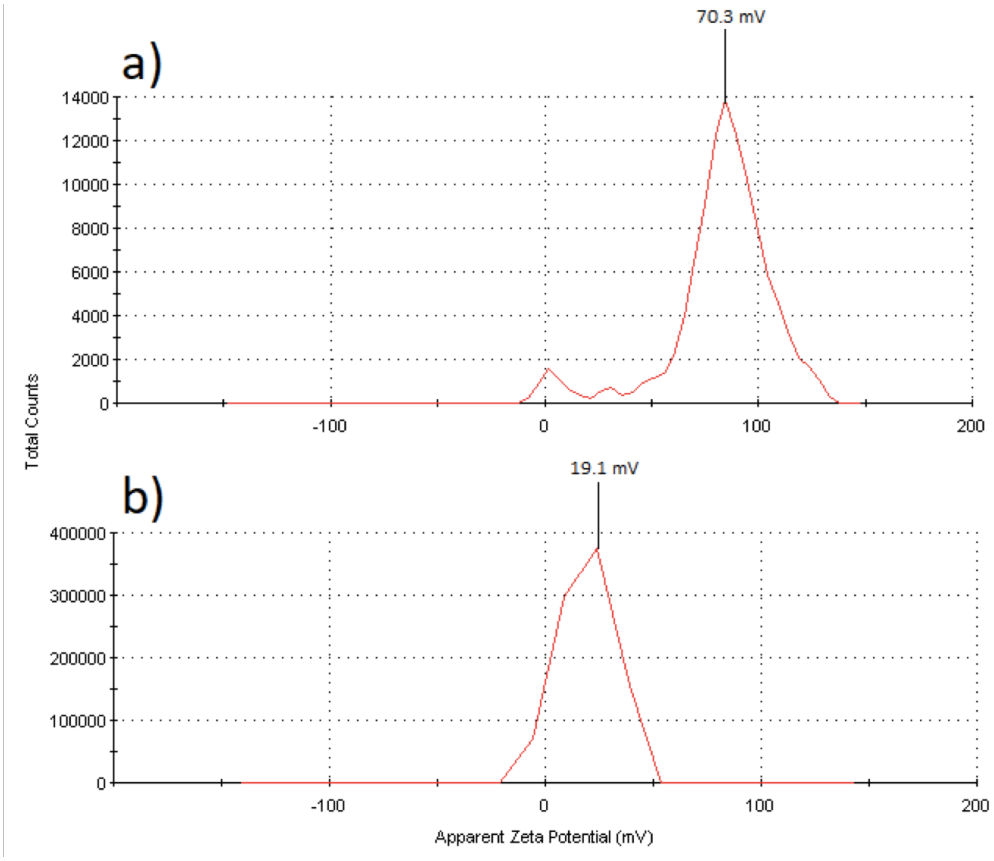

Figure 4.5: Zeta-potential measurements for PAH-stabilised magnetite at (A) 5.71 x 10^{-5} M and (B) 5.71 x 10^{-6} M.

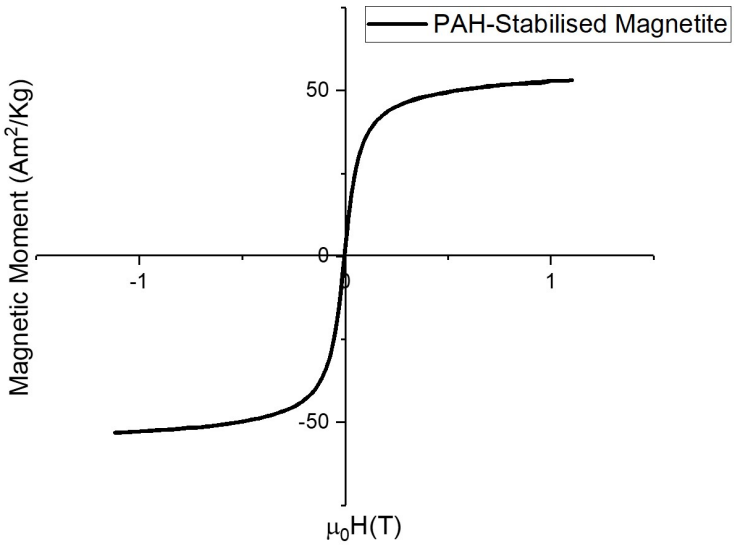

Figure 4.6: VSM plot of PAH-stabilised magnetite nanoparticles.

TEM imaging was also carried out on the PAH-stabilised magnetite nanoparticles, and this is shown in Figure 4.7. As is evident in the TEM images, the additional layer of PAH had no impact on the monodispersity of the nanoparticles.

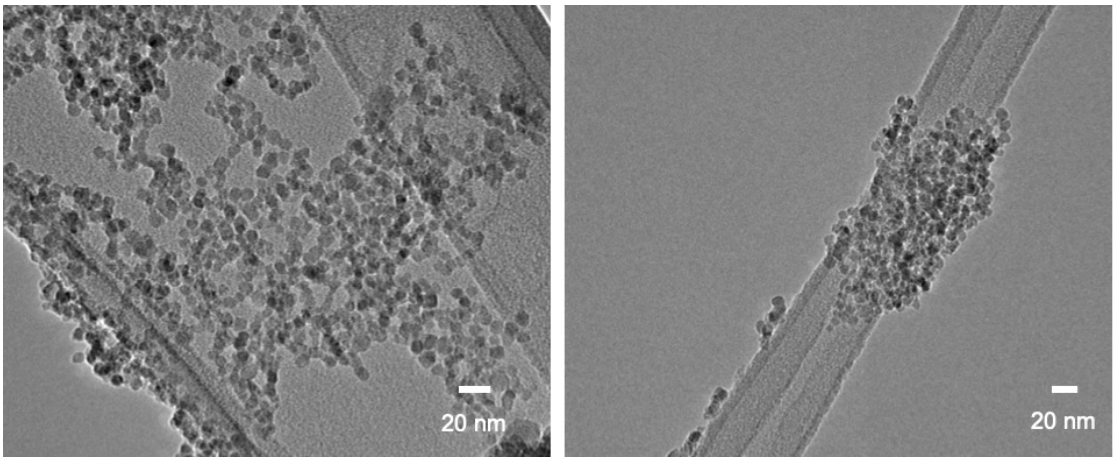

Figure 4.7: TEM images of PAH-stabilised magnetite nanoparticles.

4.3.2 PAH-Stabilised Gold Nanoparticles

PAH-stabilised gold nanoparticles were synthesised through the reduction of a chloroauric acid solution using sodium borohydride in the presence of PAH, as described in Chapter 3. After 40 minutes, the colour of the solution was wine red, indicating the formation of gold nanoparticles. Three samples of these nanoparticles were prepared, and their UV-Vis spectra are shown in Figure 4.8.

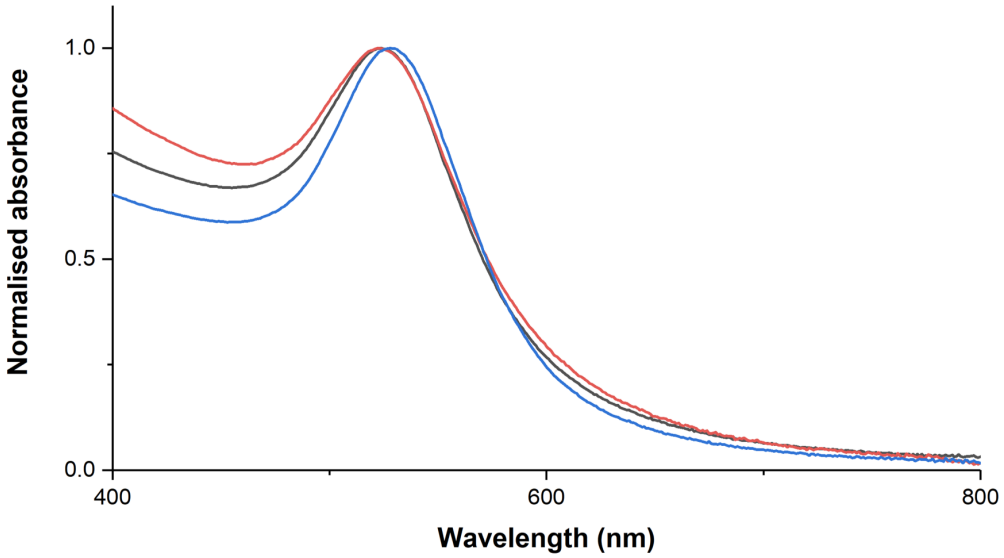

Figure 4.8: UV-Vis spectra for PAH-stabilised gold nanoparticles.

For each case, a narrow and well-defined peak was observed, which is indicative of the formation of spherical nanoparticles with a narrow size distribution. The plasmon peaks for each gold sample are in the range of 520 - 530 nm, which corresponds well to the literature values for gold nanoparticles synthesised using this approach[13].

TEM analysis was also carried out on these samples in order to investigate the size, morphology and monodispersity of the nanoparticles (Figure 4.9). The images show uniform and relatively monodisperse gold nanoparticles. Similar to those in chapter

3, there does seem to be two different populations of gold nanoparticles. This could be due to residual Au^{3+} salts in solution being reduced and causing the formation of larger gold nanoparticles. The TEM analysis for these nanoparticles was also carried out a number of weeks after their initial synthesis, so this may raise some questions about the long term stability of the nanoparticles in aqueous solution.

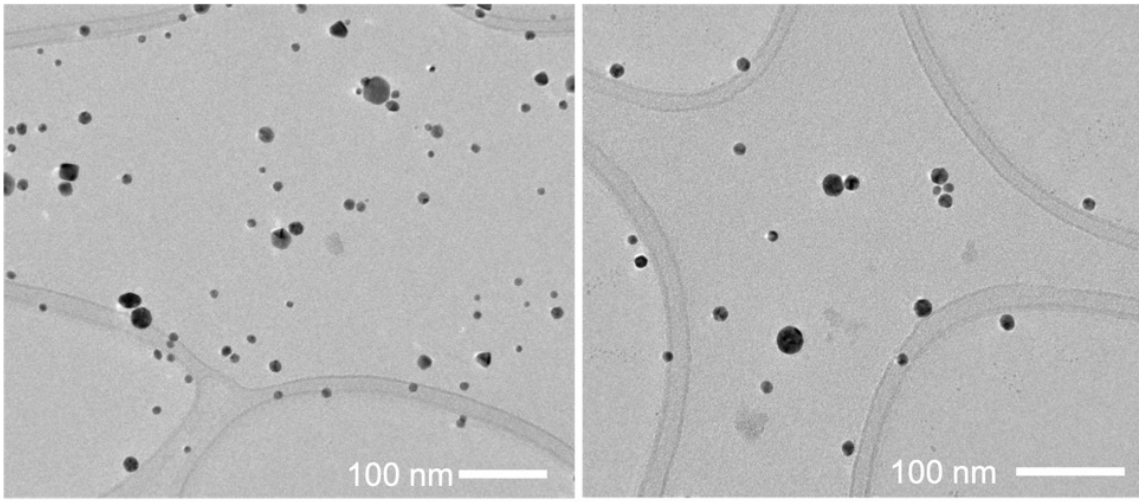

Figure 4.9: TEM images of PAH-stabilised gold nanoparticles.

More comprehensive time studies could be carried out by monitoring the broadening of the plasmon peak over time to show the growth of these larger nanoparticles. Centrifugation could also be used to precipitate the larger nanoparticles out of solution in order to separate the two different families of nanoparticles.

Size distribution analysis was also carried out on these nanoparticles, and they were found to have an average size of 10 ± 3.8 nm as shown in Figure 4.10. What is evident from this plot is that while we can see a number of larger nanoparticles in the TEM images, the vast majority of the nanoparticles present have this much lower size distribution. The larger nanoparticles appear to have an average diameter of 23 ± 1.5 nm. These PAH-stabilised gold nanoparticles will now be used to synthesise plasmonic nanowire composites.

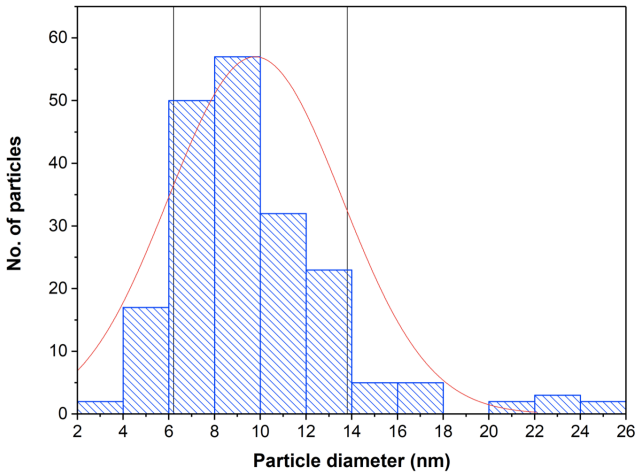

Figure 4.10: Size distribution plot for PAH-stabilised gold nanoparticles (*n=100*).

4.3.3 CTAB-stabilised Gold Nanorods

A seed-mediated approach was utilised in order to synthesize gold nanorods. Firstly, gold seeds were made through rapid reduction with sodium borohydride in the presence of sodium citrate and allowed to grow for two hours. Then, nanorod growth was achieved through the addition of the gold seeds to a solution of ascorbic acid, gold chloride, sodium hydroxide and CTAB. This approach was taken from procedures reported by Koeppl *et al.*[14].

UV-Vis analysis was carried out on the gold nanorods as a means to determine whether or not the synthesised particles were anisotropic (Figure 4.11). Two plasmon peaks in the UV-Vis spectrum is indicative of the formation of gold nanorods[15]. In this case we have the transverse SPR at 528 nm, and the longitudinal SPR at 693 nm. While this is suggestive of the formation of gold nanorods, additional TEM is required as confirmation. This is because two peaks could also correspond to other anisotropic shapes, as well as the existence of two separate size distributions of spherical nanoparticles.

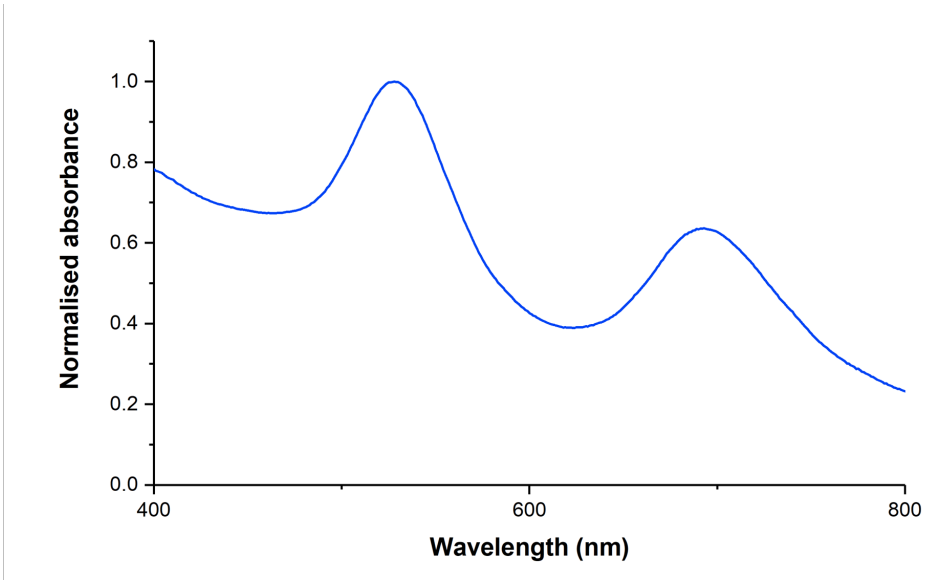

Figure 4.11: UV-Visible spectrum of gold nanorods.

TEM analysis was carried out on the sample, and these images are shown below in Figure 4.12. As can be seen in the TEM images, while there are a number of nanorods, there are also a large number of spherical nanoparticles as well as some nano-triangles. Even within the nanorods, there are two distinct populations. There are a larger number of lower aspect ratio nanorods, and a small number of high aspect nanorods. The presence of these spherical nanoparticles could explain the differences between the UV-Vis spectrum we obtained when compared with those in the literature. Normally, for gold nanorods, the longitudinal plasmon peak is much larger than the transverse plasmon peak. It may be the case that the spherical gold nanoparticles are enhancing the transverse peak at 528 nm, which is traditionally around where one would expect the plasmon peak for spherical gold nanoparticles.

The mean aspect ratios of the two different aspect ratio nanorods were calculated using ImageJ. The majority of the nanorods have a lower aspect ratio of 2.8 $\pm$ 0.3. These nanorods account for the peak in the UV-Vis spectrum at 693 nm. This correlates well with the literature, in which nanorods with an aspect ratio of 2.34 are reported to have a longitudinal plasmon peak at 658 nm, and nanorods with an

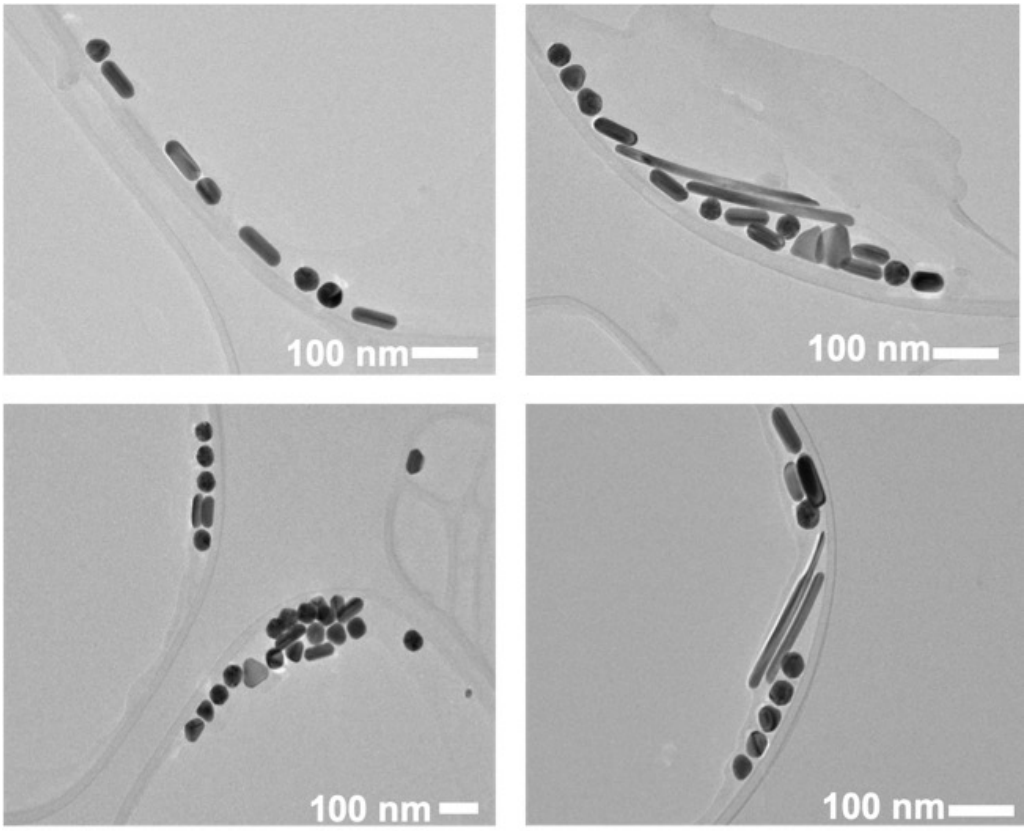

Figure 4.12: TEM analysis of the gold nanorod solution.

aspect ratio of 3.39 are reported to have a longitudinal plasmon peak at 728 nm[16].

While gold nanorods were prepared, the presence of 4 distinct shapes of nanoparticles (high and low aspect nanorods, spherical nanoparticles and nanotriangles) shows the difficulty in selectively synthesizing anisotropic nanoparticles. Despite every effort being made in terms of glassware being extensively cleaned using aqua regia to prevent any unwanted seeding of nanoparticles, as well as precise adherence to all reagent concentrations and quantities, a monodisperse sample of nanorods was still not achieved. Due to this, these nanoparticles were not further utilised in the synthesis of multimodal AuAg nanowire composites.

4.3.4 Gold Nanostars

The preparation of gold nanostars was carried out in two stages - the preparation of silver seeds and the subsequent anisotropic gold growth using the silver seeds as nucleation points. These will each be discussed in turn below.

Silver Seed Synthesis

Silver seeds act as nucleation sites for anisotropic gold growth in the synthesis of the gold nanostars. While the exact mechanism of how this occurs is disputed, it has been postulated that the silver undergoes galvanic replacement by the gold salts in the gold nanostar formation step, resulting in anisotropic growth. Smaller and more monodisperse silver seeds are obtained through cooling the reducing agent, sodium borohydride to 0 °C. This slows down the reaction such that the growth will be slower, allowing for smaller and more monodisperse seeds. The seeds from this synthesis were approximately 10 nm in diameter. The initial protocol described by Kereselidze *et al.* recommends that the silver seeds are used within several days of the initial synthesis[17]. The growth and morphology of the silver seeds were studied over a more extended time period.

UV-Vis spectroscopy was used to monitor any changes in the spectra of the silver seeds over and outside the recommended time frame. Firstly, the spectra of the seeds at 4 days and 10 days were compared (Figure 4.13). Samples that had been aged for under 10 days have an absorption peak at 390 nm, as well as a shoulder at 425 nm. This is in agreement with the literature that states that 10 nm silver seeds will absorb at 400 nm, and a blue shift in the UV-Vis spectra is indicative of a decrease in size[18]. The shoulder in these spectra could be indicative of two different size populations of nanoparticles, or possibly an indication of anisotropic growth.

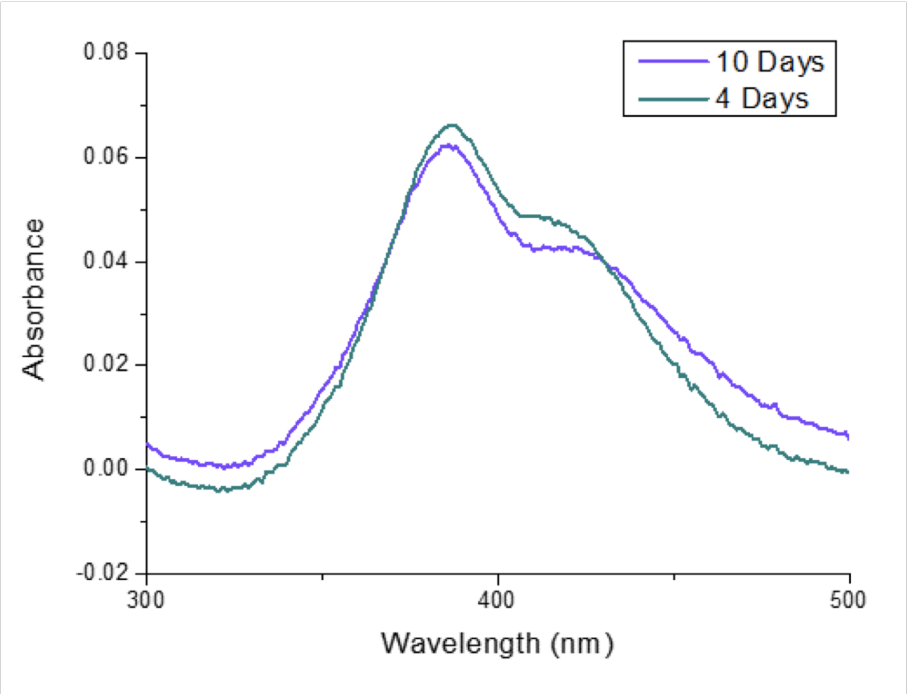

Figure 4.13: UV-Vis spectra comparing the silver seeds at 4 and 10 days post-synthesis.

The growth of the silver seeds over an extended time period was also investigated, as illustrated in Figure 4.14. The spectra for the seeds aged over approximately one month are distinctly different to those aged for under 10 days. As can be seen in Figure 4.14, the seeds aged for 16 days are quite similar to those aged for 10 days and under - they have a peak around 400 nm and a shoulder at 430 nm. However, the seeds aged for 36, 37 and 38 days show a significant red shift, which is an indication that these nanoparticles have increased in size. This is as expected, as over time Ostwald ripening would occur.

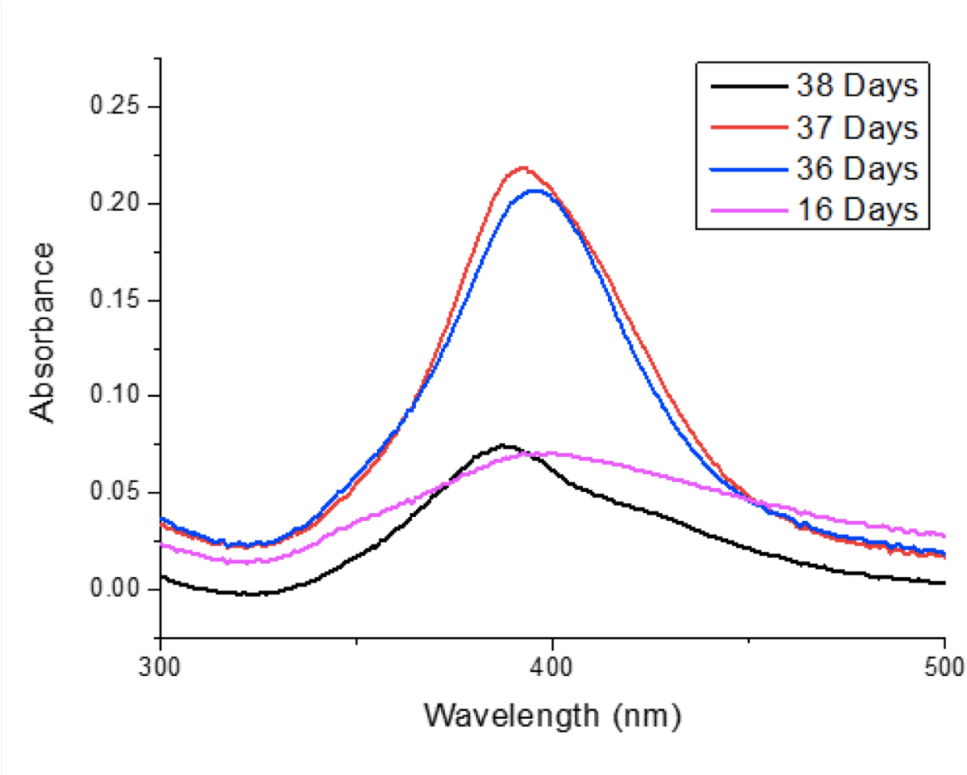

Figure 4.14: UV-Vis spectra comparing the silver seed spectra over extended ageing periods.

TEM analysis was also carried out to investigate the size, morphology and monodispersity of the silver seeds over the time period described above. Silver seeds that had been allowed to age for 7 days are shown in Figure 4.15 (A) and (B); and seeds that had been allowed to age for 38 days are shown in Figure 4.15 (C) and (D). In (A) it can be seen that the nanoparticles that have been aged for a shorter period of time are smaller, which is as expected. In (B) we can see that some small clusters of the nanoseeds have fused together to form small nanowire structures. This offers an explanation for the shoulder observed in the UV-Vis spectrum for these seeds.

The 38 day old silver seeds were larger than those aged for a week, which again is to be expected. The seeds aged for 38 days have an average diameter of 12.4 $\pm$ 3.2 nm; while those aged for 7 days have an average diameter of 10.3 $\pm$ 4.2 nm (n=*100*). These silver seeds were then further used in the synthesis of the gold nanostars.

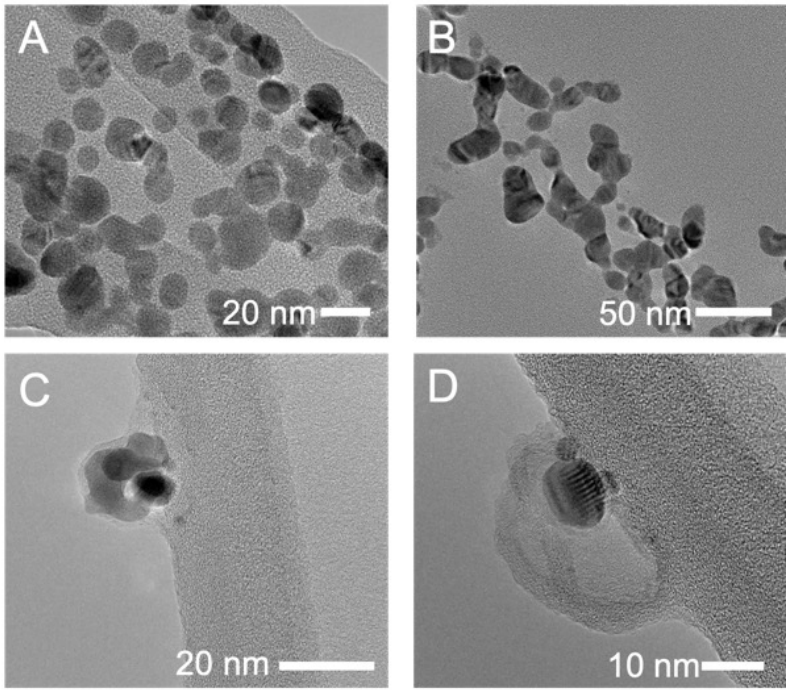

Figure 4.15: TEM images of the silver seeds after ageing for (A) and (B) 7 days and (C) and (D) 38 days.

Gold Nanostar Synthesis

The preparation of a stable, monodisperse solution of gold nanostars is a difficult procedure that is affected by many factors including time, light, temperature, stirring speed, capping agent and gold salt concentration. The growth of anisotropic gold nanostructures relies heavily on the concentration of the reagents and the precise time at which they are added, as it is the kinetic product that we aim to isolate.

In this work, the synthesis of gold nanostars was attempted using a number of different silver seed samples that had been aged for different amounts of time, and also for two different relative CTAB concentrations. It was found that the colour of the resulting nanostar solution depended heavily on the age of the silver seeds used. This is illustrated in the UV-Vis analysis in Figure 4.16. In each case, the broad absorption peaks would indicate that nanostars have not been formed, and

that instead we have a polydisperse sample. The absorbance peaks also appear at wavelengths longer than would be expected for spherical gold nanoparticles, which would suggest that larger aggregates or asymmetrically shaped, larger nanoparticles had been formed.

Ag Seed Age	Sample Colour	Absorption Max (nm)
2 hours	Brown-purple	509
1 day	Brown	460
2 days	Brown-purple	501
3 days	Dark purple	562
4 days	Brown-purple	511
5 days	Brown	494
6 days	Dark purple	518
7 days	Purple	653
8 days	Purple	546
9 days	Dark blue	580
10 days	Purple	548
23 days	Brown	481
25 days	Purple	548
26 days	Brown	493

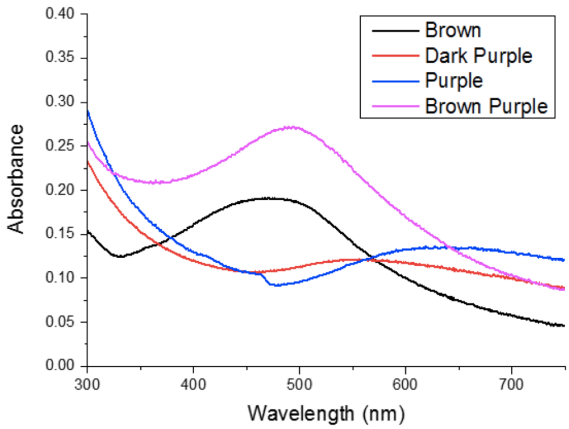

Figure 4.16: A table showing the silver seed ageing time, sample colour and absorption max for each sample alongside a UV-Vis spectrum for each colour solution obtained.

Reported UV-Vis spectra of gold nanostars have three peaks - a main absorbance band between 600 - 740 nm, and two shoulders at 530 - 570 nm and 800 - 1000 nm. A sample TEM image and UV-Vis spectrum taken from Sau *et al.* shows the gold nanostars and the corresponding spectrum[18] (Figure 4.17).

SEM and TEM analysis were carried out on the synthesised nanoparticles and a selection of these images are shown in Figure 4.18. There did not appear to be any correlation between the colour/peak of the UV-Vis spectrum and the synthesised microparticles. There also appears to be no correlation between seed age and the structure formed. In each case, large aggregates were formed with a variety of different shapes. This shows that any anisotropic growth is uncontrolled and unspecific.

The synthetic approach for these nanostars was then modified through alteration of the amount of silver nitrate added in the gold growth step. In the first syntheses

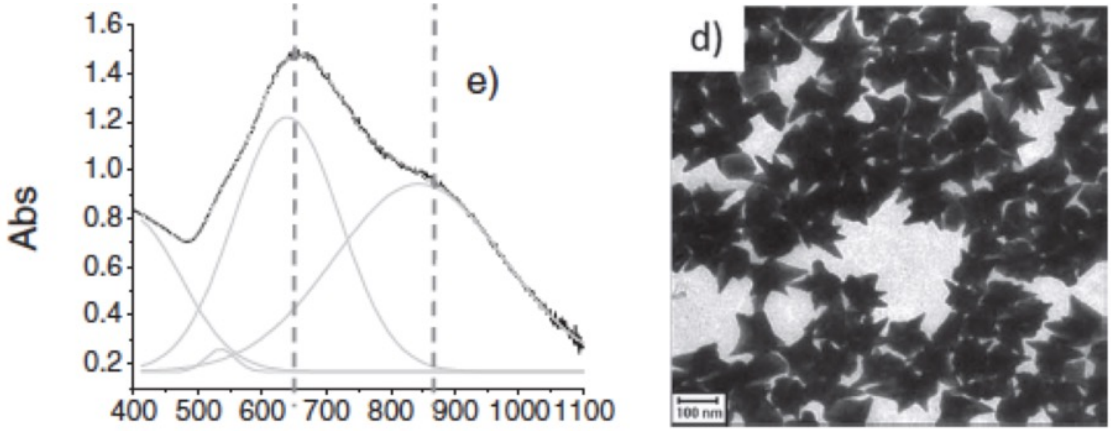

Figure 4.17: UV-Vis spectrum corresponding to the nanostars in the adjacent TEM image. Taken from article by Sau *et al*[18].

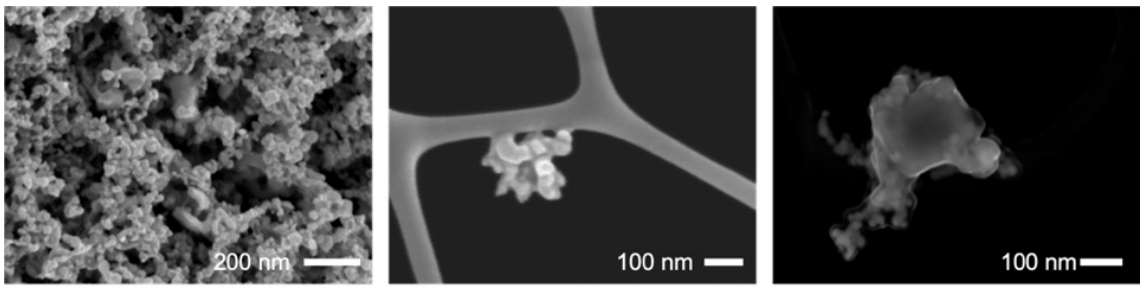

Figure 4.18: SEM and TEM images showing nanostructures prepared using silver seeds and the the lower relative CTAB concentration.

described above, 1 mmol CTAB and 1 mM $AgNO_3$ were used - in the second synthesis, only 0.01 mM $AgNO_3$ was used, meaning that the relative concentration of CTAB was much higher. The higher CTAB concentration should serve to promote more anisotropic growth and prevent aggregation. For this procedure, it is worth noting that all silver seeds used were under seven days aged. The nanostar solution in each case was red-brown in colour, in contrast to the purple, brown and blue solutions that were obtained in the first approach. UV-Vis analysis for the second approach show a more complex spectrum, more similar to that described by Sau *et al.* Instead of a simple broad absorption spectrum, a main absorption band was obtained at 690 nm, with a shoulder in the region of 950 nm. Shown in Figure 4.19 is the absorption spectrum for the nanostars at 0 and 24 hours ageing.

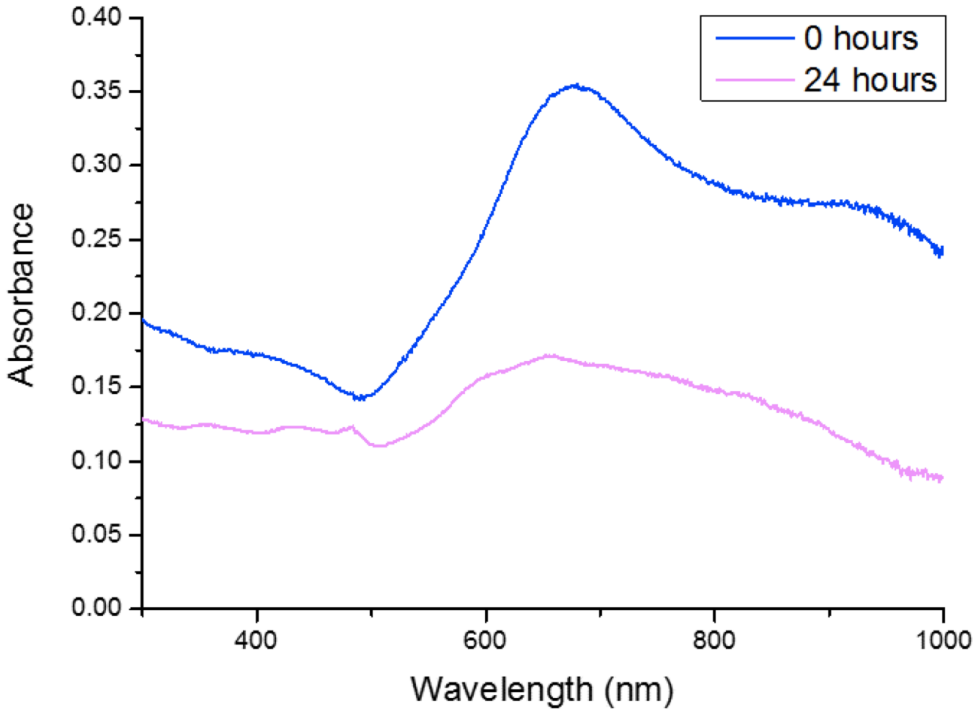

Figure 4.19: UV-Vis spectra of nanostars synthesised with a higher CTAB concentration, taken immediately after synthesis and then after 24 hours ageing.

SEM analysis was also carried out (Figure 4.20). This confirmed the presence of gold nanostars, among other anisotropic structures. The nanostars are in the region of 200 nm in diameter, with the core ranging in size between 50 - 80 nm and the core to tip distance ranging between 100 - 170 nm. This varies across the sample, and the concentration of nanostars in the solution is quite low. The sample is significantly more monodisperse than the sample prepared with the relative lower concentration of CTAB, however, as the size of the nanostars is near to the lower resolution limit of the SEM, it is difficult to discern how monodisperse the sample truly is. The SEM analysis does show however that all of the gold does have some degree of anisotropic growth. It also appears, particularly in the image on the right, that the nanostars have formed through a number of smaller nanoparticles fusing together. This supports the self-assembly theory for nanostar formation proposed by Zhou *et*

al.[19]. This could aid in the optimisation of any further syntheses for future work. It is also thought that further optimisation of this work would also involve the synthesis of smaller silver seeds, as this would allow the formation of more spiky nanostars.

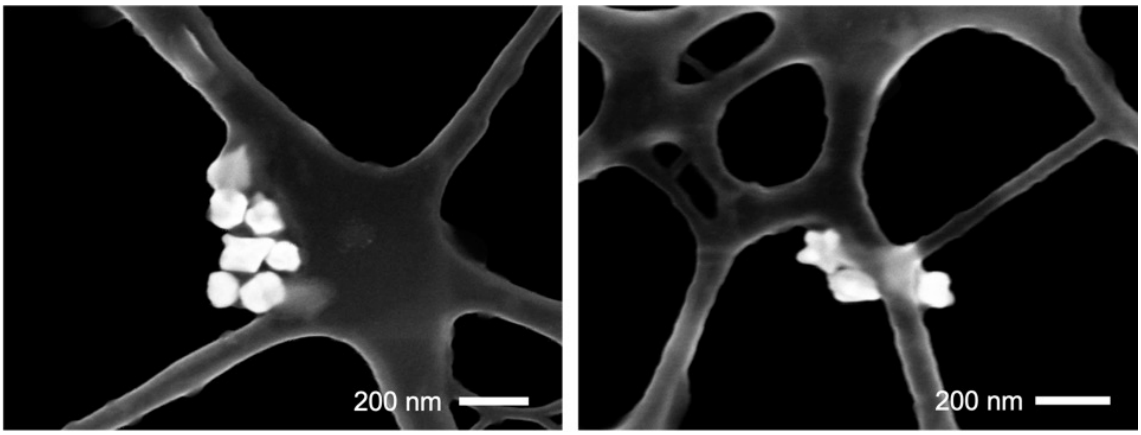

Figure 4.20: SEM images of the gold nanostar solution.

TEM analysis of the nanostars was also carried out (Figure 4.21). This provides a clearer picture of the morphology and monodispersity of the nanostars. As can be seen in the TEM images, while the structures are all anisotropic and roughly the same size, the sample is quite polydisperse. There is a huge amount of variation between each nanostar structure, with spikes varying in both size and length across the sample.

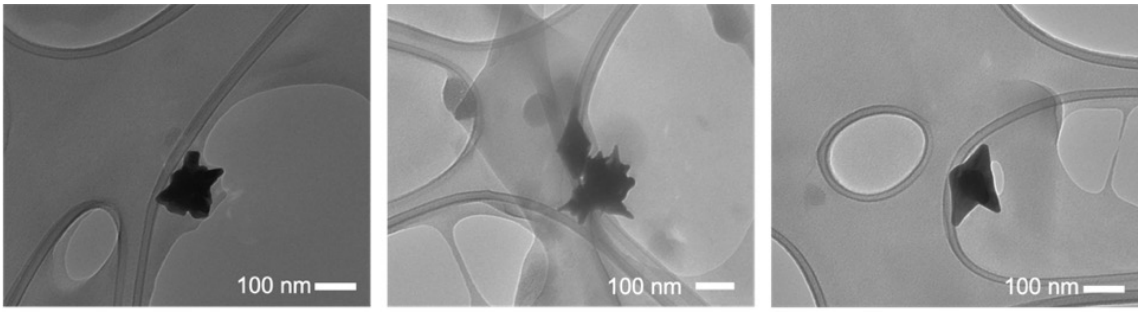

Figure 4.21: TEM images of the nanostars showing polydispersity.

Gold anisotropic nanostar structures were synthesised using a silver seed mediated approach, resulting in a sample with a high degree of polydispersity. Although

nanostars were synthesised, as they lack any uniformity it was decided that they would not be used in further experiments with AuAg nanowires. The optimisation of these nanostar structures will be performed in future work.

4.3.5 Composite Nanowire Structures

The AuAg nanowires used in this work were synthesised in-house by Dr. Daniel Kehoe. They were prepared via a well-documented modified polyol approach[10]. Briefly, $AgNO_3$ is reduced in an ethylene glycol solution at 130 ^{0}C for 60 minutes in the presence of $FeCl_3$ and polyvinylpyrrolidone (PVP). The resulting ultra-long nanowires were characterised by UV-Vis spectroscopy and SEM (Figure 4.22). SEM images show a high concentration of ultra-long nanowires. Size distribution analysis was carried out on these nanowires and their average diameter was found to be 83.4 nm and they have lengths of up to several microns. The UV-Vis spectrum shows the expected absorbance profile for this material, with peaks at 400 nm and 350 nm, which correspond to the transverse plasmon peak and the bulk silver peak[20]. The longitudinal plasmon peak for the nanowires is missing due to the very high aspect ratio of the structures.

Magnetite-Nanowire Composite Structures

Three different concentrations of the previously prepared PAH-stabilised magnetite nanoparticles were added to the silver nanowire solution in order to prepare a magnetic-plasmonic nanocomposite. Briefly, three concentrations were prepared using a serial dilution method. First, 2 mg of the dried magnetite powder was dispersed in 10 mL of MP water. Using this stock solution, three concentrations were prepared for testing with the nanowires - 20 % (v/v), 2 % (v/v) and 0.2 % (v/v). For each (v/v) concentration, two samples were prepared. This is to examine any differences

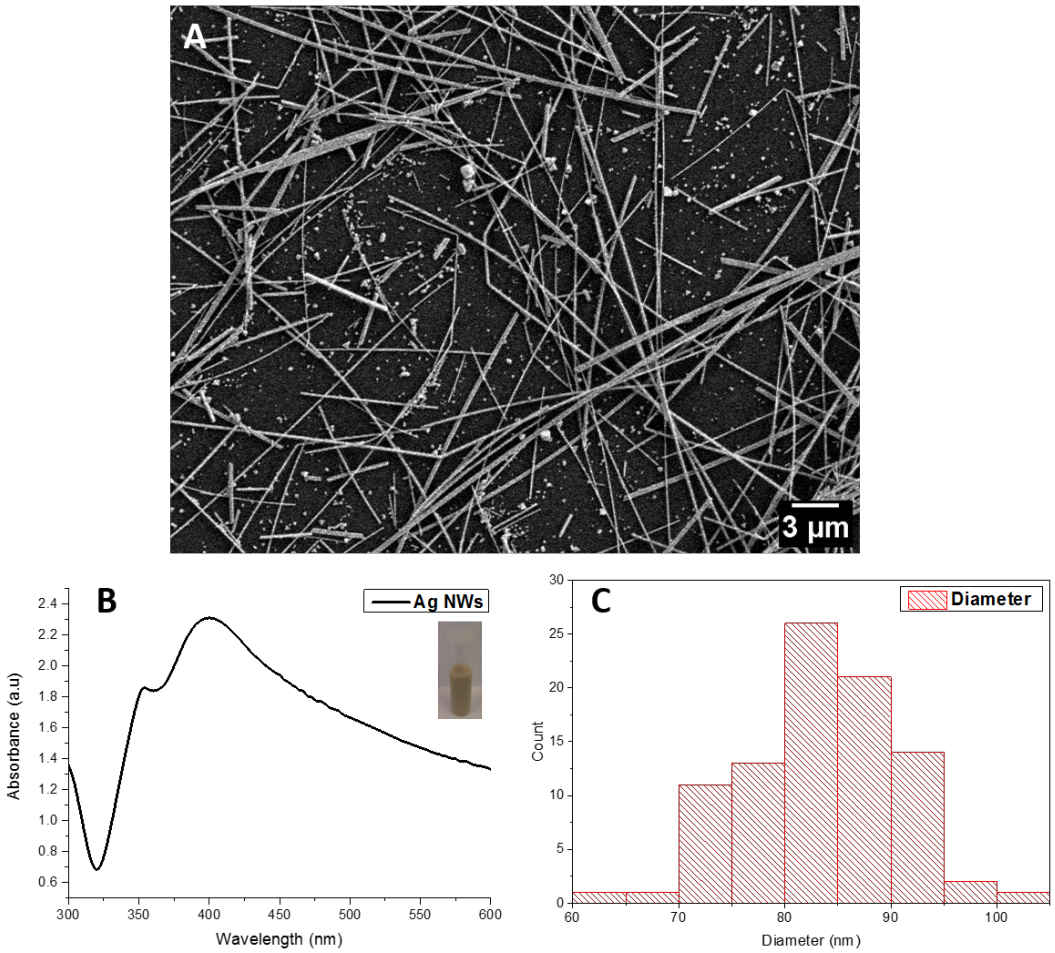

Figure 4.22: (A) SEM images showing the AuAg nanowires, (B) UV-Vis spectrum of the nanowires with an image of the solution inset, (C) A size distribution showing the diameter of the nanowires.

that arise as a result of the sample being stirred. The first sample was stirred for 5 minutes before being put into the fridge at 4 °C, while the other sample was allowed to stay at room temperature for 5 minutes before also being put into the fridge. Previous work in the group has shown that vortexing achiral nanowire structures induced chiroptical activity in the structure[21]. These tests were carried out to determine whether the formation of the nanowire composites would demonstrate any helical formations in the stirred sample versus the non-stirred sample.

SEM analysis was initially carried out on all concentrations, for both stirred and non-stirred samples, at three intervals - namely at 2, 5 and 8 days, in an attempt

to monitor the formation of the nanocomposite, as well as to determine whether or not stirring made any discernible difference to the solution. The first point of note for these solutions is that there was no observable difference between the stirred and non-stirred samples. In addition to this, the lowest concentration of magnetite (0.2 % (v/v)) was the only magnetite solution to produce meaningful results, while the higher concentrations had large clusters that did not interact with the wires, and in some cases completely obscured them.

SEM images of the 0.2 % (v/v) solution of magnetite are shown in Figure 4.23. At two days aggregation of the magnetite around the nanowire structures can be seen. While a large proportion of the magnetite does seem to be around the nanowires, there is still a significant amount of magnetite on the TEM grid that doesn't appear in any way bound to the nanowires and there does not appear to be any order to the manner in which the magnetite coats the nanowires. The nanowires and magnetite also appear to be in clusters; as the samples are taken directly from solution and dropped onto TEM grids without any further modification it is impossible to tell whether this is a drying effect or whether this is the case in the nanowire solution.

The solutions appear very similar at 5 days. In the second image shown, it appears that the magnetite has completely obscured the nanowire, suggesting not only that more of the magnetite had migrated to the surface of the nanowire, but that even a 0.2 % (v/v) magnetite concentration may still be too high.

At 8 days we see an even coating of the magnetite on the nanowires. This suggests that 8 days is a sufficient time frame over which the nanocomposites can self-assemble. It is unclear why the excess magnetite seen in the SEM images from earlier days is not seen, but perhaps the larger magnetite clusters, or the nanowires with a very high concentration of magnetite coordinated to them may have fallen out of solution, leaving only those nanowires with a lower concentration of magnetite still suspended. This could be due to the presence of clusters of nanowires in solution as shown in the SEM images from Day 5. These clusters would have a higher

relative charge density than the individual PVP-coated nanowires and would thus attract the magnetite across a steeper potential gradient. This would then lead to large and heavy magnetite-nanowire composite structures which would likely then fall out of solution.

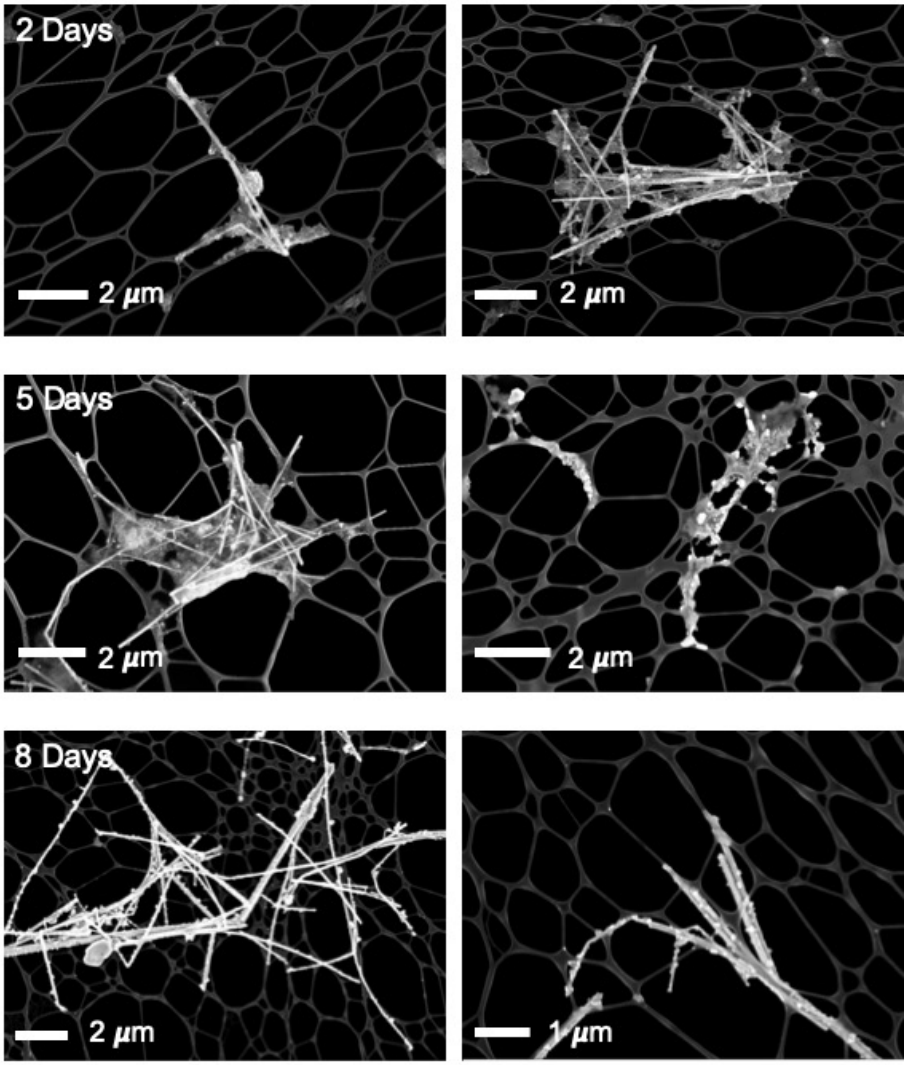

Figure 4.23: SEM images of the 0.2 % (v/v) magnetite AuAg nanowire composite structures.

UV-Vis spectroscopic analysis was also carried out at 2, 5 and 8 days to monitor any changes that occur during the formation of the nanocomposites. These can be seen for each concentration of magnetite used (20, 2 and 0.2 % (v/v) respectively) as shown in Figure 4.24.

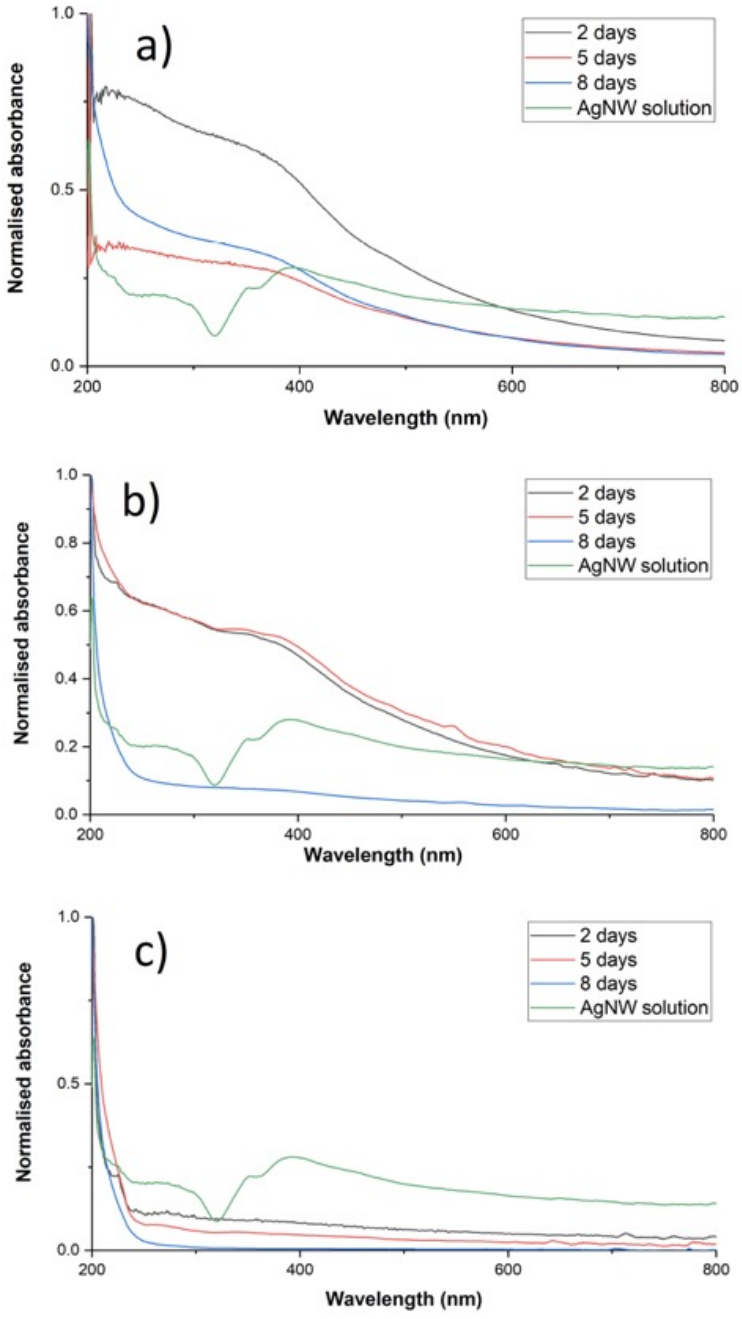

Figure 4.24: UV-Vis spectra of 3 of the nanocomposite samples showing the spectra at 2, 5 and 8 days for each concentration of magnetite (a) 20, (b) 2 and (c) 0.2 % (v/v).

In each case, it is evident that as the time increases, the plasmon peak of the nanowires at 400 nm diminishes in intensity. This indicates that the magnetite is

coating the nanowires. As the concentration of magnetite is increased it will mask the plasmonic response of the nanowires. For this reason, lower concentrations of magnetite are preferred for this nanocomposite, as ideally a balance will be reached by which there will be enough magnetite on the nanowires to endow them with magnetic functionality, but still not enough to completely obscure the plasmon peak of the nanowires. This is evidenced by the fact that the sample with the lowest concentration of magnetite (0.2 % (v/v)) here still has a plasmon peak visible after 5 days.

A more detailed SEM time study was carried out for the lowest concentration of magnetite over a time period of ten days, with a sample being taken every 24 hours. The results of this can be seen in Figures 4.25 - 4.35. At days 1, 2, 3 and 4, clusters of magnetite can be observed closer to the nanowire itself, and in the instance of day 4 (Figure 4.29) the nanowire appears to be embedded into the magnetite cluster. At days 5 - 7, smaller quantities of magnetite nanoparticles can be seen coating the nanowires, however, smaller magnetite clusters remain in solution unbound to any nanowires. Days 8 through 10 show nanowires coated with magnetite, however, in each case there does still appear to be magnetite nanoparticle clusters in solution. Further work will be required in order to optimise this system such that all added magnetite can be used to coat the nanowires, which could then be magnetically separated from solution.

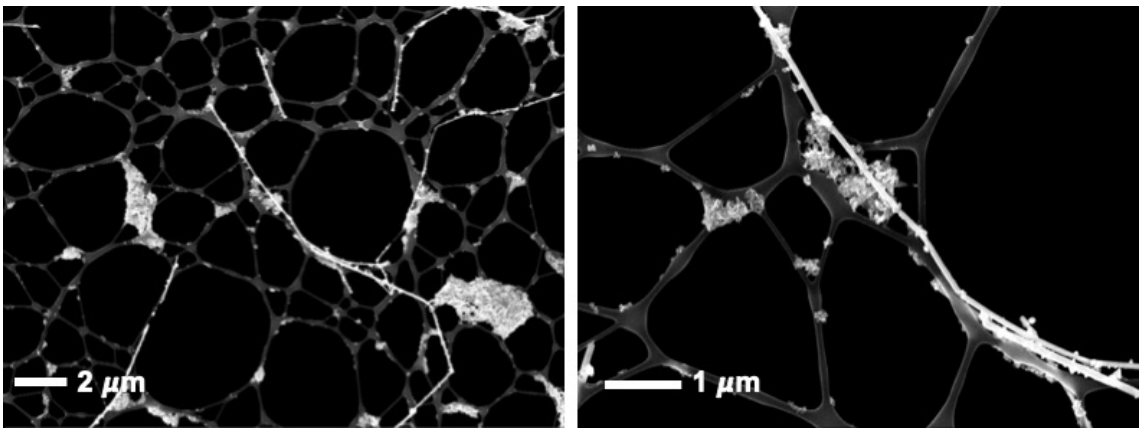

Figure 4.25: SEM images of magnetite NPs and Nanowires Day 0.

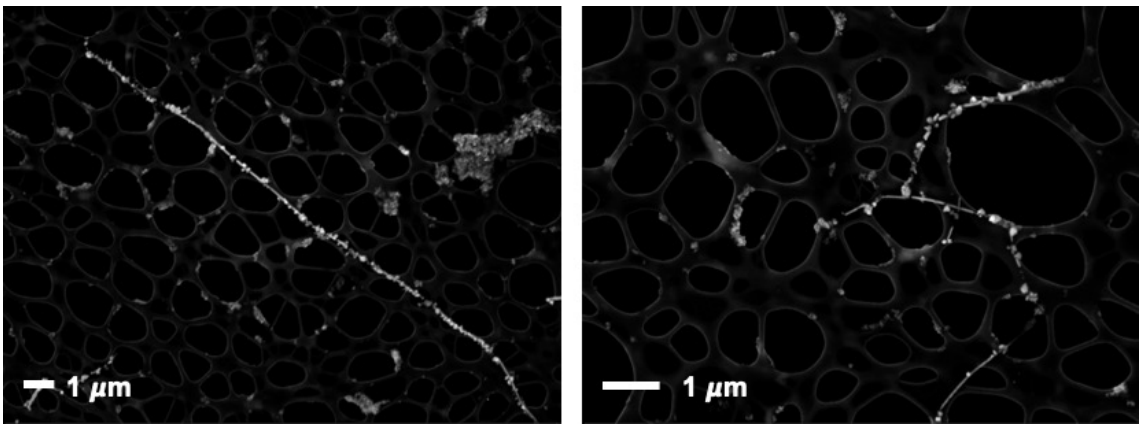

Figure 4.26: SEM images of magnetite NPs and Nanowires Day 1.

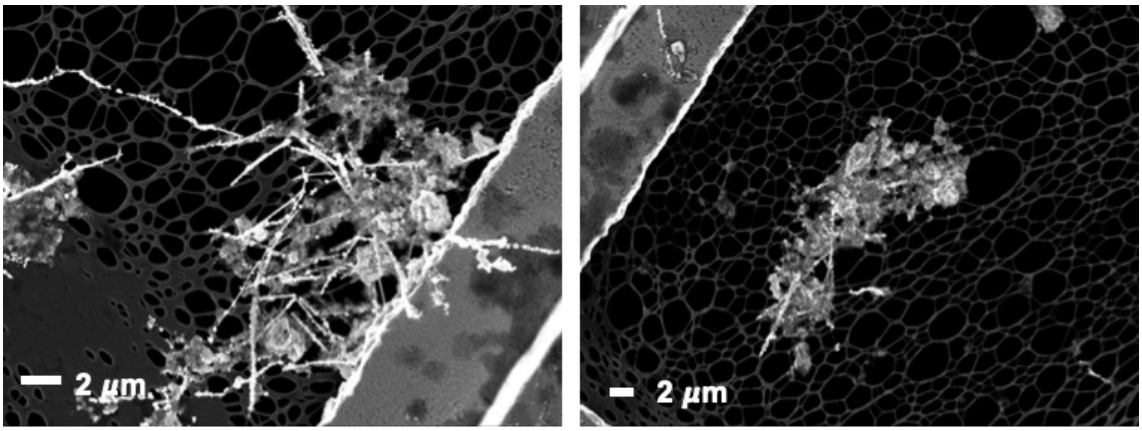

Figure 4.27: SEM images of magnetite NPs and Nanowires Day 2.

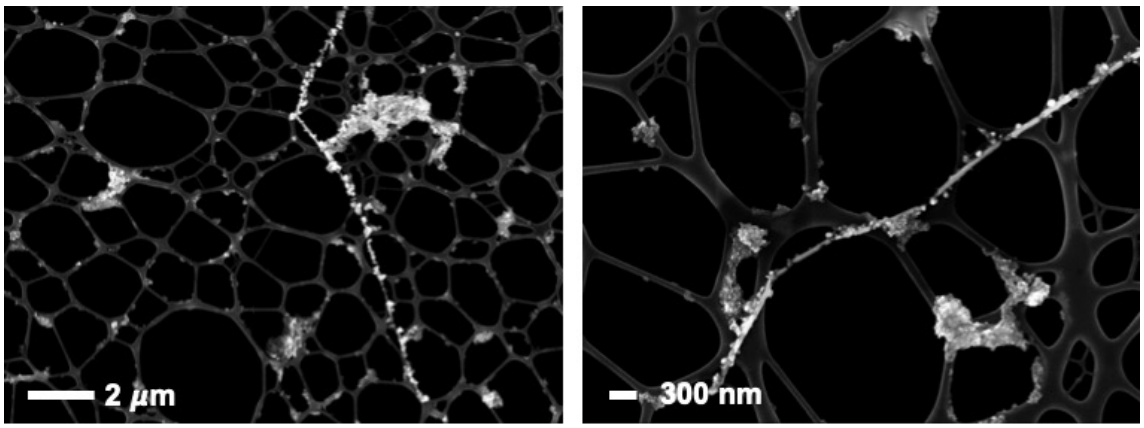

Figure 4.28: SEM images of magnetite NPs and Nanowires Day 3.

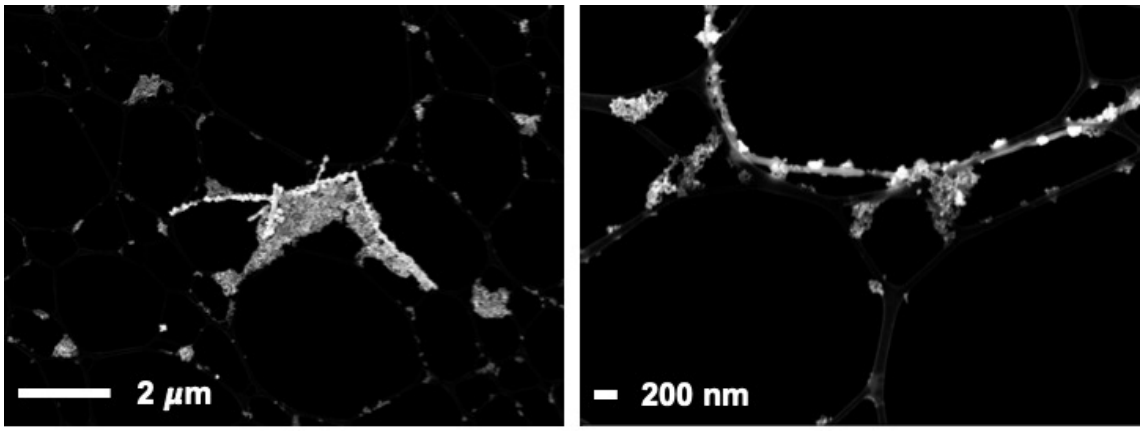

Figure 4.29: SEM images of magnetite NPs and Nanowires Day 4.

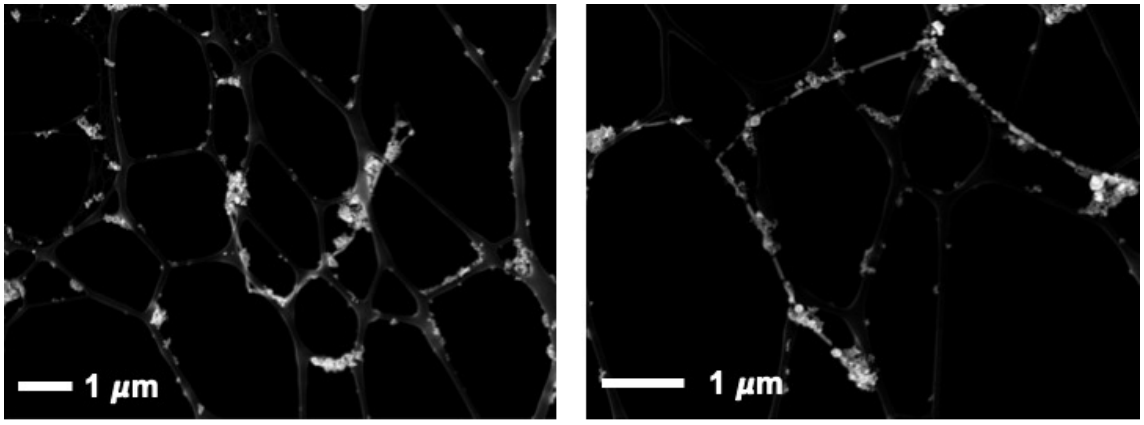

Figure 4.30: SEM images of magnetite NPs and Nanowires Day 5.

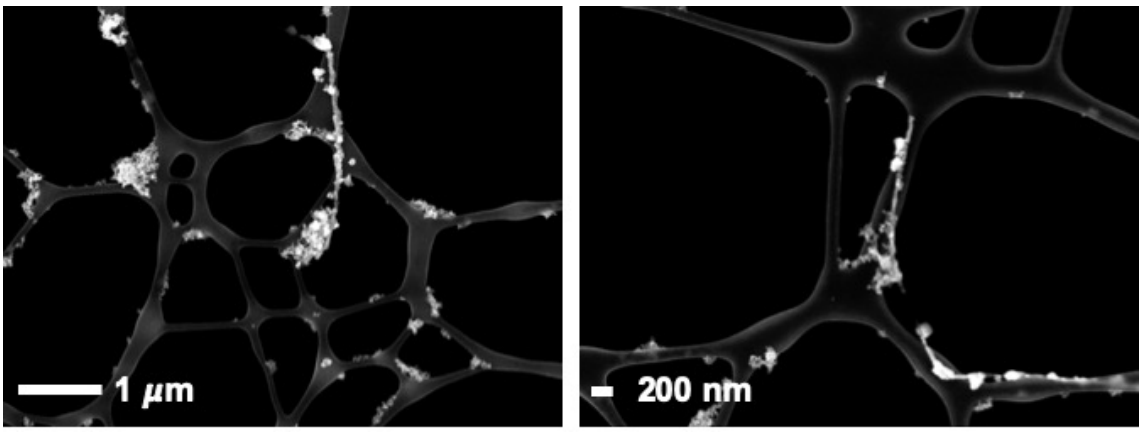

Figure 4.31: SEM images of magnetite NPs and Nanowires Day 6.

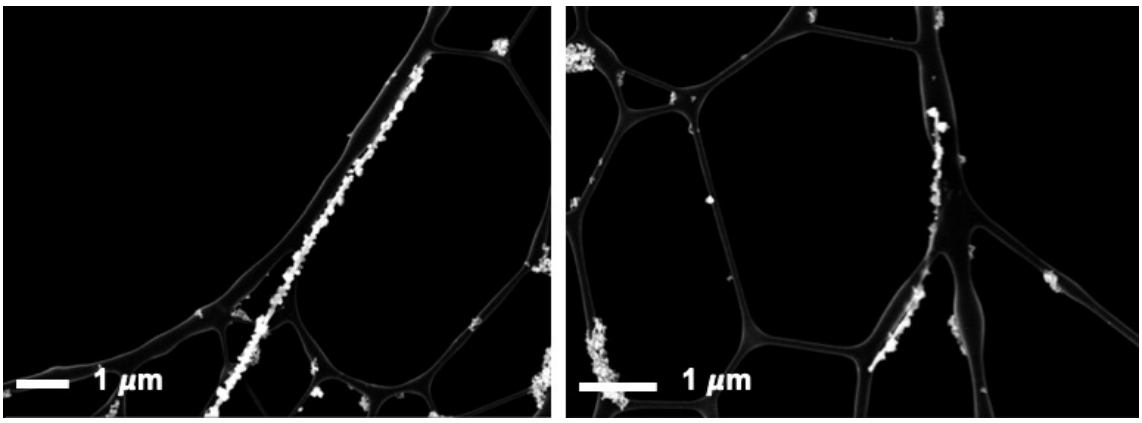

Figure 4.32: SEM images of magnetite NPs and Nanowires Day 7.

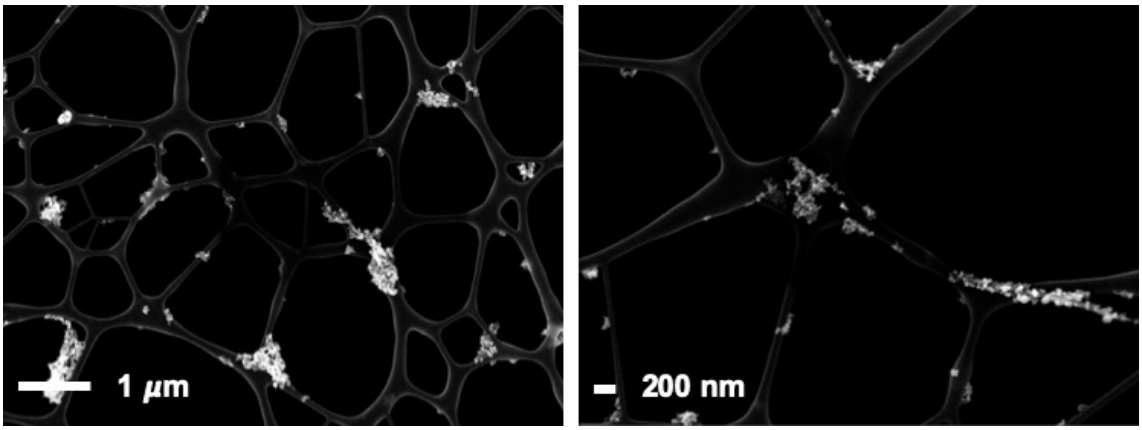

Figure 4.33: SEM images of magnetite NPs and Nanowires Day 8.

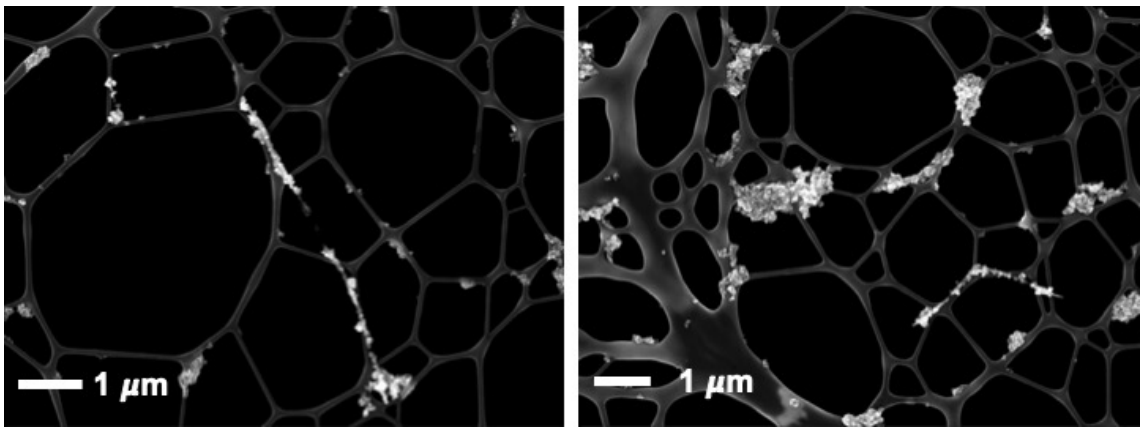

Figure 4.34: SEM images of magnetite NPs and Nanowires Day 9.

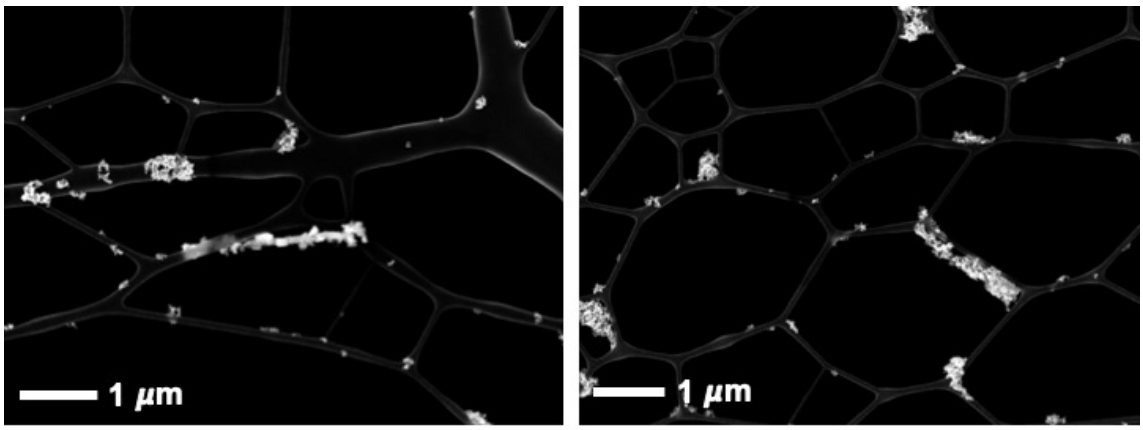

Figure 4.35: SEM images of magnetite NPs and Nanowires Day 10.

EDX analysis was also carried out on a sample of the magnetite nanoparticle/AuAg nanowire composites in order to confirm the presence of magnetite in the sample as shown in Figure 4.36. Silver and gold can be seen throughout the nanowire structure itself, whereas magnetite is shown throughout the sample, not just on the nanowire structure. This is indicative that the magnetite has only partially bound to the nanowire. These images were taken using the day 2 study of magnetite and AuAg nanowires.

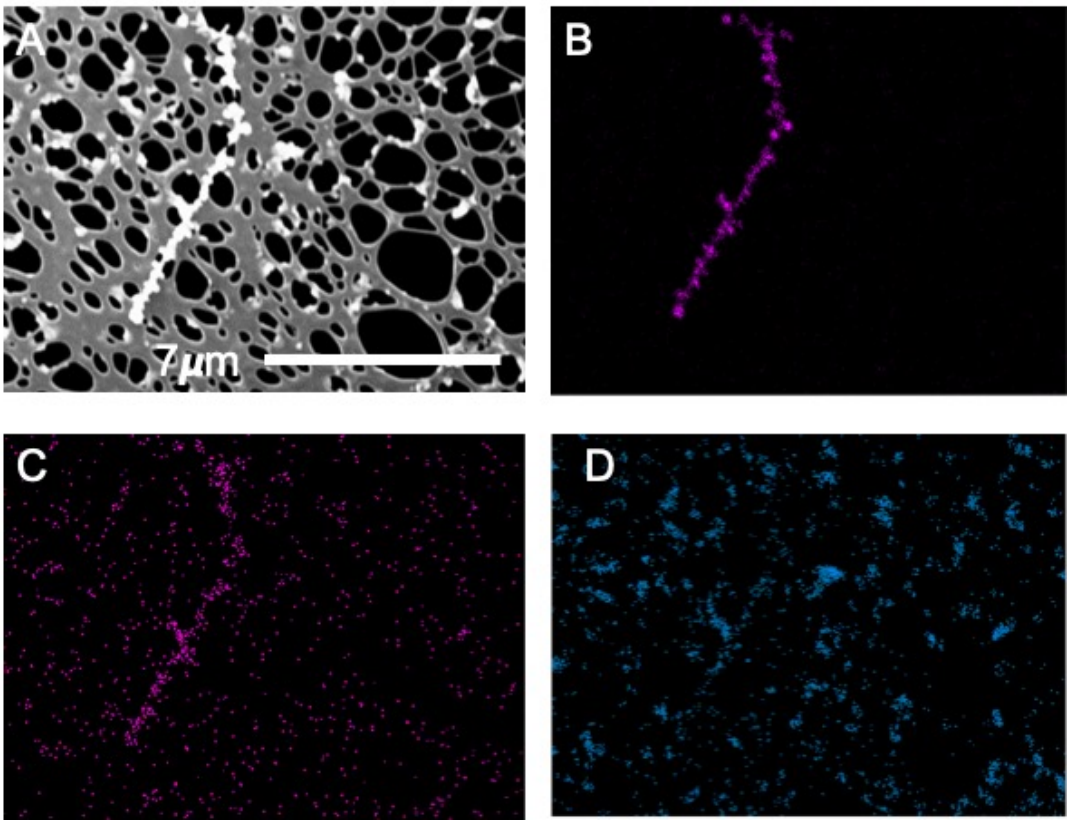

Figure 4.36: EDX analysis of a magnetite nanoparticle AuAg nanowire solution where (A) is the SEM image, (B) shows the Ag map, (C) shows the Au map and (D) shows the Fe map.

Gold-Nanowire Composite Structures

The gold nanoparticles synthesised were stabilised in PAH, which, as mentioned, is a positively charged polyelectrolyte, in order to endow the nanoparticles with a positive surface charge. Thus, the nanoparticles require no further modification in order to interact electrostatically with the negatively-charged PVP-coated AuAg nanowires. Similar to the magnetite, three different concentrations of gold stock solutions were prepared and added to a 10 % (v/v) solution of the nanowires. A serial dilution approach was utilised in order to determine the correct concentration of gold nanoparticles. Using a stock solution of PAH-stabilised gold nanoparticles, three diluted solutions were made to be tested with the nanowires - 20 % (v/v), 2 % (v/v) and 0.2 % (v/v).

For each concentration of the gold nanoparticle/AuAg nanowire composites, two solutions were prepared; one was stirred and one was not stirred and both were then placed into a fridge at 4 °C for 8 days. Aliquots were taken for SEM and UV-Vis analysis at 2, 5 and 8 days to monitor the time-dependence of the gold coating of the nanowires.

As with magnetite it was found that there was no discernible difference between the two samples. The most successful sample was the 2 % (v/v) solution. It appears that the formation of the nanocomposites was considerably faster for the gold nanocomposite formation. Representative images are shown in Figure 4.37.

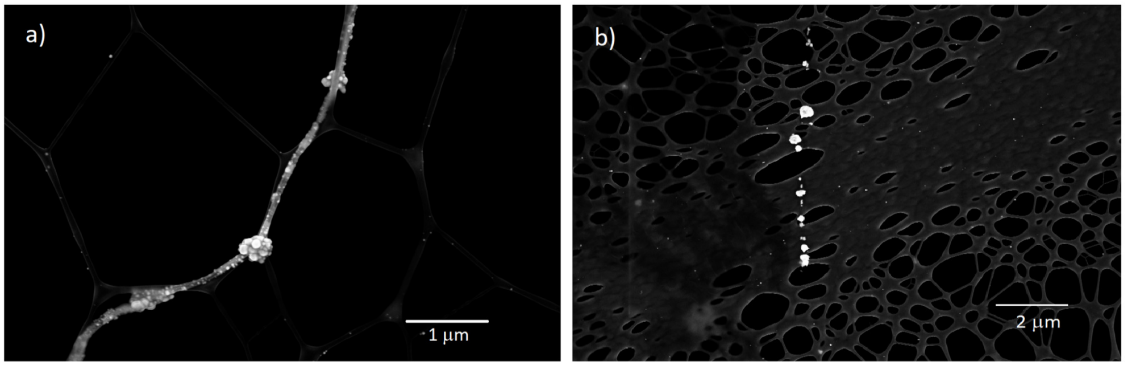

Figure 4.37: SEM images of (a) 2 % (v/v) PAH-stabilised gold nanoparticle-AuAg nanowire composite structure after 2 days and (b) the AuAg nanoparticles resulting from the galvanic replacement of Ag by excess Au^{3+}.

After 2 days, the nanowires seemed to be uniformly coated with gold. However, one issue found with the formation of the gold nanoparticle-nanowire composites was that the nanowires degraded into nanoparticles over time. This is likely due to the presence of excess Au^{3+} ions in solution. As gold has a higher reduction potential than silver, the gold will be reduced and dissolve the silver resulting in galvanic replacement. This likely means that the large nanoparticles formed are AuAg nanoparticles. This can be seen in Figure 4.37 (b). This may be remedied by a number of extra cleaning steps with methanol in order to remove any excess Au^{3+} in solution.

A UV-Vis time-study was carried out in tandem to the SEM study in order to determine any spectroscopic changes over time as shown in Figure 4.38. After 8 days, for each initial concentration of PAH-stabilised gold nanoparticles used, the plasmon peaks for both the silver nanowires and the gold nanoparticles are both visible.

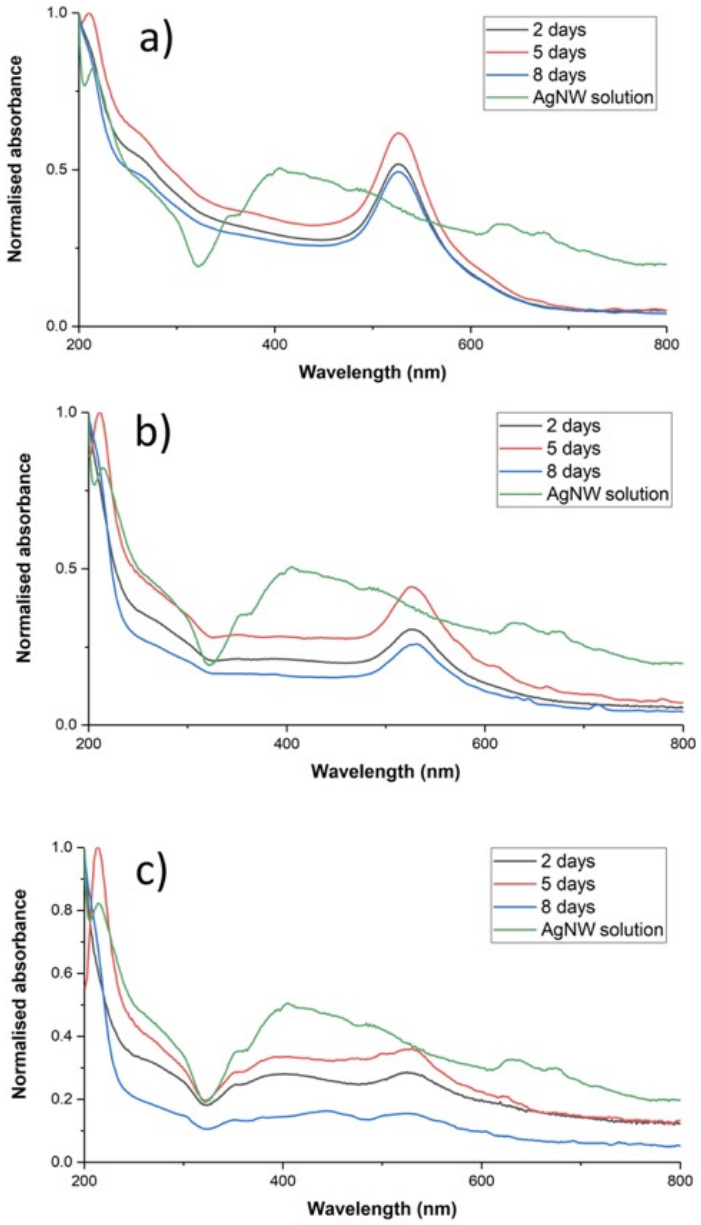

Figure 4.38: UV-Vis spectra of the gold nanoparticle-silver nanowire composite structures after 2, 5 and 8 days at (a) 20, (b) 2 and (c) 0.2 % (v/v).

A more detailed time-study using SEM was also carried out to investigate the forma-

tion of the gold nanoparticle - AuAg nanowire composites in more detail (Figures 4.39 - 4.49). From Day 0, immediately there is a visible interaction of the gold nanoparticles with the AuAg nanowires, and at days 2 and 3 a high concentration of nanoparticles are visible on the nanowire structures. Between days 4 and 7 an even coating of gold nanoparticles can be seen on the nanowire, as well as gold nanoparticles that are unbound to the nanowire along the SEM grid. As the nanowire is not evenly coated, this could suggest that there is repulsion between the gold nanoparticles and also that the electrostatic interaction between the PVP on the nanowires and the PAH on the nanoparticles is insufficient to cause a higher binding concentration of gold nanoparticles at the surface. From day 1 onwards the nanowires can be seen to degrade, and it is suspected that the large microparticles visible on Day 10 are composed of the gold and silver from the nanowires. This could be due to excess Au^{3+} in the gold nanoparticle solution causing etching of the nanowires themselves, or could also be due to poor long term stability of the nanowires themselves.

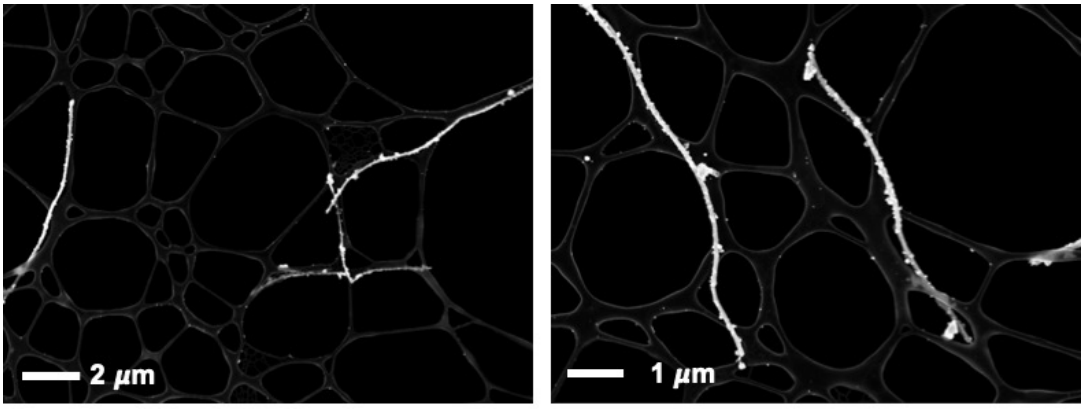

Figure 4.39: SEM images of the gold nanoparticle AuAg nanowire composite on Day 0.

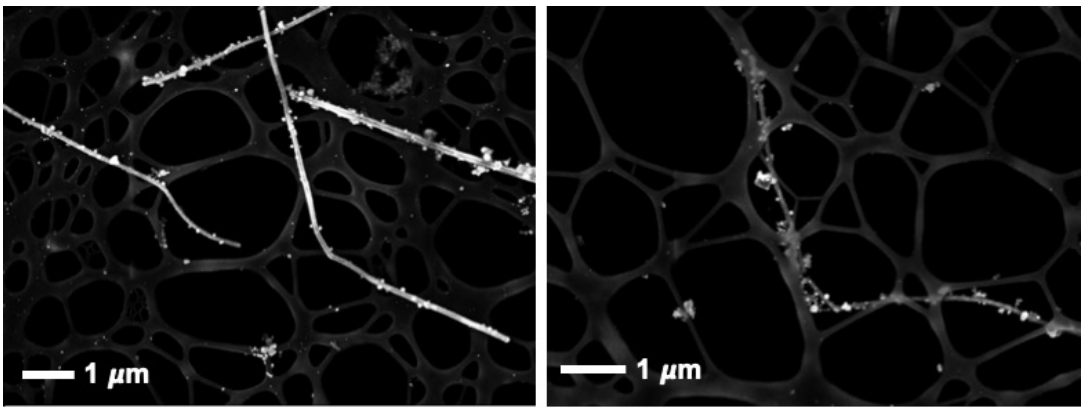

Figure 4.40: SEM images of the gold nanoparticle AuAg nanowire composite on Day 1.

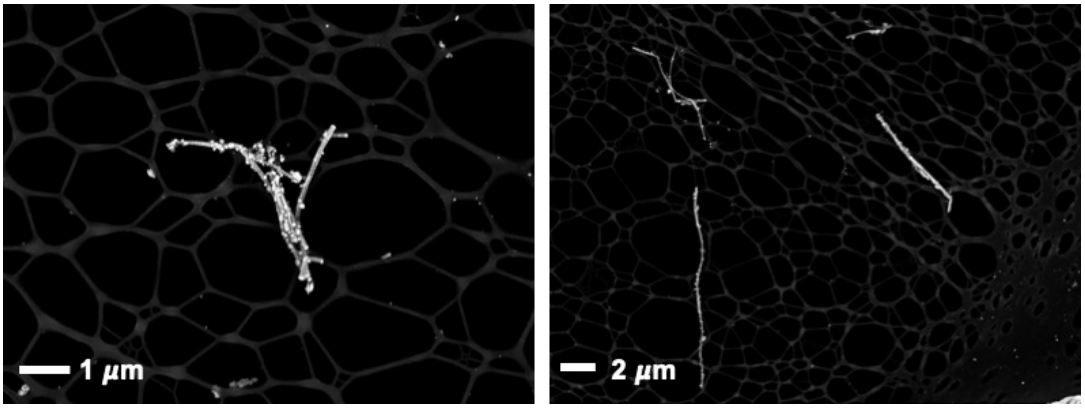

Figure 4.41: SEM images of the gold nanoparticle AuAg nanowire composite on Day 2.

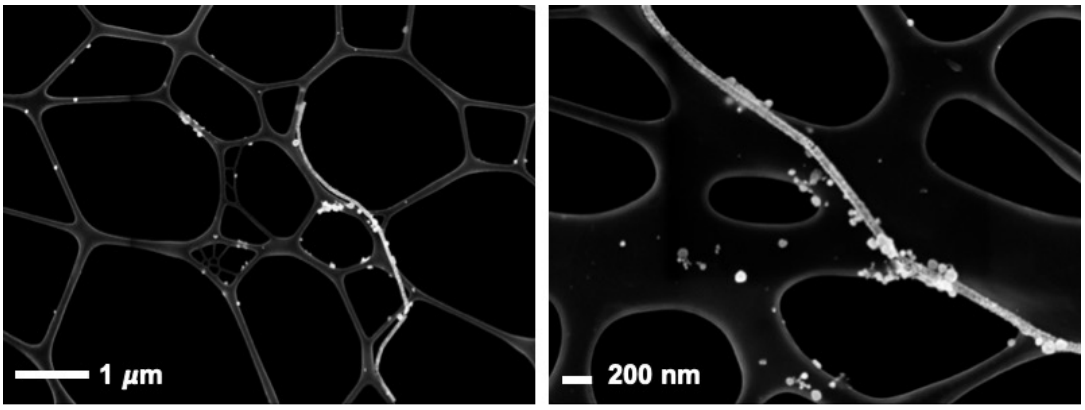

Figure 4.42: SEM images of the gold nanoparticle AuAg nanowire composite on Day 3.

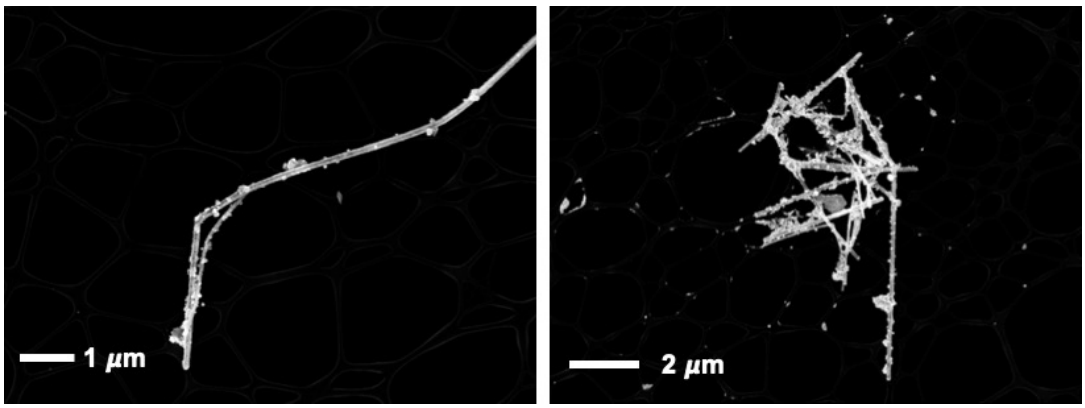

Figure 4.43: SEM images of the gold nanoparticle AuAg nanowire composite on Day 4.

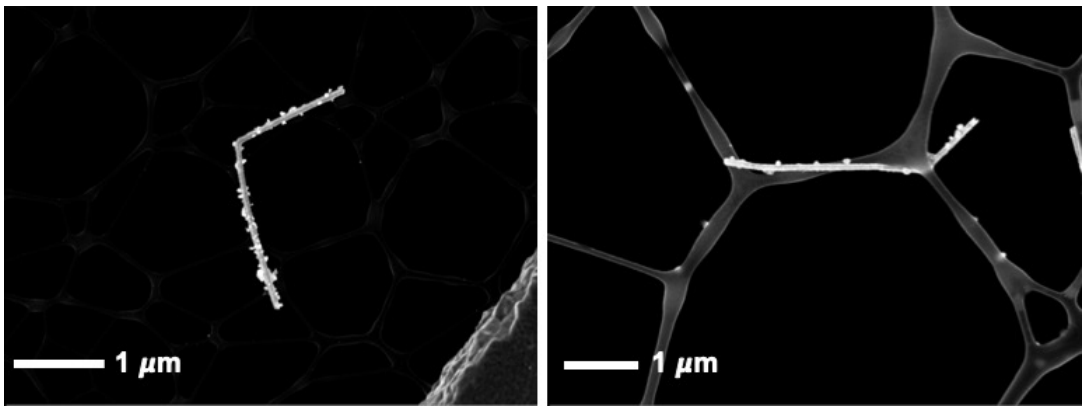

Figure 4.44: SEM images of the gold nanoparticle AuAg nanowire composite on Day 5.

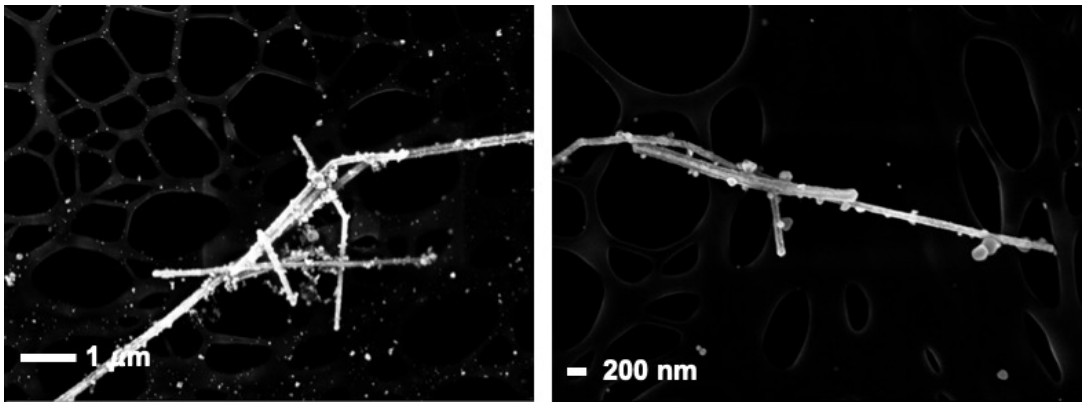

Figure 4.45: SEM images of the gold nanoparticle AuAg nanowire composite on Day 6.

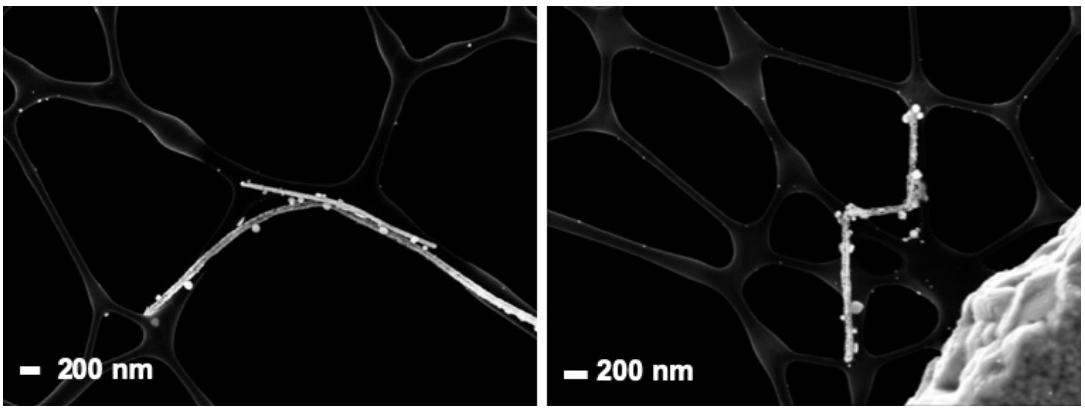

Figure 4.46: SEM images of the gold nanoparticle AuAg nanowire composite on Day 7.

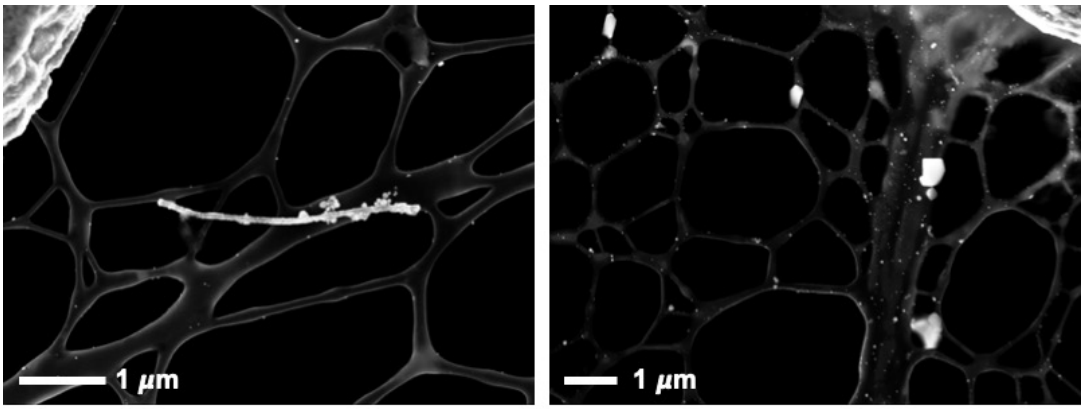

Figure 4.47: SEM images of the gold nanoparticle AuAg nanowire composite on Day 8.

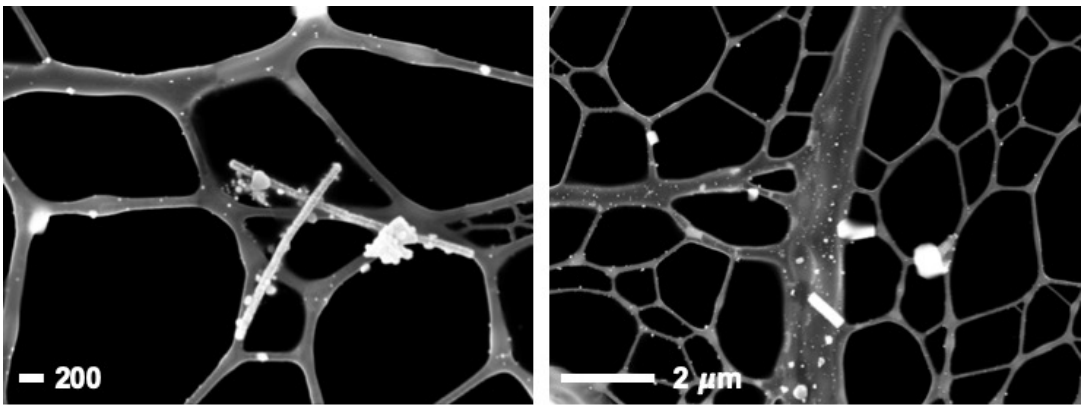

Figure 4.48: SEM images of the gold nanoparticle AuAg nanowire composite on Day 9.

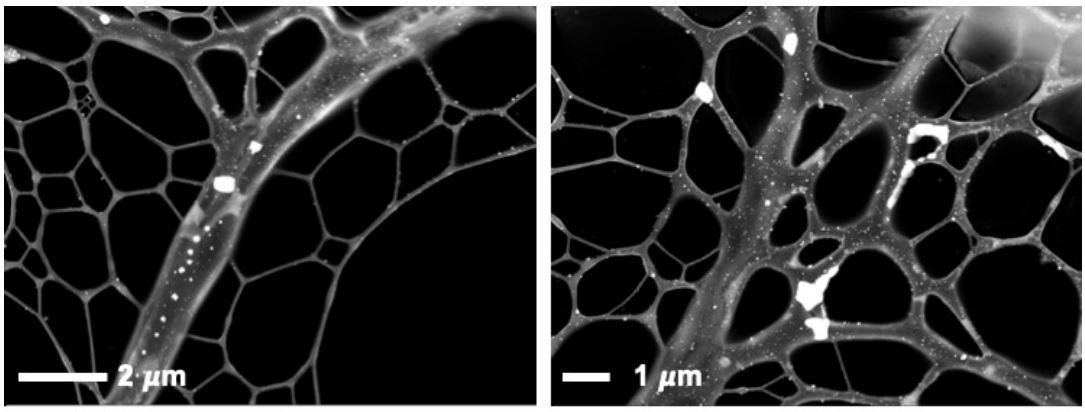

Figure 4.49: SEM images of the gold nanoparticle AuAg nanowire composite on Day 10.

EDX studies were also carried out on the gold nanoparticle/AuAg nanowire composite structures as shown in Figure 4.50. The EDX studies for these structures were also performed on Day 2 of the time study. Both silver and gold are clearly visible in the nanowire structure through mapping, with the unbound gold nanoparticles in Figure 4.50 (C) visible on the SEM grid. However, as both the nanowire and the nanoparticles are composed of gold, it is difficult to fully ascertain the degree of gold coating with the nanoparticles through EDX.

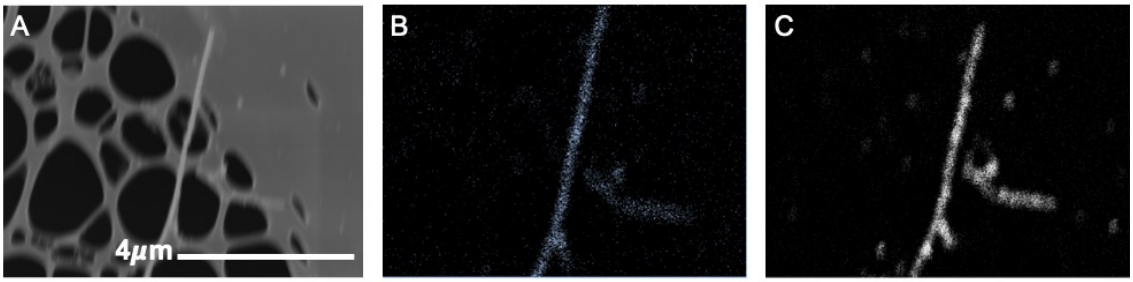

Figure 4.50: EDX studies on the gold nanoparticle and AuAg nanowire structure. In this instance (A) shows the SEM image of the mapped area, (B) shows the Ag map and (C) shows the gold map.

4.4 Conclusions

In this chapter, two new nanocomposites were developed and investigated: a magnetic-plasmonic nanocomposite comprised of PAH-stabilised magnetite and PVP-stabilised Ag nanowires, and a hybrid plasmonic nanocomposite composed of PAH-stabilised gold nanoparticles and PVP-stabilised nanowires.

PSS-stabilised magnetite nanoparticles were prepared and the length of the reflux time was examined. It was found that refluxing the magnetite for a longer time period (100 minutes) resulted in more monodisperse nanoparticles with a higher magnetic moment. To further functionalise the nanoparticles such that they would interact electrostatically with the negatively charged PVP-stabilised nanowires, a layer of PAH was added to the surface of the nanoparticles. Firstly, this was performed with a PAH concentration of 5.71 x 10^{-5} M. However, it was found that this concentration was too high, such that magnetic separation could no longer be carried out. This concentration was then lowered by a factor of ten to 5.71 x 10^{-6} M to great effect, as the particles were easily pulled out of solution using magnetic separations, and were found to have the appropriate surface charge and stability through zeta-potential analysis.

PAH-stabilised gold nanoparticles were also prepared, with a single plasmon peak at 528 nm. TEM analysis confirmed the presence of monodisperse gold nanoparticles with an average size of 10 ± 3.8 nm. CTAB-stabilised gold nanorods with two different aspect ratios were produced, alongside gold nanoparticles and gold nanotriangles in the same synthesis. The two aspect ratios were 28 ± 0.3 and 10.6 ± 2.4. The UV-Vis spectrum for this sample shows two peaks, one at 693 nm and 528 nm corresponding to the longitudinal and transverse plasmon bands respectively. However, due to the resulting solution being highly polydisperse with a number of nanoparticle species present, and also CTAB being necessary as the stabilising

agent, these nanorods were not used to synthesise a new nanocomposite. In addition to the polydisperse nature of the solution, CTAB is highly toxic and therefore would be inappropriate for any potential biological applications. Future work will include optimisation of the nanorod synthesis to prepare a single aspect ratio solution of nanorods, as well as a ligand exchange reaction to replace the surface capping agent with one with a lower cytotoxicity.

CTAB-stabilised gold nanostars were also prepared in this work via a silver seed mediated growth method. Two syntheses were used to prepare these nanoparticles, with both a lower and higher relative concentration of CTAB. The lower concentration of CTAB produced a highly polydisperse solution of gold nanoparticles, while the higher relative concentration of CTAB produced a more monodisperse solution of nanostars, however, these nanoparticles still had a higher degree of polydispesity than desired for the goal of preparing a nanocomposite with the PVP-capped nanorods. A UV-Vis spectrum for these nanostars shows a broad peak at 690 nm, with a shoulder in the region of 950 nm. The core of the nanostars varied between 50 and 80 nm, with the core-to-tip distance being in the range of 100 - 170 nm. Due to the polydispersity, in addition to the cytotoxic CTAB being used as the capping agent, it was decided not to use the nanostars in the synthesis of the nanocomposites with the PVP-coated Au-Ag nanorods.

The main goal of this chapter was to prepare multi-modal anisotropic nanowire structures, and so the two species with appropriate monodispersity and capping agents (PAH-stabilised magnetite and PAH-stabilised gold) were then used in the formation of the composite nanostructures. This was achieved through complementary charges on the capping agents of the two species. In the first case, a magnetic-plasmonic nanocomposite was prepared using the magnetite and AuAg nanowires. The resulting material has a magnetic response and a weak plasmonic response. Optimum coating of the AuAg nanowires seemed to occur between 5 and 8 days.

A more detailed time study of the formation of this material was also carried out which showed the progressive coating of the AuAg nanowires over a time period of 10 days, including EDX studies which confirmed the presence of iron, silver and gold throughout the sample.

PAH-stabilised gold nanoparticles and PVP-stabilised nanowires were also used to prepare a hybrid plasmonic composite structure. In these structures the plasmon peaks of both the AuAg nanowire and gold nanoparticles were preserved. Optimum coating of the AuAg nanowires occurred after 48 hours. A more detailed time study of the formation of these structures was also carried out, again including EDX, which confirmed the progressive coating of the nanowires with gold nanoparticles for a period of 7 days, but also showed the progressive decomposition of the nanowire structures from 8 days onwards. EDX analysis confirmed the presence of gold and silver in the nanowires, as well as gold nanoparticles throughout the sample.

The plasmonic properties make these structures promising candidates for a number of potential applications, including a new class of theranostic materials. Future work will involve optimising the coating of the nanowires with the magnetic and plasmonic nanoparticles discussed here, as well as optimisation of the syntheses of both the gold nanorods and gold nanostars such that they may also be coated onto the nanowires. Cytotoxicity tests may also be conducted to confirm that these new nanomaterials are biocompatible and to test their suitability for any potential medical applications.

Bibliography

(1) L. Yang, Z. Zhou, J. Song and X. Chen, *Anisotropic nanomaterials for shape-dependent physicochemical and biomedical applications*, 2019.

(2) R. Zsigmondy, *Colloids and the ultramicroscope a manual of colloid chemistry and ultramicroscopy,* J. Wiley & Sons, New York, 1st ed., 1909.

(3) R. Gans, *Annalen der Physik*, 1912, **342**, 881–900.

(4) N. D. Burrows, A. M. Vartanian, N. S. Abadeer, E. M. Grzincic, L. M. Jacob, W. Lin, J. Li, J. M. Dennison, J. G. Hinman and C. J. Murphy, *Journal of Physical Chemistry Letters*, 2016, **7**, 632–641.

(5) C. Xue and C. Mirkin, *Angewandte Chemie International Edition*, 2007, **46**, 2036–2038.

(6) Z. Li and X. Peng, *Journal of the American Chemical Society*, 2011, **133**, 6578–6586.

(7) D. Huo, M. J. Kim, Z. Lyu, Y. Shi, B. J. Wiley and Y. Xia, *One-Dimensional Metal Nanostructures: From Colloidal Syntheses to Applications*, 2019.

(8) K. A. Dick, *A review of nanowire growth promoted by alloys and non-alloying elements with emphasis on Au-assisted III-V nanowires*, 2008.

(9) S. Rahong, T. Yasui, N. Kaji and Y. Baba, *Lab on a Chip*, 2016, **16**, 1126–1138.

(10) J. Jiu, T. Araki, J. Wang, M. Nogi, T. Sugahara, S. Nagao, H. Koga, K. Suganuma, E. Nakazawa, M. Hara, H. Uchida and K. Shinozaki, *Journal of Materials Chemistry A*, 2014, **2**, 6326–6330.

(11) R. Thompson, F. Oldfield, R. Thompson and F. Oldfield, in *Environmental Magnetism*, Springer Netherlands, 1986, pp. 21–38.

(12) R. W. O'Brien, B. R. Midmore, A. Lamb and R. J. Hunter, *Faraday Discussions of the Chemical Society*, 1990, **90**, 301–312.

(13) X. Huang and M. A. El-Sayed, *Gold nanoparticles: Optical properties and implementations in cancer diagnosis and photothermal therapy*, 2010.

(14) *Towards a Reproducible Synthesis of High Aspect Ratio Gold Nanorods [Online, accessed April 2020]*.

(15) T. Jun, L. Yong-Hua, Z. Rong-Sheng, L. Kai-Qun, X. Zhi-Guo, L. Zhao-Feng, L. Sheng-Li, W. Pei and M. Hai, *Chinese Physics Letters*, 2008, **25**, 4459.

(16) W. Feng, X. Zhou, W. Nie, L. Chen, K. Qiu, Y. Zhang and C. He, *ACS Applied Materials & Interfaces*, 2015, **7**, 4354–4367.

(17) Z. Kereselidze, V. H. Romero, X. G. Peralta and F. Santamaria, *Journal of visualized experiments : JoVE*, 2012, DOI: 10.3791/3570.

(18) T. K. Sau, A. L. Rogach, M. Döblinger and J. Feldmann, *Small (Weinheim an der Bergstrasse, Germany)*, 2011, **7**, 2188–94.

(19) H. Zhou, J.-P. Kim, J. H. Bahng, N. A. Kotov and J. Lee, *Advanced Functional Materials*, 2014, **24**, 1439–1448.

(20) M. B. Gebeyehu, T. F. Chala, S. Y. Chang, C. M. Wu and J. Y. Lee, *RSC Advances*, 2017, **7**, 16139–16148.

(21) D. K. Kehoe, J. McCarthy, J. J. Gough, A. L. Bradley and Y. K. Gun'Ko, *Journal of Physical Chemistry C*, 2019, **123**, 15307–15313.

Chapter 5

DNA Based Magnetic-Plasmonic Nanocomposites

5.1 Introduction

The development of DNA-stabilised nanomaterials has been an avid area of research in recent years[1]. Overall, in nanoscience and theranostics, there has been a huge drive towards the use of biologically based stabilisers for nanoparticles, for example viral capsids derived from biopolymers such as nucleic acids[2–4].

Previous chapters have described the use of polystyrene sulfonate (PSS) and poly-(allyl)amine hydrochloride (PAH) as suitable, biocompatible polyelectrolytes used for the stabilisation and functionalisation of both magnetite and gold nanoparticles. DNA can be itself considered as a charged polyelectrolyte, it possesses a weak negative charge due to the phosphate groups in the DNA backbone[5]. DNA consists of two long chains wound around a common axis to form a double helix structure. DNA is a biocompatible coating agent, and binds covalently with nanoparticles. Moreover, as it is composed of small repeating units called nucleotides, specific DNA sequences can be used in targeted DNA delivery[6].

Both double-stranded and single-stranded DNA can be conjugated to nanoparticles. Single-stranded DNA (ssDNA) shows an enhanced peak in the UV-Visible spectrum when compared to double-stranded DNA (dsDNA). Also, ssDNA has been shown to conjugate to unmodified and uncoated gold nanoparticles under certain conditions[7]. The use of single-stranded DNA on two species of nanoparticles, for example gold and magnetite nanoparticles, may offer the functionality of recombining the DNA such that a new nanocomposite structure may be formed.

In recent years, large amounts of research have been carried out on the development of both DNA-stabilised magnetite nanoparticles and DNA-stabilised gold nanoparticles. Several approaches to the stabilisation of magnetic nanoparticles with DNA have been reported[8], including the direct binding of nucleic acid fragments to nanoparticles, and the use of an intermediate species (such as citric acid) to facilitate the binding of the magnetic nanoparticle and the DNA[9–11]. Arguably, an even larger body of work has been carried out investigating the conjugation of DNA to gold nanoparticles, with a wide array of reviews on the methods used to prepare DNA-stabilised plasmonic gold nanoparticles, all detailing the different mechanisms by which DNA of varying lengths can be added to the surface of the nanoparticles[12–14]. The motivation for this work lies in the biocompatibility and high versatility of the resulting nanoparticles, which offer multiple potential applications in biosensing, as well as gene and drug delivery.

5.2 Aims

The aim of this work is to prepare a series of DNA-stabilised magnetite and gold nanoparticles. For both the preparation of DNA-stabilised gold and magnetite, a one-pot synthetic approach is used. In the case of magnetite, a modified co-precipitation approach is to be used in the presence of DNA solutions with different concentrations, in order to determine optimal initial DNA concentrations. These same concentrations of DNA will then be used to synthesise DNA-stabilised gold nanoparticles through a modified sodium borohydride reaction, in which ascorbic acid is first used to reduce the nanoparticles from Au^{3+} to Au^{1+}, before final reduction to the metal nanoparticles using a small quantity of sodium borohydride. These experiments are planned to be repeated for the magnetite and gold nanoparticles using single-stranded DNA. A wide variety of DNA-based magnetic-plasmonic nanocomposites are then to be prepared through titration and examined using Raman and UV-Vis spectroscopy.

We then aim to fully characterise the resulting nanoparticles with UV-Vis, Raman, FT-IR, TGA and TEM analysis.

5.3 Results and Discussion

An *in-situ* approach to preparing DNA-stabilised magnetite and gold nanoparticles was carried out for both double-stranded DNA (dsDNA) and single-stranded DNA (ssDNA) for a range of concentrations. These nanoparticles were then investigated by UV-Vis and Raman spectroscopy, as well as examined using a variety of instrumentation techniques. The resulting nanoparticles were then used to prepare a wide variety of DNA-stabilised magnetic-plasmonic nanocomposite structures, which were then analysed by UV-Vis and Raman spectroscopy.

5.3.1 DNA-Stabilised Magnetite Nanoparticles

DNA-stabilised magnetite nanoparticles were prepared *in-situ* using DNA solutions of varying concentrations by a modified co-precipitation approach at room temperature. The magnetite was precipitated using ammonia causing the formation of the nanoparticles in the DNA solutions. Initially, several concentrations of DNA (5, 10, 15, 20, 30, 40, 50, 60, 70, 80, 90 and 100 mg of herring sperm DNA in a 25 mL solution of MP water) were tested.

For each of the concentrations, the synthesis of the dsDNA-magnetite nanocomposites was attempted. An interesting observation was that above an initial dsDNA concentration of 15 mg/25 mL, the nanoparticles did not respond to a magnetic field. As one of the primary objectives for this work is for the resulting nanocomposites to be retrievable through magnetic separation, it was decided that only the 5, 10 and 15 mg solutions would be used from this point onwards. The second point to note was that after the synthesis, the UV-Vis spectra of the DNA composites did not show any DNA peak. This could be due to a number of reasons - the first being that the conjugation of the DNA to the nanoparticles was unsuccessful. The

second reason could simply be that the dark colour of the magnetite nanoparticles obscures the DNA peak at 250 nm in the UV-Vis spectra. The UV-Vis spectra for the 5, 10 and 15 mg dsDNA-magnetite nanoparticles are shown in Figure 5.1. The higher absorbances of the 10 mg and 15 mg dsDNA in the region of the DNA peak could also be an indication that that peak is being obscured. As can be seen in Figure 5.1, UV-Visible spectroscopy of the DNA-magnetite nanoparticles may not be a suitable metric for determining whether or not conjugation of the DNA to the magnetite has occurred.

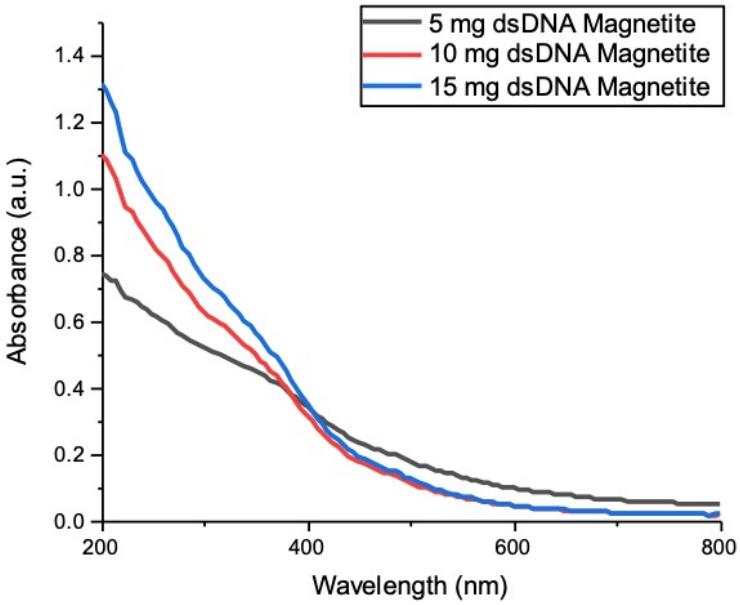

Figure 5.1: UV-Vis spectra of the ds-DNA-magnetite nanoparticles for concentrations of 5, 10 and 15 mg dsDNA.

As a means of determining whether or not the dsDNA had bound to the surface of the magnetite nanoparticles, FTIR analysis was carried out and this is shown in Figure 5.2. The peak for DNA at 1650 cm^{-1} can be seen at slightly lower wavenumbers in each of dsDNA-stabilised magnetite spectra, which is indicative that it has conjugated to the surface of the nanoparticles. However, DNA bound to the mag-

netite could also be attributed to the peak at 1630 cm^{-1} wavenumbers[15]. The region between 900 - 1200 cm^{-1} of the herring sperm DNA can be found in each of the spectra of the magnetite nanoparticles, which suggests that there is DNA bound to the surface of the nanoparticle. The DNA peaks at 1071 cm^{-1} and 1097 cm^{-1} can be attributed to the phosphodiester backbone, and the PO_2^- asymmetric stretch can be seen at 1244 cm^{-1}. The peaks in the region between 1200 - 1800 cm^{-1} are attributed to the nucleobases[16]. In addition, these peaks are the least discernible in the 5 mg dsDNA-stabilised magnetite sample, which would be expected as this should be the sample with the least DNA present.

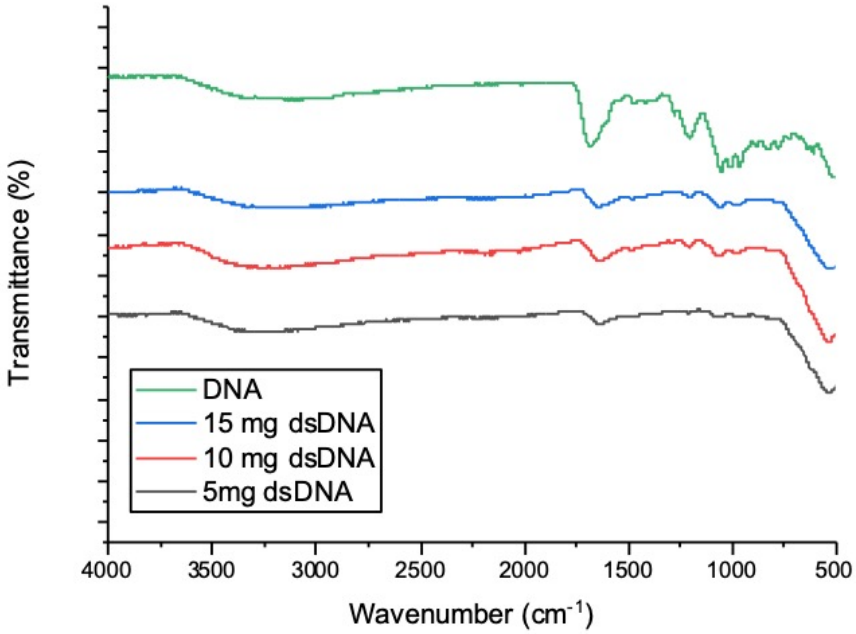

Figure 5.2: FTIR spectra showing the spectra for the herring Sperm DNA and each of the concentrations of dsDNA-stabilised magnetite nanoparticles.

In order to further investigate the DNA bound to the surface of the magnetite nanoparticles, TGA was carried out, and the corresponding curves are shown in Figure 5.3. The TGA results are inconclusive, with the first point to note being that only 1 mg of sample could be retrieved for the 10 mg dsDNA-stabilised magnetite sample, and so this can be immediately disregarded. In the cases of the 5

mg and 15 mg samples, the samples were run at a heating rate of 10 °C/min up to 600 °C. The first region of weight loss for each of these samples occurs between 0 - 200 °C and can be attributed to the water bound to the DNA and any residual water bound to the surface of the nanoparticles. The broad weight loss region between 200 - 400 °C for the 5 mg dsDNA-stabilised magnetite and the region between 200 - 600 °C for the 15 mg dsDNA-stabilised magnetite can be attributed to the weight loss corresponding to the DNA bound to the nanoparticle. The difference in % weight loss between the 5 mg and 15 mg dsDNA-stabilised magnetite samples suggests that DNA was bound to the surface and lost through heating, as the 15 mg dsDNA-stabilised magnetite has a much higher weight loss (*c.a.* 10 %) compared to the 5 mg dsDNA-stabilised magnetite sample (*c.a.* 5 %). This is an indication that a larger proportion of organic surface groups, in this case DNA, were present in the 15 mg dsDNA-stabilised magnetite.

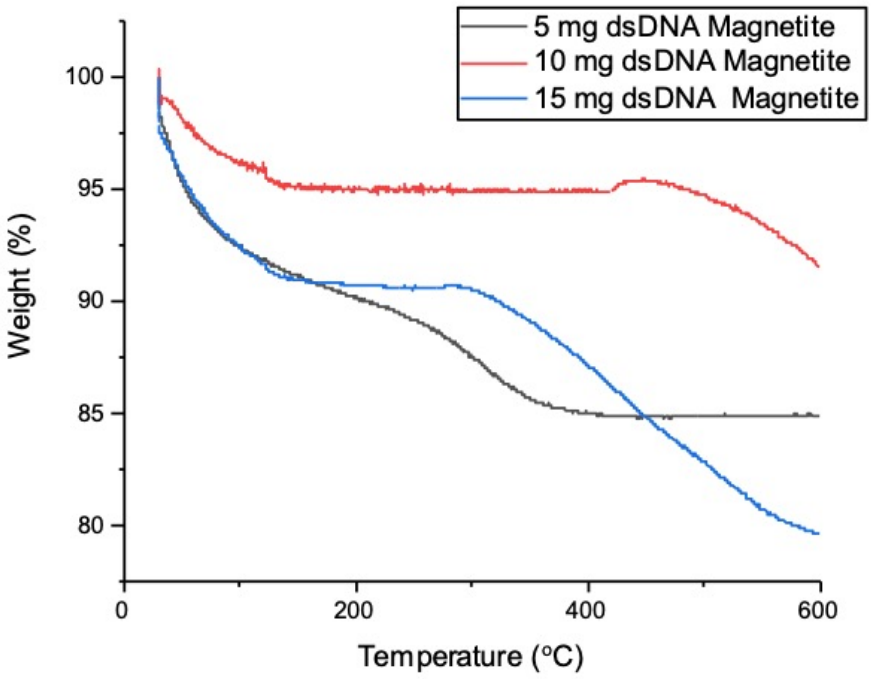

Figure 5.3: TGA curves of each concentration of dsDNA-stabilised magnetite.

VSM analysis was also carried out to investigate the magnetic properties of the nanoparticles, and it too can be used for a rough estimation of the amount of bound stabilising groups as shown in Figure 5.4. This is because a non-magnetic stabilising agent bound to the nanoparticle will contribute to the weight of the sample but not the magnetic moment, and so as the concentration of the stabilising agent is increased, the magnetic moment of the nanoparticles will decrease slightly while their magnetic behaviour (ferro/ferrimagnetic or superparamagnetic) is preserved. In each case, the magnetite is superparamagnetic with the magnetic moments for the 5, 10 and 15 mg samples being 60.8, 47, and 24.3 Am^2/Kg respectively.

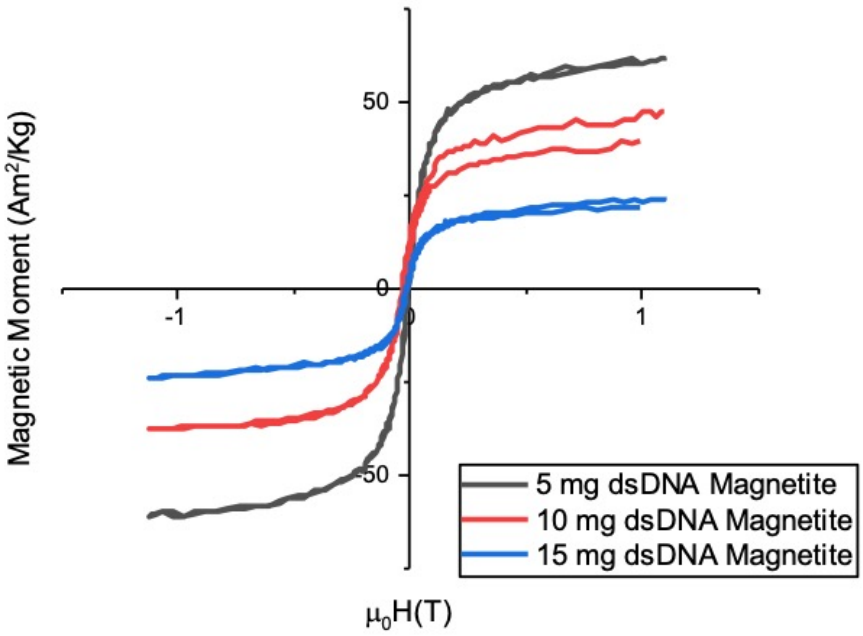

Figure 5.4: VSM analysis for the 5, 10 and 15 mg dsDNA-stabilised magnetite.

TEM analysis was also carried out on the dsDNA-stabilised magnetite nanoparticles, as shown in Figure 5.5. In each case the images display large clusters of magnetite nanoparticles that appear aggregated. This could be due to multiple nanoparticles binding along one strand of DNA. Size distribution analysis was carried out on these nanoparticles and can be found in Figure 5.6, and shows a large size distribu-

tion. The mean nanoparticle sizes and standard deviation for the 5, 10 and 15 mg dsDNA-stabilised magnetite nanoparticles are 17.9 nm ± 6.7 nm, 24.2 nm ± 9.6 nm and 19.2 nm ± 7.1 nm respectively. This larger distribution when compared with previously synthesised magnetite nanoparticles is likely due to the lack of heating in the synthetic procedure. However, the higher temperatures normally required to prepare monodisperse solutions of magnetite nanoparticles would denature the DNA.

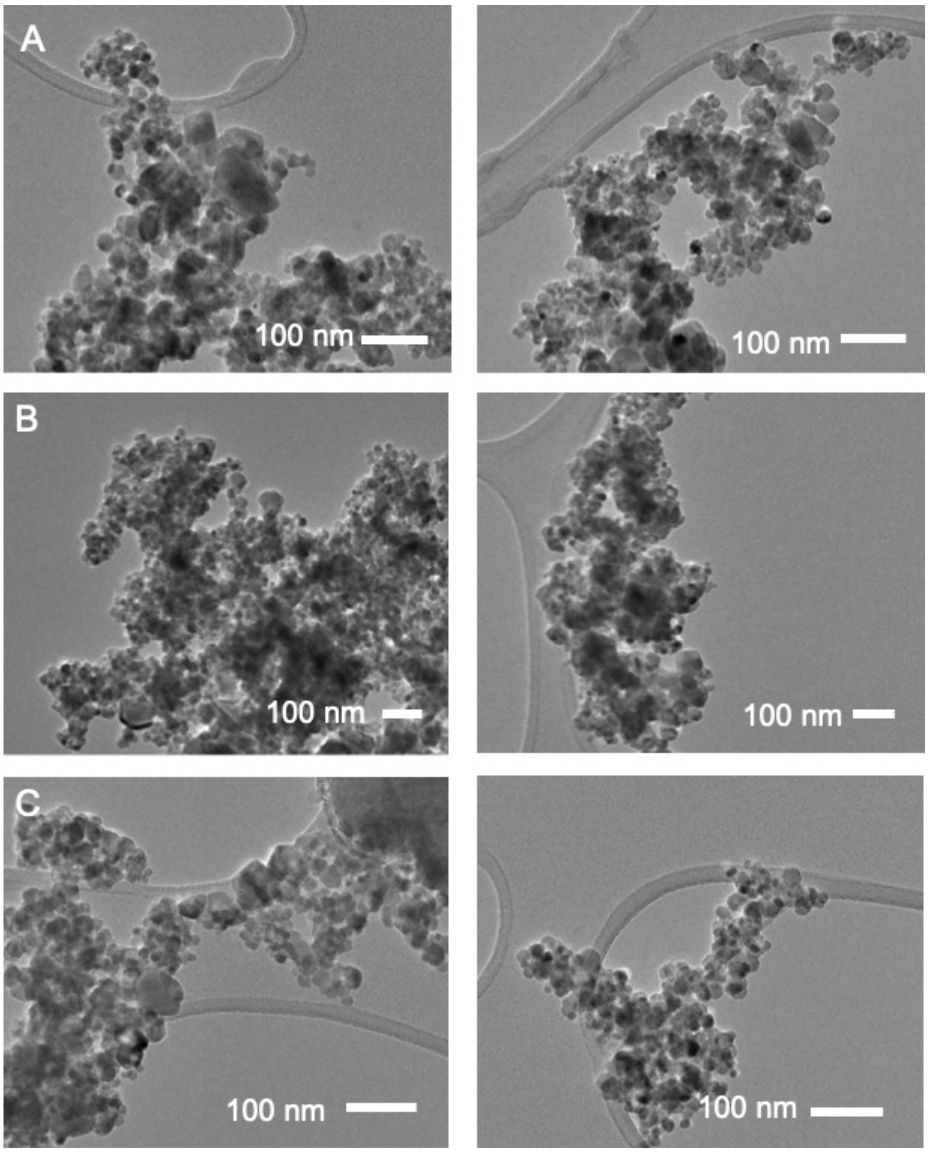

Figure 5.5: TEM images for (A) 5 mg dsDNA-stabilised magnetite, (B) 10 mg dsDNA-stabilised magnetite, and (C) 15 mg dsDNA-stabilised magnetite

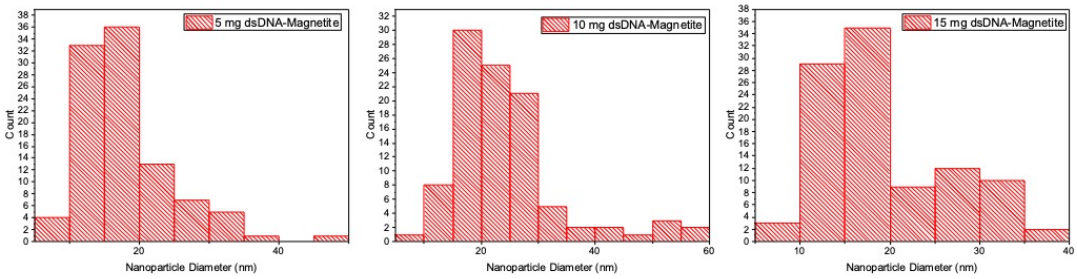

Figure 5.6: Size distributions for each concentration of the dsDNA-stabilised magnetite.

In-situ ssDNA-stabilised magnetite nanoparticles were also prepared though coprecipitation using ammonia in each of the 5, 10 and 15 mg ssDNA solutions. The UV-Vis spectra for ds- and ssDNA should be different. The ssDNA should show a higher absorption peak at 260 nm due to the separation and denaturation of the DNA - this is known as the hypochromic effect[17]. Denaturing the DNA involved heating each DNA solution to 80 °C and then immediately cooling in ice before the use in the synthesis of the nanoparticles. UV-Vis spectra for each of the three DNA concentrations before and after denaturation are shown in Figure 5.7.

In each case, it can be clearly seen that the ssDNA peak has a higher absorbance than the dsDNA peak. This is to be expected due to the hypochromic effect. This ssDNA was then further used in the preparation of ssDNA-stabilised magnetite nanoparticles, as well as ssDNA-stabilised gold nanoparticles.

Similarly to the dsDNA-stabilised magnetite nanoparticles, the UV-Vis spectra for the ssDNA-stabilised magnetite particles did not show any DNA peak. Once again, this is likely due to the dark colour of the magnetite masking any DNA peaks. UV-Vis spectra of the 5, 10 and 15 mg ssDNA-stabilised magnetite nanoparticles are shown in Figure 5.8.

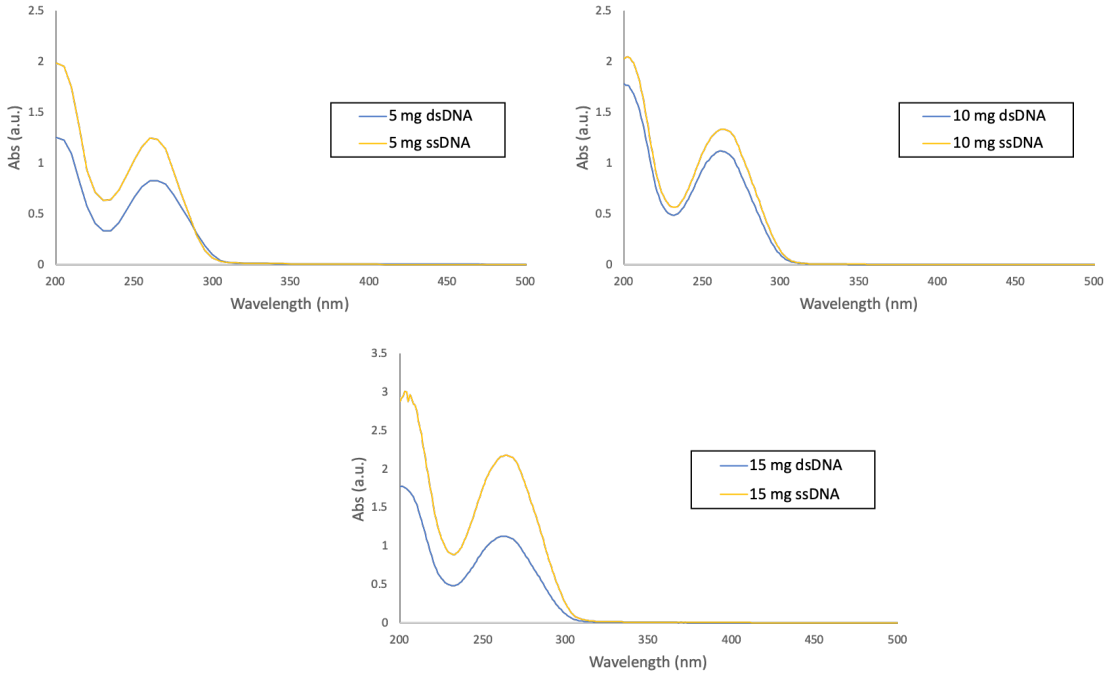

Figure 5.7: UV-Vis spectra for the 5, 10 and 15 mg samples of ds- and ss-DNA that was immediately cooled in ice after reaching 80 °C. The blue spectra correspond to the dsDNA and the yellow spectra correspond to the denatured ssDNA.

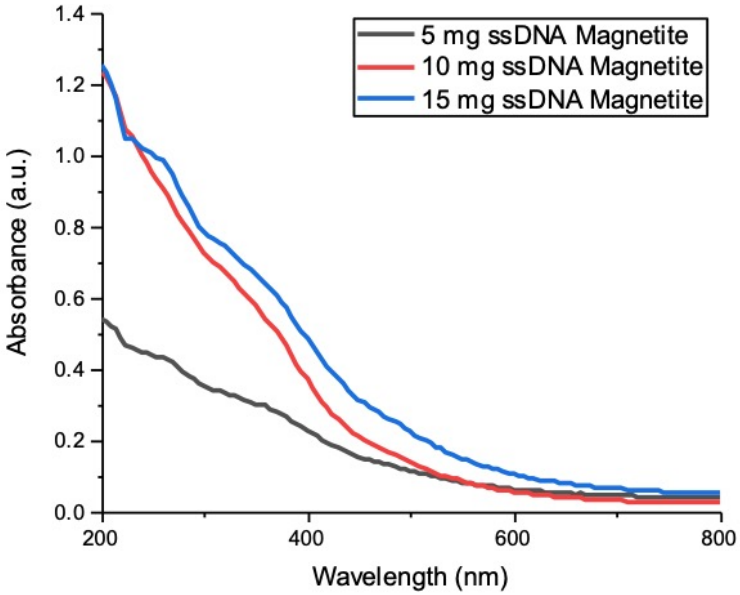

Figure 5.8: UV-Vis spectra for the ssDNA-stabilised magnetite nanoparticles.

FTIR analysis was also carried out on the ssDNA-stabilised magnetite nanoparticles (Figure 5.9), and the results are very similar to those obtained for the dsDNA-stabilised magnetite samples. The DNA peak at 1700 cm^{-1} is visible in each of the three samples of ssDNA-stabilised magnetite, and corresponds to the nucleobases. However the series of DNA peaks between 750 - 1100 cm^{-1} are not as clearly visible in the spectra for the ssDNA-stabilised magnetite. These peaks correspond to the phosphodiester backbone of the DNA[16].

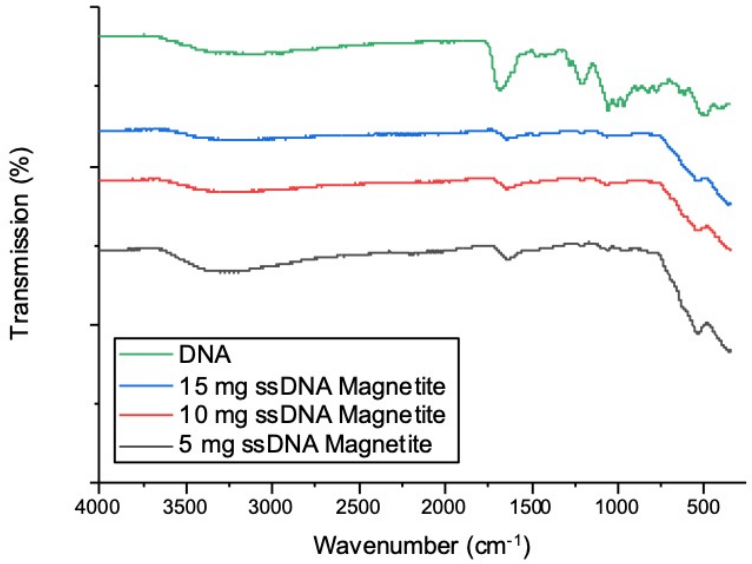

Figure 5.9: FTIR spectra of the ssDNA-stabilised magnetite nanoparticles.

VSM analysis was also carried out to examine the magnetic behaviour of the nanoparticles, and also as a means to infer whether or not the coating of the nanoparticles with ssDNA was successful (Figure 5.10). In each case, the absence of a hysteresis loop indicates that the synthesised nanoparticles are superparamagnetic. What is noteworthy is that in each case, the ssDNA-stabilised magnetite have a higher magnetisation moment than the corresponding dsDNA-stabilised magnetite nanoparticles. In the case of the ssDNA-stabilised magnetite the magnetic moment for the 5, 10 and 15 mg samples are 71.4, 59.4 and 63.7 Am^2/Kg respectively. This suggests

that there is significantly less non-magnetic material, in this case herring sperm DNA, coating the nanoparticles.

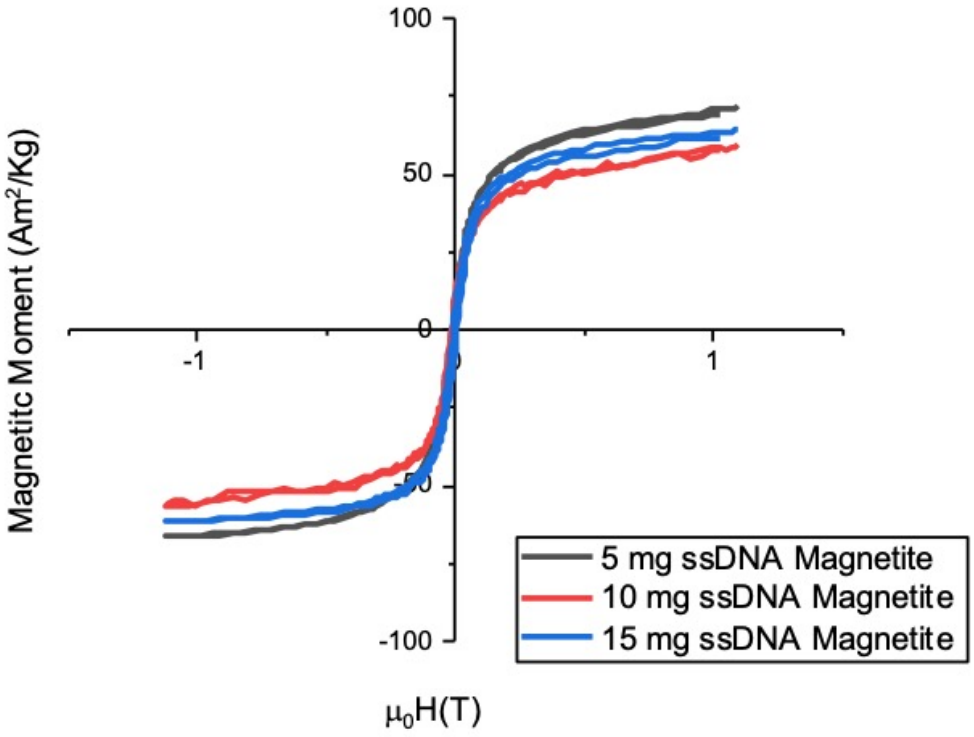

Figure 5.10: VSM curves for the 5, 10 and 15 mg ssDNA-stabilised magnetite nanoparticles

In order to further investigate the amount of DNA on the nanoparticles, TGA was carried out (Figure 5.11). In this instance, the weight loss % for the 10 and 15 mg ssDNA-stabilised magnetite nanoparticles are identical (18 %), whereas the weight loss percentage for the 5 mg ssDNA-stabilised magnetite sample is considerably lower (12 %). The magnetic moment for both the 10 mg and 15 mg samples of dsDNA-stabilised magnetite were also very similar. This may mean that there is a maximum loading of the ssDNA to the magnetite nanoparticles, or perhaps that the binding of the single-stranded DNA is less effective than the double-stranded DNA.

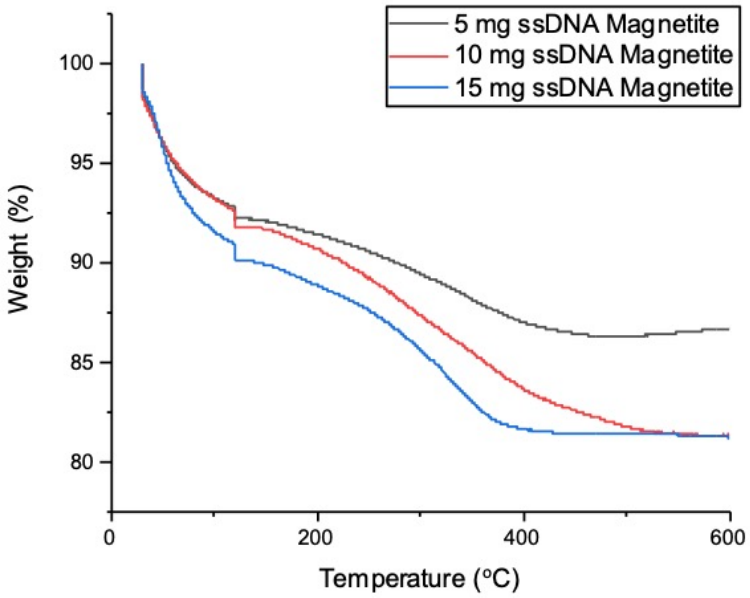

Figure 5.11: TGA curves of the ssDNA-stabilised magnetite nanoparticles.

TEM analysis was also carried out on these samples (Figure 5.12). These nanoparticles, which were prepared using an identical procedure to the dsDNA-stabilised magnetite, appear very different under the electron beam. In this case the nanoparticles appear much smaller, in the range of 1 - 5 nm. This smaller size could be the cause of their significantly higher magnetic moments when compared with the dsDNA-stabilised magnetite nanoparticles. It may be the case that the ssDNA is more capable of stabilising the magnetite nanoparticles earlier in their growth process, resulting in a lower concentration of ssDNA being needed as a stabilising agent, and smaller nanoparticles and an enhanced magnetic moment when compared with the dsDNA-stabilised magnetite. Due to the lack of clarity in the dispersity of the nanoparticles, size distribution analysis could not be carried out for this sample.

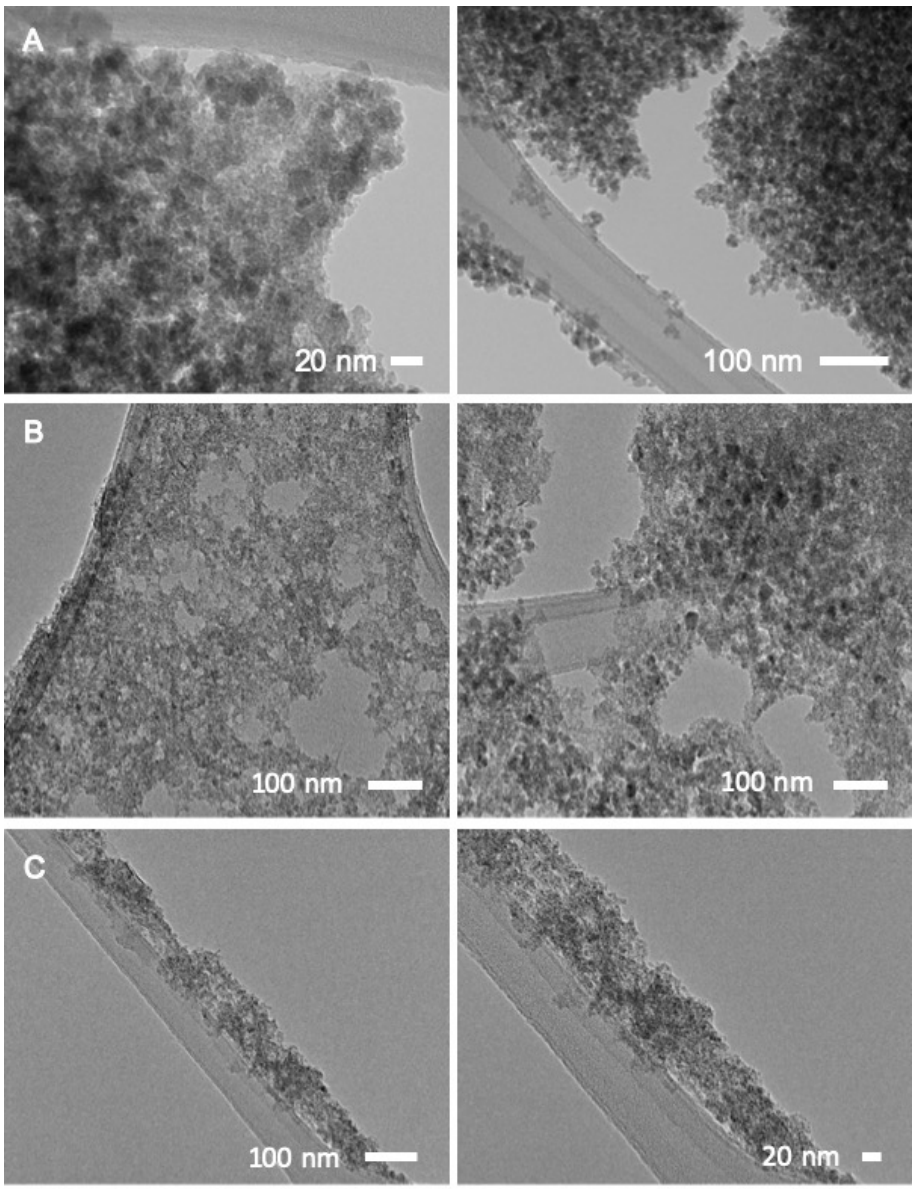

Figure 5.12: TEM images of (A) 5 mg ssDNA-stabilised magnetite, (B) 10 mg ssDNA-stabilised magnetite and (C) 15 mg ssDNA-stabilised magnetite.

Raman spectroscopy was also carried out on these nanoparticles, however, in this instance the obtained signals for each concentration of the DNA were within the noise of the instrument and so no meaningful results could be drawn from this technique. The Raman spectra for these particles can be found in Appendix A5.

5.3.2 DNA-Stabilised Gold Nanoparticles

Similarly to the DNA-stabilised magnetite nanoparticles, gold nanoparticles were synthesised and stabilised with both double-stranded and single-stranded DNA. The synthesis and coating of dsDNA-stabilised gold nanoparticles was attempted in one step. All glassware was thoroughly cleaned with aqua regia before any reactions were carried out. Briefly, in order to prepare the dsDNA- or ssDNA-stabilised nanoparticles, chloroauric acid was added to 10 mL of either the 5, 10 or 15 mg dsDNA or ssDNA solution. After allowing to stir for ten minutes, ascorbic acid was added dropwise and allowed to stir for a further 10 minutes before the addition of $NaBH_4$. The solution was allowed to stir for a further 15 minutes and the resulting nanoparticles were cleaned using methanol and was centrifuged at 10,000 RPM for 10 minutes.

In each case, a wine red solution was obtained, which is indicative of the formation of gold nanoparticles. UV-Vis analysis of the dsDNA-stabilised gold nanoparticles show, for each concentration, a sharp plamson peak at 530 nm, and a sharp DNA peak at 270 nm (Figure 5.13). These are very promising initial results as they suggest that dsDNA has bound to the surface of the gold nanoparticles.

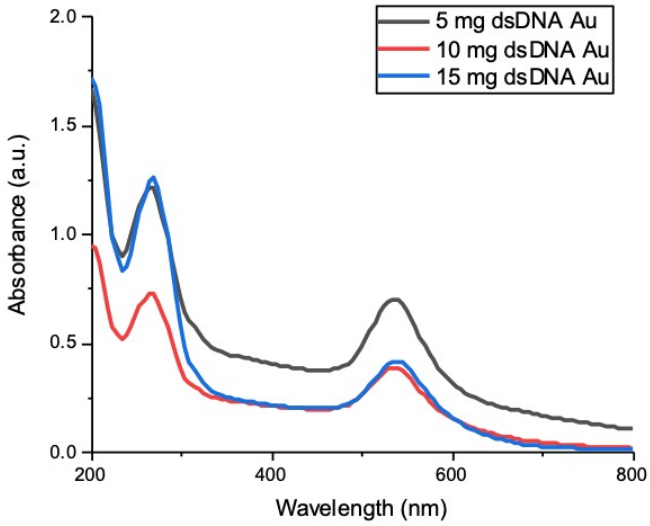

Figure 5.13: UV-vis spectra of the 5, 10 and 15 mg concentrations of dsDNA-stabilised gold nanoparticles.

FTIR was also carried out to investigate the presence of DNA on the surface of the nanoparticles (Figure 5.14). The dsDNA-stabilised gold nanoparticles were measured in solution, which is the reason for the broad H_2O peak at 3250 cm^{-1}. Similarly to the DNA-stabilised magnetite samples, the DNA peak at 1670 cm^{-1} is clearly visible in each of the three gold nanoparticle concentrations, which is a further indication that the DNA has bound to the gold nanoparticles. The sharper weaker DNA peaks in the region between 1250 - 1000 cm^{-1} cannot be seen in the nanoparticle sample however, and this could be due to the broad absorption of the water in the DNA solution.

Raman spectroscopy was carried out on these nanoparticles using an ANT Flipper instrument with a laser wavelength of 683 nm. Each measurement was carried out at 40% laser power with an average of 3 measurements. The results for the 5, 10 and 15 mg dsDNA-stabilised gold nanoparticles are shown in Figure 5.15. To illustrate the enhancement of the DNA peaks due to the presence of the gold nanoparticles, the Raman spectra of each concentration of the initial herring sperm DNA solution

and the corresponding concentration of the dsDNA-stabilised gold nanoparticles are shown in Figures 5.16 - 5.18.

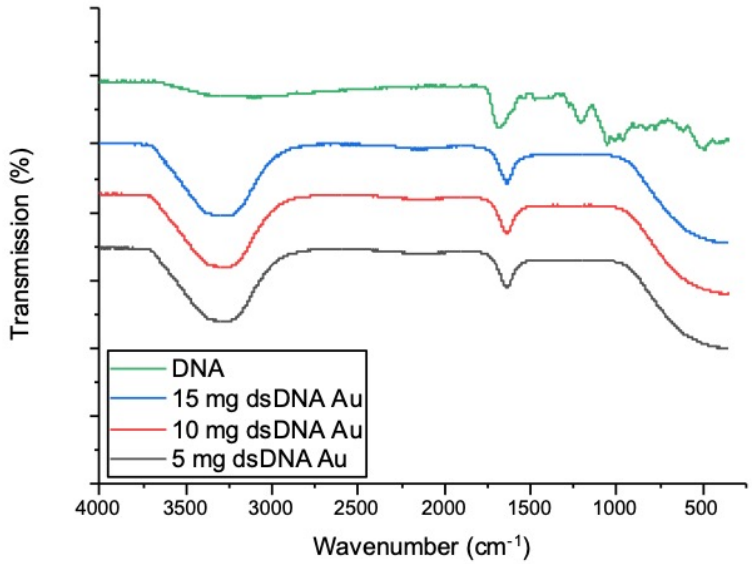

Figure 5.14: FTIR spectra of the 5, 10 and 15 mg dsDNA-stabilised gold nanoparticles.

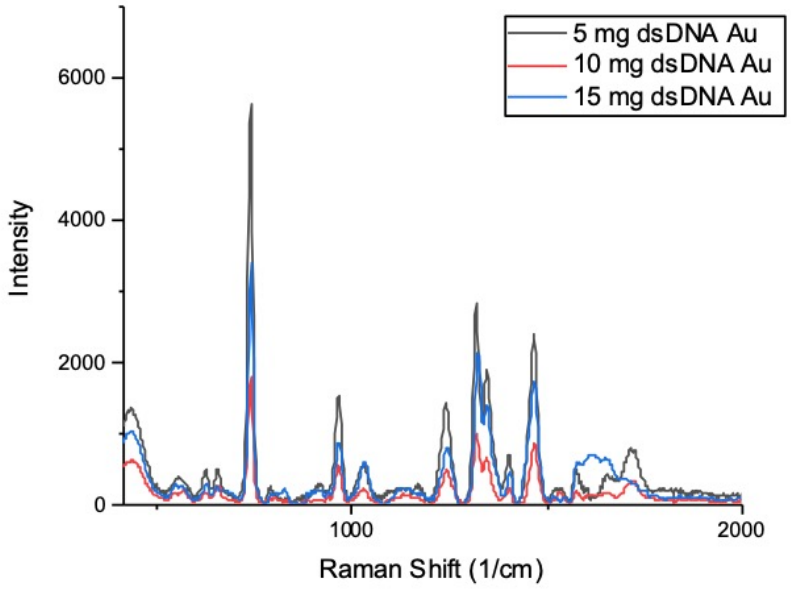

Figure 5.15: Raman spectra of the 5, 10 and 15 mg dsDNA-stabilised gold nanoparticles.

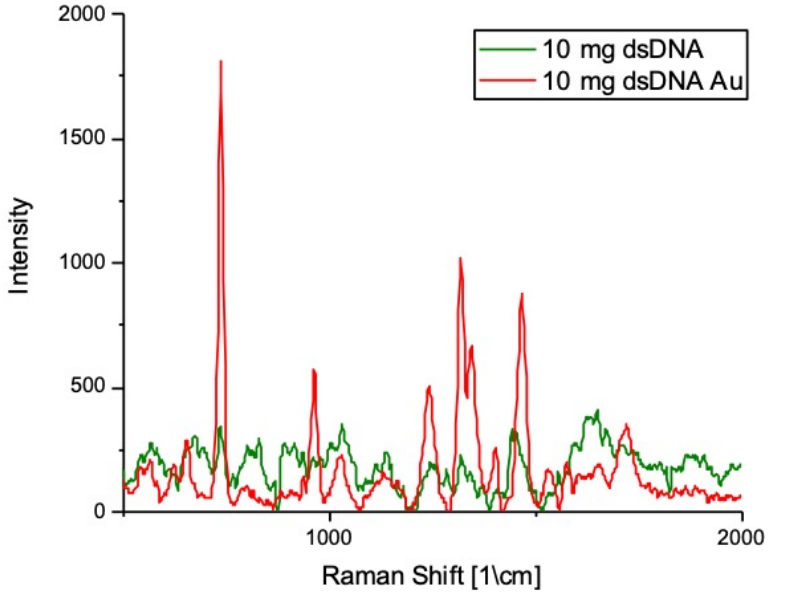

Figure 5.17: Raman spectra of the 10 mg dsDNA solution and the 10 mg dsDNA-stabilised gold nanoparticles.

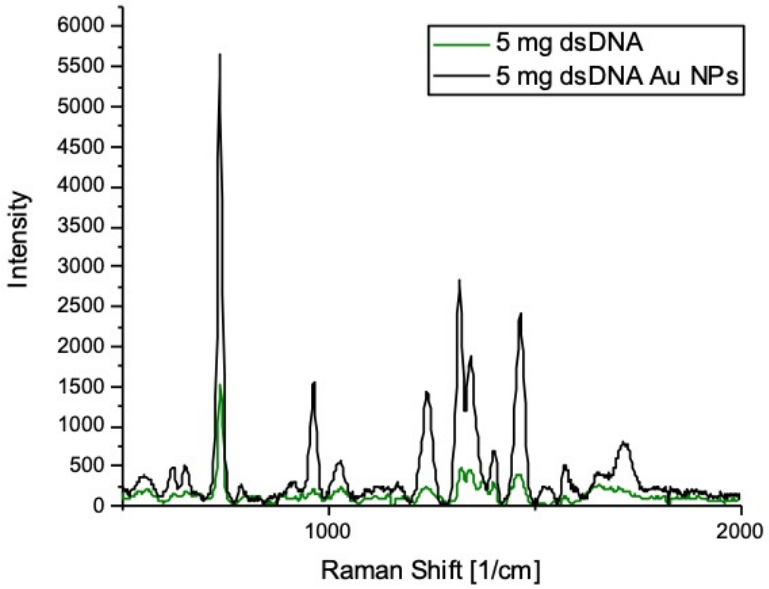

Figure 5.16: Raman spectra of the 5 mg dsDNA solution and the 5 mg dsDNA-stabilised gold nanoparticles.

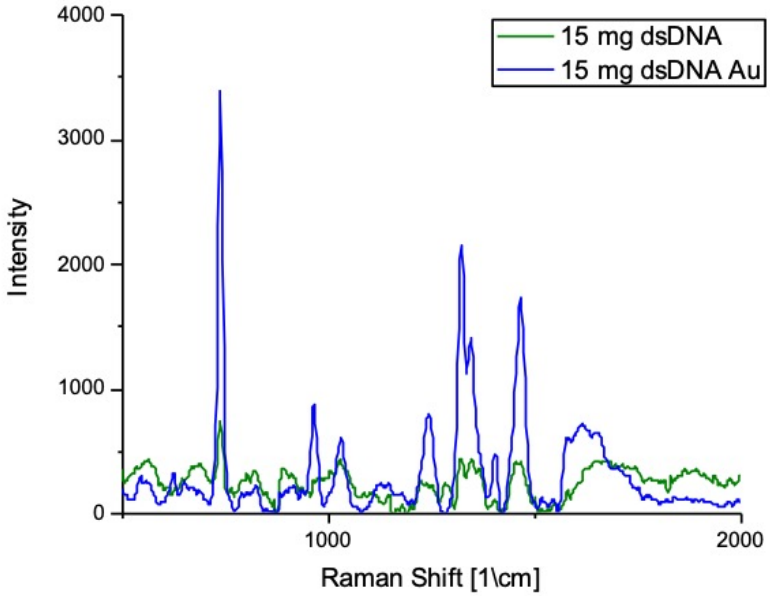

Figure 5.18: Raman spectra of the 15 mg dsDNA solution and the 15 mg dsDNA-stabilised gold nanoparticles.

As can be seen, there is a significant enhancement of the DNA peaks by the gold nanoparticles. The sharp peak at 800 cm^{-1} is assigned to the DNA-phosphate bond, and the peaks in the region between 1200 - 1400 cm^{-1} are attributed to the phosphodiester bonds. In each graph the DNA peak at 1250 cm^{-1} is considered - this peak is attributed to the phosphodiester groups[18]. For the 5 mg dsDNA-stabilised gold nanoparticles, this peak intensity increases in intensity from 250 to 1500, which represents an increase in intensity by a factor of 6. For the 10 mg dsDNA-stabilised gold nanoparticles, this peak increases from an intensity of 250 to 550; in this case the presence of the gold nanoparticles doubles the intensity of this peak. Similarly, the peak for the 15 mg dsDNA increases by a factor of 3, from 250 to 750 in intensity when coated on the gold nanoparticles. In order to determine the enhancement factor more accurately, each study must be repeated with a number of known gold nanoparticle concentrations for each of the known dsDNA concentrations. More comprehensive SERS studies will be carried out in future work, however, these are highly promising initial results.

TEM analysis was also performed on the gold nanoparticles, and this is shown in Figure 5.19. The images show primarily spherical gold nanoparticles with a large size distribution, however, there is the presence of a few anisotropic gold particles, such as gold nano-triangles, throughout the sample. In addition to this, a wide size distribution was obtained in each case: 16.3 nm ± 13.4 nm for the 5 mg dsDNA-stabilised gold nanoparticles, 18.2 nm ± 13.4 nm for the 10 mg dsDNA-stabilised gold nanoparticles and 11.47 nm ± 6.8 nm for the 15 mg dsDNA-stabilised gold nanoparticles (Figure 5.20).

TGA was carried out on the dsDNA-stabilised gold nanoparticles. However, as the concentrations of chloroauric acid used in the synthesis of the gold nanoparticles were very low, the dried weights of the prepared gold nanoparticles were below the minimum weight of detection of the instrument in the majority of cases. In order to maximise the amount of the dsDNA-stabilised gold nanoparticles present

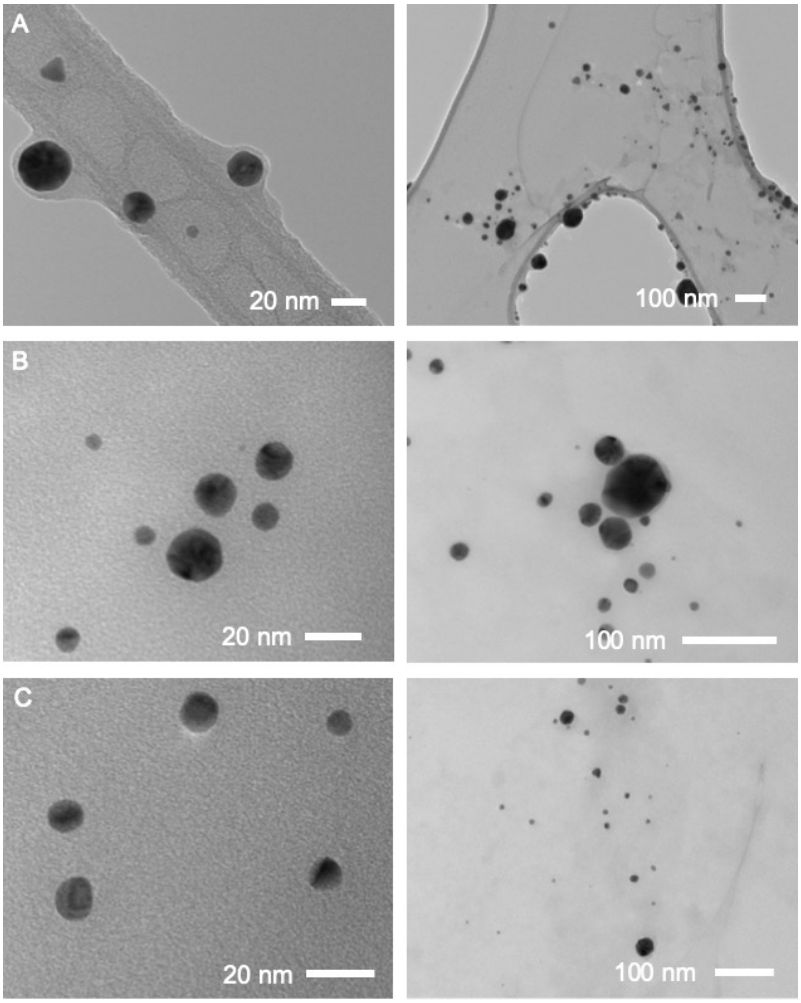

Figure 5.19: TEM images of the (A) 5 mg dsDNA-stabilised gold nanoparticles, (B) 10 mg dsDNA-stabilised gold nanoparticles and (C) 15 mg dsDNA-stabilised gold nanoparticles.

in the crucible for TGA, the dsDNA gold nanoparticle solutions were concentrated through centrifugation before being deposited into the crucible. TGA curves of these nanoparticles can be found in Appendix A6.

ssDNA-stabilised gold nanoparticles were also prepared using the same synthetic approach, simply substituting dsDNA with ssDNA. ssDNA was prepared through heating the dsDNA solution to 80 °C and cooling in ice before use in the preparation of the gold nanoparticles. The same concentrations of DNA were used in this

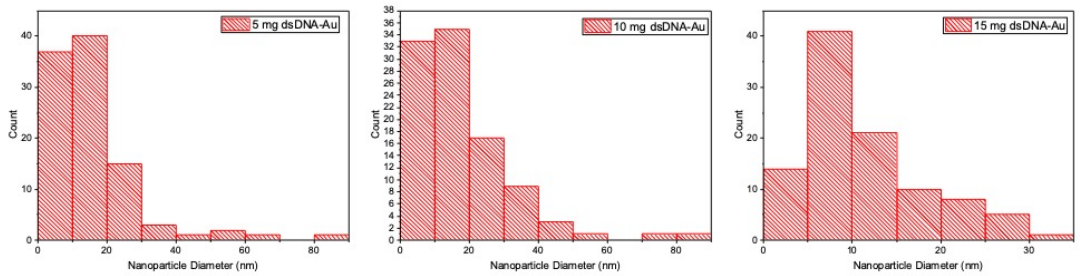

Figure 5.20: Size distribution plots for each concentration of dsDNA-stabilised nanoparticles (*n=100*).

approach. UV-Vis analysis of the 5, 10 and 15 mg ssDNA-stabilised gold nanoparticles can be found in Figure 5.21. In each case, similarly to the dsDNA-stabilised gold nanoparticles, both the DNA peak at 270 nm and the plasmon peak at 530 nm are visible for each concentration of the gold nanoparticles. However, in this instance the plasmon peak for the 5 mg ssDNA-stabilised gold nanoparticles appears much broader than both the 10 mg and 15 mg ssDNA-stabilised gold nanoparticle samples. This would point to a broader size distribution of nanoparticles that may have arisen as a result of insufficient stabilisation of the nanoparticles by the DNA during the synthesis. This could also be an indication that a concentration of 5 mg ssDNA is too low to stabilise the gold nanoparticles, where a concentration of 10 mg dsDNA is sufficient to stabilise the particles. This will be further examined through size distribution analysis of the relevant TEM images.

FTIR analysis was carried out on the ssDNA-stabilised gold nanoparticles (Figure 5.22). The results were almost identical to those obtained for the analysis of the dsDNA-stabilised gold nanoparticles, which is as expected. In each case, the DNA peak at 1650 cm^{-1} is found in each of the three samples of gold nanoparticles, and the peaks between 100 and 750 cm^{-1} are not observed in the gold nanoparticle spectra. This could be due to water obscuring these peaks.

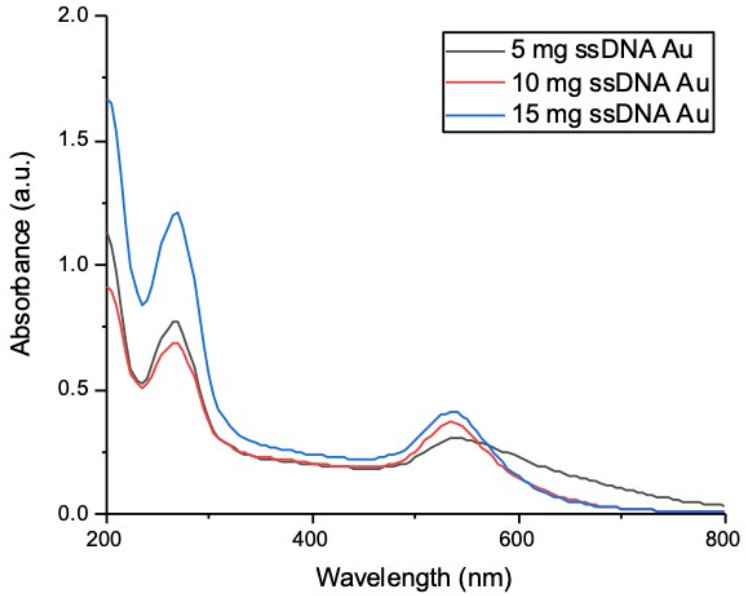

Figure 5.21: UV-Vis spectra for 5, 10 and 15 mg ssDNA-stabilised gold nanoparticles.

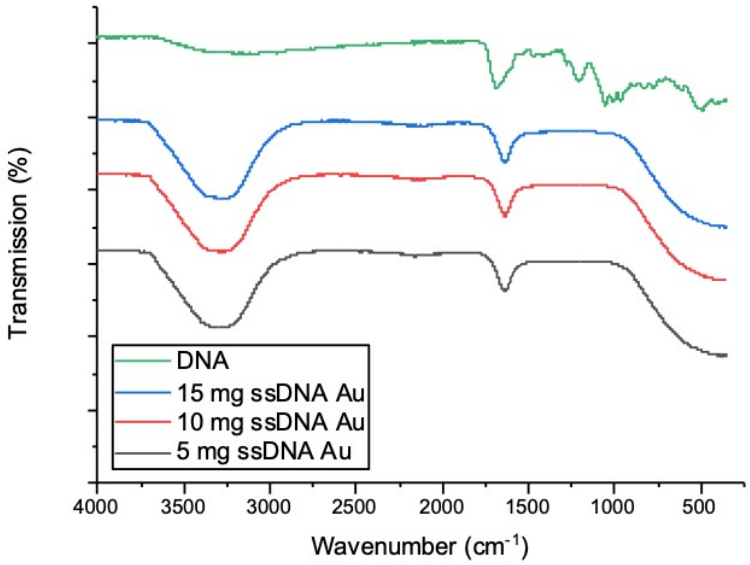

Figure 5.22: FTIR analysis of the pure DNA and the 5, 10, 15 mg ssDNA-stabilised gold nanoparticles.

Raman spectroscopic analysis was carried out for each concentration of ssDNA-

stabilised gold nanoparticles, and also on each of the initial single-stranded DNA solutions. These spectra are shown in Figures 5.23 to 5.26. Interestingly, only the 5 mg ssDNA-stabilised gold nanoparticles show enhancement of the DNA peak to a similar level to the dsDNA samples, both the 10 and 15 mg ssDNA-stabilised gold nanoparticles show the DNA peaks but only at an intensity marginally higher than the noise of the instrument and above the signal of the DNA solution itself. For the DNA signal at 1200 cm^{-1} in the 5 mg ssDNA-stabilised gold nanoparticle sample, the intensity of the peak increased from 100 to 450, representing a four-fold increase in intensity. In the other two samples the peaks of the DNA solution and the ssDNA-stabilised gold nanoparticles are comparable to each other. Further investigations into why the double-stranded DNA solutions perform dramatically better as SERS agents will be carried out in future work.

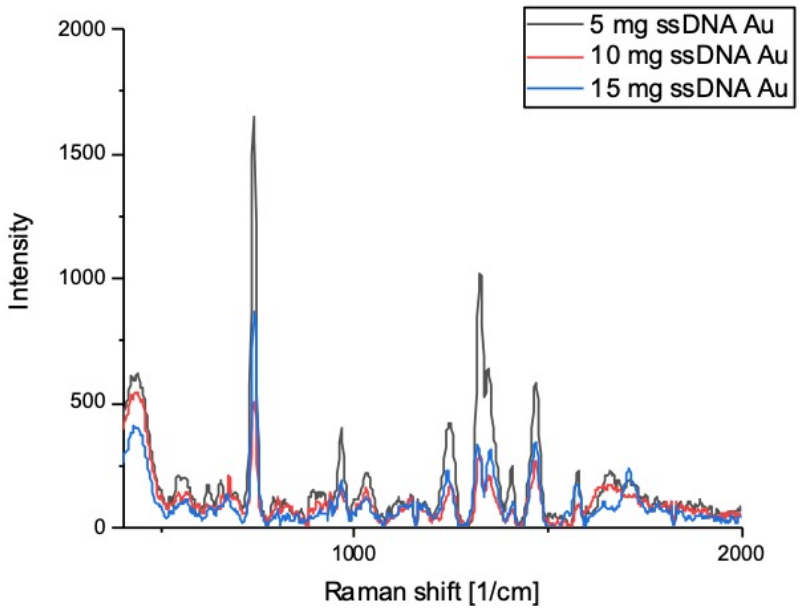

Figure 5.23: Raman spectra for 5mg, 10 mg and 15 mg ssDNA-stabilised gold nanoparticles.

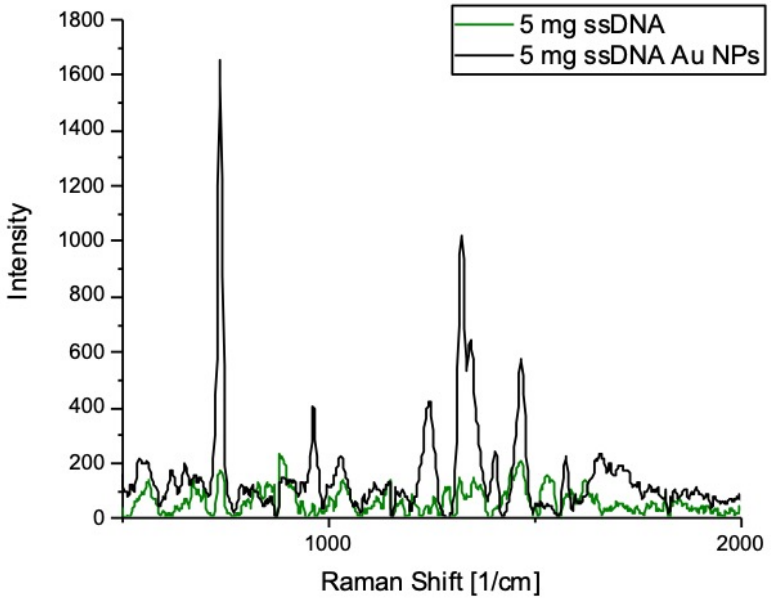

Figure 5.24: Raman spectra for the 5 mg ssDNA solution and the 5 mg ssDNA-stabilised gold nanoparticles.

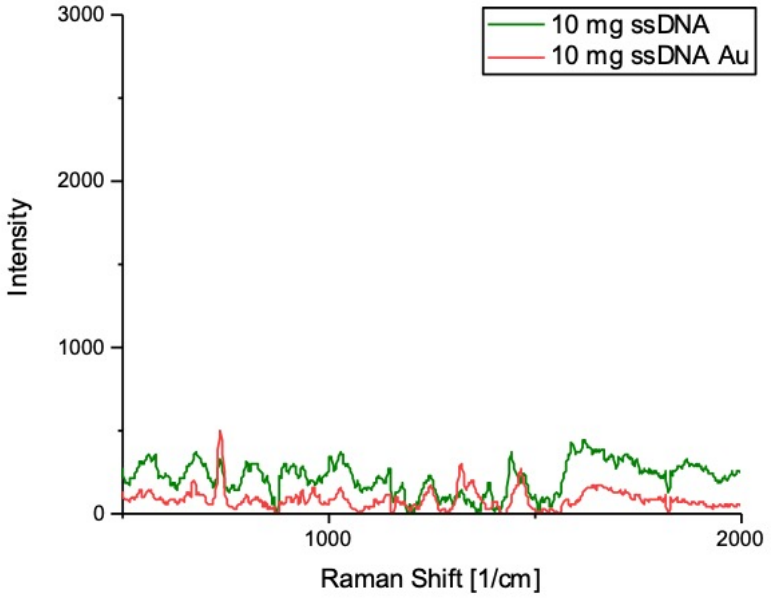

Figure 5.25: Raman spectra for the 10 mg ssDNA solution and the 10 mg ssDNA-stabilised gold nanoparticles.

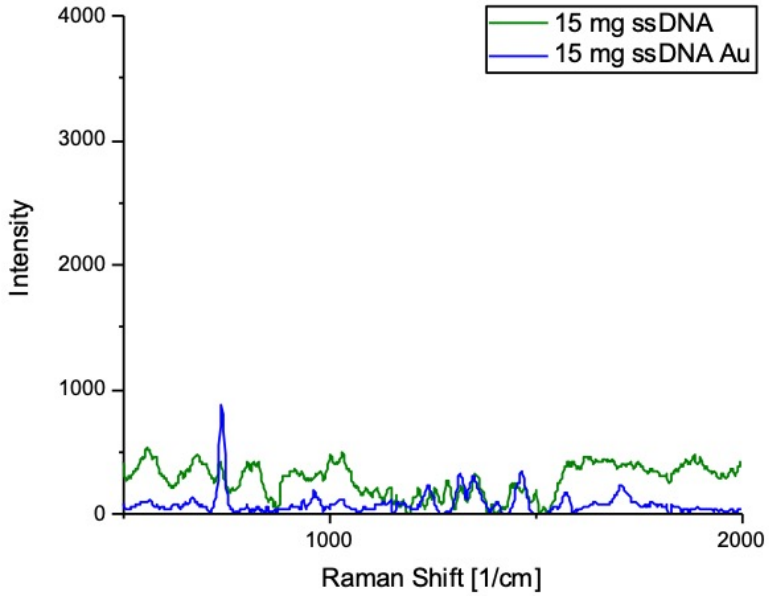

Figure 5.26: Raman spectra for the 15 mg ssDNA solution and the 15mg ssDNA-stabilised gold nanoparticles.

TEM analysis was carried out on the ssDNA-stabilised gold nanoparticles to investigate the morphology and polydispersity of the sample (Figure 5.27). It is immediately evident that there is a large size distribution and range of particle shapes throughout the three nanoparticle samples. This is most pronounced in the case of the 5 mg ssDNA-stabilised gold nanoparticles.

The polydispersity of these samples was analysed more formally through size distribution analysis (Figure 5.28). This analysis shows a large size distribution of the gold nanoparticles similar to that found for the dsDNA-stabilised gold nanoparticles. From the UV-Vis analysis a wider size distribution was expected for the 5 mg ssDNA-stabilised gold nanoparticles, however, this was not found to be the case. The average size and standard deviation for the 5 mg, 10 mg and 15 mg ssDNA-stabilised gold nanoparticles are 9.79 nm $\pm$ 6.5 nm, 16.8 nm $\pm$ 9.8 nm and 8.45 nm $\pm$ 7.7 nm respectively.

TGA was also carried out on the ssDNA-stabilised gold nanoparticles. As with the dsDNA-stabilised gold nanoparticles, the weight of the gold nanoparticles is below the minimum weight specified by the instrument. However, in the case of these nanoparticles, the TGA was still able to record a very small percentage weight loss, in the region of 0.5 % for each of the three concentrations of the ssDNA stabilised gold. These spectra are shown in Figure 5.29. In each case, the sample was run at a heating rate of 10 °C/min, and the temperature was held at 80 °C for 20 minutes in order to evaporate the water from the gold nanoparticle sample. The TGA curve showing the weight loss over the full range of temperature can be found in Appendix A7.

Both the dsDNA- and ssDNA-stabilised gold nanoparticles prepared in this work show great promise as potential SERS agents, and could be of great potential for many sensing applications.

5.3.3 Magnetic-Plasmonic DNA-Stabilised Nanocomposites

A wide variety of DNA-stabilised magnetic-plasmonic nanocomposites were prepared by mixing each concentration of the ds- and ssDNA-stabilised magnetite with each concentration of the ds- and ssDNA-stabilised gold nanoparticles and also PAH-stabilised gold nanoparticles, yielding 42 nanocomposites in total. Each nanocomposite was cleaned twice using magnetic separation. Each of these nanocomposites was given an alphanumeric code in order to easier identify the differences between composites. A full table detailing the components of each of the nanocomposites can be found in Appendix A8. Raman and UV-Vis spectroscopy were run for each nanocomposite. A representative sample is shown below, with the remaining six UV-Vis spectra and six Raman spectra to be found in Appendix A9 - A13. The

Raman spectra for nanocomposites B1 - B7 are shown in Figure 5.30. In each case the DNA peaks are still visible, however, the intensity of the peaks is much lower than that of the gold nanoparticles by themselves, and the noise in the baseline of the spectra is, in most cases, comparable to the intensity of the peaks obtained. Preliminary results from these spectra are indicative that the gold has been lost through the magnetic separation. In the optimal DNA-based magnetic-plasmonic nanocomposite, the DNA-stabilised gold would be retained to an extent that it still acted as a SERs agent in the material, and the nanocomposite would be magnetically separable from solution.

In order to investigate whether or not the gold was being leeched from the nanocomposite solution during magnetic separations, and if in fact the initial gold concentration was sufficient to obtain any SERs effects, a Raman spectra of one of the nanocomposites, B3, before and after magnetic separation is shown in Figure 5.31. It is clear from the large enhancement of the DNA peak in the nanocomposite before the magnetic separation that the DNA-stabilised gold nanoparticles could still be used as SERs agents in the magnetic-plasmonic nanocomposites. However, higher concentrations of DNA along with other charged stabilising agents must be used in order to obtain better gold retention through multiple cleaning cycles. This testing of other agents in conjunction with the DNA stabilised gold and/or magnetite nanoparticles, alongside comprehensive zeta-potential studies, will be carried out in future work.

Finally, each nanocomposite was examined using UV-Vis spectroscopy in order to determine whether or not both the DNA and plasmon peaks were visible, as the presence of both these peaks could be valuable in numerous potential sensing applications. UV-Vis spectra for the several "B" nanocomposites are shown in Figure 5.32. Unfortunately the peak for the DNA is obscured by the broad absorption from the magnetite nanoparticles in each case, with small shoulders where the peak

would be expected visible in each nanocomposite. Similarly, due to the loss of gold through magnetic separation and the broad absorbance of the magnetite, only slight shoulders are visible in the region of 530 nm where one would expect the plasmon peak.

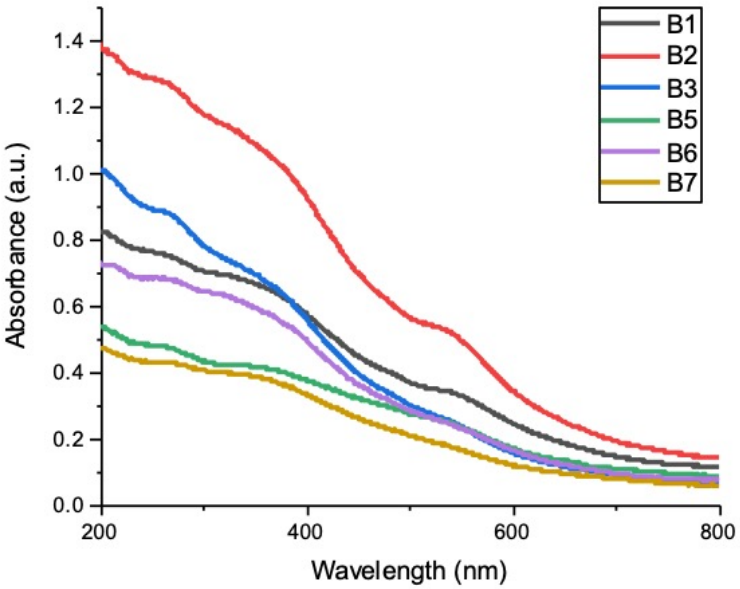

Figure 5.32: UV-Vis spectra of nanocomposite made using 10 mg dsDNA magnetite and (B1) 5 mg dsDNA Au, (B2) 10 mg dsDNA Au, (B3) 15 mg dsDNA Au, (B4) 5 mg ssDNA Au, (B5) 10 mg ssDNA Au, (B6) 15 mg ssDNA Au and (B7) PAH stabilised Au.

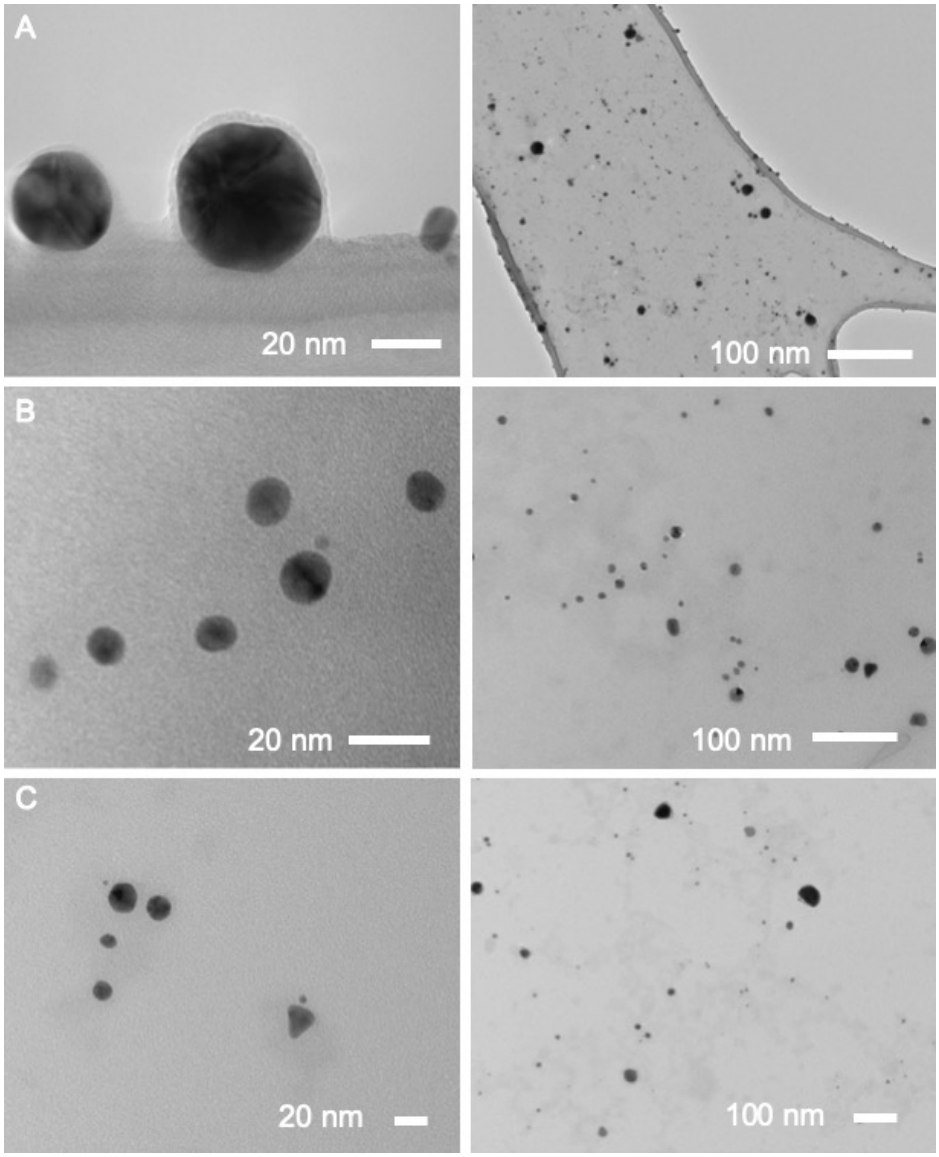

Figure 5.27: TEM images of (A) 5 mg ssDNA-stabilised gold nanoparticles, (B) 10 mg ssDNA-stabilised gold nanoparticles and (C) 15 mg ssDNA-stabilised gold nanoparticles.

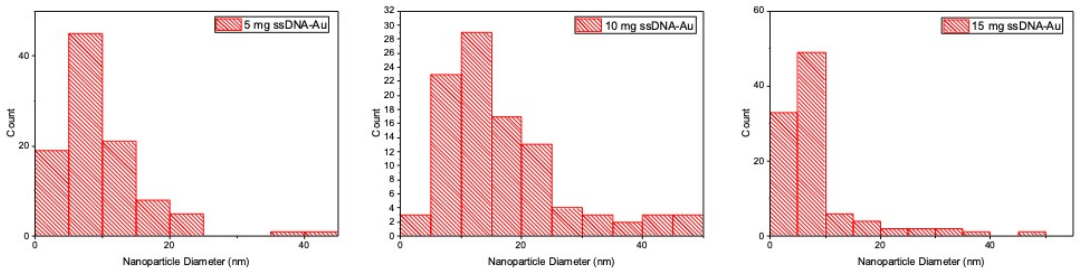

Figure 5.28: Size distribution analysis for each concentration of the ssDNA-stabilised gold nanoparticles (*n=100* in each case).

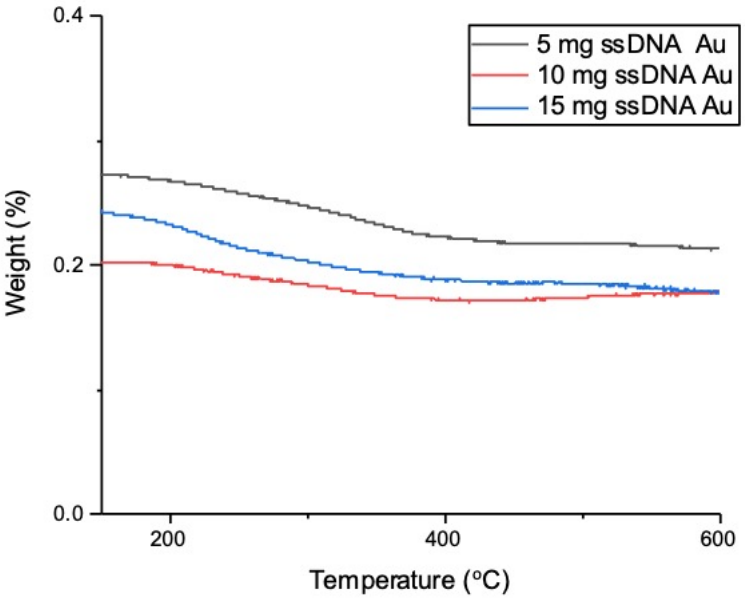

Figure 5.29: TGA curves for the ssDNA-stabilised gold nanoparticles.

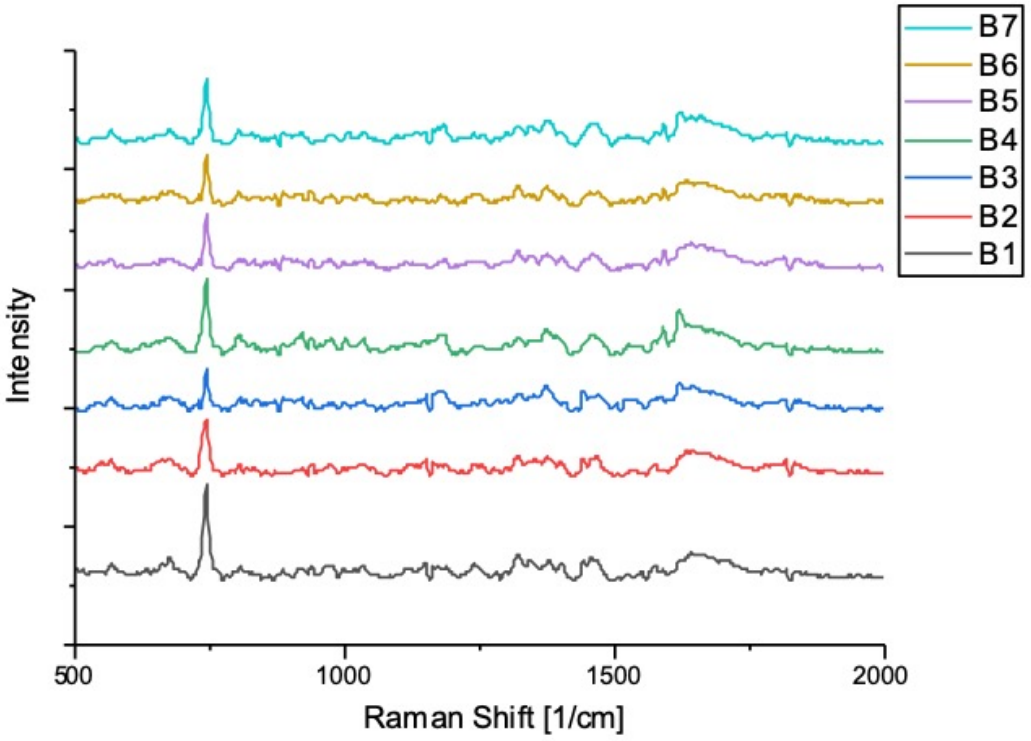

Figure 5.30: Raman spectra of nanocomposite made using 10 mg dsDNA magnetite and (B1) 5 mg dsDNA Au, (B2) 10 mg dsDNA Au, (B3) 15 mg dsDNA Au, (B4) 5 mg ssDNA Au, (B5) 10 mg ssDNA Au, (B6) 15 mg ssDNA Au and (B7) PAH stabilised Au.

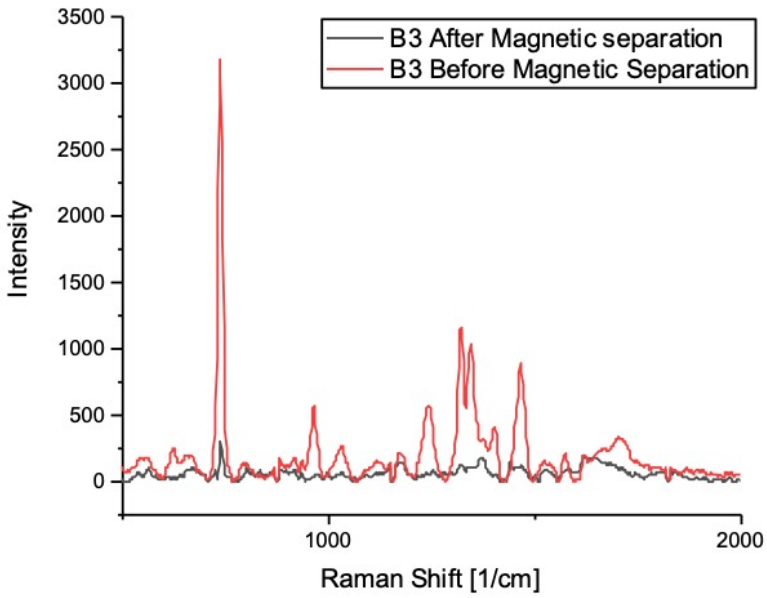

Figure 5.31: Raman spectra of the nanocomposite B3 (10 mg dDNA Magnetite and 15 mg dsDNA Au NPs) before and after magnetic separation. It is clear that the gold, which causes the enhancement of the DNA, is being lost through the separation.

5.4 Conclusions

Thus, in this work, the synthesis of both DNA-stabilised magnetite nanoparticles and DNA-stabilised gold nanoparticles, as well as magnetic-plasmonic DNA-stabilised hybrid nanomaterials were carried out.

DNA-stabilised magnetite was prepared using both double-stranded and single-stranded DNA for three initial DNA concentrations of 5, 10 and 15 mg DNA in 25 mL MP water. For each concentration, and for both the double-stranded and single-stranded samples of DNA, superparamagnetic magnetite nanoparticles were obtained. FTIR and the magnetic measurements showed that it is likely that there is DNA conjugated to the surface of the nanoparticles for each concentration of the dsDNA- and ssDNA-stabilised particles; while TGA for the ssDNA-stabilised magnetite nanoparticles showed that a weight loss occurs from each sample in the region expected for the decomposition of DNA. TEM analysis illustrated a polydisperse sample of nanoparticles, however, this is to be expected as the use of heat was not used in the preparation of the sample as it would have resulted in the DNA being denatured or partially destroyed.

The preparation of both dsDNA- and ssDNA-stabilised gold nanoparticles was carried out for three concentrations of DNA solutions, 5 mg, 10 mg and 15 mg DNA in 25 mL MP water. UV-Vis studies showed peaks for both DNA and the gold plasmon, which was the first indication that the DNA had successfully been coated around the gold nanoparticle. FTIR studies also showed the presence of characteristic DNA peaks in each of the three concentrations of DNA-stabilised particles for both the double-stranded and single-stranded DNA. Raman studies conducted on the dsDNA-stabilised and ssDNA-stabilised gold nanoparticles showed the dsDNA-stabilised gold nanoparticles to be effective SERs agents, while the ssDNA-stabilised gold nanoparticles did not show any SERs enhancement. TEM analysis of all 6 sam-

ples found them to be quite polydisperse, however, this polydispersity may in fact have contributed to the effectiveness of the SERs for these samples[19–21].

A wide variety of DNA-based magnetic-plasmonic nanocomposites were prepared using each concentration of the dsDNA- and ssDNA-stabilised magnetite and gold nanoparticles, as well as a sample of PAH-stabilised gold nanoparticles. In each case, it was found that a large proportion of the gold nanoparticles were being lost in cleaning steps, resulting in reduced SERs ability and the loss of plasmon peaks in the UV-Vis spectra. However, further optimisation of the synthesis of composites at different concentrations of DNA used in these nanocomposites will be carried out in future work. It is thought that these nanocomposites could have a variety of potential applications in SERs and testing.

Bibliography

(1) A. Samanta and I. L. Medintz, *Nanoparticles and DNA-a powerful and growing functional combination in bionanotechnology*, 2016.

(2) L. Hu, Y. Sun and Y. Wu, *Nanoscale*, 2013, **5**, 3103–3111.

(3) F. Zhang, J. Nangreave, Y. Liu and H. Yan, *Structural DNA nanotechnology: State of the art and future perspective*, 2014.

(4) I. Yildiz, S. Shukla and N. F. Steinmetz, *Applications of viral nanoparticles in medicine*, 2011.

(5) D. Vasilescu, H. Grassi and M.-A. Rix-Montel, in *Polyelectrolytes and their Applications*, Springer Netherlands, 1975, pp. 197–216.

(6) M. Magro, T. Martinello, E. Bonaiuto, C. Gomiero, D. Baratella, G. Zoppellaro, G. Cozza, M. Patruno, R. Zboril and F. Vianello, *Biochimica et Biophysica Acta - General Subjects*, 2017, **1861**, 2802–2810.

(7) D. Evanko, *Nature Methods*, 2004, **1**, 102.

(8) J. R. Sosa-Acosta, C. Iriarte-Mesa, G. A. Ortega and A. M. Díaz-García, *DNA–Iron Oxide Nanoparticles Conjugates: Functional Magnetic Nanoplatforms in Biomedical Applications*, 2020.

(9) S. L. Sahoo and C. H. Liu, *Colloids and Surfaces A: Physicochemical and Engineering Aspects*, 2015, **482**, 184–194.

(10) Y. Haddad, K. Xhaxhiu, P. Kopel, D. Hynek, O. Zitka and V. Adam, *International Journal of Molecular Sciences*, 2016, **17**, DOI: 10.3390/ijms17040550.

(11) I. Robinson, L. D. Tung, S. Maenosono, C. Wälti and N. T. Thanh, *Nanoscale*, 2010, **2**, 2624–2630.

(12) B. Liu and J. Liu, *Methods for preparing DNA-functionalized gold nanoparticles, a key reagent of bioanalytical chemistry*, 2017.

(13) R. K. DeLong, C. M. Reynolds, Y. Malcolm, A. Schaeffer, T. Severs and A. Wanekaya, *Nanotechnology, Science and Applications*, 2010, **3**, 53–63.

(14) A. Heuer-Jungemann, P. K. Harimech, T. Brown and A. G. Kanaras, *Gold nanoparticles and fluorescently-labelled DNA as a platform for biological sensing*, 2013.

(15) M. Stoia, R. Istratie and C. Păcurariu, *Journal of Thermal Analysis and Calorimetry*, 2016, **125**, 1185–1198.

(16) S. M. Watson, H. D. A. Mohamed, B. R. Horrocks and A. Houlton, *Nanoscale*, 2013, **5**, 5349–5359.

(17) M. D'Abramo, C. L. Castellazzi, M. Orozco and A. Amadei, *Journal of Physical Chemistry B*, 2013, **117**, 8697–8704.

(18) M. B. Fenn, P. Xanthopoulos, G. Pyrgiotakis, S. R. Grobmyer, P. M. Pardalos and L. L. Hench, *Advances in Optical Technologies*, **2011**, 1–20.

(19) M. Moskovits, *Physical Chemistry Chemical Physics*, 2013, **15**, 5301–5311.

(20) P. K. Aravind and H. Metiu, *Chemical Physics Letters*, 1980, **74**, 301–305.

(21) K. Kneipp, H. Kneipp, I. Itzkan, R. R. Dasari and M. S. Feld, *Surface-enhanced Raman scattering and biophysics*, tech. rep., 2002, pp. 597–624.

Chapter 6

Magnetic-Plasmonic $CaCO_3$-Based Microstructures

6.1 Introduction

Calcium carbonate has a wide range of existing and potential biomedical applications. Due to its biocompatibility, $CaCO_3$ has already found uses as an essential component in a number of drug delivery systems, as a packing agent in pharmaceutical tablets, as an antacid, and as calcium supplements[1–3].

Calcium carbonate microparticles are also of huge research interest. For example, their use can expand the therapeutic window due to the slow degradation of $CaCO_3$, and also due to the fact that the targeted system delivers more of the drug to the desired site in the body, thus requiring a lower effective load and reducing any latent side effects related to the medication. This allows sustained release of a drug from the microparticle. $CaCO_3$ can degrade in the body in two ways - by phagocytosis and by dissolution in bodily fluids. CO_3^{2-} is stored in the body, causing no harm to cells, and Ca^{2+} is metabolised and excreted[4].

These favourable properties make $CaCO_3$ a promising candidate as a substrate for the preparation of new magnetic-plasmonic composite structures for a wide range of potential biological applications[5]. The porous nature of the microspheres make them suitable for the deposition of smaller nanoparticles, while the hollow centre present in some $CaCO_3$ microspheres could facilitate the encapsulation of magnetic nanoparticles inside the structure, endowing magnetic functionality and also allowing scope for the nanoparticles to be released at a site of interest[6]. Furthermore, the surface of the microspheres can be functionalised with polymers which would allow for layer-by-layer deposition of any desired species or nanoparticles[7]. Previous work carried out with our collaborators involved the synthesis of magnetic fluorescent microspheres that could be used for the detection of Legionella pneumophila bacteria[8]. In some instances, a sufficient number of layers could be deposited such that the calcium carbonate can be dissolved resulting in a hollow stable polymer microsphere.

In this chapter, different approaches to the preparation of multimodal magnetic-plasmonic calcium carbonate microspheres were explored for potential theranostic applications.

6.2 Aims

In this chapter the main aim is to prepare a variety of $CaCO_3$ based magnetic-plasmonic microstructures. First, magnetite nanoparticles and gold nanoparticles must be prepared to a high quality and monodispersity. Then, three different approaches will be used in order to prepare the magnetic plasmonic microstructures. The first involves a template-directed synthesis of the microspheres in which the magnetic nanoparticles are encapsulated within pores of the hollow microsphere structure. The second approach involved the formation of framboidal microstructures that utilise the magnetic nanoparticles as nucleation sites for the growth of the calcium carbonate. The third approach involves the template-directed synthesis of hollow microspheres in the presence of gold nanoparticles, after which they will be further functionalised via a layer-by-layer approach using magnetite and gold nanoparticles.

These multimodal microparticles will then be characterised by XRD, FTIR, SEM, VSM and EDX analysis. We believe that the new multimodal micro-structures will find a range of important applications including magnetic separation, sensing, diagnostics and drug delivery.

6.3 Results and Discussion

In order to prepare multimodal magnetic-plasmonic calcium carbonate based microstructures, firstly both magnetite and gold nanoparticles must be synthesised and characterised. These nanoparticles will then be used in the synthesis or functionalisation of the calcium carbonate microstructures.

6.3.1 Synthesis of Magnetite Nanoparticles

Magnetite nanoparticles were synthesised using a modified coprecipitation approach. Sodium bicarbonate was used to precipitate the nanoparticles from a solution of iron (II) and iron (III) salts, which were then allowed to reflux for 100 minutes, building on work discussed in Chapter 4.

Depending on the desired application or encapsulation method, both *L*-Cysteine and PSS were used as stabilising agents. The use of *L*-Cysteine stabilised magnetite in the formation of the multimodal microspheres is expected to make them chiral. In each case, the resulting nanoparticle solutions were brown/black in colour, which is indicative of the formation of magnetite. The resulting nanoparticles were cleaned multiple times using magnetic separation.

VSM analysis was carried out on this magnetite, and the magnetisation curve is shown in Figure 6.1. The curve shown is for *L*-Cysteine stabilised magnetite, and it is consistent with the nanoparticles stabilised in PSS. The magnetite was found to have a magnetisation moment of 59.1 Am^2/Kg, which is comparable with similarly synthesised magnetite nanoparticles. VSM again shows that there is no hysteresis loop, which indicates that the synthesised nanoparticles are superparamagnetic.

Powder XRD analysis was also carried out on the synthesised nanoparticles, to en-

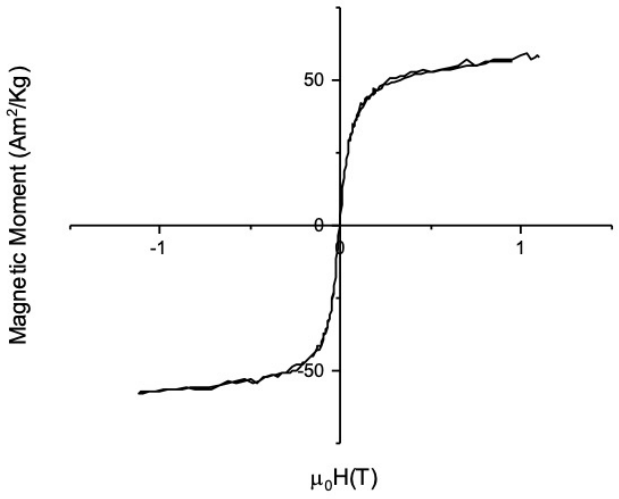

Figure 6.1: VSM curve for *L*-Cysteine stabilised magnetite.

sure that it was magnetite that was formed, and not maghemite or another oxidised iron oxide species. The XRD pattern obtained is shown in Figure 6.2, and shows that the peaks correlate well with those for confirmed samples of magnetite.

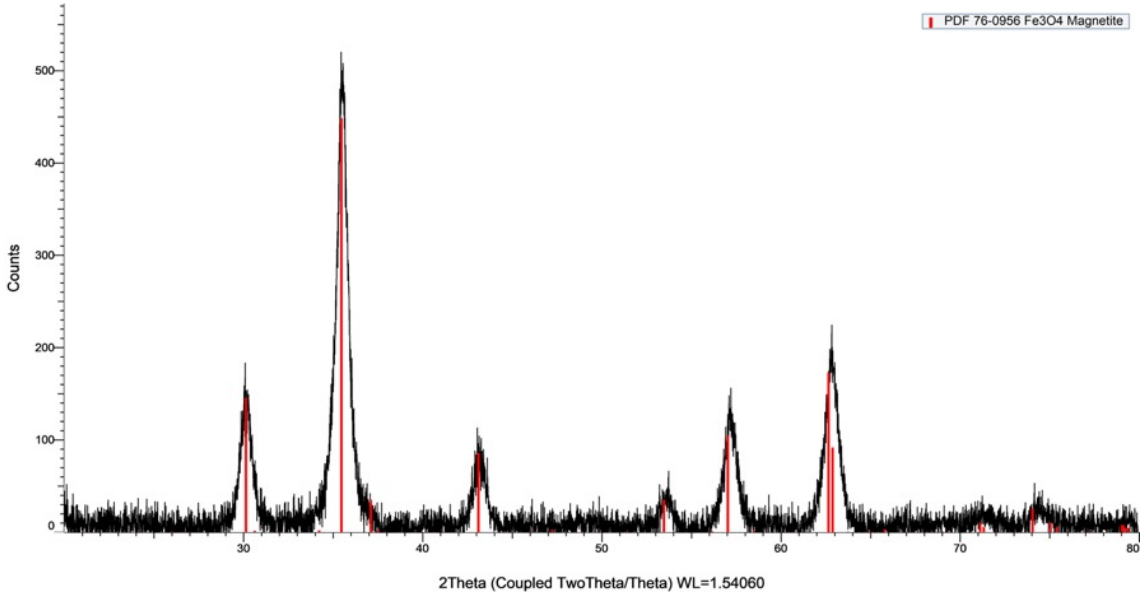

Figure 6.2: Powder XRD pattern for magnetite nanoparticles.

TEM analysis was also carried out on the magnetite nanoparticles in order to deter-

mine their size distribution and morphology (Figure 6.3). The nanoparticles were spherical and appear monodisperse, with no large aggregates and only one apparent size distribution. The nanoparticles have an average size of 17.5 ± 5 nm as shown in Figure 6.4.

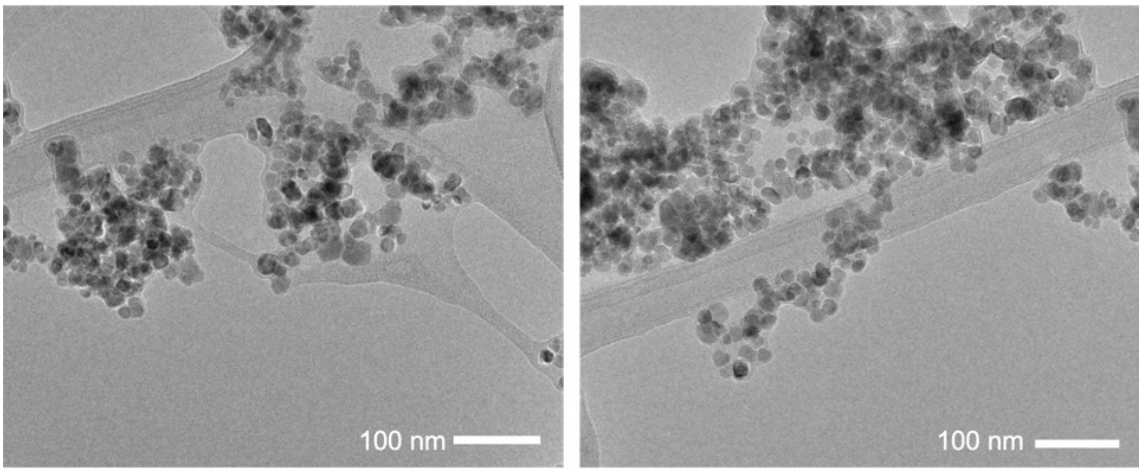

Figure 6.3: TEM images showing magnetite nanoparticles.

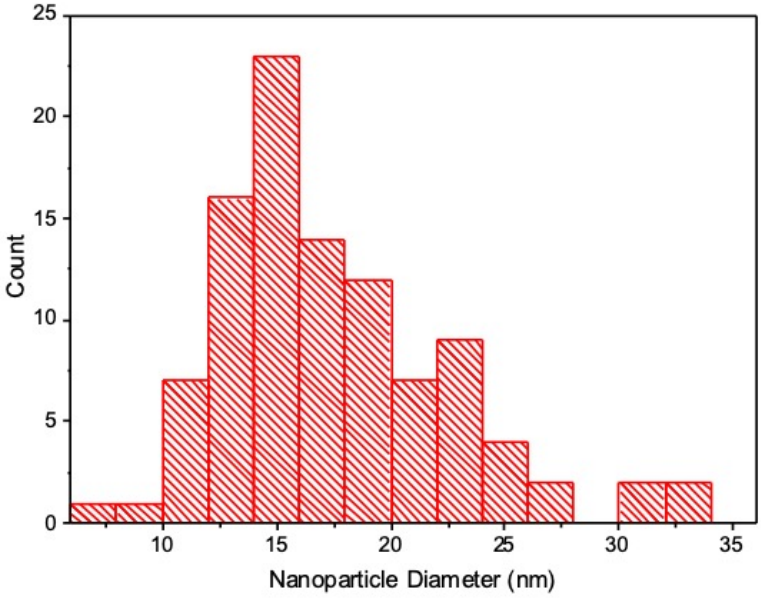

Figure 6.4: Size distribution of magnetite nanoparticles (*n=100*)

Having used VSM and TEM analysis to confirm that the synthesised PSS-stabilised and *L*-Cysteine stabilised magnetite nanoparticles are magnetic, spherical and monodisperse, these nanoparticles will then be further utilised in the preparation of the three different types of $CaCO_3$ microstructured materials.

6.3.2 Citrate-Stabilised Gold Nanoparticles

Citrate-stabilised gold nanoparticles were prepared using the aforementioned Turkevich method. Briefly, a solution of chloroauric acid and NaOH was brought to the boil. Sodium citrate was added quickly and the solution was allowed to stir for 30 minutes until the nanoparticle solution was wine red, indicating the formation of gold nanoparticles.

UV-Vis analysis was carried out to confirm the presence of the gold nanoparticles, as shown in Figure 6.5. A single plasmon peak at 530 nm was observed, indicating the presence of spherical gold nanoparticles.

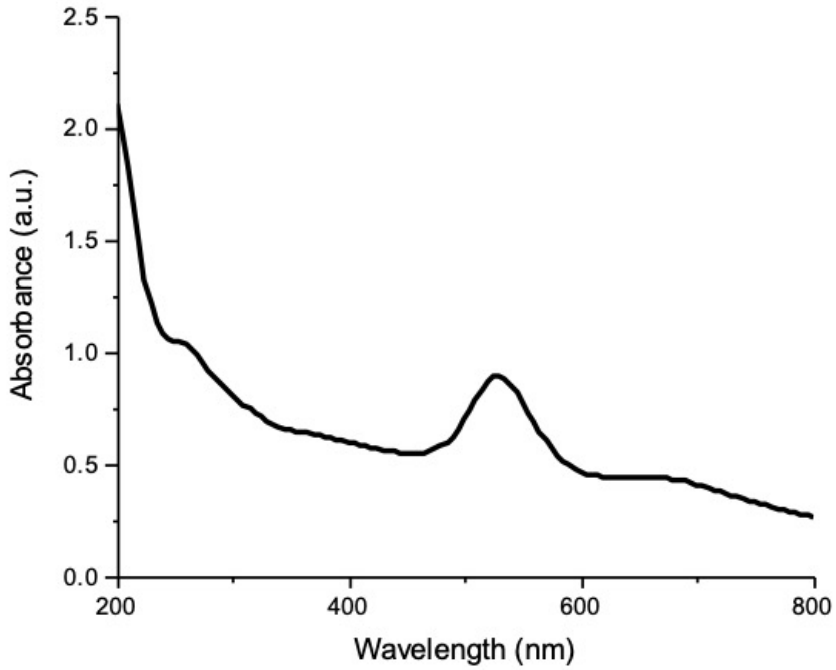

Figure 6.5: UV-Vis spectrum of citrate-stabilised gold nanoparticles.

TEM analysis was carried out to examine the size and morphology of the citrate-stabilised nanoparticles as shown in Figure 6.6. The gold nanoparticles are spherical and monodisperse, and do not appear to have any large aggregates. They have an average size of 11.7 ± 1.8 nm as shown in the size distribution plot in Figure 6.7.

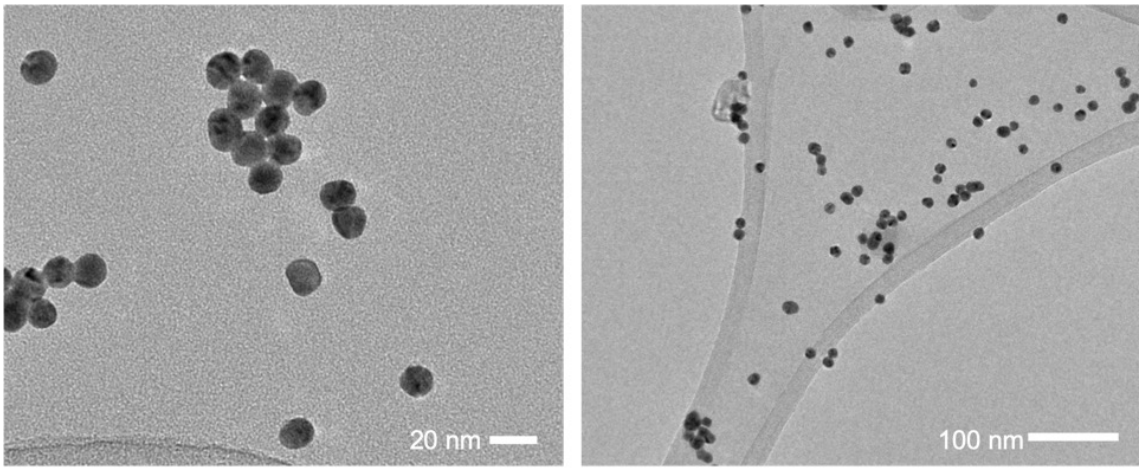

Figure 6.6: TEM images showing citrate-stabilised gold nanoparticles.

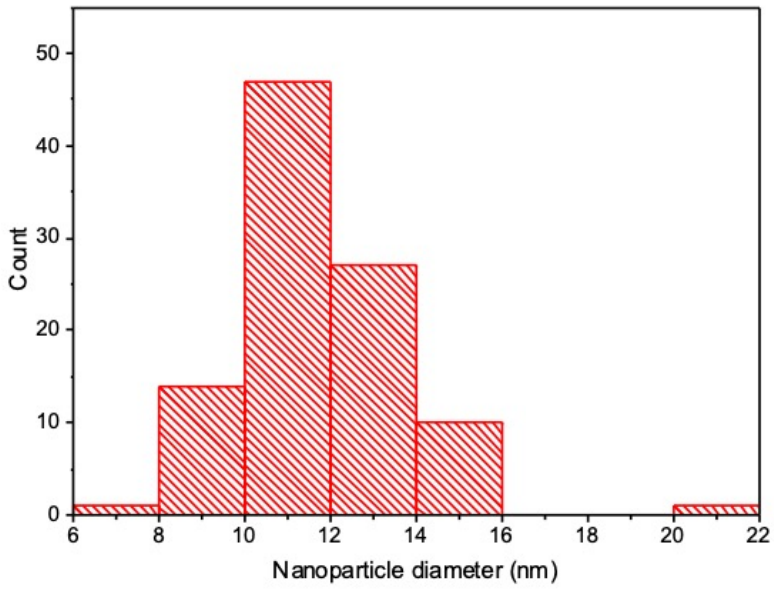

Figure 6.7: Size distribution plot of the citrate-stabilised gold nanoparticles (*n=100*).

The citrate-stabilised gold nanoparticles display a plasmon peak at 530 nm in the UV-Vis (Figure 6.5) and appear uniform and monodisperse in the TEM analysis. These nanoparticles will then be further used in the preparation of the magnetic-plasmonic calcium carbonate microsphere structures.

6.3.3 Preparation of Calcium Carbonate Microstructures

As mentioned previously, three different approaches to the development of calcium carbonate microstructures were explored. Two of these methods are based on a template-directed approach to the development of hollow microsphere structures. In one of these approaches, the citrate-stabilised gold nanoparticles are incorporated into the hollow microspheres *in-situ* by adding them to the initial reaction mixture. The other approach is based on the work by Sergeeva *et al.*[9]. This involves the preparation of raspberry-like calcium carbonate polycrystals that contain magnetite nanoparticles. The magnetite nanoparticles are included in the synthesis and act as nucleation points for the growth of the calcium carbonate structures. Each of these three approaches will be discussed in turn below.

Preparation of Hollow Magnetic Calcium Carbonate Microspheres

Sodium dodecyl sulfate (SDS) and polyvinylpyrrolidone (PVP) were used as templates for the growth of hollow calcium carbonate microspheres. The SDS and PVP form complex micelles on which the calcium carbonate can nucleate. Once the microspheres have formed, the structures are dried at 80 ^{o}C for either 24 or 72 hours, which removes the two organic species, resulting in hollow $CaCO_3$ microspheres. A scheme depicting this process is shown in Figure 6.8.

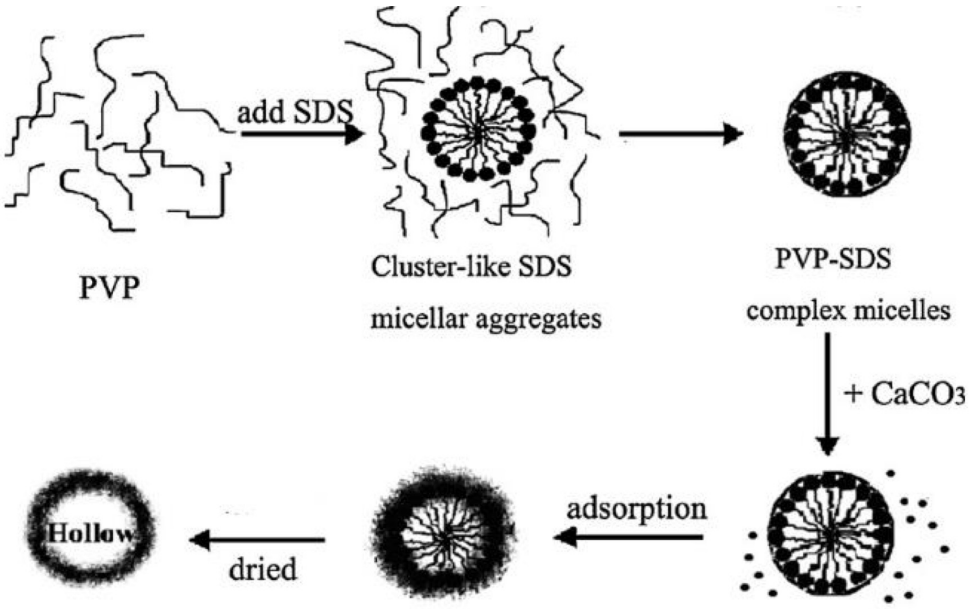

Figure 6.8: Reaction scheme showing formation of hollow microspheres. Adapted from Zhao *et al.*[10].

Initially, two samples of these microspheres were prepared; the first were allowed to dry for 24 hours, and the second were allowed to dry for 72 hours, both at 80 ^{o}C in air. SEM analysis (Figure 6.9) shows that the sample that was dried for a longer period was slightly more monodisperse and showed less overall aggregation. However, in both syntheses there were two distinct size distributions formed. This is quite typical for this particular syntheses, and a number of centrifugation steps should be carried out in order to separate these two distributions. As $CaCO_3$ is a non-conductive material, it charges under the electron beam, as can be seen in the SEM images. This can be controlled to an extent by lowering the accelerating voltage of the electron beam, however, the charging can be a useful indication of whether or not the material has been coated with a conductive material, for example magnetite or gold.

Size distribution analysis was also carried out on the 24 hour and 72 hour samples of calcium carbonate microspheres. These can be found in Figure 6.10. The mi-

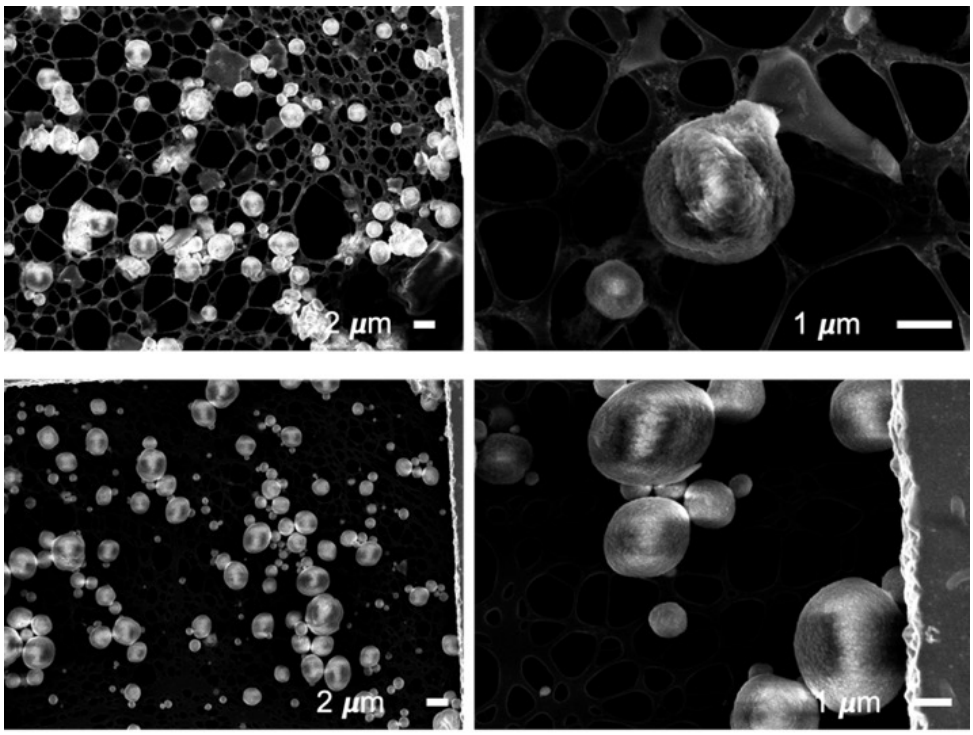

Figure 6.9: SEM images showing calcium carbonate microspheres dried for 24 hours (top row) and 72 hours (bottom row).

crospheres dried for 24 hours had a mean diameter of 1.28 μm $\pm$ 0.61 μm, and the microspheres dried for 72 hours had a mean diameter of 1.4 μm $\pm$ 0.9 μm. Although the microspheres dried for a shorter period of time appear to have a smaller standard deviation, the SEM images for the microspheres dried for 72 hours shows a much cleaner sample. This is likely due to any excess organic material being burned off over the longer drying time. As a result, the 72 hour dried microspheres were used in the further synthetic steps.

A high resolution image showing the porous and uneven nature of the surface of the hollow microspheres is shown in Figure 6.11. The porous nature of these nanoparticles should aid their further functionalisation with a number of nanoparticle species. This is because the nanoparticles could penetrate in or adhere to the pores in the structure.

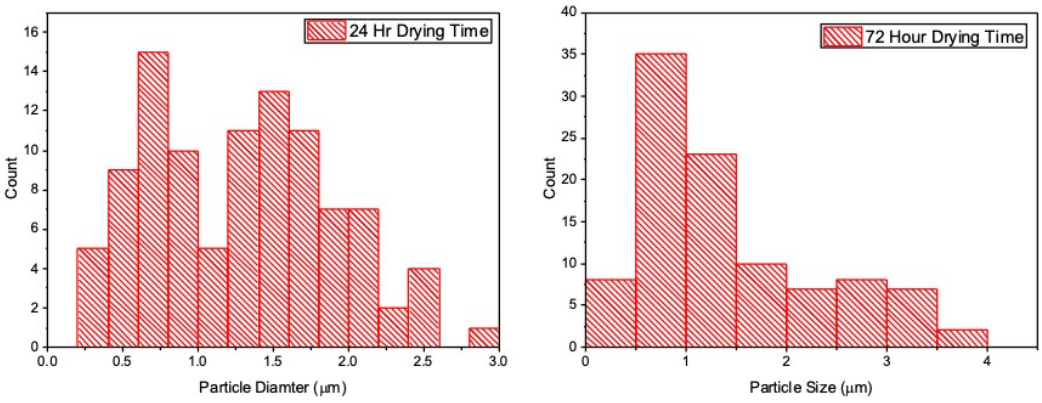

Figure 6.10: Size distribution plots for the $CaCO_3$ microspheres dried for 24 and 72 hours. *N=100* in each case.

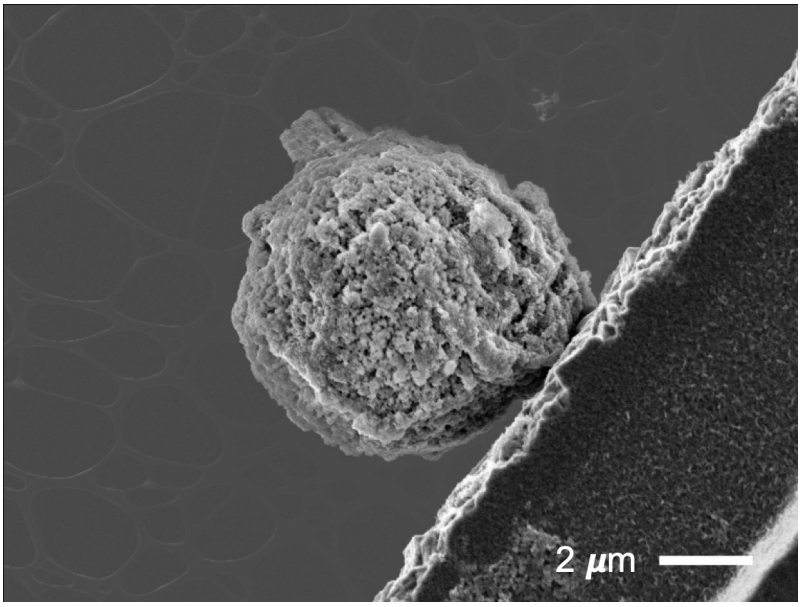

Figure 6.11: SEM image showing the porosity of the structure of a $CaCO_3$ microspheres.

These $CaCO_3$ microspheres were then further functionalised with magnetite nanoparticles. Three different kinds of nanoparticles were tested - bare Fe_3O_4 nanoparticles, PSS-stabilised Fe_3O_4 and *L*-Cysteine-stabilised Fe_3O_4. The coating was carried out by simply shaking the magnetite nanoparticles with the microspheres for 30 minutes. It is thought that the nanoparticles will either be encapsulated into the pores or rest

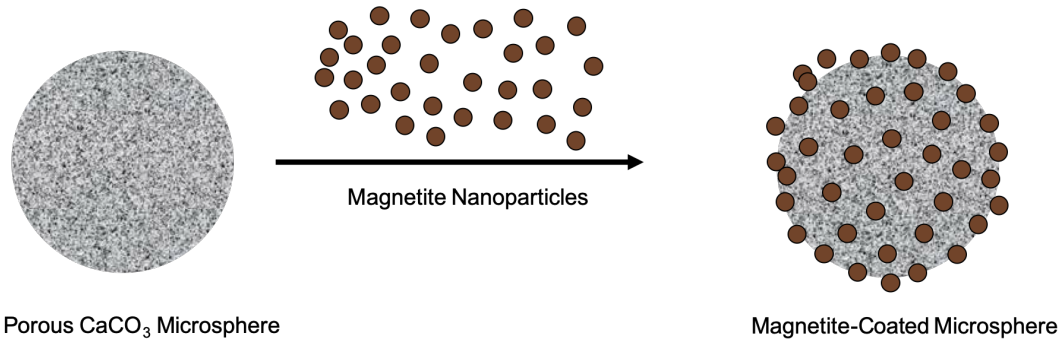

Figure 6.12: Scheme showing coating of porous $CaCO_3$ microspheres with magnetite nanoparticles.

in the spaces on the uneven surface of the particles. A scheme showing the synthetic approach to preparing these magnetic microparticles is presented in Figure 6.12.

The microparticles were cleaned 3 times using centrifugation at 5,000 RPM and dried for 24 hours in air at 80 °C. A relatively low centrifugation speed was chosen in the hope that the larger microspheres would fall out of solution, and any free magnetite would remain in solution. XRD analysis was carried out on the resulting microspheres (Figure 6.13). There was not sufficient magnetic material to utilise magnetic separation as a cleaning technique, however, the solution did appear to be attracted to an applied magnet over a time period of approximately 30 minutes.

The XRD pattern shows both the characteristic peaks for calcite and magnetite. The XRD indicates that calcite is the only polymorph present in the microspheres. This is consistent with the works by Zhao *et al.* The XRD also shows that there is magnetite present. While this is indicative that the magnetite is in the microspheres, further evidence is needed to prove this.

SEM images of the coating steps using the unstabilised Fe_3O_4, PSS-stabilised Fe_3O_4 and the *L*-Cysteine stabilised Fe_3O_4 are shown in Figure 6.14. In Figure 6.14(A) it can be seen that the unstabilised magnetite is partially coated, this can be concluded from the change in surface structure and charging of the microspheres. The

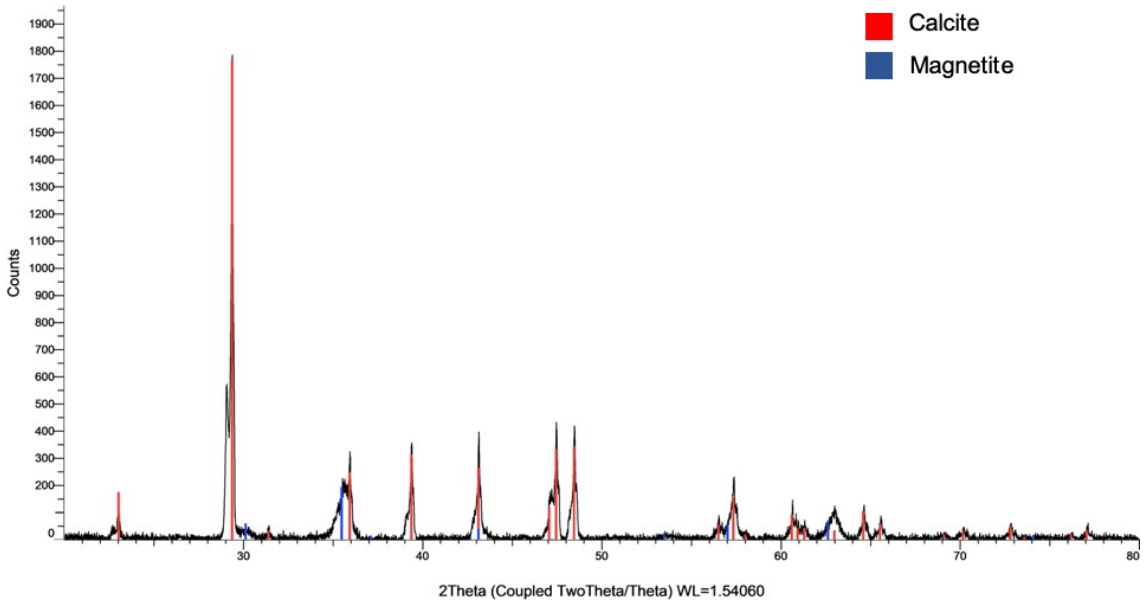

Figure 6.13: XRD pattern for Fe_3O_4@$CaCO_3$ microstructures.

PSS-stabilised magnetite sample appears to show more uniform coating than the unstabilised magnetite (Figure 6.14(B)). Here it seems that the magnetite coating represents a much larger proportion of the microspheres, however this will be further investigated using EDX. The microspheres were also coated using *L*-Cysteine stabilised magnetite nanoparticles, and these SEM images are shown in Figure 6.14(C). In the first image A (left), we can see a coated and uncoated microsphere - this is clear from the change in morphology and contrast in the two microspheres. It can also be seen in the second image A (right) that the magnetite nanoparticles can be seen to coat the majority of the microspheres, however, this too will need to be confirmed by EDX analysis.

EDX analysis was carried out on the PSS-stabilised Fe_3O_4@$CaCO_3$ and the *L*-Cysteine stabilised Fe_3O_4@$CaCO_3$ samples to determine the elemental composition of the microspheres, and to find whether or not the magnetite nanoparticles had been deposited/encapsulated by the microspheres. EDX mapping for the PSS-stabilised Fe_3O_4@$CaCO_3$ microspheres is shown in Figure 6.15. In Figure 6.15 (A), the SEM image showing the area that was mapped is presented. The contrast is much more

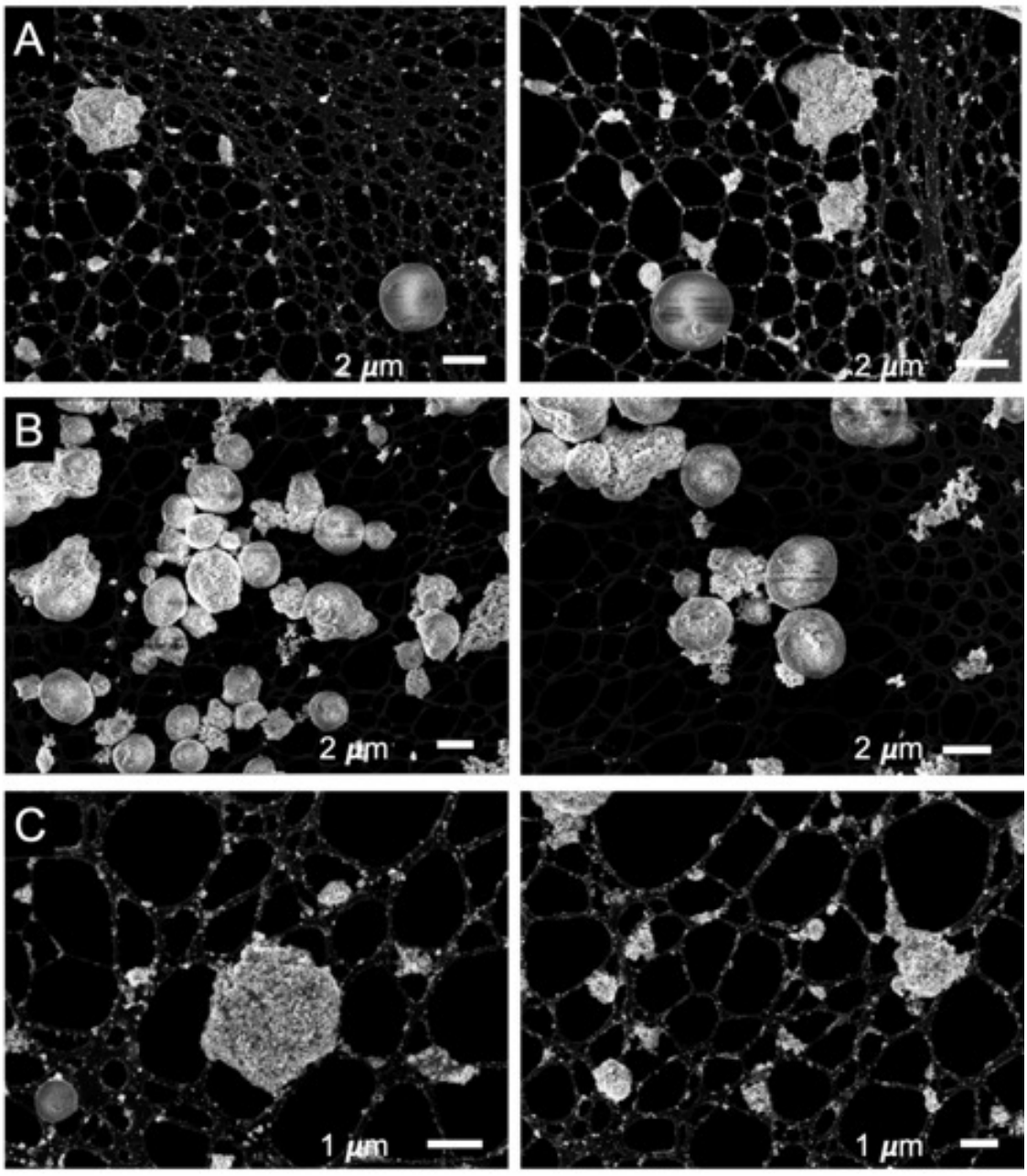

Figure 6.14: SEM images of the Fe_3O_4@$CaCO_3$ for (A) unstabilised Fe_3O_4, (B) PSS-stabilised Fe_3O_4 and (C) 0.2 M *L*-Cysteine stabilised Fe_3O_4.

stark than previous microscopy due to the higher accelerating voltage that must be applied in order to carry out the elemental analysis. Figure 6.15 (B), (C) and (D) show the carbon, calcium and oxygen that are as expected for the $CaCO_3$ microspheres. The mapping shows the clearly defined microsphere structures. The iron map is shown in Figure 6.15 (E). The map shows that there is a presence of iron that appears to be on or in the microspheres. Once again, the shape of the microspheres can be clearly seen through the iron mapping, indicating successful coating of the microspheres. The clusters of unbound magnetite can also be seen in the mapping with a higher iron concentration. The lower iron concentration relative to the other elements is as expected, as they are simply coating the material.

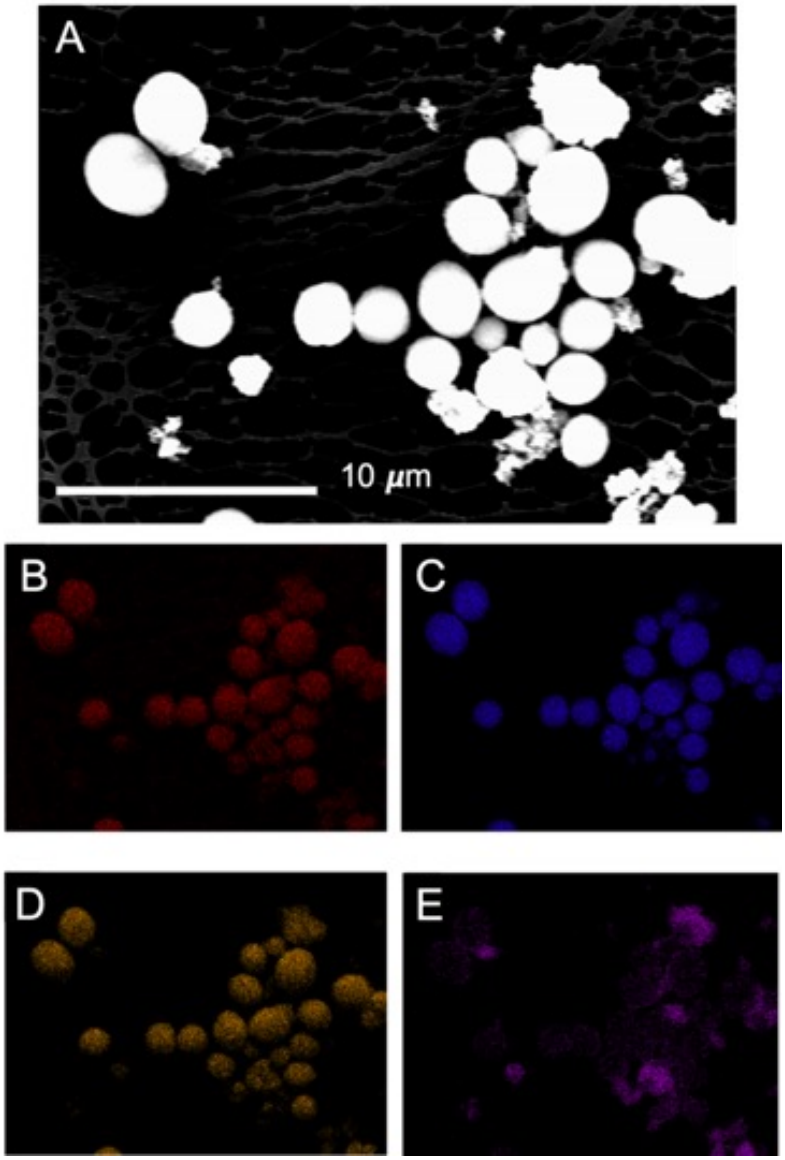

Figure 6.15: EDX mapping of the PSS-stabilised Fe_3O_4@$CaCO_3$ microspheres. (A) SEM image used for mapping, (B) Carbon map, (C) Calcium map, (D) Oxygen map and (E) Iron map.

EDX analysis was also carried out on a sample of the *L*-Cysteine stabilised microspheres, and this is shown in Figure 6.16. The SEM image of the area used for elemental mapping is shown in Figure 6.16 (A). Similarly to the images shown in Figure 6.16, the contrast in the SEM image is much higher than those for previous SEM images due to the high accelerating voltage required for elemental analysis. The mapping for (B) Carbon, (C) Calcium and (D) Oxygen are as expected, and show

clearly the composition of the microspheres. The map for iron shown in Figure 6.16 (E) shows the magnetite nanoparticles uniformly coating the $CaCO_3$ microspheres, both the large microsphere in the centre of the image and the microsphere that can be partially seen in the upper left-hand corner of the image. In addition to the magnetite nanoparticles coating the microspheres, the iron mapping also shows the clusters of unbound magnetite nanoparticles that can also be seen in Figure 6.16 (A) that are not highlighted in any of the other maps.

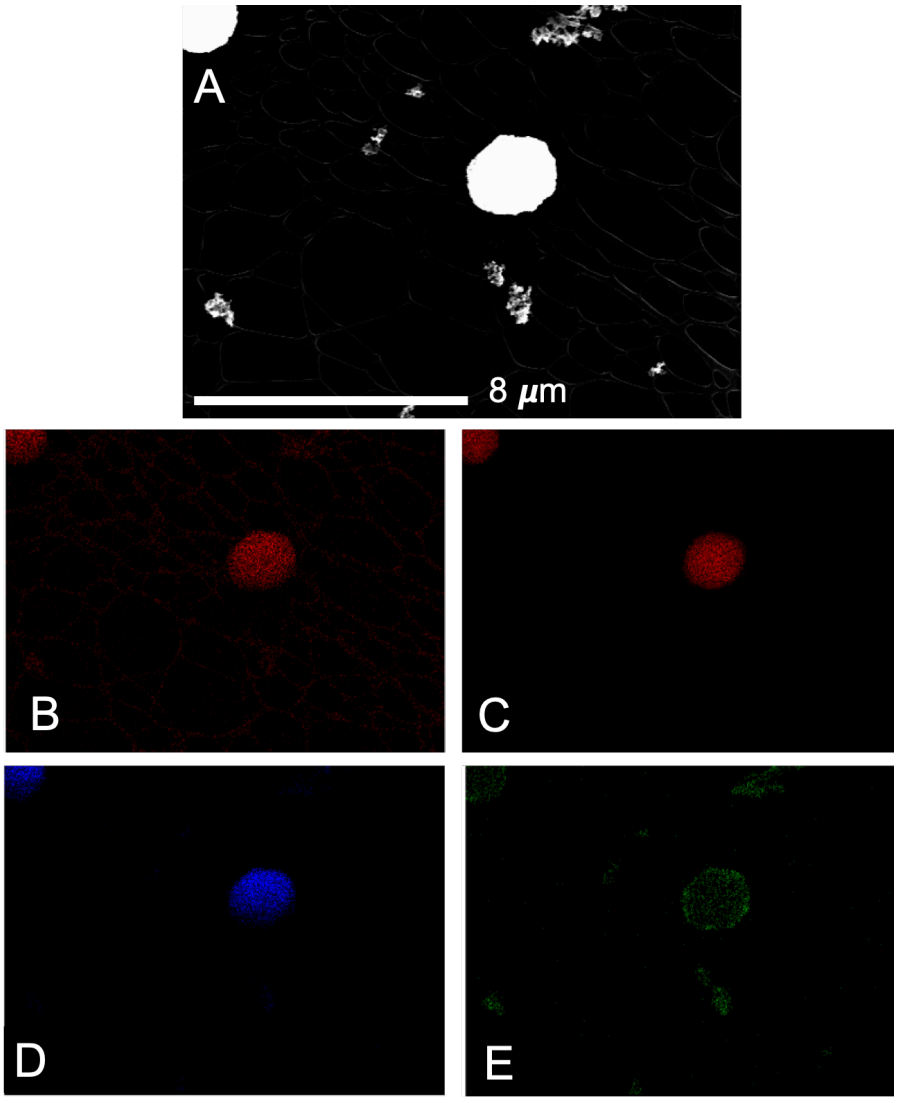

Figure 6.16: EDX mapping of the *L*-Cysteine stabilised EDX Fe_3O_4@$CaCO_3$ microspheres. (A) SEM image used for mapping, (B) Carbon map, (C) Calcium map, (D) Oxygen map and (E) Iron map.

The EDX analysis of both the PSS-stabilised Fe_3O_4@$CaCO_3$ microstructures, and the *L*-Cysteine stabilised Fe_3O_4@$CaCO_3$ microstructures show the sufficient coating of the microspheres with magnetite. While there is still some unbound magnetite, the EDX analysis shows successful coating of the majority of the microspheres. Further magnetic susceptibility measurements are required for these structures, however, SQUID measurements would be required due to the low magnetism per unit mass of the $CaCO_3$ structures. This will be carried out in future work.

These magnetic microsphere structures were then further functionalised with a bilayer of polyelectrolytes and PAH-stabilised gold nanoparticles. A scheme illustrating this is shown in Figure 6.17. Firstly, the Fe_3O_4@$CaCO_3$ microspheres were sonicated with a solution of PAH, followed by a solution of PSS. Following this, the microspheres were then sonicated with a solution of PAH-stabilised gold nanoparticles. This approach was only carried out for the PSS-stabilised magnetite nanoparticles, as it will facilitate the easier coating of the layer of PAH onto already PSS-stabilised microstructures. These nanoparticles were then cleaned multiple times with Millipore water and centrifugation at 5,000 RPM.

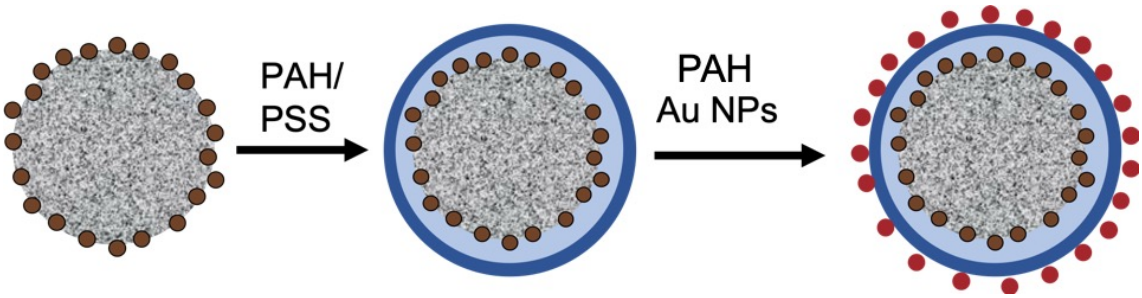

Figure 6.17: Scheme showing the synthetic approach to Au@Fe_3O_4@$CaCO_3$ microspheres.

UV-Vis spectroscopic analysis of these particles shows a plasmon peak at 530 nm corresponding to the gold nanoparticles (Figure 6.18). As the microparticles have been cleaned multiple times using centrifugation, it is thought that this peak corresponds to nanoparticles immobilised on the surface of the $CaCO_3$ microspheres.

However, it is still possible that some large gold aggregates were trapped in between but not on the microspheres that could cause the presence of this plasmon peak. Further SEM and EDX analysis is required to conclusively state that the gold has been adsorbed onto the surface of the microparticles.

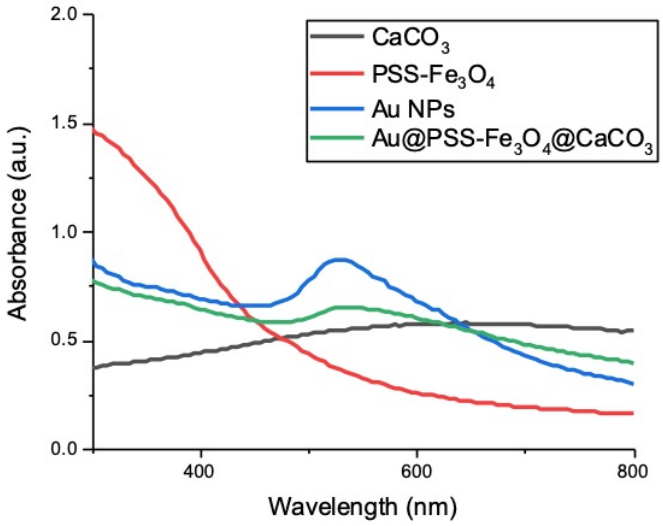

Figure 6.18: UV-Vis spectra of bare $CaCO_3$ microspheres, PAH-stabilised gold nanoparticles, PSS-stabilised magnetite and the gold and magnetite coated $CaCO_3$ microspheres.

SEM analysis of the composite structures was also carried out. These are shown in Figure 6.19. On initial inspection, the microparticles look almost identical to the Fe_3O_4@$CaCO_3$ particles prepared previously. One observation is that the microspheres appear much more aggregated than in previous samples. This might be due to some cross-linking of the microspheres by the long chain polymers used for the layer-by-layer stabilisation of both the microspheres, and also the PAH that is stabilising the gold nanoparticles.

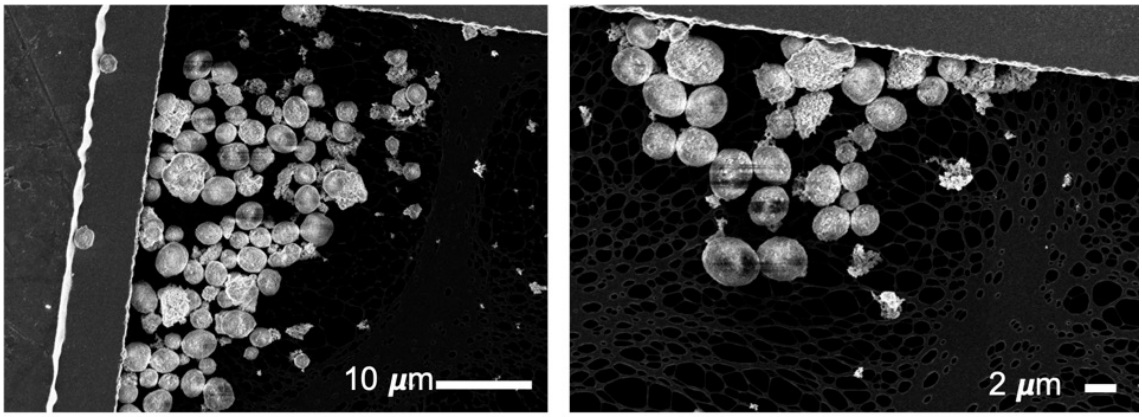

Figure 6.19: SEM images of the Au@Fe_3O_4@$CaCO_3$ microspheres.

EDX studies to determine whether or not gold was present on the microspheres were also carried out. The detection of small quantities of gold nanoparticles on large calcium carbonate microstructures is a challenge, as the $CaCO_3$ will emit a large quantity of secondary and backscattered electrons compared to the gold nanoparticles. In addition to this, a high electron voltage (20 keV) is required in order to detect gold, and a high electron voltage will also increase the number of electrons and x-rays being emitted from the $CaCO_3$. This has a significant impact on the dead-time of the instrument, and may make detection of the gold quite difficult. However, through choosing an area with a lower density of $CaCO_3$ microspheres, these studies were carried out and are shown in Figure 6.20. The mapping has shown the clear presence of gold on the surface of microspheres.

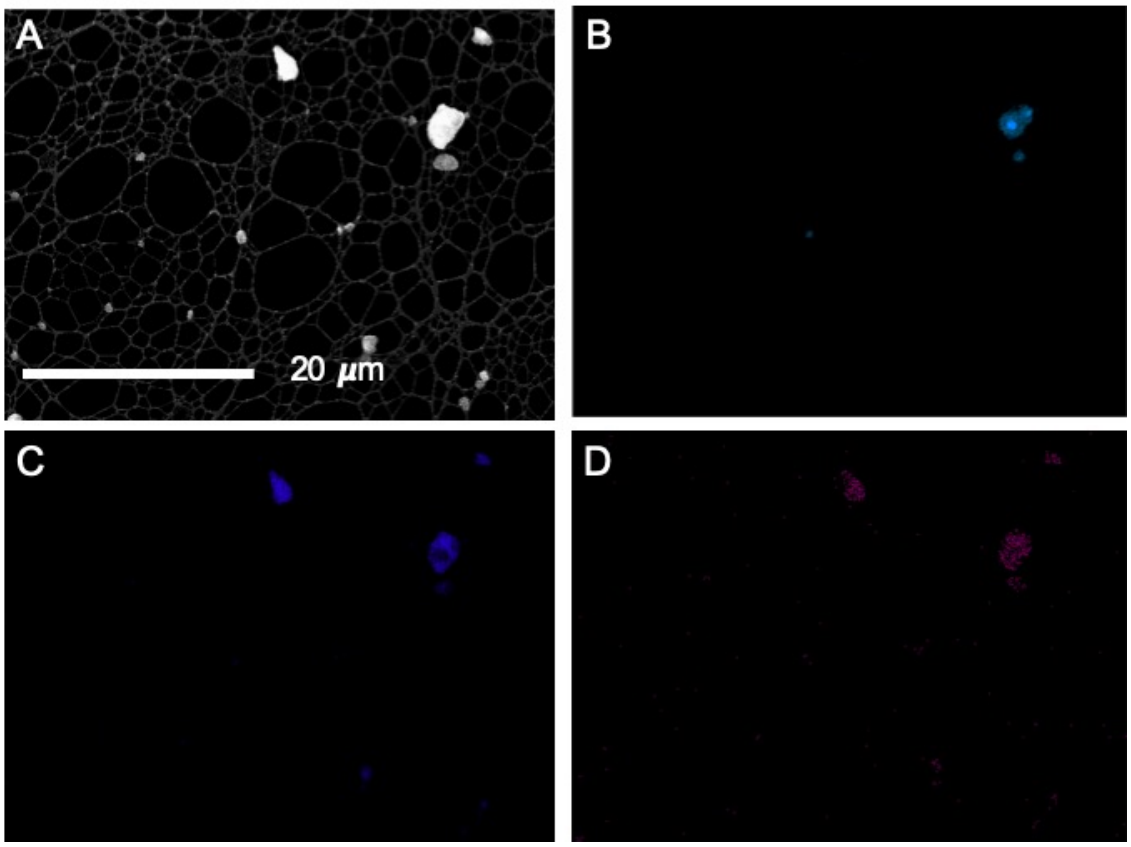

Figure 6.20: EDX mapping of the Au@Fe_3O_4@$CaCO_3$ microspheres, where (A) shows the area over which the mapping was carried out, (B) shows the calcium map, (C) shows the iron map and (D) shows the gold map.

Magnetic Calcium Carbonate Micro-Raspberries

In this approach, *L*-Cysteine stabilised magnetite nanoparticles are used as nucleation points for the preparation of vaterite "micro-raspberries". This method was adapted from work by Sergeeva *et al.*[9]. Briefly, Fe_3O_4 nanoparticles are suspended in Millipore water. Two solutions, one of 1 M Na_2CO_3 and one of 1 M $CaCl_2$ are added simultaneously, and the resulting solution is allowed to stir at room temperature (21 °C) for 30 seconds. The solution was then left to stay at room temperature for a further 3 minutes before cleaning using centrifugation and drying the product in air at 80 °C.

The microraspberry structures can then be further stabilised using three bilayers of PSS/PAH, added through successive sonications in the polyelectrolyte solutions. This is used to slow the degradation of the vaterite microparticles into calcite. Vaterite is not thermodynamically stable and so will transform over time into calcite, which is the most thermodynamically stable of the calcium carbonate crystal polymorphs.

XRD analysis was used to investigate the composition of the PE-stabilised microraspberries, and the patterns are shown in Figure 6.21. The XRD pattern shows the presence of calcite, vaterite and magnetite. This is indicative of the fact that the three bilayers of PSS and PAH are insufficient to completely stabilise the vaterite microraspberries. This could be due to the fact that the microraspberries were already partially transformed to calcite at the time of the polyelectrolyte coating, or that more bilayers are needed to stabilise the vaterite microstructures. An alternative method to obtaining vaterite preferentially over calcite could be carrying out the synthesis in an alcohol/water mixture, as alcohols have been known to stabilise the vaterite crystal phase[11,12].

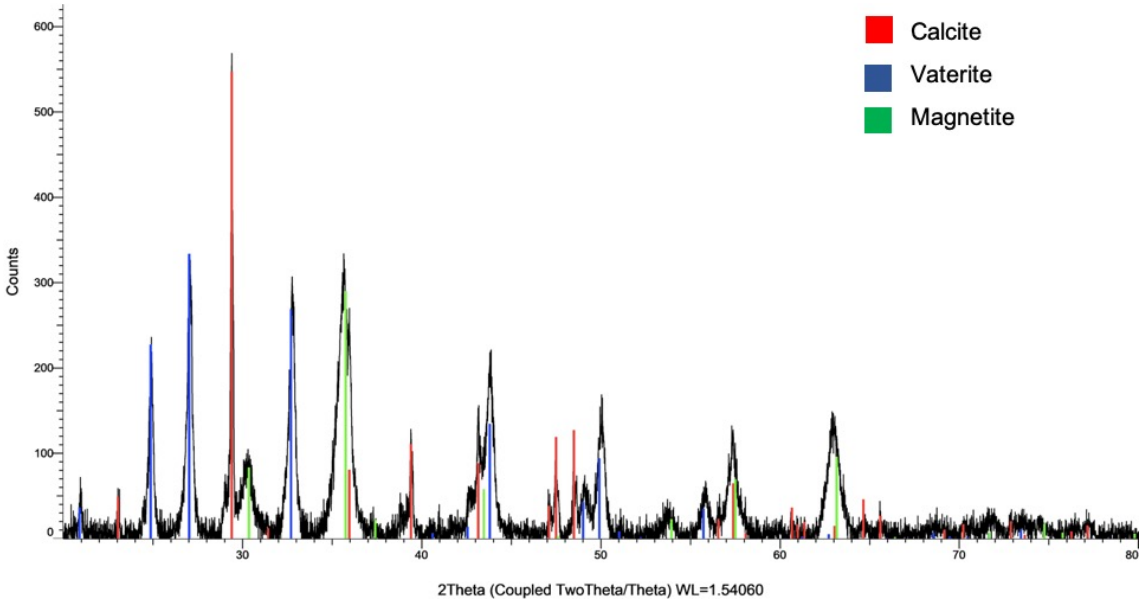

Figure 6.21: XRD pattern of the $CaCO_3$ microraspberry.

The XRD analysis does show the presence of Fe_3O_4 in the structure, which is indicative that the nanoparticles were successfully incorporated into the $CaCO_3$ matrix. However, further SEM and EDX analysis is required to determine whether or not the Fe_3O_4 nanoparticles acted as nucleation sites in the formation of the microraspberries, or whether the magnetite peaks in the XRD pattern should be attributed to excess magnetite nanoparticles present in the solution.

SEM analysis was carried out on both the unstabilised and stabilised microraspberry structures. SEM images of the unstabilised microraspberry structures are shown in Figure 6.22. The sample is highly polydisperse, with no single consistent morphology across the sample. However, no free magnetite can be seen in the sample, which does indicate that the magnetic nanoparticles are acting as nucleation sites for the growth of the $CaCO_3$ crystals. The magnetic nanoparticles used in this experiment are the *L*-Cysteine stabilised magnetite nanoparticles described earlier in this chapter, which have an average size of 17.5 ± 1.8 nm.

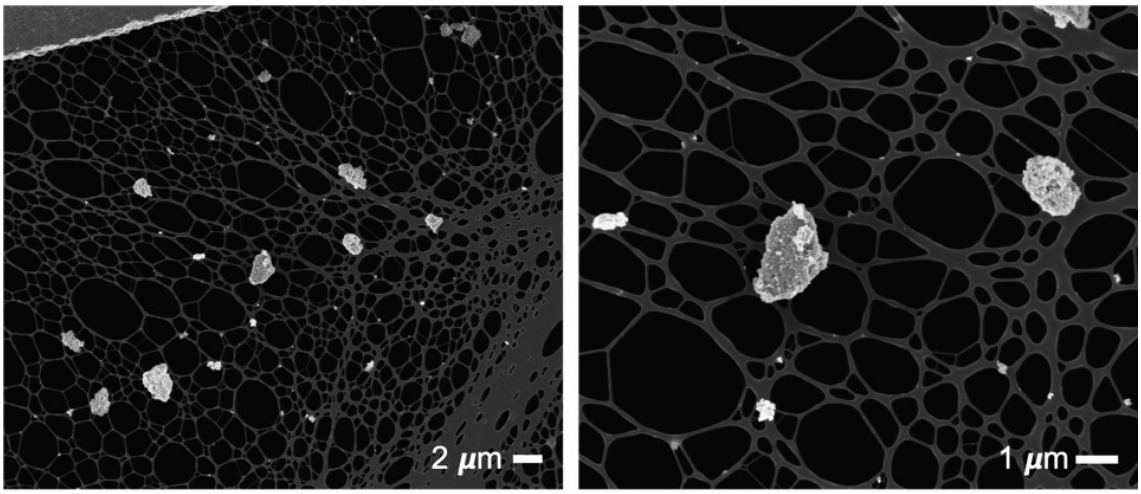

Figure 6.22: SEM images of the unstabilised magnetic $CaCO_3$ microstructures.

SEM analysis was also carried out on the stabilised micro-raspberry structures. These SEM images are shown in Figure 6.23. Somewhat surprisingly, this sample shows a higher degree of polydispersity than the unstabilised sample. The use

of polyelectrolytes to stabilise the structures after their initial syntheses results in the formation of larger aggregates. This could be due to the long chain PSS and PAH polymers causing cross-linking of multiple separate microraspberry structures, which, as the vaterite transforms over time into calcite, causes the formation of these larger aggregated structures. Future work could include both the use of an alcohol/water mixture in order to firstly attempt to obtain phase-pure vaterite microstructures, and also the *in-situ* stabilisation of the microraspberries using polyelectrolytes or other capping agents.

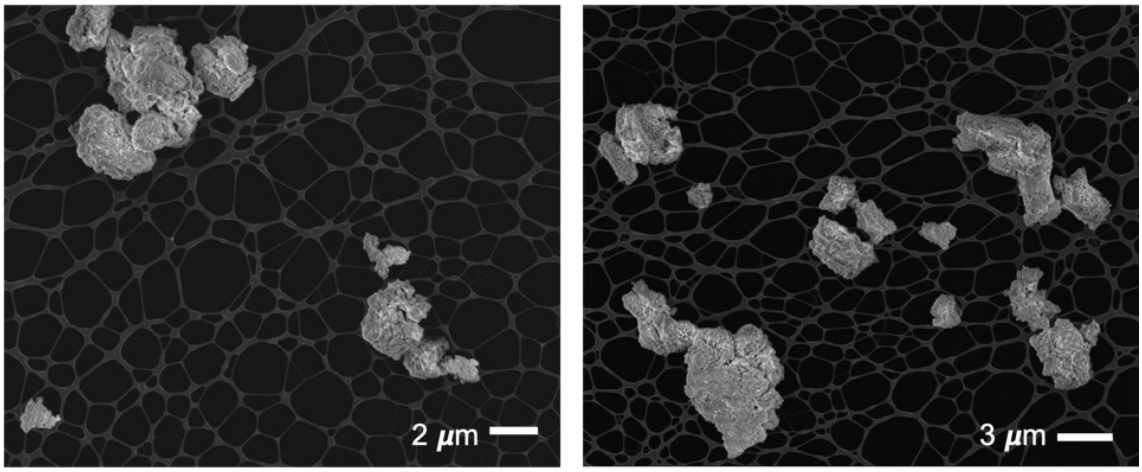

Figure 6.23: SEM images of the magnetic $CaCO_3$ micro-raspberries stabilised with 3 bilayers of PSS and PAH.

EDX analysis was also carried out on the microraspberries in order to investigate whether the magnetite nanoparticles are present throughout the microstructures themselves. The EDX maps are shown in Figure 6.24. Figure 6.24(A) shows a single microraspberry structure. The carbon, calcium and oxygen maps show the high concentration of these elements as expected. In Figure 6.24(E) the iron map shows a high concentration of iron in the microraspberry structure. In addition to this, no iron can be seen around the micro-raspberry or in clusters that are not associated with the microstructures. This shows conclusively that the magnetite nanoparticles acts as nucleation points for the growth of the $CaCO_3$ structures and are fully incorporated within the microstructures.

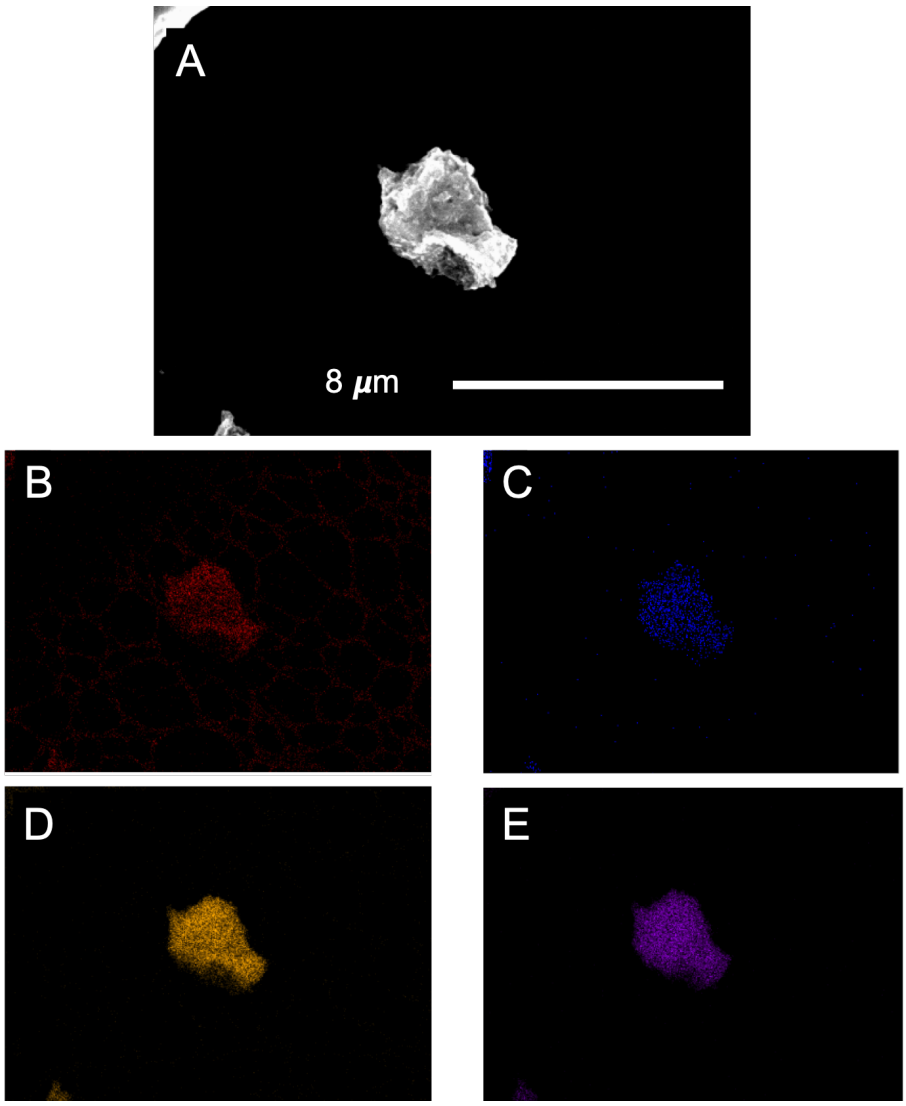

Figure 6.24: EDX mapping of the unstabilised magnetic $CaCO_3$ microraspberry structures, (A) shows the SEM image illustrating the area over which the mapping was carried out, and (B) carbon map, (C) calcium map, (D) oxygen map and (E) is the iron map.

Future work on these microstructures will involve refinement of the experimental approach such that more monodisperse microraspberries are obtained, as well as further functionalisation of the microraspberries with gold nanoparticles. This could be done with these microstructures first in order to determine whether such a reaction would be feasible. These steps, alongside investigations into further functionalisation with gold nanoparticles, will be carried out in future work.

Template-Directed Synthesis of $CaCO_3$ Microspheres.

The synthesis of these microstructures was performed using the first method described in this chapter, with certain modifications. Firstly, no *L*-Cysteine was used in the initial reaction mixture, and 0.1 mL of a citrate-stabilised gold nanoparticle solution was used. Briefly, the reaction was carried out as follows - PVP, SDS and the gold nanoparticles were added to an aqueous solution of Na_2CO_3 solution and allowed to stir for 30 minutes. In a separate vessel, SDS and $CaCl_2$ were added to Millipore water, and then this was added to the first solution. The resulting microparticles were stirred for an hour, cleaned by centrifugation and dried at 80 ^{o}C for 24 hours. It is thought that either the gold particles will act as nucleation sites for the formation of $CaCO_3$ micro-structures similar to that which was the case for magnetic microraspberries, or that the gold nanoparticles will occupy the central hollow area in the microsphere.

SEM analysis was first carried out in order to determine whether or not the microsphere synthesis had been successful with the resulting images shown below in Figure 6.25. The images obtained show quite monodisperse $CaCO_3$ microspheres. The images at a lower magnification show the narrow dispersity of the sample and the porous surface structure of the microspheres can be seen in the third SEM image. Size distribution analysis was also carried out on these particles, and it was found that they have an average size of 1.7 $\pm$ 0.34 μm (*n=103*). The size distribution plot for these nanoparticles is shown in Figure 6.26.

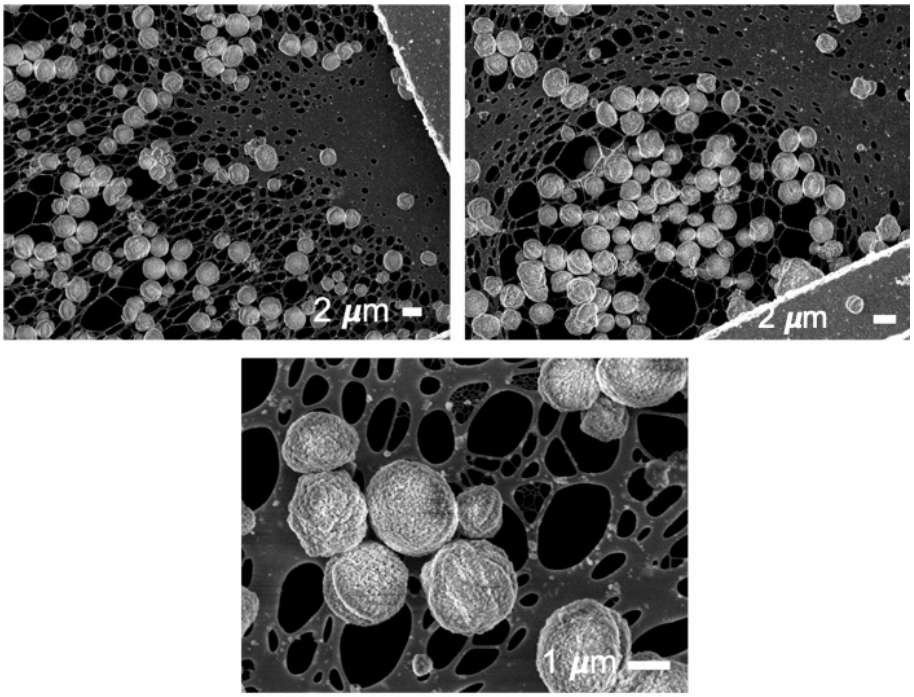

Figure 6.25: SEM images of the $CaCO_3$ microspheres prepared via the third synthetic approach.

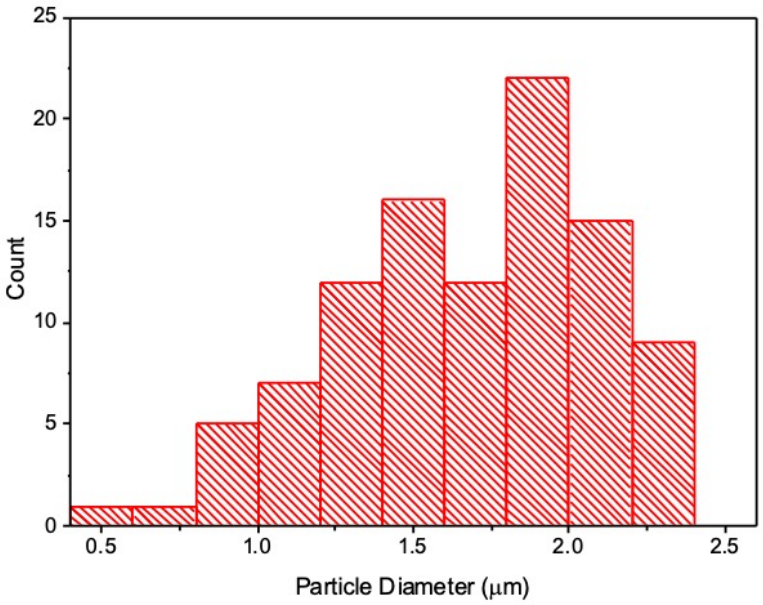

Figure 6.26: Size distribution plot for $CaCO_3$ microspheres prepared in the presence of gold nanoparticles (*n=103*)

These microspheres closely resemble those synthesised via the first approach, so it is unlikely that the gold nanoparticles act as nucleating agents for the growth of the $CaCO_3$ shell around the reverse micelle template. Thus, the more likely scenario is either that the gold nanoparticles are inside the hollow microspheres, or that they were uninvolved in the reaction and were removed in the washing steps.

XRD analysis was carried out to investigate whether or not gold nanoparticles were contained within the microspheres or not. XRD is also used to determine which crystal polymorph the microspheres are composed of. The XRD pattern obtained is shown in Figure 6.27 and shows that the microspheres are composed of both calcite and vaterite. The presence of vaterite in this XRD is interesting, as it differs from the $CaCO_3$ microspheres prepared via a very similar approach in the first method described. It is unclear why this structure is a mixture of the two most common polymorphs rather than phase-pure calcite. It could be due to the omission of *L*-Cysteine in the initial reaction mixture, which may favour calcite formation, or it could be due in part to some level of stabilisation that occurs due to the inclusion of the citrate-stabilised gold nanoparticles in the synthesis. However, the XRD shows no crystalline gold in the microsphere structures, so they may have been removed during the washing steps.

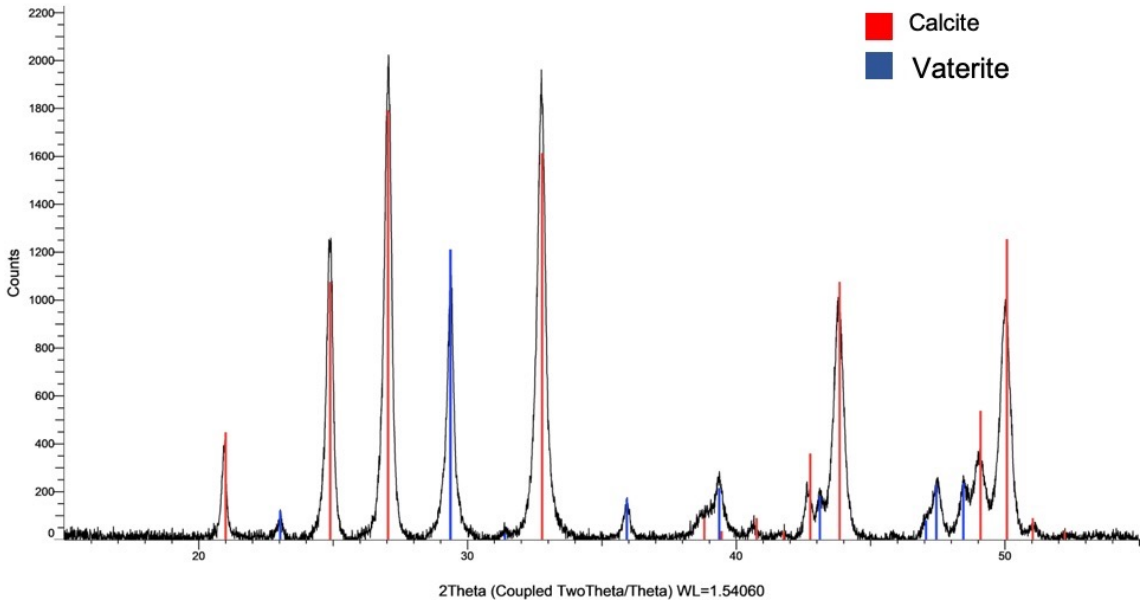

Figure 6.27: XRD pattern of the $CaCO_3$ microspheres synthesised in the presence of citrate-stabilised gold nanoparticles.

FTIR analysis was also carried out, which offered further confirmation that the microstructures were composed of calcium carbonate, with the characteristic peaks shown at 745 cm^{-1}, 873.5 cm^{-1} and 1398.1 cm^{-1} corresponding well with those reported in the literature[10]. This spectrum can be found in Appendix A14.

The $CaCO_3$ microspheres were then further functionalised with Fe_3O_4 nanoparticles stabilised with *L*-Cysteine. This was achieved by adding 5 mg of the dried magnetite nanoparticles to the microspheres, sonicating for 20 minutes and then shaking the mixture for a further 2 hours. The colour of the $CaCO_3$ suspension was observed to change from white to brown after this synthesis.

SEM analysis of the resulting nanoparticles are shown in Figure 6.28. The SEM images show some partially coated microspheres, as well as large unbound aggregates of magnetite. What is also remarkable about these structures is that they appear less porous than the microspheres before the magnetite conjugation step, and, in

particular in the first picture it appears that there is some rhombohedral $CaCO_3$ present that is not associated with a microsphere. This could be attributed to a vaterite microsphere thermally decomposing into calcite, which most often presents as a rhombohedral structure[13].

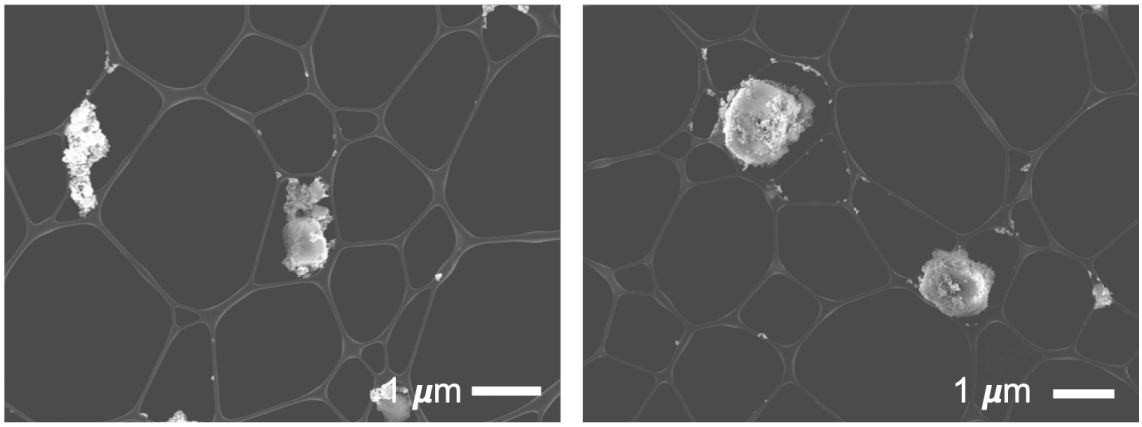

Figure 6.28: SEM images of the Fe_3O_4 coated microspheres.

EDX analysis was also carried out on this sample, in order to determine whether or not magnetite had bound to the surface of the microspheres. These results are shown in Figure 6.29. The carbon, calcium and oxygen maps show the expected distribution of elements. The iron map is shown in Figure 6.29 (E) and shows a high concentration of iron on the microspheres. This is indicative that the coating of microspheres with magnetite was successful. However, it was noted that the microspheres were not sufficiently magnetic such that magnetic separation and cleaning could be utilised, and the addition of more magnetite would not necessarily increase coating to facilitate this, but could simply result in more large clusters of unbound magnetite. The microspheres were observed to slowly be pulled out of solution by a magnet over a time period of approximately 60 minutes.

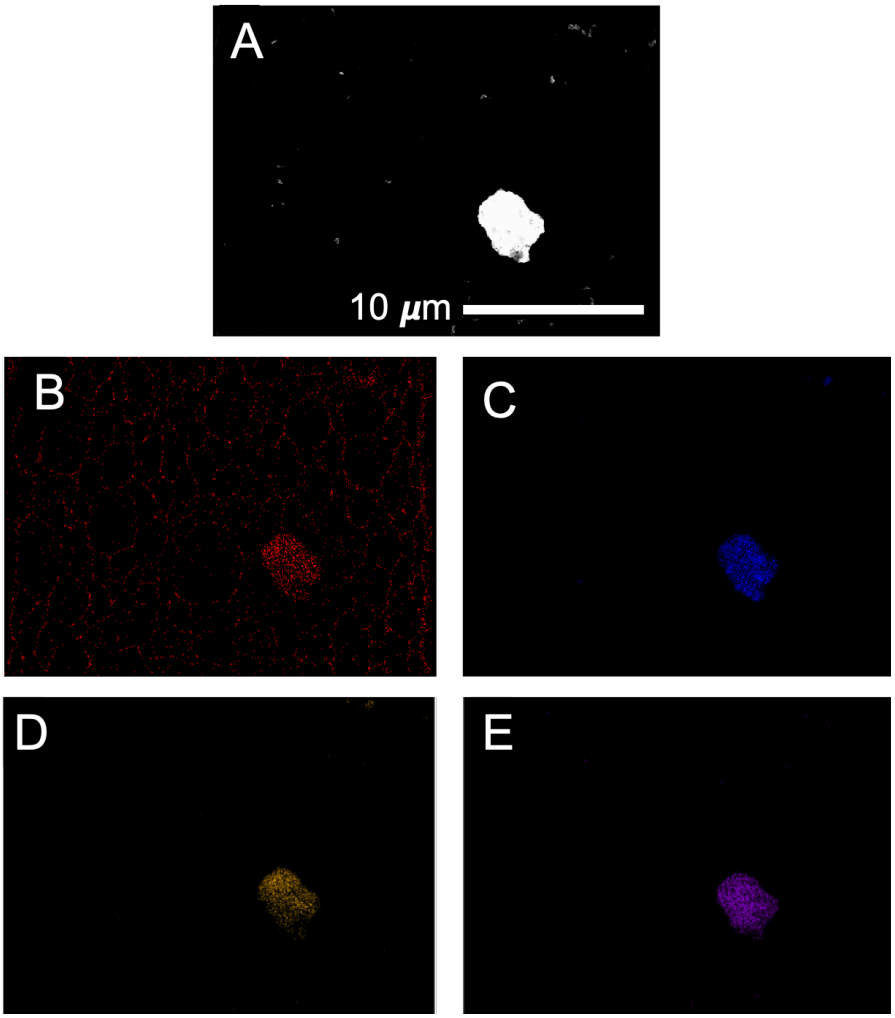

Figure 6.29: EDX maps for the Fe_3O_4 coated $CaCO_3$ microspheres showing (A) the SEM image of the area which was mapped, (B) carbon map, (C) calcium map, (D) oxygen map, (E) iron map.

The magnetite-coated $CaCO_3$ were then further functionalised with gold nanoparticles. This was done in the same manner as the coating with the magnetite nanoparticles - briefly, 0.1 mL of a concentrated citrate-stabilised gold nanoparticle solution was added to a Fe_3O_4@$CaCO_3$ microsphere solution. This solution was then sonicated for 60 minutes. The resulting solution was cleaned using centrifugation.

The UV-Vis spectra for the Fe_3O_4@$CaCO_3$ microspheres and the gold-coated Fe_3O_4@$CaCO_3$ microspheres are shown in Figure 6.30. The UV-Vis spectrum of

the uncoated $CaCO_3$ microspheres shows a typical absorbance spectrum for calcium carbonate, and the gold-coated $CaCO_3$ microspheres show the plasmon peak of the gold nanoparticles in the region of 550 nm. This is encouraging, however, it may be the case that the gold is present in solution and not on the microspheres themselves.

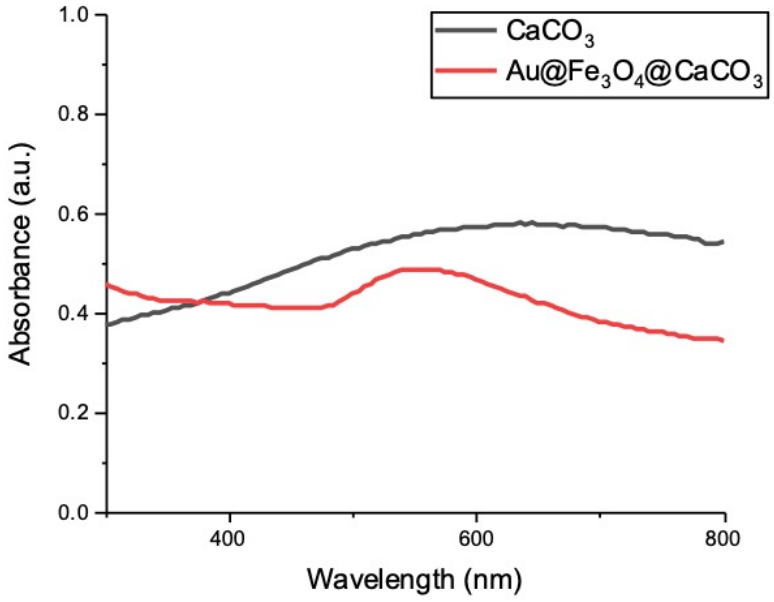

Figure 6.30: UV-Vis spectra of $CaCO_3$ microspheres and $Au@Fe_3O_4@CaCO_3$ microspheres.

SEM analysis was carried out on the gold-coated $CaCO_3$ microspheres (Figure 6.31). Four images are shown below in order to give a representation of the entire sample. What can be clearly seen is that there is two distinct species of microspheres present in the images. In addition to this, bright nanoparticle aggregates can also be seen throughout the four images. The gold and $CaCO_3$ behave differently under the electron beam, $CaCO_3$ readily charges under an electron beam, whereas gold, which is conductive, is stable under the electron beam. Thus the gold-coated and uncoated microspheres will appear visually very different in the SEM. What this suggests is partial coating of the $CaCO_3$ microspheres.

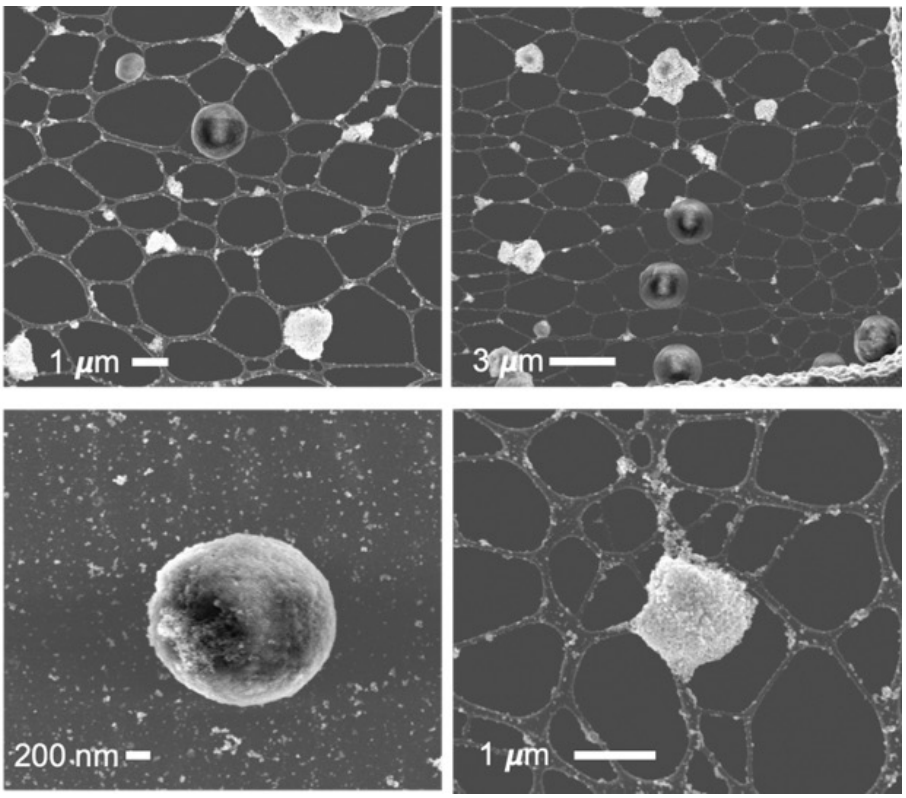

Figure 6.31: SEM analysis of the gold-coated $CaCO_3$ microspheres.

An SEM image clearly differentiating between the coated and un-coated microspheres is shown in Figure 6.32. Due to the presence of gold on the TEM grid, in addition to coating a portion of the microspheres, it is not thought that the addition of further quantities of gold would result in a more even coating of the microspheres. Perhaps longer reaction times would result in a more even coating of the microspheres. Further optimisation of this synthesis will be carried out in future work.

EDX studies were also carried out on the microspheres to confirm the presence of both iron and gold on the microstructures. These studies are shown in Figure 6.33. The map in Figure 6.33 (B) shows three microsphere structures, and gold can clearly be seen in on these microsphere structures in Figure 6.33(D). However, iron does not seem to be coating the microspheres in this instance, and it may be the case that gold nanoparticles will deposit primarily onto uncoated $CaCO_3$ microspheres, however, investigations into this will be carried out in future work.

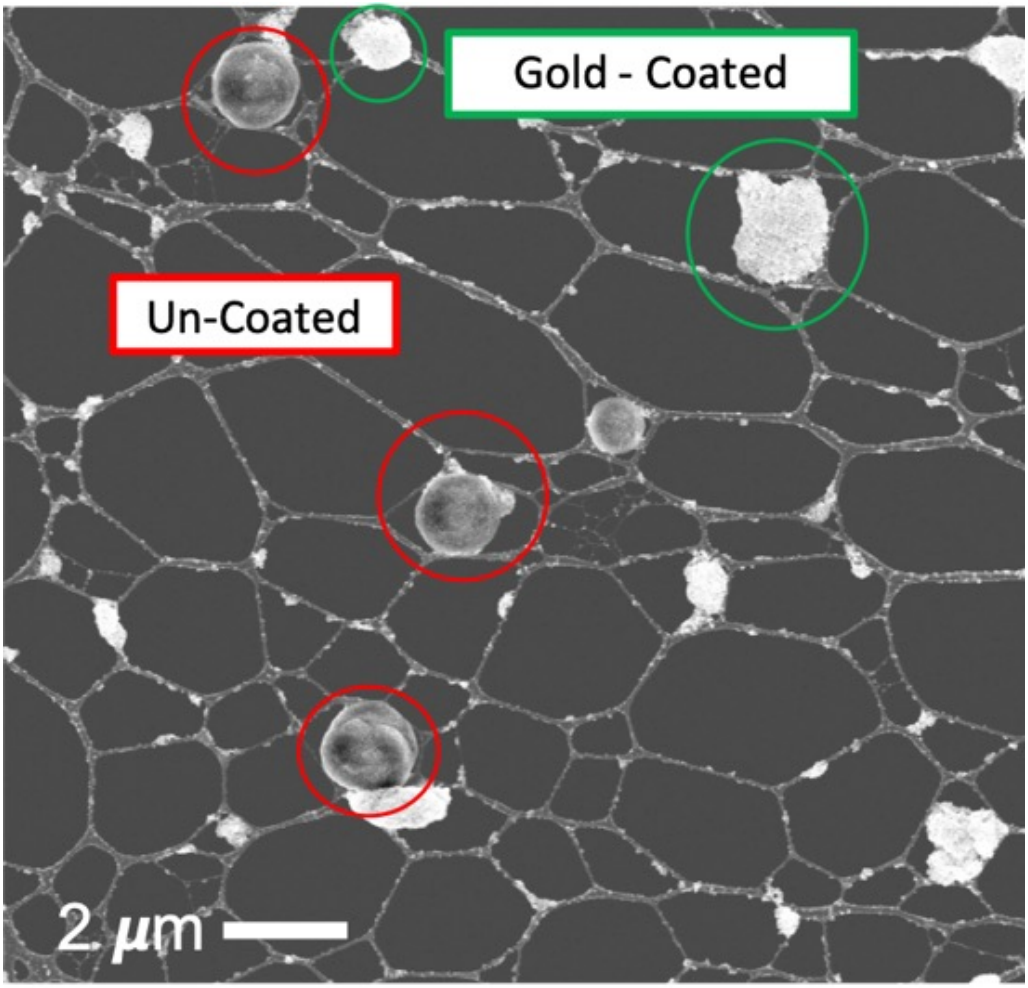

Figure 6.32: SEM image of the gold-coated $CaCO_3$ microspheres clearly showing the uncoated and coated microspheres.

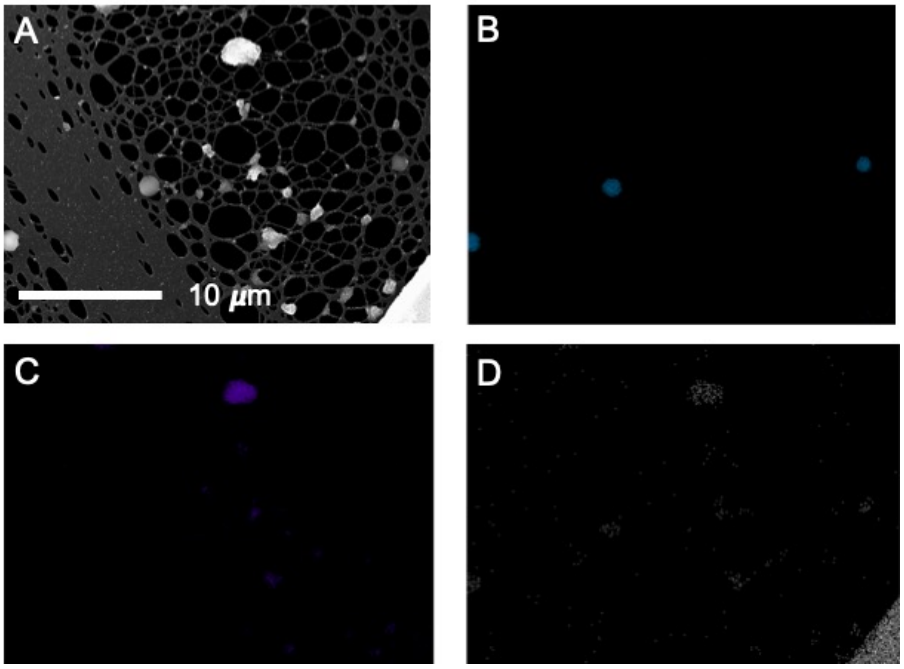

Figure 6.33: EDX mapping of the Au@Fe_3O_4@$CaCO_3$ microspheres, where (A) shows the area over which the mapping was carried out, (B) shows the calcium map, (C) shows the iron map and (D) shows the gold map.

Further to this work, in a collaboration with Martynenko *et al.*, magnetic-fluorescent calcium carbonate microparticles were prepared[8]. In this synthesis, a layer-by-layer approach was used in order to functionalise the $CaCO_3$ microspheres first with a layer of superparamagnetic magnetite nanoparticles, and then further functionalised with a layer of Ag-in-S ternary quantum dots (Figure 6.34). These microparticles were then fluorescent and magnetically separable. These microparticles were further coated with antibodies and used to successfully detect *Legionella pneumophila* bacteria.

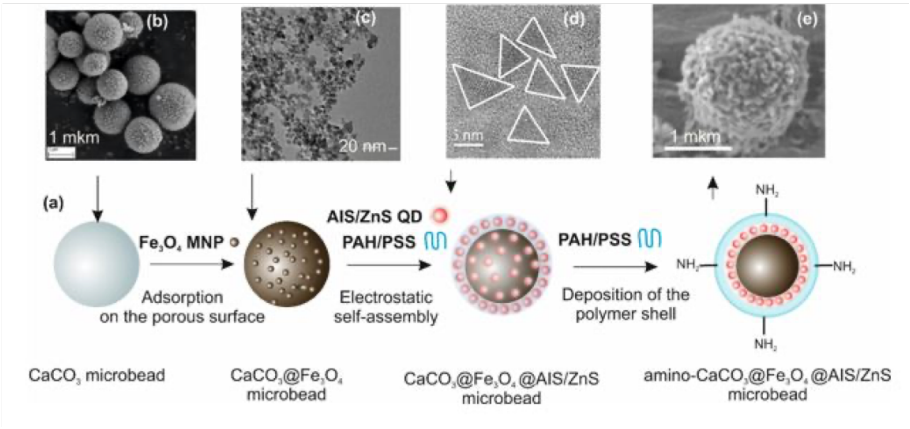

Figure 6.34: Scheme showing the preparation of multi-modal magnetic-fluorescent $CaCO_3$ microspheres. Taken from ref[8].

6.4 Conclusions

In this chapter, three different approaches were developed in order to produce multimodal calcium carbonate microstructures. Each approach resulted in morphologically different microstructures.

Firstly, magnetite and gold nanoparticles were prepared for use in the synthesis and further functionalisation of the $CaCO_3$ microstructures. Unstabilised, PSS-stabilised and *L*-Cysteine stabilised Fe_3O_4 nanoparticles were produced and characterised. In each case, the Fe_3O_4 nanoparticles were superparamagnetic, had strong magnetisation and were monodisperse. Citrate-stabilised gold nanoparticles were shown to have the correct plasmonic behaviour and were found to be monodisperse through TEM analysis.

The first method involved the template-directed synthesis of *L*-Cysteine stabilised $CaCO_3$ microspheres. Two distinct size distributions were found for these microspheres. The three types of magnetite nanoparticles were added to the $CaCO_3$ microspheres. No major difference was found between the Fe_3O_4 nanoparticle coating between the three stabilising agents used. Further functionalisation with gold nanoparticles was attempted with varying levels of coating achieved. The presence of both iron and gold on the microspheres was confirmed using EDX mapping.

The second approach towards the preparation of multimodal $CaCO_3$ microspheres involved the use of *L*-Cysteine stabilised Fe_3O_4 nanoparticles as nucleation sites for the growth of the calcium carbonate microstructures. While magnetic $CaCO_3$ microstructures were obtained, the crystals had a high degree of polydispersity across the sample. Due to this high degree of polydispersity, further optimisation of the initial synthetic approach would be required before further functionalisation with gold nanoparticles.

The third approach follows a similar reaction to the first method, however, in this case *L*-Cysteine was omitted from the initial synthesis and 0.1 mL of a concentrated citrate-stabilised gold nanoparticle solution was added. This was to determine whether or not the *in-situ* gold nanoparticles would be contained within the hollow microspheres, or if they would act as nucleation points in the growth of the $CaCO_3$ crystals. It was found that no plasmon peak was visible, and the resulting microspheres appeared white in colour after multiple washing steps. For these reasons, it was concluded that the gold nanoparticles were not encapsulated or incorporated into the microsphere structures. However, the microspheres were found to be highly monodisperse, and it is unsure whether this is due to the omission of the *L*-Cysteine in the initial synthesis, or the citrate-stabilised gold nanoparticles having some spectator effect in the synthesis of the microspheres. These microspheres were then coated with *L*-Cysteine stabilised Fe_3O_4 nanoparticles, which was confirmed through SEM and EDX analysis. A gold coating was then added to these $CaCO_3$ microspheres. Interestingly, it was found that some microspheres were completely coated and others were uncoated, along with a number of aggregates of gold present in the solution. This may indicate that even though the concentration of gold was correct, some other reaction parameter, such as the sonication time or temperature, may need to be altered in order to obtain better coating of the microspheres. The presence of gold on the microspheres was also confirmed using EDX spectroscopy.

Thus, three distinct samples of multimodal calcium carbonate microparticles were synthesised and characterised. With some further modifications, these microparticles could offer a vast range of potential biomedical and sensing applications, as demonstrated in a collaboration with Martynenko *et al.*[8].

Bibliography

(1) E. A. Genina, Y. I. Svenskaya, I. Y. Yanina, L. E. Dolotov, N. A. Navolokin, A. N. Bashkatov, G. S. Terentyuk, A. B. Bucharskaya, G. N. Maslyakova, D. A. Gorin, V. V. Tuchin and G. B. Sukhorukov, *Biomedical Optics Express*, 2016, **7**, 2082.

(2) S. Maleki Dizaj, M. Barzegar-Jalali, M. H. Zarrintan, K. Adibkia and F. Lotfipour, *Calcium carbonate nanoparticles as cancer drug delivery system*, 2015.

(3) A. Som, R. Raliya, L. Tian, W. Akers, J. E. Ippolito, S. Singamaneni, P. Biswas and S. Achilefu, *Nanoscale*, 2016, **8**, 12639–12647.

(4) X. Guo, L. Liu, W. Wang, J. Zhang, Y. Wang and S. H. Yu, *CrystEngComm*, 2011, **13**, 2054–2061.

(5) K. M. Z. Hossain, U. Patel and I. Ahmed, *Progress in Biomaterials*, 2015, **4**, 1–19.

(6) H. Yang, Y. Wang, T. Liang, Y. Deng, X. Qi, H. Jiang, Y. Wu and H. Gao, *Progress in Natural Science: Materials International*, 2017, **27**, 674–677.

(7) M. F. Butler, W. J. Frith, C. Rawlins, A. C. Weaver and M. Heppenstall-Butler, *Crystal Growth and Design*, 2009, **9**, 534–545.

(8) I. V. Martynenko, D. Kusić, F. Weigert, S. Stafford, F. C. Donnelly, R. Evstigneev, Y. Gromova, A. V. Baranov, B. Rühle, H.-J. Kunte, Y. K. Gun'ko and U. Resch-Genger, *Analytical chemistry*, 2019, **91**, 12661–12669.

(9) A. Sergeeva, R. Sergeev, E. Lengert, A. Zakharevich, B. Parakhonskiy, D. Gorin, S. Sergeev and D. Volodkin, *ACS Applied Materials and Interfaces*, 2015, **7**, 21315–21325.

(10) L. Zhao and J. Wang, *Colloids and Surfaces A: Physicochemical and Engineering Aspects*, 2012, **393**, 139–143.

(11) S. Rodrigues, M. Dionísio, C. Remuñán López and A. Grenha, *Journal of Functional Biomaterials*, 2012, **3**, 615–641.

(12) F. C. Donnelly, F. Purcell-Milton, V. Framont, O. Cleary, P. W. Dunne and Y. K. Gun'ko, *Chemical Communications*, 2017, **53**, 6657–6660.

(13) A. W. Ritchie, M. I. Watson, R. Turnbull, Z. Z. Lu, M. Telfer, J. E. Gano, K. Self, H. F. Greer and W. Zhou, *CrystEngComm*, 2013, **15**, 10266–10271.

Chapter 7

Conclusions and Future Work

7.1 Conclusions

This project has resulted in the development of a wide range of new magnetic and plasmonic materials, as well as a variety of new magnetic-plasmonic nanocomposite materials. This was achieved through the use of, and building on, established experimental techniques, as well as the development of novel new approaches to the synthesis of new nanomaterials and new composite materials. All materials prepared have been characterised extensively using a number of experimental techniques which allowed us to establish and understand the properties and morphologies of these materials.

Through the use of a modified classic coprecipitation technique, and various concentrations of a polyelectrolytes, three concentrations of PSS-stabilised magnetite nanoparticles were prepared. In combination with gold nanoparticles prepared using $NaBH_4$ reduction and stabilised in an oppositely charged polyelectrolyte, PAH, a number of new magnetic-plasmonic nanocomposites were obtained. These magnetic-plasmonic nanocomposites were found to retain the gold nanoparticles by virtue of the electrostatic interactions between the two polymer species over multiple mag-

netic separation cycles. To the best of our knowledge, this is the first magnetic-plasmonic nanocomposite with components completely bound through electrostatic interactions. The use of this approach enabled us to completely avoid many of the difficulties encountered when preparing core-shell magnetic-plasmonic nanocomposites, such as the need for intermediate layers due to the structural mismatch of the magnetic ferrites and noble metals, and reproducibility issues that arise from separate seeding of nanoparticles and preferential growth of individual material particles rather than seeding onto the core nanoparticle.

The binding effectiveness of the two complementary polyelectrolyte stabilisers after multiple magnetic separations was demonstrated through testing the same method using unstabilised- and acetic acid-stabilized gold nanoparticles. It was found in each of these cases that the majority of the gold that was initially present in the nanocomposite was removed during the magnetic separations. These nanocomposites were further used in the sensing of Hg^{2+} ions, which showed promising initial results. A distinct blue-shift in the UV-Vis spectrum was obtained when the PAH-stabilised gold nanoparticles interacted with the mercury ions, but further development will be needed in order to produce more robust magnetic-plasmonic nanocomposite sensors. This highly reproducible and scalable approach to magnetic-plasmonic nanocomposites is believed to have a wide range of potential applications in biosensing.

A study on a range of anisotropic gold structures was carried out, and two new composite materials were formed using PAH-stablilised magnetite nanoparticles, PAH-stabilised gold nanoparticles and PVP-stabilised AuAg nanowires. PAH-stabilised nanoparticles were used in the preparation of new magnetic-plasmonic nanowire structures. The magnetite nanoparticles were found to self-assemble around the micron-scale nanowires over a time period of several days, and this was confirmed through SEM monitored time-studies. A hybrid plasmonic composite structure was prepared by the self-assembly of PAH-stabilised gold nanoparticles and PVP-

stabilised AuAg nanowires. This is an extension of the work on the initial polyelectro lyte-stabilised nanocomposites prepared in chapter 3, and illustrates the broad scope of this approach to the preparation of magnetic-plasmonic nano- and micro-materials. It is thought that these nanowire composites could have a range of applications in sensing, biology, medicine as well as potential use in electronics. Cytotoxicity studies should be carried out in the future in order to investigate their biocompatibility for use *in-vivo*.

A new and highly reproducible one-pot synthetic approach to DNA-stabilised magnetic and plasmonic nanoparticles was developed. In this work double-stranded and single-stranded DNA-stabilised magnetite and gold nanoparticles were prepared at room temperature and pressure in a simple reaction procedure. The magnetite nanoparticles were superparamagnetic, and FTIR, TGA and VSM provided sufficient evidence to suggest that the DNA was successfully conjugated to the surface of the nanoparticles. Similarly, UV-Vis, FTIR, and TGA studies confirmed the presence of both dsDNA and ssDNA on the surface of the gold nanoparticles. In addition to this, interesting SERS behaviour was found for the herring sperm DNA in the Raman spectra of the gold nanoparticles, showcasing their potential as sensing agents. These two magnetic and plasmonic moeities were then combined to form a wide variety of nanocomposite structures. Initial studies show huge potential for these materials, which offer both magnetic separation, SERs and sensing potential due to the two highly pronounced UV-Vis peaks. These materials will be further developed for rapid antigen sensing in response to the current COVID-19 pandemic.

A number of new $CaCO_3$-based magnetic plasmonic materials were prepared in this work. This initially involved the preparation of magnetite coated with a variety of stabilising agents, namely PSS, *L*-Cysteine and citric acid, as well as the synthesis of citric-acid stabilised and PAH-stabilised gold nanoparticles. Hollow $CaCO_3$ microspheres were prepared, as well as magnetite-doped microraspberries.

These formed the basis for the formation of new magnetic-plasmonic structures. For the two hollow microsphere structures, magnetic nanoparticles were first deposited onto these structures, followed by the use of a layer-by-layer approach to coat the magnetic microstructures with bilayers of PSS and PAH. These bilayers provided the electrostatic gradient necessary in order to facilitate the deposition of the gold nanoparticles onto the surface of the microspheres. The presence of the magnetite and gold nanoparticles on the microspheres was confirmed using EDX. The resulting microstructures are highly biocompatible and acid-sensitive, and as such have broad scope for a litany of biomedical applications.

7.2 Future Work

This project has revealed a wide variety of new research avenues to explore, with the aim of developing more highly sensitive and easily reproducible magnetic-plasmonic nano- and micro-structures. The aim is to carry out the following research which is believed will advance the field of magnetic-plasmonic nano- and micro-structural materials:

1. Further optimisation of the concentration of PSS and PAH used in the fabrication of the polyelectrolyte-stabilised magnetic plasmonic nanocomposites in order to further enhance their heavy metal ion sensing.

2. Further development of the nanocomposites to detect a range of heavy metal ions including cadmium, chromium, lead, arsenic and antimony; all of which are known to affect water systems.

3. Optimisation of the concentration of magnetite and gold nanoparticles on the surface of the AuAg nanowires and further investigations into the cause of the degradation of the nanowires after day 7 with the gold nanoparticles.

4. Testing of the magnetic and plasmonic nanowire hybrid structures for SERs by Raman spectroscopy, as well as further optimisation of the magnetite concentration in the nanowire composite structure such that the materials are easily separable from aqueous solutions.

5. Testing of the nanowire composite structures for the detection of various heavy metal ion sensing in aqueous solutions.

6. Comprehensive SERs enhancement factor studies on the dsDNA-stabilised gold nanoparticles, and investigations into the cause of the SERs performance difference between the dsDNA and ssDNA stabilised gold nanoparticles.

7. Optimisation of the concentrations of the DNA, gold and magnetite for the preparation of the DNA-based magnetic-plasmonic nanocomposites such that the gold nanoparticles are retained through multiple magnetic separation cycles, both the DNA and plasmon peaks are visible in the UV-Vis spectrum and all SERs behaviour is maintained.

8. Use of the DNA-based magnetic-plasmonic nanocomposites for the testing of antigens in aqueous solutions, and the development of a rapid antigen sensing platform in response to the current COVID-19 pandemic.

9. The development of other magnetic-plasmonic nanocomposite structures based on the DNA-stabilised magnetite and gold, as well as the AuAg nanowires. Preliminary studies for this work are shown in Figures 7.1 and 7.2. In these instances, what is shown is the nanocomposite that self-assembles after 10 days left unstirred at 4 ^{o}C. It is believed these materials will have interesting plasmon and SERs effects.

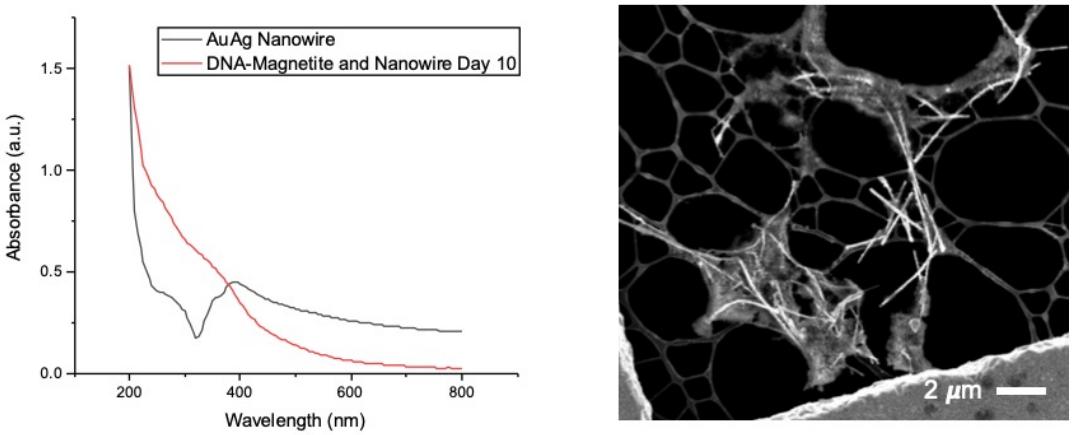

Figure 7.1: UV-Vis spectra for the DNA-stabilised magnetite nanoparticles and AuAg nanowire composite structure after 10 days ageing at 4 °C alongside an SEM image of the corresponding structure.

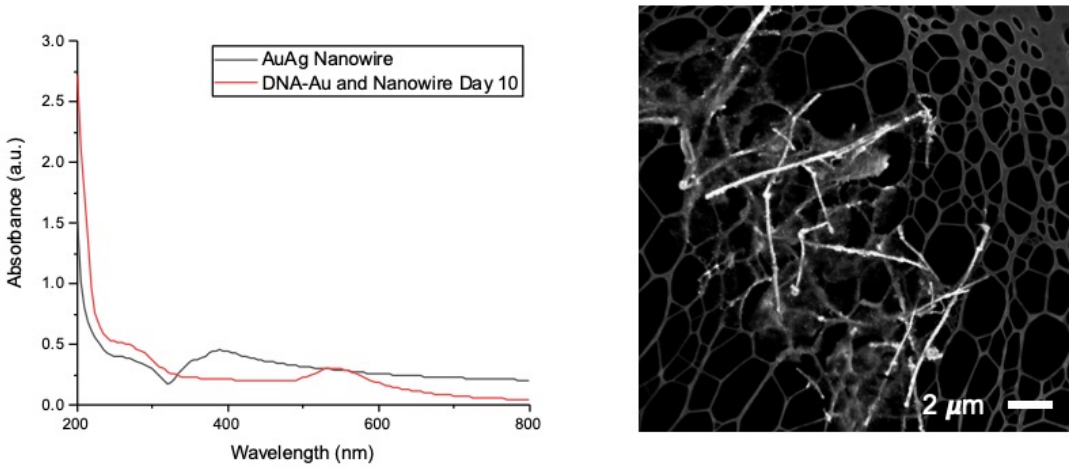

Figure 7.2: UV-Vis spectra for the DNA-stabilised gold nanoparticles and AuAg nanowire composite structure after 10 days ageing at 4 °C alongside an SEM image of the corresponding structure.

10. Refinement of the synthetic approach to the magnetic $CaCO_3$ microraspberry structures such that a more monodisperse suspension of microparticles is obtained and further functionalisation of these microstructures with gold nanoparticles.

11. Further optimisation of the gold concentration in the samples of hollow $CaCO_3$ microspheres.

12. Testing of these materials for use as potential theranostic agents through loading with NSAIDs and monitoring their drug release profiles, alongside magnetic guidance and photothermal therapy abilities.

Appendix

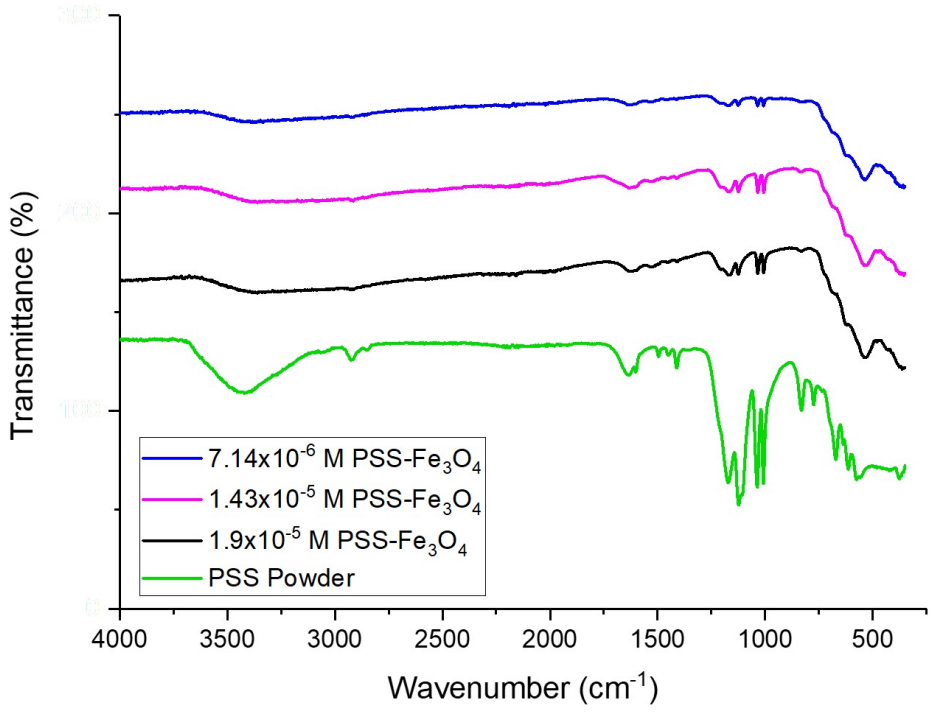

Figure A1: FTIR Spectra for PSS powder and each concentration of PSS-stabilised magnetite nanoparticles.

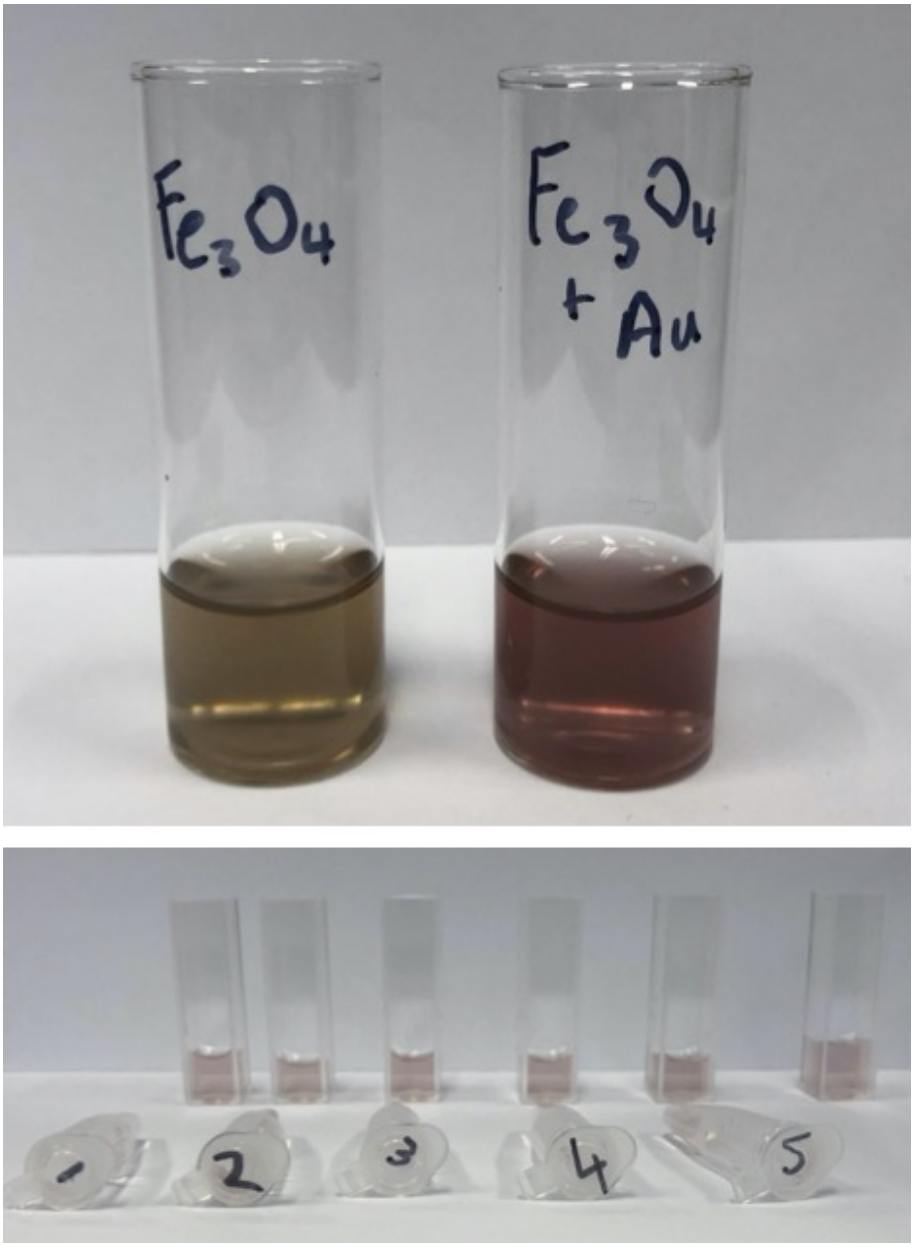

Figure A2: Photographs showing the magnetite and magnetic-plasmonic nanocomposite solution, and the nanocomposite solution in each (1-5) dilution of mercury solution.

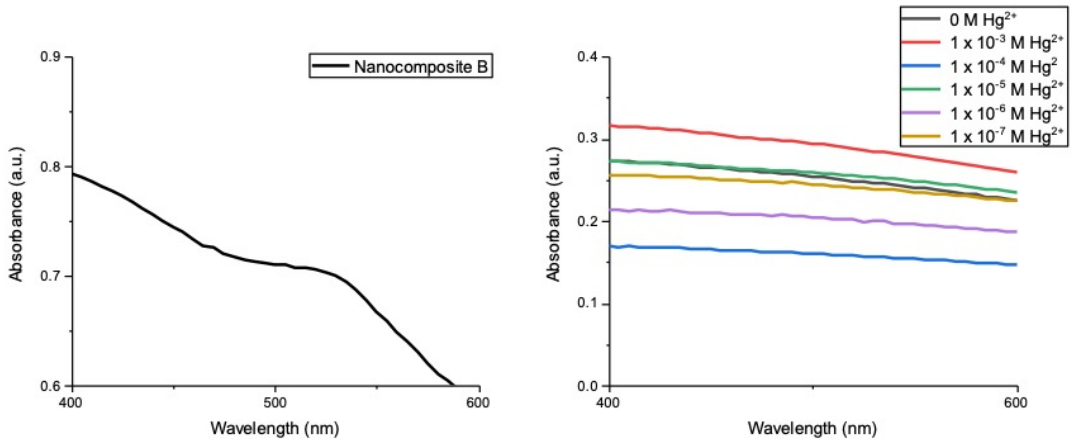

Figure A3: UV-Vis spectra of nanocomposite B, and UV-Vis spectra of nanocomposite B with each of the solutions of mercury.

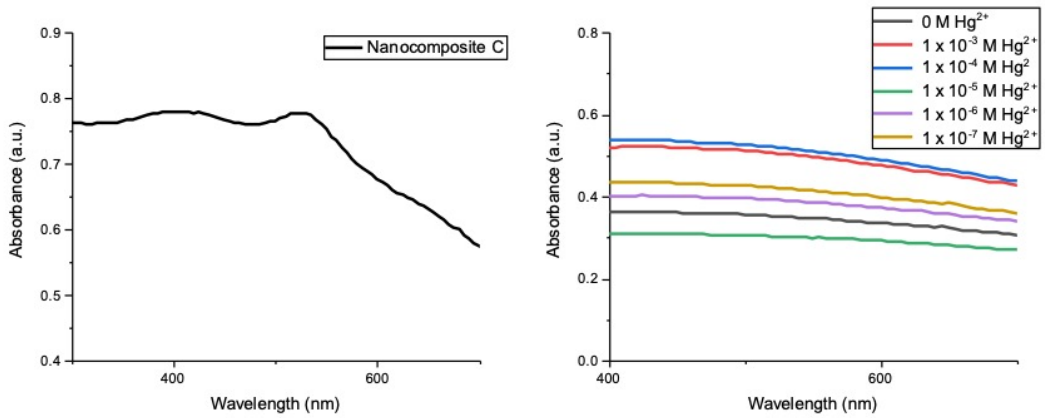

Figure A4: UV-Vis spectra of nanocomposite C, and UV-Vis spectra of nanocomposite C with each of the solutions of mercury.

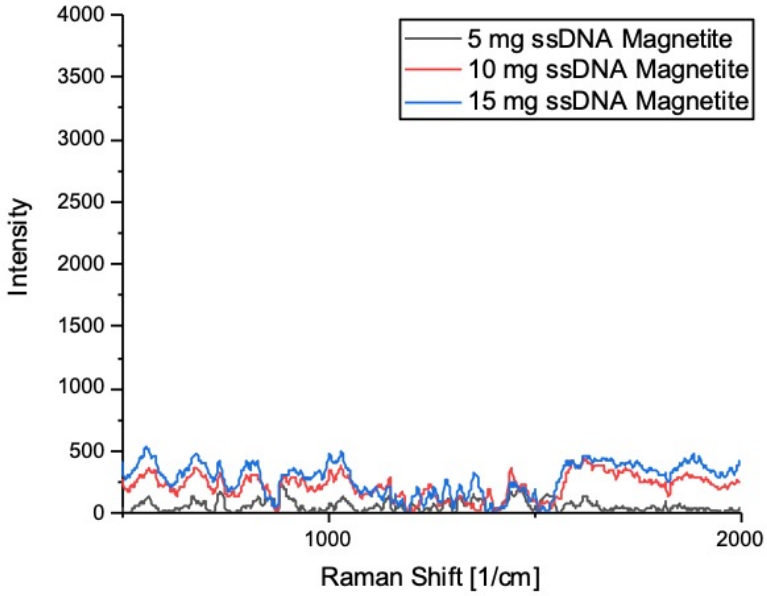

Figure A5: Raman spectra of each concentration of the ssDNA-stabilised magnetite nanoparticles.

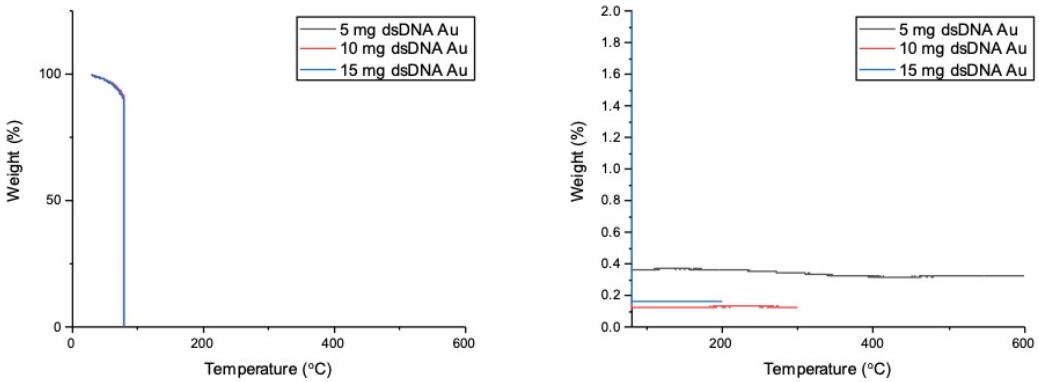

Figure A6: TGA curves for each concentration of the dsDNA-stabilised gold nanoparticles.

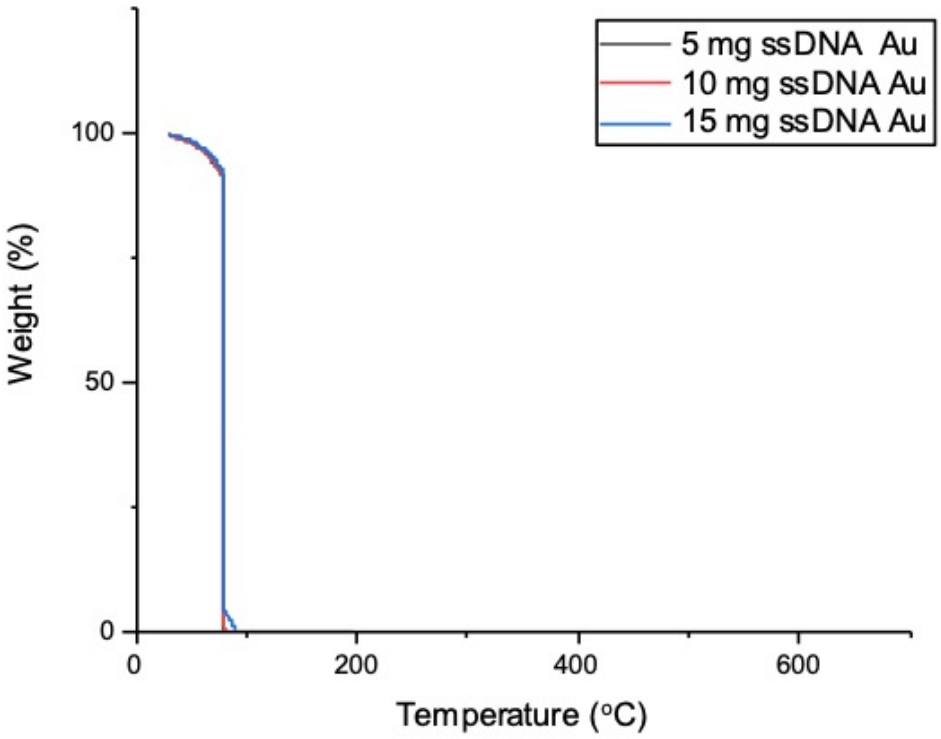

Figure A7: TGA curves for the ssDNA-stabilised gold nanoparticles.

	1	2	3	4	5	6	7
A	5 mg dsDNA magnetite and 5 mg dsDNA gold nanoparticles	5 mg dsDNA magnetite and 10 mg dsDNA gold nanoparticles	5 mg dsDNA magnetite and 15 mg dsDNA gold nanoparticles	5 mg dsDNA magnetite and 5 mg ssDNA gold nanoparticles	5 mg dsDNA magnetite and 10 mg ssDNA gold nanoparticles	5 mg dsDNA magnetite and 15 mg ssDNA gold nanoparticles	5 mg dsDNA magnetite and PAH gold nanoparticles
B	10 mg dsDNA magnetite and 5 mg dsDNA gold nanoparticles	10 mg dsDNA magnetite and 10 mg dsDNA gold nanoparticles	10 mg dsDNA magnetite and 15 mg dsDNA gold nanoparticles	10 mg dsDNA magnetite and 5 mg ssDNA gold nanoparticles	10 mg dsDNA magnetite and 10 mg ssDNA gold nanoparticles	10 mg dsDNA magnetite and 5 mg ssDNA gold nanoparticles	10 mg dsDNA magnetite and PAH gold nanoparticles
C	15 mg dsDNA magnetite and 5 mg dsDNA gold nanoparticles	15 mg dsDNA magnetite and 10 mg dsDNA gold nanoparticles	15 mg dsDNA magnetite and 15 mg dsDNA gold nanoparticles	15 mg dsDNA magnetite and 5 mg ssDNA gold nanoparticles	15 mg dsDNA magnetite and 10 mg ssDNA gold nanoparticles	15 mg dsDNA magnetite and 15 mg ssDNA gold nanoparticles	15 mg dsDNA magnetite and PAH gold nanoparticles
D	5 mg ssDNA magnetite and 5 mg dsDNA gold nanoparticles	5 mg ssDNA magnetite and 10 mg dsDNA gold nanoparticles	5 mg ssDNA magnetite and 15 mg dsDNA gold nanoparticles	5 mg ssDNA magnetite and 5 mg ssDNA gold nanoparticles	5 mg ssDNA magnetite and 10 mg ssDNA gold nanoparticles	5 mg ssDNA magnetite and 15 mg ssDNA gold nanoparticles	5 mg ssDNA magnetite and PAH gold nanoparticles
E	10 mg ssDNA magnetite and 5 mg dsDNA gold nanoparticles	10 mg ssDNA magnetite and 10 mg dsDNA gold nanoparticles	10 mg ssDNA magnetite and 15 mg dsDNA gold nanoparticles	10 mg ssDNA magnetite and 5 mg ssDNA gold nanoparticles	10 mg ssDNA magnetite and 10 mg ssDNA gold nanoparticles	10 mg ssDNA magnetite and 15 mg ssDNA gold nanoparticles	10 mg ssDNA magnetite and PAH gold nanoparticles
F	15 mg ssDNA magnetite and 5 mg dsDNA gold nanoparticles	15 mg ssDNA magnetite and 10 mg dsDNA gold nanoparticles	15 mg ssDNA magnetite and 15 mg dsDNA gold nanoparticles	15 mg ssDNA magnetite and 5 mg ssDNA gold nanoparticles	15 mg ssDNA magnetite and 10 mg ssDNA gold nanoparticles	15 mg ssDNA magnetite and 15 mg ssDNA gold nanoparticles	15 mg ssDNA magnetite and PAH gold nanoparticles

Figure A8: Table showing the nanocomposite corresponding to each code.

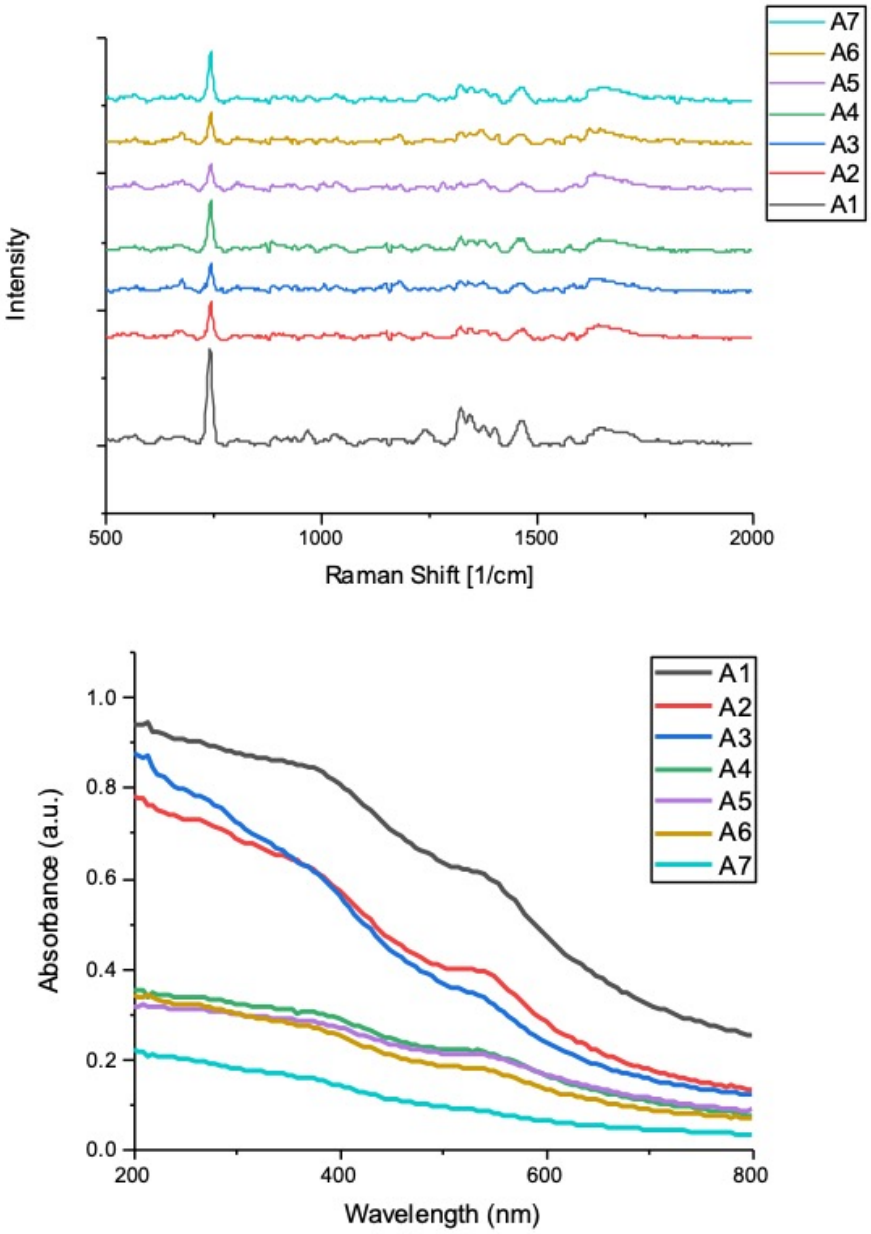

Figure A9: Raman and UV-Vis spectra for nanocomposites A1 - A7.

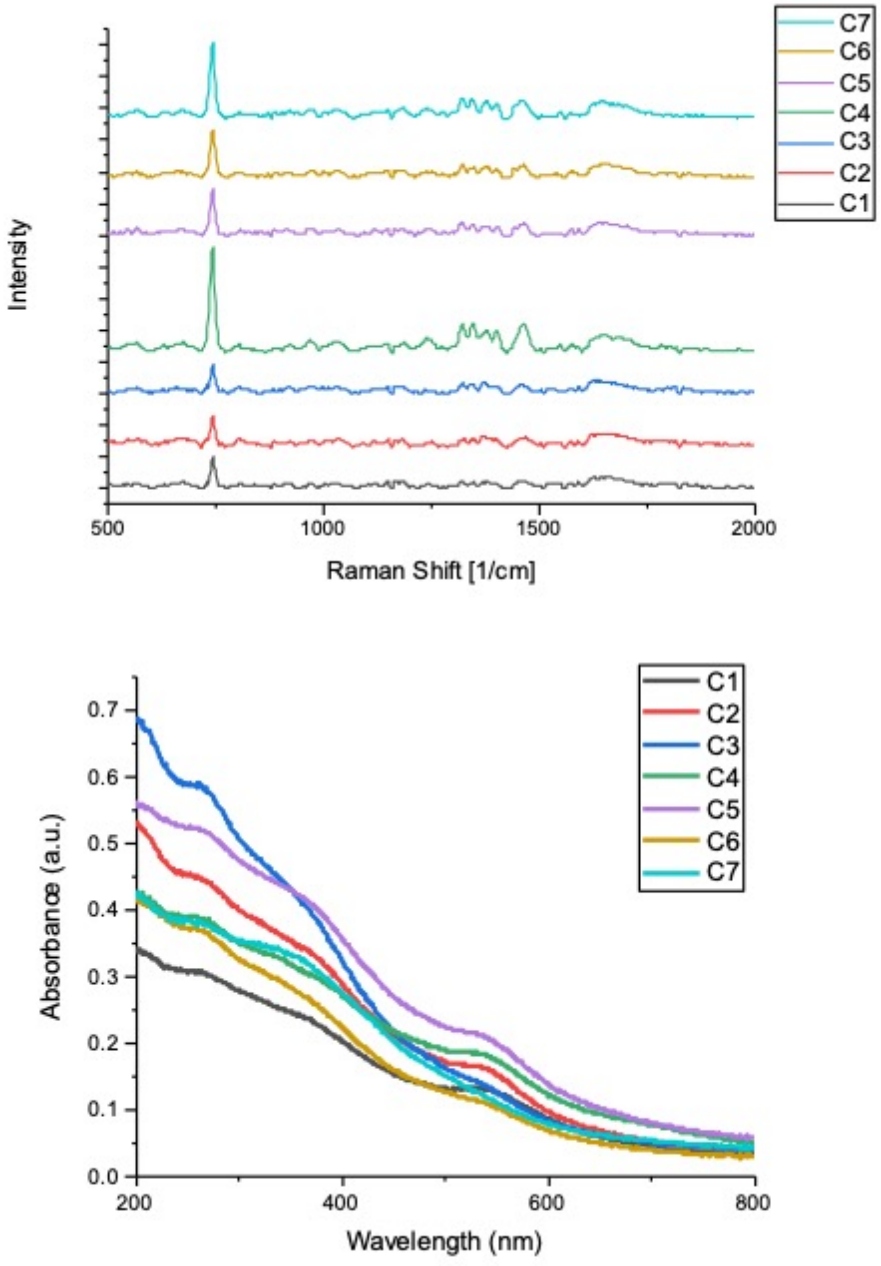

Figure A10: Raman and UV-Vis spectra for nanocomposites C1 - C7.

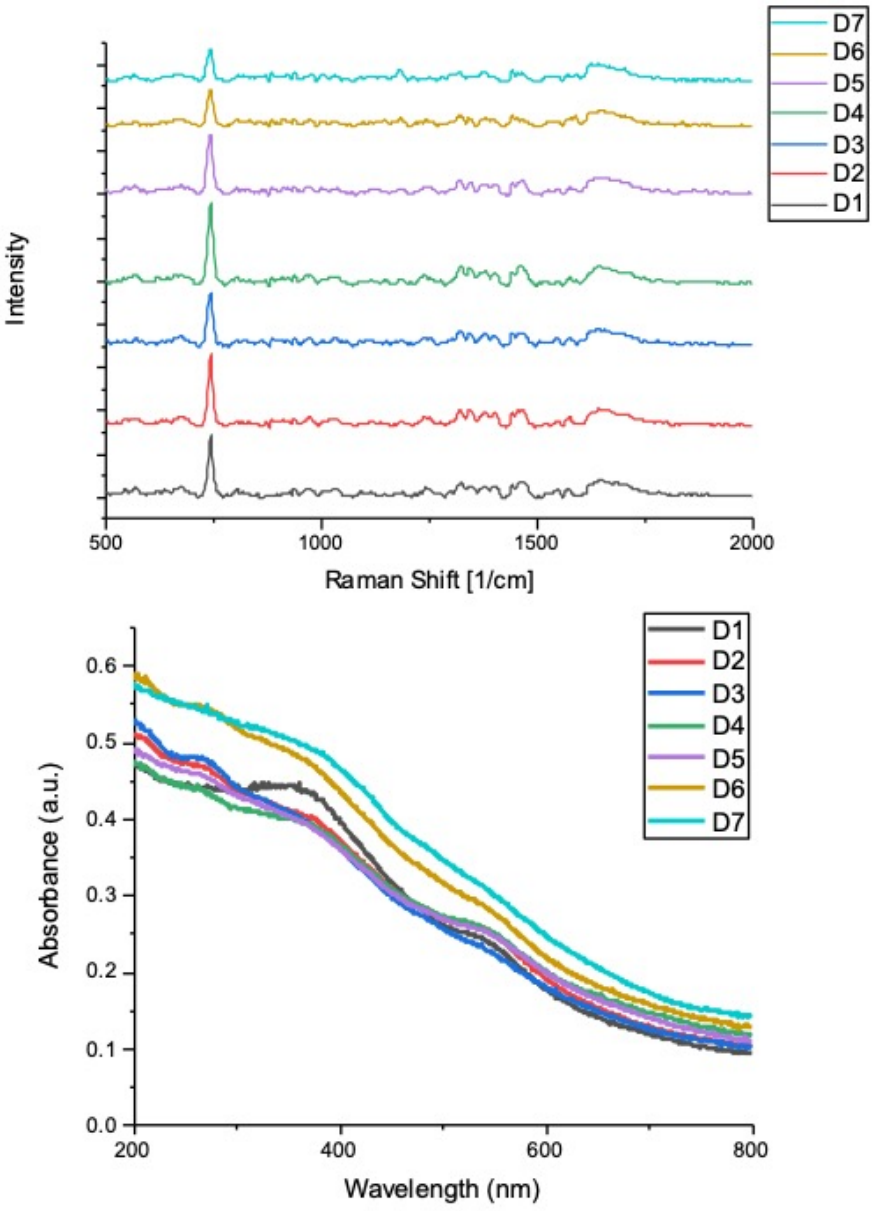

Figure A11: Raman and UV-Vis spectra for nanocomposites D1 - D7.

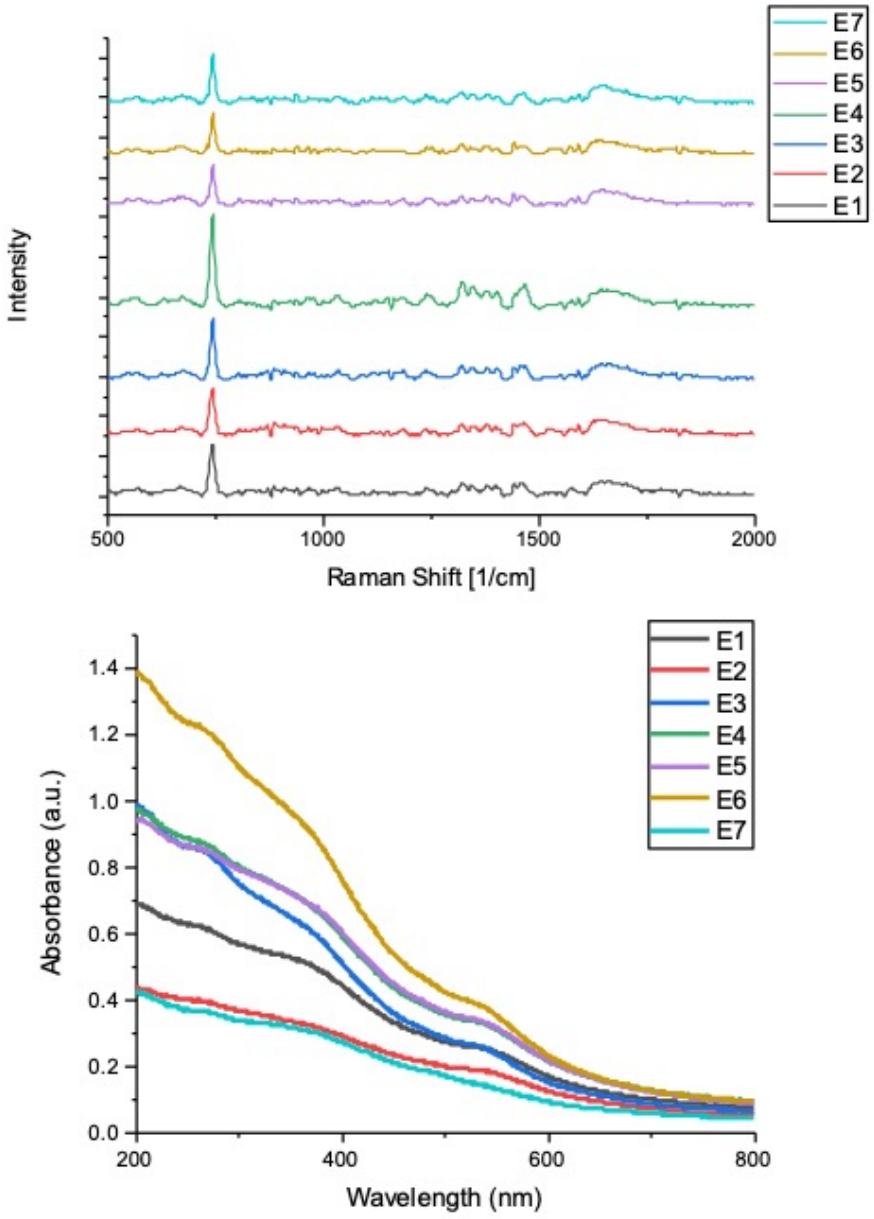

Figure A12: Raman and UV-Vis spectra for nanocomposites E1 - E7

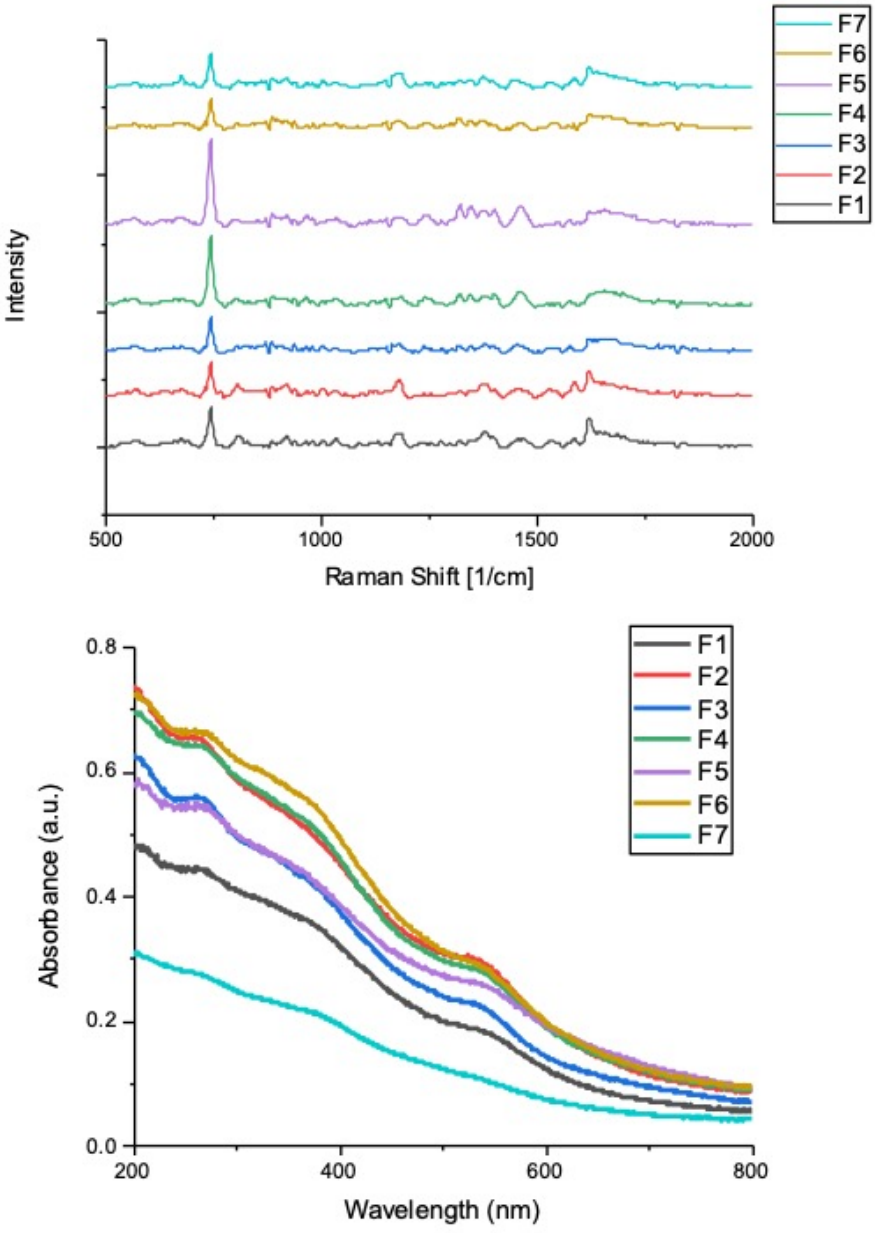

Figure A13: Raman and UV-Vis spectra for nanocomposites F1 - F7

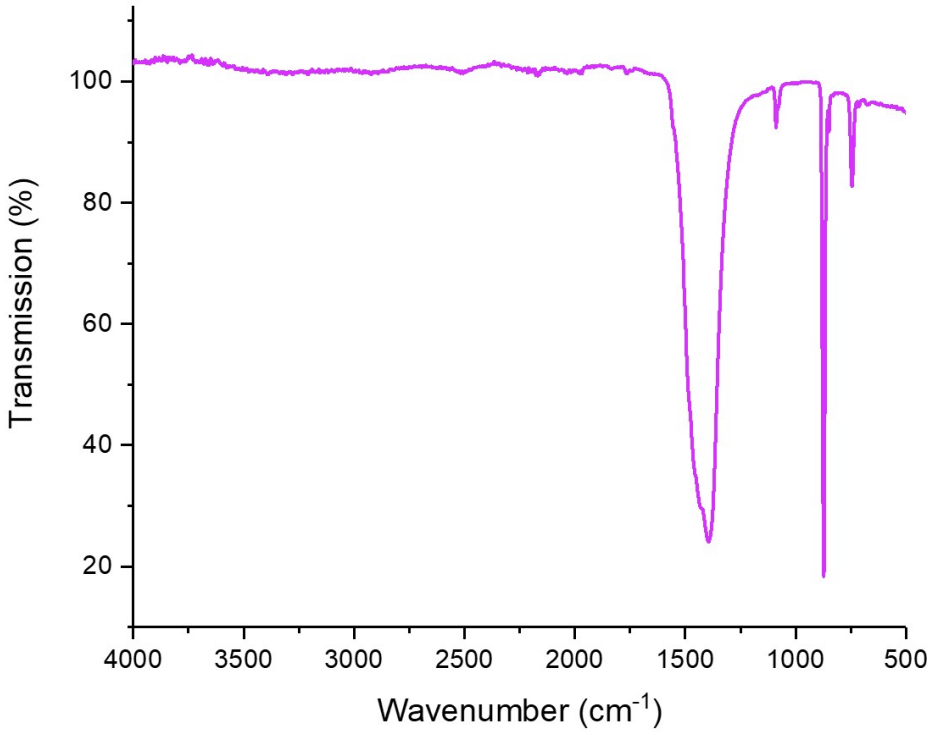

Figure A14: FTIR spectra of $CaCO_3$ microspheres

Publications

Publication List

S. Stafford, C. Garnier, Y. K. Gun'ko, *Nanomaterials*, 2018, **12**, 1044.

S. Stafford, R. Serrano Garcia, Y. K. Gun'ko, *Applied Sciences*, 2018, **8**, 97.

R. Serrano Garcia, **S. Stafford**, Y. K. Gun'ko, *Applied Sciences*, 2018, **8**, 172.

I. V. Martynenko, D. Kusíc, F. Weigert, **S. Stafford**, F. C. Donnelly, R. Evstigneev, Y. Gromova, A. V. Baranov, B. Rühle, H. J. Kunte, Y. K. Gun'ko, and U. Resch-Genger, *Analytical Chemistry*, 2019, **91**, 12661.

M. P. Moloney, C. Cabaud, **S. Stafford**, Y. K. Gun'ko, M. Venkatesan, A. Grandjean, *Colloids and Surfaces A: Physicochemical and Engineering Aspects*, 2019, **582**, 123758.

A. Grandjean, M. P. Moloney, C. Cabaud, **S. Stafford**, Y. K. Gun'ko, M. Venkatesan, *New Journal of Chemistry*, 2019.

Conference Presentations

2019 MRS Spring Meeting and Exhibit, *The Development of Novel Multimodal Magnetic Plasmonic Nanocomposites for Applications in Biosensing and Theranostics*, April 24, 2019